



**Università
degli Studi
di Palermo**

AREA QUALITÀ, PROGRAMMAZIONE E SUPPORTO STRATEGICO
SETTORE STRATEGIA PER LA RICERCA
U. O. DOTTORATI

Dottorato di Ricerca in Scienze della Terra e del Mare
Dipartimento di Scienze della Terra e del Mare (DiSTeM)
Settore Scientifico Disciplinare – SSD GEO/08 – Geochimica e Vulcanologia

GEOGENIC CARBON DIOXIDE DEGASSING FROM ACTIVE TECTONIC AREAS OF THE BALKAN PENINSULA

LA DOTTORESSA
LORENZA LI VIGNI

IL COORDINATORE
ALESSANDRO AIUPPA

IL TUTOR
FRANCESCO PARELLO

CO TUTOR
WALTER D'ALESSANDRO

CICLO XXXV
ANNO CONSEGUIMENTO TITOLO 2023



UNIVERSITÀ DEGLI STUDI DI PALERMO



ISTITUTO NAZIONALE
DI GEOFISICA E VULCANOLOGIA



Unione europea
Fondo sociale europeo



FSE FONDO SOCIALE EUROPEO
SICILIA 2020
PROGRAMMA OPERATIVO



Università degli Studi di Palermo (Palermo, Italy)
Dipartimento di Scienze della Terra e del Mare (DiSTeM)

Istituto Nazionale di Geofisica e Vulcanologia (sez. Palermo, Italy)

DOTTORATO DI RICERCA IN SCIENZE DELLA TERRA
SSD GEO/08 – GEOCHIMICA & VULCANOLOGIA
XXXV CICLO

Geogenic carbon dioxide degassing from active tectonic areas of the Balkan Peninsula

PhD thesis by:
Lorenza Li Vigni

IL COORDINATORE
Aiuppa Alessandro

SUPERVISOR
Parello Francesco

CO-SUPERVISOR
D'Alessandro Walter



HELLENIC REPUBLIC
National and Kapodistrian
University of Athens



Izotóp
Klimatológiai
és Környezetkutató
Központ



UNIVERSITATEA
BABEŞ-BOLYAI

Index

PREFACE.....	4
ACKNOWLEDGEMENT.....	5
ABSTRACT	8
RIASSUNTO	10
PART I	12
CHAPTER 1 - INTRODUCTION.....	13
CHAPTER 2 - GEOLOGICAL SETTINGS OF THE SOUTHERN BALKAN PENINSULA	18
2.1 SOUTHERN BALKAN PENSINSULA: A GEODYNAMIC OVERVIEW	18
2.2 GREECE.....	23
2.2.1 <i>Geodynamic setting</i>	24
2.3 NORTH MACEDONIA	26
2.3.1 <i>Geothermal fields</i>	30
CHAPTER 3 - KARST HYDROSYSTEMS IN GREECE	32
3.1 GENERAL INFORMATION ABOUT THE KARST ENVIRONMENT	32
3.2. KARST HYDROSYSTEMS IN GREECE	33
CHAPTER 4 - MATERIALS & METHODS	37
4.1 WATER SAMPLING AND ANALYTICAL METHODS	37
4.2 GAS SAMPLING AND ANALYTICAL METHODS	39
4.2.1 <i>Gas sampling</i>	39
4.2.2 <i>Analytical methods</i>	39
4.3 CARBON DIOXIDE FLUX MAPS	41
PART II.....	43
CHAPTER 5 - HELLENIC KARST HYDROSYSTEMS: GEOGENIC AND ANTHROPOGENIC PROCESSES AFFECTING THEIR GEOCHEMISTRY AND WATER QUALITY	44
5.1. RESULTS.....	45
5.1.1 <i>Major ions</i>	45
5.1.2 <i>Trace elements</i>	47
5.2. DISCUSSION	48
5.2.1. <i>Geogenic processes</i>	48
5.2.2 <i>Quality issues</i>	52
5.2.2.1 <i>Salinity issues</i>	52
5.2.2.2 <i>Nitrate</i>	56
5.2.2.3 <i>Strontium</i>	58
5.2.2.4 <i>Chromium and Nickel</i>	60
5.2.2.5 <i>Arsenic</i>	61
5.2.2.6 <i>Lead</i>	62
5.3 CONCLUSION.....	63
CHAPTER 6 - IMPACT OF GEOGENIC DEGASSING ON C-ISOTOPIC COMPOSITION OF DISSOLVED CARBON IN KARST SYSTEMS OF GREECE	64
6.1 GAS GEOCHEMISTRY.....	64
6.2 CARBON MASS BALANCE OF THE AQUIFERS.....	68
6.3 CARBON BALANCE OF THE HELLENIC KARST AQUIFERS	69
6.4 CONCLUSIONS	75
PART III	76
CHAPTER 7 - GEOCHEMISTRY OF GAS MANIFESTATIONS OF NORTH MACEDONIA	77

7.1 RESULTS.....	78
7.1.1 Chemical composition of the gases	78
7.1.2 Isotopic composition of the gases.....	81
7.2. DISCUSSION	83
7.2.1 Origin of CO ₂ and He.....	83
7.2.2 Origin of methane and light hydrocarbons	86
7.2.3 Geological implication in a regional context	90
7.3 CONCLUSIONS.....	94
CHAPTER 8 - DEGASSING AREAS OF NORTH MACEDONIA.....	96
8.1 GAS MANIFESTATIONS OF BITOLA BASIN	96
8.2 GAS MANIFESTATIONS OF THE SOUTHWESTERN REGION	99
8.3 CARBON DIOXIDE OUTPUT ESTIMATION OF PETKONIVA AND BOTUN	100
8.4 CONCLUSIONS.....	104
CHAPTER 9 - DUVALO “VOLCANO”: A PURELY TECTONIC RELATED CO₂ DEGASSING SYSTEM ...	105
9.1 INTRODUCTION	105
9.2 GEOLOGICAL SETTINGS.....	107
9.3 RESULTS.....	109
9.4 DISCUSSION	112
9.4.1 Origin of the gases	112
9.4.2 Processes affecting gas composition in the soil	116
9.4.3 CO ₂ flux mapping and CO ₂ output estimation.....	118
9.5 DUVALO IN THE REGIONAL CONTEXT	120
9.6 CONCLUSIONS.....	123
REFERENCES	124
APPENDIX.....	141
APPENDIX A1 - THE GEOTHERMAL FIELDS OF REPUBLIC OF NORTH MACEDONIA	142
A.1 GEVGELJIA GEOTHERMAL FIELD.....	142
A.2 KATLANOVO GEOTHERMAL FIELD	143
A.3 KEZOVICA GEOTHERMAL FIELD.....	144
A.4 KOCHANI GEOTHERMAL FIELD	144
A.5 KUMANOVKO GEOTHERMAL FIELD	145
A.6 STRUMICA GEOTHERMAL FIELD.....	145
APPENDIX A2.....	147
TABLE A1	147
TABLE A2	152
TABLE A3	159
TABLE A4	166
TABLE A5	173
TABLE A6	177
TABLE A8	182

Preface

This thesis is subdivided in three parts. The part I consists of an introduction presented in Chapter I; the description of the investigated areas in Chapter II; a brief description of karst environment in Chapter III and, materials and methods in Chapter IV. The part II consists of the hydrogeochemical investigation and geogenic carbon estimation (results, discussion and conclusion) regarding the main karst hydro-systems of Greece, presented in Chapters V and VI. Lastly, the part III presents the results on the geochemistry of the main gas manifestation in the Republic of North Macedonia evidencing their possible origins and investigating their relationship with the tectonic framework of the region (from Chapter VII to Chapter IX).

The case studies presented in this work are the results, discussions and conclusions of the articles in progress, under review or already published in international journal by the author of the thesis. The Chapter V is an article under review, whereas the Chapter IX is an already published article.

Acknowledgement

The present study has been made in the framework of many international collaborations between researchers of Università degli Studi di Palermo, Istituto Nazionale di Geofisica e Vulcanologia – sezione di Palermo (INGV – sez. Pa), Università degli Studi di Perugia, National and Kapodistrian University of Athens (Greece), University of Potsdam (Germany), Institute for Nuclear Research, Hungarian Academy of Sciences (ICER) and Babes-Bolyai University (Cluj-Napoca, Romania).

The research in Greece and Republic of North Macedonia were funded by the DCO Grant no. 10881-TDB “Improving the estimation of tectonic carbon flux”, by the European Social Fund (PO FSE Sicilia 2014–2020) in the frame of the project “Metodi di controllo geochimico e geofisico dei fenomeni naturali sul campo ed in laboratorio” (CUP: G77B17000200009), by the Italian Ministero Istruzione Università e Ricerca (MIUR, under Grant PRIN2017-2017LMNLAW “Connect-4Carbon”). Furthermore, the research in Republic of North Macedonia was also supported by the European Union and the State of Hungary, co-financed by the European Regional Development Fund in the project of GINOP-2.3.2-15-2016-00,009 “ICER.” Fieldworks were carried out under Research Permits Nos. UP1-11/1-691/2019 and UP1-11/1-1829/2019 issued by the Ministry of Environment and Physical Planning of the Republic of North Macedonia.

I would like to thank my supervisor, Prof. Francesco Parello, for his presence and his precious help in preparing the final talk, which means getting out of my comfort zone. I am really grateful to my co-tutor, Dr. Walter D'Alessandro (INGV - sez. PA), sincere mentor, for his endless patience and for generously sharing his knowledge and expertise. Thanks should also to Dr. Sergio Calabrese (University of Palermo), who provided me with the opportunity to join not only a research team but also the big family of Associazione Naturalistica Geode. I would like to express my gratitude to my colleague, Filippo Brugnone, companion in this great adventure, for his scientific and moral support and the continuous exchange of ideas.

I am thankful to the Istituto Nazionale di Geofisica e Vulcanologia (INGV) and his staff (Sergio Bellomo, Lorenzo Brusca, Francesco Salerno, Mariano Tantillo, Ygor Oliveri and Aldo Sollami) for their kind analytical support. I would like to extend my sincere thanks to Prof. Konstantinos Kyriakopoulos (University of Athens), Kata Molnàr (Institute for Nuclear Research, Hungarian Academy of Sciences) and Artur Ionescu (Babes-Bolyai University) for their helping in field trips, and to Kyriaki Daskalopoulou (University of Postdam), Marjan Temovski (Institute for Nuclear Research, Hungarian Academy of Sciences) and Prof. Carlo Cardellini (University of Perugia) for their help in the organizing of field trips and for the continuous sharing of their scientific discussion and suggestions. I would also like to acknowledge the two reviewers, Franco Tassi (University of Firenze) and Fatima Viveiros (University of Azores), for their precious suggestions and comments to improve this PhD. Thesis.

I am deeply thankful to my whole family for their support and taking care of my son, Davide, during the entire PhD period and, especially, during the field trips. I must express my very profound gratitude to my husband, Giovanni, for providing me with unfailing support and continuous encouragement throughout my years of study and research.

Last but not least, I wish to thank myself for holding out until the end despite periods when I wanted to give up.

*I want to dedicate this thesis to Davide and Alessandra,
so that they can always follow their dreams
and look at the world with their curious childlike eyes.*

Abstract

Since the 1970s, scientific research evidenced the close relationship between deeply-derived carbon degassing and active tectonic zones, highlighting the utmost importance of tectonic degassing contribution within the global carbon cycle.

Large-scale degassing of mantle-derived carbon, Quaternary volcanic activity, seismic activity, and regional active fault systems are widespread in the Balkan Peninsula. However, the estimation of geogenic CO₂ release from this area is currently still poorly quantified. This PhD research is focused on (*i*) the estimation of endogenous carbon release from the main karst hydro-systems of Greece and on (*ii*) the chemical and isotopic characterization of the main gas manifestation in North Macedonia. Moreover, a study about the geogenic and anthropogenic processes affecting the water quality of Hellenic karst aquifers was carried out.

Three main water types were recognized in the Hellenic karst aquifers: (*i*) calcium-bicarbonate for hinterland springs; (*ii*) sodium-chloride for coastal springs; (*iii*) calcium-sulfate derived from gypsum dissolution. Results in terms of major ions and trace elements were compared with the drinking water limits set by the Directive 98/83/EC and the Directive 2020/2184/EC, which are rarely exceeded except for parameters related to marine intrusion along the coastal areas (EC, Na, Cl, B). In these springs, the highest nitrate levels are also found, though always below the drinking water limit. Regarding the chemical composition of the dissolved and free gases collected in the above-mentioned springs, the nitrogen is the dominant gas (up to 985,300 μmol mol⁻¹). The δ¹³C_{TDIC} varies between -16.6 ‰ and -0.10 ‰ (vs. V-PDB), whereas the δ¹³C_{CO₂} in free gases ranged from -29.9 ‰ to -7.41 ‰ (vs. V-PDB). The isotopic composition of helium was measured in few samples (R/R_A = 0.20 - 0.33), with values indicating a mainly crustal source. An estimation of the endogenous carbon (1.43 × 10⁹ mol a⁻¹) released from these systems was carried out, applying the isotope-carbon mass balance. The geogenic source of carbon may be associated to multiple sources, such as thermo-metamorphism of buried carbonates associated to intrusions of Quaternary

magmatic bodies and/or regional tectonic structures.

The research about the gas manifestations in North Macedonia represented a first catalogue, although still incomplete. The collected gas manifestations, comprising both thermal and cold systems, were subdivided in three groups: (*i*) N₂-dominated group; (*ii*) CO₂-dominated group; (*iii*) H₂S-rich group. These categories are geographically well separated, mainly, related to the extensional tectonic regime of the area and, sometimes, associated with boundaries between the major geotectonic units. The $\delta^{13}\text{C}_{\text{CO}_2}$ varies between -15.7 ‰ and +1.0 ‰, whereas the R/R_A values vary from 0.1 to 1.8, suggesting a prevailing crustal source with a mantle contribution up to 20%. On the other hand, the isotope composition of methane showed $\delta^{13}\text{C}_{\text{CH}_4}$ values ranging between -57.8 ‰ and -7.2 ‰ and $\delta^2\text{H}_{\text{CH}_4}$ varying from -303 ‰ to -80 ‰. Furthermore, soil CO₂ flux measurements were carried out at Duvalo Kosel, Petkoniva and Botun. Regarding the former, a detailed investigation was carried out, estimanting a total CO₂ output of 66.9 t × d⁻¹. A preliminary investigation was done at Petkoniva and Botun, limited only to patches with heavy soil alteration and devoid of vegetation, revealing a CO₂ output of 0.20 t × d⁻¹ at Petkoniva and of 0.59 t × d⁻¹ at Botun.

Riassunto

Sin dagli anni '70, la ricerca scientifica ha evidenziato una forte relazione tra il degassamento di carbonio profondo e le aree tettonicamente attive, sottolineando l'elevata importanza del contributo di queste emissioni nella quantificazione del carbonio globale.

La Penisola Balcanica presenta grandi aree caratterizzate da degassamento di carbonio di origine mantellica, da attività vulcaniche Quaternarie, da un'elevata sismicità e da strutture tettoniche a scala regionale. Purtroppo, la stima del degassamento di anidride carbonica profonda in quest'area è ancora poco studiata. La ricerca di questa tesi di dottorato si è focalizzata sulla (i) stima dell'output di carbonio profondo dalle grandi sorgenti carsiche della Grecia, e sulla (ii) caratterizzazione della composizione chimica e isotopica delle principali manifestazioni gassose della Macedonia del Nord. Inoltre, è stato condotto anche uno studio sull'impatto dei processi geogenici ed antropogenici sulla qualità delle acque dei grandi sistemi carsici della Grecia.

Negli acquiferi carsici delle Grecia sono state riconosciute tre principali composizioni chimiche dell'acqua: (i) bicarbonato-calcica per le sorgenti continentali; (ii) cloruro-sodica per le sorgenti in area di costa, (iii) solfato-calcica dovuta a processi di dissoluzione di gesso all'interno dell'acquifero. I risultati, in termini di specie maggiori ed elementi in traccia, sono stati comparati con i limiti sulle acque potabili imposte dalle Direttive della Comunità Europea, CE/98/83 e CE/2020/2184, i quali raramente vengono superati tranne per quei parametri che risentono della influenza dell'intrusione marina (Conduttività Elettrica, Na, Cl, B). In queste sorgenti, sono stati rivelati elevati valori di nitrato, sebbene sempre al di sotto del limite di potabilità.

Per quanto riguarda la composizione chimica dei gas disciolti e liberi, l'azoto risulta essere il gas dominante, con concentrazioni fino a $985,300 \mu\text{mol mol}^{-1}$. Il $\delta^{13}\text{C}_{\text{TDIC}}$ varia tra -16.6 ‰ e -0.10 ‰ (vs. V-PDB), mentre il $\delta^{13}\text{C}_{\text{CO}_2}$, misurato nel gas libero, varia da -29.9 ‰ a -7.41 ‰ (vs. V-PDB).

La composizione isotopica dell'elio è stata misurata solo in pochi campioni ($R/R_A = 0.20 - 0.33$), con valori che indicano una sorgente principalmente crostale. Applicando il bilancio di massa del

carbonio, è stata fatta una stima del carbonio endogenico (1.43×10^9 mol a⁻¹), la quale sorgente potrebbe essere associata a diverse sorgenti, tra cui termo-metamorfismo di carbonati indotto dall’intrusione di corpi magmatici di età Quaternaria e/o strutture tettoniche regionali.

La ricerca condotta in Macedonia del Nord rappresenta un primo catalogo delle principali manifestazioni gassose presenti nell’area, sebbene ancora incompleto. Le manifestazioni gassose campionate, comprendenti sia sistemi caldi sia sistemi freddi, sono stati suddivisi in tre gruppi: (i) dominati in N₂; (ii) dominati in CO₂; (iii) ricchi in H₂S. Queste categorie sono ben separate geograficamente, associate, soprattutto, al regime tettonico estensionale e, spesso, associati alle aree di confine tra le principali unità geotettoniche. Il $\delta^{13}\text{C}_{\text{CO}_2}$ varia tra -15.7 ‰ e +1.0 ‰, mentre i valori di R/R_A variano da 0.1 a 1.8, suggerendo un’origine perlopiù crostale con un contributo mantellico fino al 20%. La composizione isotopica del metano presenta valori di $\delta^{13}\text{C}_{\text{CH}_4}$ tra -57.8 ‰ e -7.2 ‰ e valori di $\delta^2\text{H}_{\text{CH}_4}$ tra -303 ‰ e -80 ‰.

Inoltre, misure di flusso di CO₂ al suolo sono state condotte a Duvalo Kosel, Petkoniva e Botun. Per quanto riguarda Duvalo Kosel, un’area studiata in dettaglio, si è stimato una emissione di CO₂ di 66.9 t × d⁻¹. A Petkoniva and Botun sono state condotte delle misure preliminari, limitate ad aree caratterizzate da forte alterazione del suolo e mancanza di vegetazione, rivelando un flusso di CO₂ di 0.20 t × d⁻¹ a Petkoniva e di 0.59 t × d⁻¹ a Botun.

Part I

Chapter 1 - Introduction

During the last decades, scientific research concerning the estimation of endogenous carbon degassing to the atmosphere sharply increased due to the major role of this element in controlling the Earth climate over geological time (*Forster et al.*, 2017). Indeed, among the greenhouse gases, carbon dioxide and methane are considered to be the most effective species in contributing to the changing of global climate. The observations reported by NOAA Mauna Loa Observatory, updated to February 2023, reports a mean abundance of CO₂ and CH₄ respectively of 421.2 ppm and 1920 ppb in the atmosphere, with an increment of about 3% respect to the observations of 2018 reported in the fifteenth WMO Greenhouse Gas Bulletin (CO₂ = 407.8 ± 0.1 ppm; CH₄ 1,869 ± 2 ppb).

On geological timescale, the stability of climate indicates that greenhouse gas amounts into atmosphere are controlled by an internal thermostat (*Walker et al.*, 1981). In particular, the long-term climate is regulated by the *Earth's carbon cycle*, a complex cycle that encompasses two interconnected reservoirs, the exogenic and the endogenic carbon systems (*Fig.1.1*).

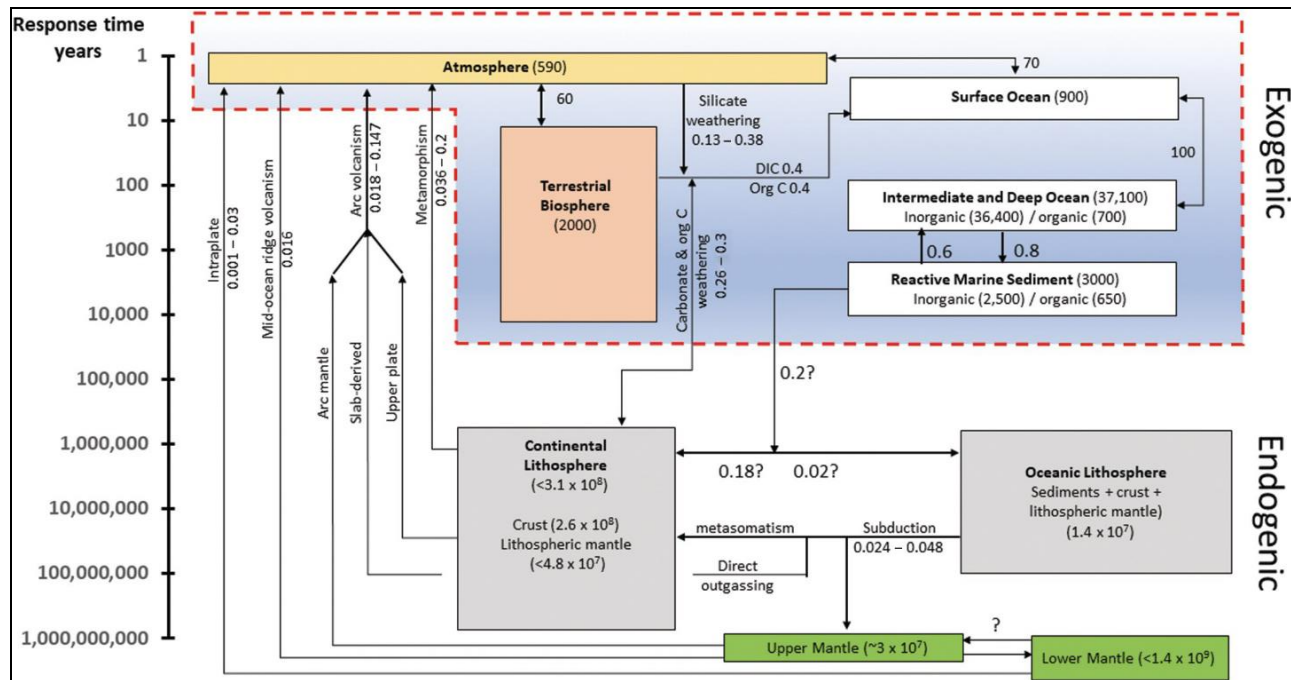


Fig.1.1. Box model of the Earth carbon cycle from *Lee et al.* (2019). Numbers by arrow represent the carbon fluxes expressed in Gton C y⁻¹.

The surface or exogenic system is defined as the sum of the hydrosphere, atmosphere, and biosphere, which cycle rapidly between each other, allowing for short-term variability of atmospheric CO₂. The exogenic sinks encompass the sequestration of carbonate in silicate weathering, photosynthesis, burial of organic carbon and subduction of altered crust, serpentized lithospheric mantle and seafloor sediments. The amount of non-anthropogenic carbon into the exogenic system is controlled by outgassing of the deep or endogenic system, which includes carbon degassing from core, mantle and lithosphere at plate boundary and intraplate settings (*Lee et al., 2019; Suarez et al., 2019; Wong et al., 2019*). The carbon enters the mantle through subduction processes and returns to exogenic reservoir during magmatic and tectonic activity (*Fig.1.2*). Thus, the relative motion of tectonic plates is the first key-control on the magnitude of Earth Carbon degassing (*Wong et al., 2019*). Nowadays, among the main perturbations of Earth's carbon cycle, the flux of anthropogenic carbon sources, such as the combustion of coal and other fossil fuels, shall also be considered (*Suarez et al., 2019*). Indeed, *Scott & Lindsey (2016)* estimate that the amount of CO₂ released by human activities is 60 times or more than that emitted by volcanoes.

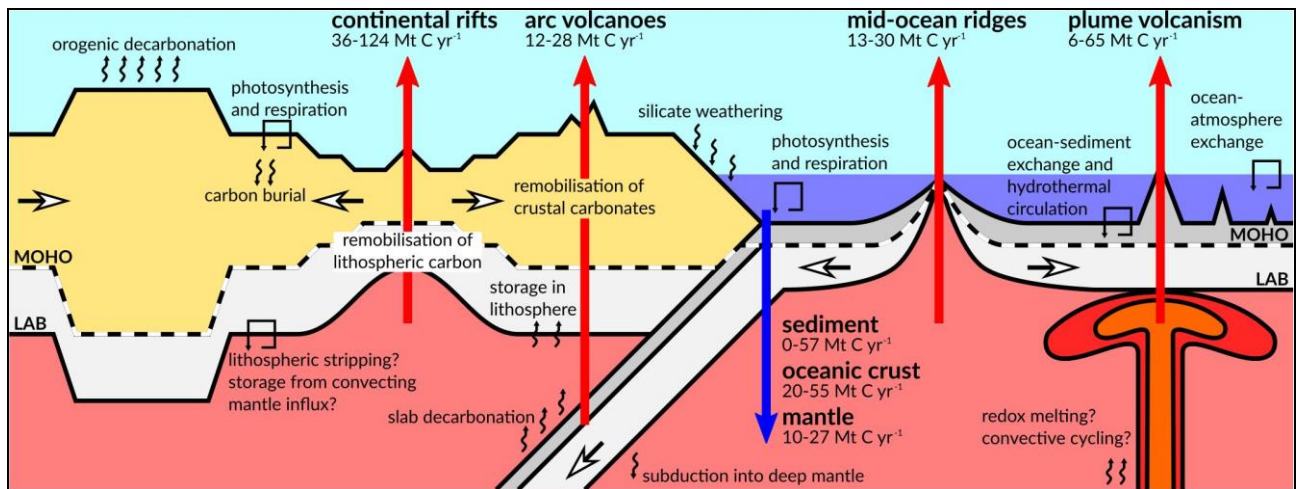


Fig.1.2. Major fluxes of carbon between exogenic and endogenic systems of the Earth from *Wong et al. (2019)*.

Despite a significant improvement in the worldwide dataset, the global flux of CO₂ degassing from the Earth's interior is still the least well-quantified part of the global cycle (*Berner & Lasaga, 1989*). Many studies have been devoted to the quantification of the release of geogenic CO₂ to the

atmosphere from different geological settings (e.g., *Kerrick, 2001; Mörner & Etiope, 2002; Brune et al., 2017*) and most of them have focused on the present-day CO₂ emission from volcanoes (*Brantley & Koepenick, 1995; Burton et al., 2013; Werner et al., 2019*). Although most volcanic sources are still unknown, the estimation of volcanic carbon budget is the most studied. The recent study of *Fischer et al. (2019)*, estimates a global volcanic CO₂ flux budget of 51.3 ± 5.7 Tg a⁻¹ for weakly emitting volcanoes and 1.8 ± 0.9 Tg a⁻¹ for eruptive degassing during the 2005-2015 period, converting CO₂ fluxes from the combination of either measured or estimated volcanic CO₂/S_T molar ratios and OMI-based mean SO₂ fluxes (*Aiuppa et al., 2017, 2019*).

Although the close relationship between tectonically active areas, fluid migration and geogenic diffuse carbon emissions has long been evidenced (*Barnes et al., 1978; Irwin & Barnes, 1980*), only in the last decades, several researches emphasize the tectonic carbon degassing as an important contribution to the global carbon cycle (*Seward & Kerrick, 1996; Chiodini et al., 1999; 2000; 2011; Kerrick et al., 1995; Lewicki & Brantley, 2000; Yuçe et al., 2017; Frondini et al., 2019*). Deep extensional fault systems, thanks to their enhanced permeability and porosity, play an important role in mantle-derived volatiles (e.g. CO₂ and He) transfer by creating preferential pathways for advective gas-carrying fluid rising from the deep crust or the mantle to the Earth's surface (*Faulkner et al., 2010; Hunt et al., 2017; Muirhead et al., 2016; Tamburello et al., 2018; Caracausi & Sulli, 2019*), escaping through the soil into the atmosphere as result of pressure decrease (*King, 1986*). At a global scale, the geographical distribution and the amount of deeply-derived fluids are controlled by regional normal/transcurrent faulting (*Tamburello et al., 2018*) and continental rift lengths (*Brune et al., 2017*). Furthermore, these geogenic fluids play an active role in deep earthquake generation (*Du et al., 2006; Miller et al., 1999; Chiodini et al., 2020; Caracausi et al., 2022*).

In active tectonically regions affected by flux of deep CO₂, the carbon mass balance of regional aquifers is a useful tool to quantify the non-volcanic diffuse carbon degassing. Indeed, thanks to the high solubility of CO₂ in water, regional aquifers can dissolve, transport and release huge amounts

of geogenic carbon dioxide into the atmosphere (*Rose & Davisson 1996; Sorey et al 1998*). Thus, studying the concentration of total dissolved inorganic carbon (TDIC) in groundwater, and its isotope composition ($\delta^{13}\text{C}_{\text{TDIC}}$), is a suitable method to estimate the regional flux of geogenic carbon (*Chiodini et al., 1999, 2000*). In this work, the above-mentioned approach is used to quantify the carbon dioxide emitted by big karst hydro-systems in Greece.

Large-scale degassing of mantle-derived carbon, Quaternary volcanic activity, seismic activity, and regional active fault systems are widespread in the Balkan Peninsula. However, the estimation of geogenic CO₂ release from this area is currently still poorly quantified (*Kis et al., 2017, 2019; Daskalopoulou et al., 2019a; D'Alessandro et al., 2020; Randazzo et al., 2021*).

The Hellenic territory, in southern part of Balkan Peninsula, accounts for more than one geogenic CO₂ source. Indeed, the territory is characterized by the South Aegean Active Volcanic Arc (SAAVA), several continental graben-basins, such as Sperchios basin (Central Greece) and Florina basin (North Greece), where many CO₂-rich gas manifestations are present. *Daskalopoulou et al. (2019)*, estimates a CO₂ degassing of 10⁵ t a⁻¹ from the main gas manifestation of whole Hellenic territory.

Republic of North Macedonia, in central part of Balkan Peninsula, is considered one of the richest regions in low-temperature geothermal resources (*Popovska-Vasilevska & Armenski, 2016*). Indeed, the Macedonian region is characterized by positive geothermal anomalies (from 60 mW m⁻² to 120 mW m⁻²; *Georgieva et al., 2000; Milivojevic, 1993*). The high heat flux and the thinning of the crust favoured the occurrence of 18 geothermal fields, including over 50 mineral and thermo-mineral springs. The gas characterization of these geothermal manifestation and the estimation of their outgassing are currently poorly studied (*Trojanović, 1925; Iloski et al., 1957; Markoski et al., 2019*).

The aims of this PhD project are: (i) estimate the rate of geogenic CO₂ outgassing associated with the regional karst aquifers of the Hellenic country; (ii) investigate the origin of the volatiles outgassed from the main geothermal manifestation of Republic of North Macedonia, analysing their chemical and isotopic compositions, and attempt to characterize the processes controlling their chemistry. Furthermore, the geochemical characterization of Hellenic karst springs has been used to discriminate the natural and anthropogenic processes that may affect their water quality.

The present study has been made in the framework of many international collaborations between researchers of Università degli Studi di Palermo, Istituto Nazionale di Geofisica e Vulcanologia – sezione di Palermo (INGV – sez. Pa), Università degli Studi di Perugia, National and Kapodistrian University of Athens (Greece), University of Potsdam (Germany), Institute for Nuclear Research, Hungarian Academy of Sciences (ICER) and Babes-Bolyai University (Cluj-Napoca, Romania).

Chapter 2 - Geological settings of the Southern Balkan Peninsula

2.1 Southern Balkan Peninsula: a geodynamic overview

The region of South-Eastern Europe (SEE) is one of the most geodynamically active regions in Europe. The Balkan Peninsula occupies an important segment of the Alpine–Himalayan collisional orogenic belt, that begins at the junction between the south-eastern Alps and the north-western Dinarides and comprises the entire Dinaride–Albanide–Hellenide, Carpatho–Balkan and Rhodope belts (*Fig.2.1*). The SEE region evolved during Phanerozoic geodynamic events controlled by plate convergence and collision, which occurred between the Eurasian and Gondwana (Africa) continental plates (*Blundell et al. 1992; Cvetkovic et al., 2016; Schmid et al., 2020*). This geodynamic regime was directly associated with the opening (Middle Triassic) and closure (Late Cretaceous) of the Vardar-Tethys ocean, whose remnants can be recognized in the ophiolite-bearing complex orogenic belt, the so-called Vardar-Tethyan mega-suture. Adria-derived units (e.g., Ionian zone, Pelagonian massif) dominate the basement west of the suture zone, whilst on the eastern side, Europe-derived units forming the Carpatho-Balkanides (e.g., Serbo-Macedonian massif, Circum-Rhodope). The area between the Dinarides-Hellenides and Carpatho-Balkanides orogens is known as Vardar zone (*Arsovski, 1997; Dumurdjanov et al., 2005*). The Vardar ophiolites form two sub-parallel, N-S striking belts called the Western Vardar ophiolitic belt and the Eastern Vardar ophiolitic belts (*Schmid et al., 2008*) (*Fig.2.1*). The western ophiolitic belt characterized by large ultramafic bodies and occurs as Jurassic ophiolites and ophiolitic mélanges in Bosnia (Krivaja–Konjuh), west Serbia (Zlatibor), east Albania (Mirdita) and north to central Greece (Pindos and Othris) (*Cvetkovic et al., 2016*). On the other hand, the lithological sequences of the Eastern Vardar ophiolites consist of gabbroic complexes overlain by massive lava flows, pillow lavas and rare peridotites (*Cvetković et al., 2016*).

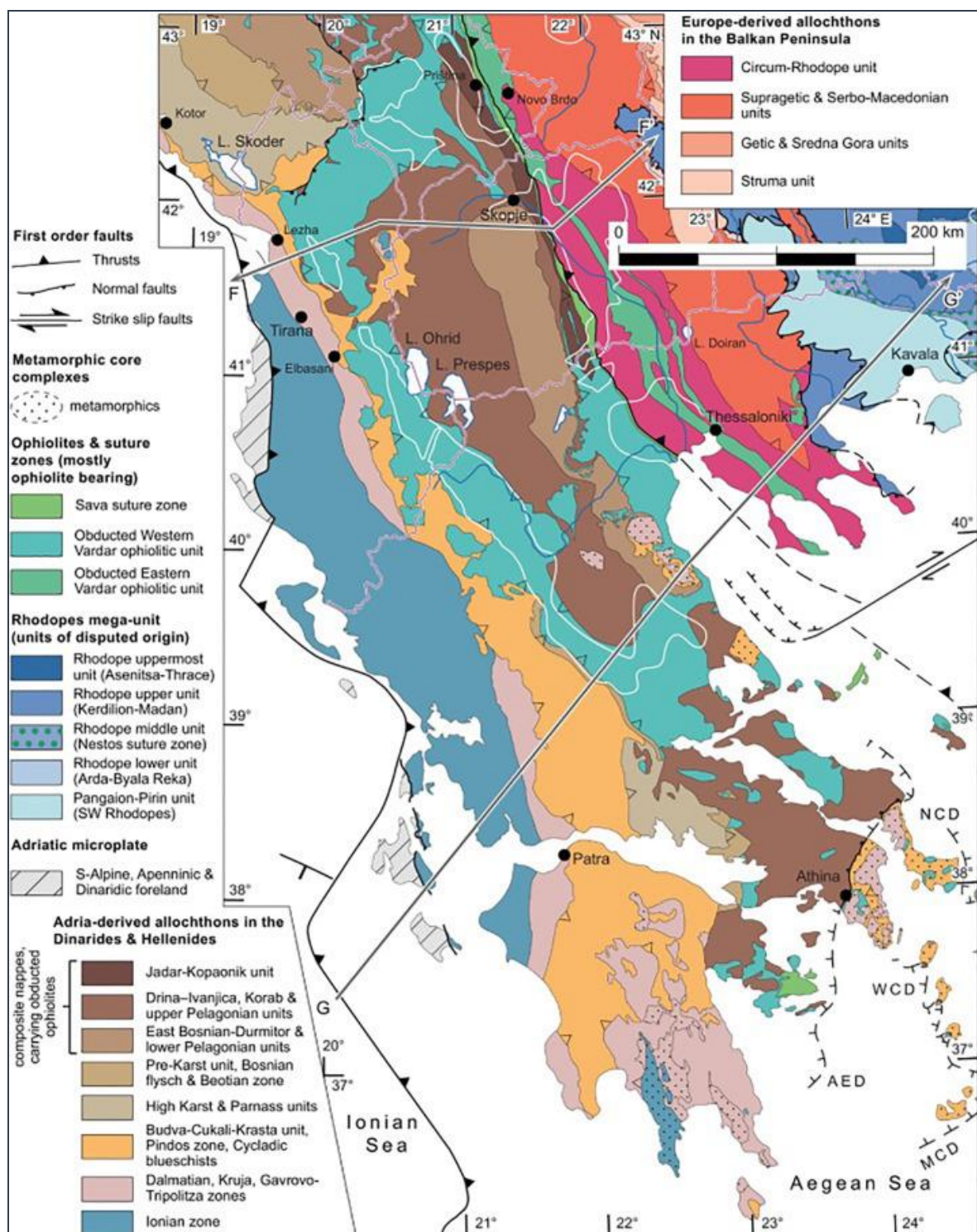


Fig.2.1. Map of tectonic units of the Hellenides and adjacent areas from Schmid *et al.* (2020).

During the Cenozoic, the Dinaride-Albanide-Hellenide-Carpathian-Balkan belts underwent remarkable tectonic reworking. Extensional tectonism began in the Late Cretaceous time during the final closure of Vardar-Tethys ocean and subsequent post-collisional deformation (Burchfiel *et al.*, 2008).

The **Cenozoic South Balkan extensional system** consists of normal faults and associated sedimentary basins within Bulgaria, North Macedonia, Albania, Greece and Turkey, and forms the northern part of regional Aegean extensional regime (Dumurdjanov *et al.*, 2005; Burchfiel *et al.*, 2008). Active extension within the South Balkan extensional systems consists of two parts: (i) the western part, consisting of E-W extension related to slab roll-back along the Hellenic subduction zone, and (ii) the eastern part, where the N-S extension is related to the slow southward motion of the South Balkan extensional system lithosphere, pulled southward by rapid movement of the Aegean Sea lithosphere, which is decoupled from the South Balkan extensional system across the North Anatolian fault zone (NAFZ) (Fig.2.2 - Burchfiel *et al.*, 2008).

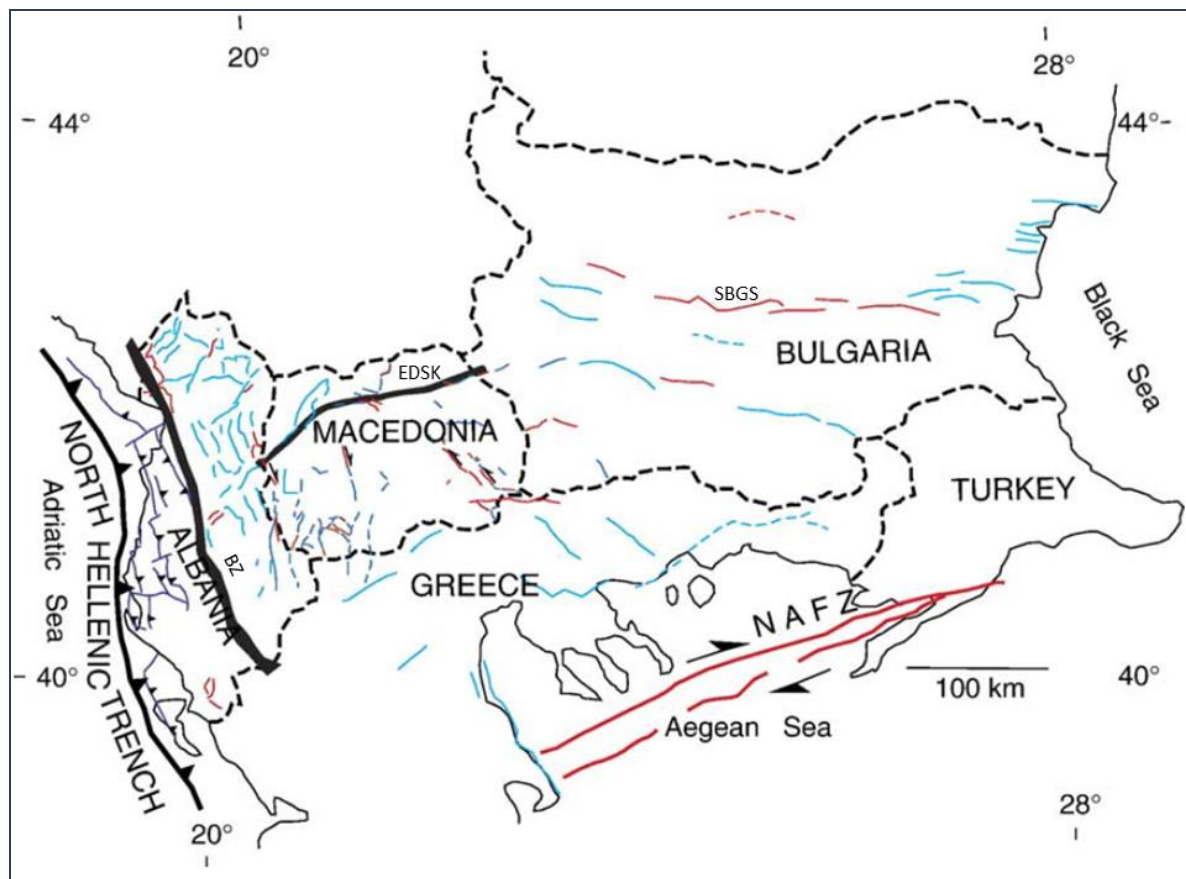


Fig.2.2. Active faults in the South Balkan extensional system from Burchfiel *et al.* (2006). Red lines are active faults; blue lines are faults with well-developed morphological evidence for recent activity; dashed blue lines are faults with weak morphological evidence for recent activity; purple ticked lines are thrust faults related to shortening in the hanging wall of the North Hellenic subduction zone. Black arrows mark the sense of displacement on strike-slip faults. **NAFZ** – North Anatolian Fault Zone; **EDSK** - Regional Elbasan-Debar-Skopje-Kjustendil fault zone; **SBGS** - South Balkan Graben System; **BZ** – Boundary Zone, indicating an abrupt change from shortening structures to the west and north-south-trending extensional structures to the east.

Extensive orogenic volcanism characterized the entire Balkan Peninsula since Late Cretaceous-Paleogene times, closely related to the complex tectonic evolution of the region (Burchfiel *et al.*, 2008; Cvetkovic *et al.* 2016). After the formation of a Late-Cretaceous large magmatic arc, with potassic to ultrapotasssic affinity (Molnár *et al.*, 2022), magmatism migrated to the Serbo-Macedonian Massif and Circum-Rhodope Belt in the Paleocene-Eocene times with the emplacement of large amounts of granitoid plutons at mid-crustal levels that have been exhumed by extension tectonics (Jolivet & Brun, 2010).

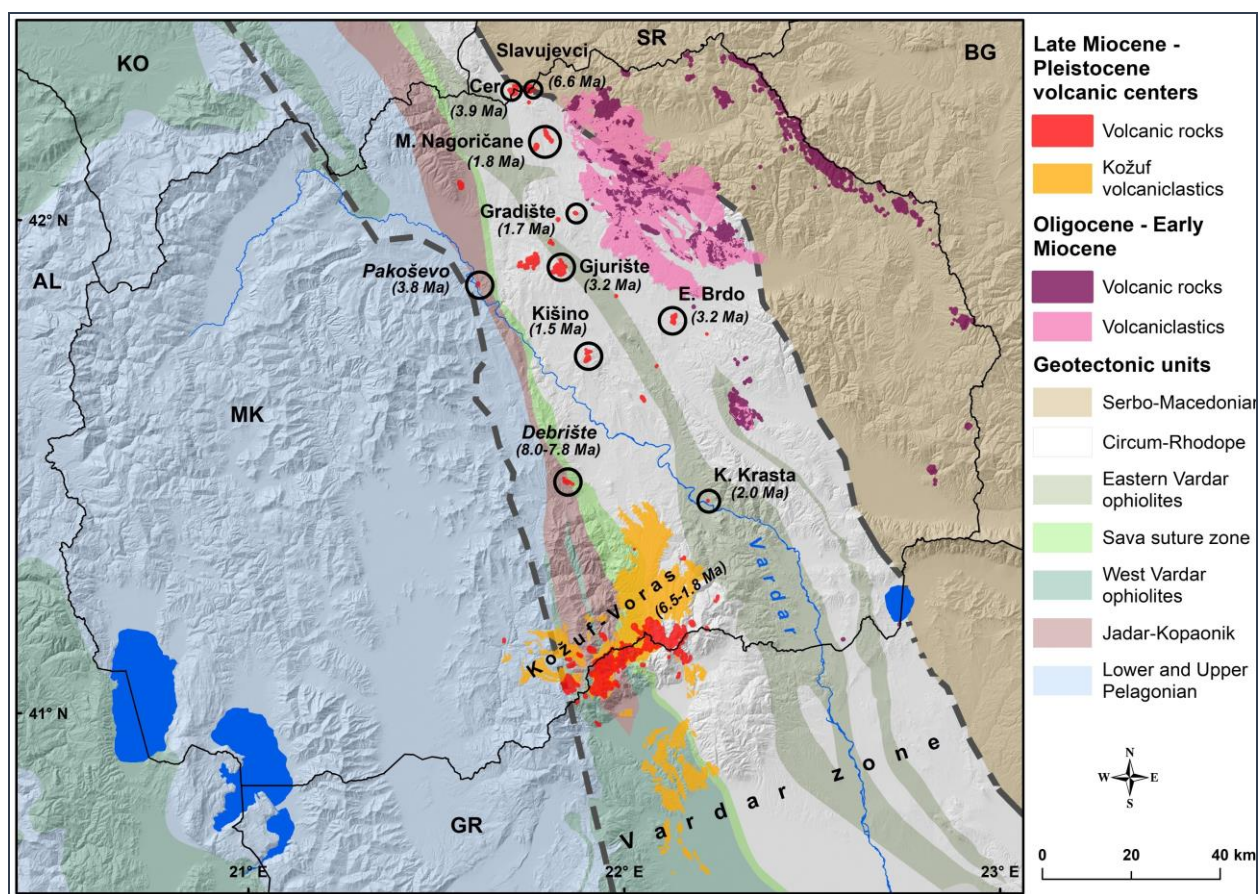


Fig.2.3. Map of the Oligocene-Early Miocene and the Late Miocene-Pleistocene volcanic centers in the Vardar zone (Molnár *et al.*, 2022).

The most intense phase of the volcanism in the central parts of the peninsula occurred during Oligocene times, related to the Dinaride collapse, retreating Aegean subduction zone and the accelerating clockwise rotation of the Hellenides from Middle/Late Miocene (Cvetkovic *et al.*, 2004; Pe-Piper & Piper, 2007). The first period occurred during Oligocene-Early Miocene in the

eastern part of the region. The second period occurred during the Late Miocene-Pleistocene time, and it was limited to the Vardar zone, related to the tectonic evolution of the South Balkan extensional system (*Yanev et al. 2008; Molnár et al., 2022*). The volcanic centers are located at the margins of the extensional basins, along fault lines or at the boundaries of the geotectonic units (*Fig.2.3*).

Nowadays, the geodynamic regime is still active in the southernmost part of the region and is controlled by the active tectonic processes in the Eastern Mediterranean: the (i) subduction of the Adriatic (Apulian) microplate beneath the Dinarides; (ii) progressive roll-back of Hellenic subducted slab; and (iii) the collision between the Eurasian and the Arabian plates, related to the westward motion of Anatolia along the North Anatolian Fault Zone (NAFZ), a right lateral E-W strike-slip fault, in the northern Aegean sea (*Fig.2.2 - Burchfiel et al., 2008*).

2.2 Greece

Greece belongs to the Southern Balkan region and together with the bordering countries is among the most seismically active regions of the Balkan Peninsula. According to *Mountrakis (1985; 2010)*, the Hellenic region is divided into three major structural zones (*Fig.2.4*), from west to east: (i) *External Hellenides*, (ii) *Internal Hellenides*, (iii) *Hellenic Hinterland*.

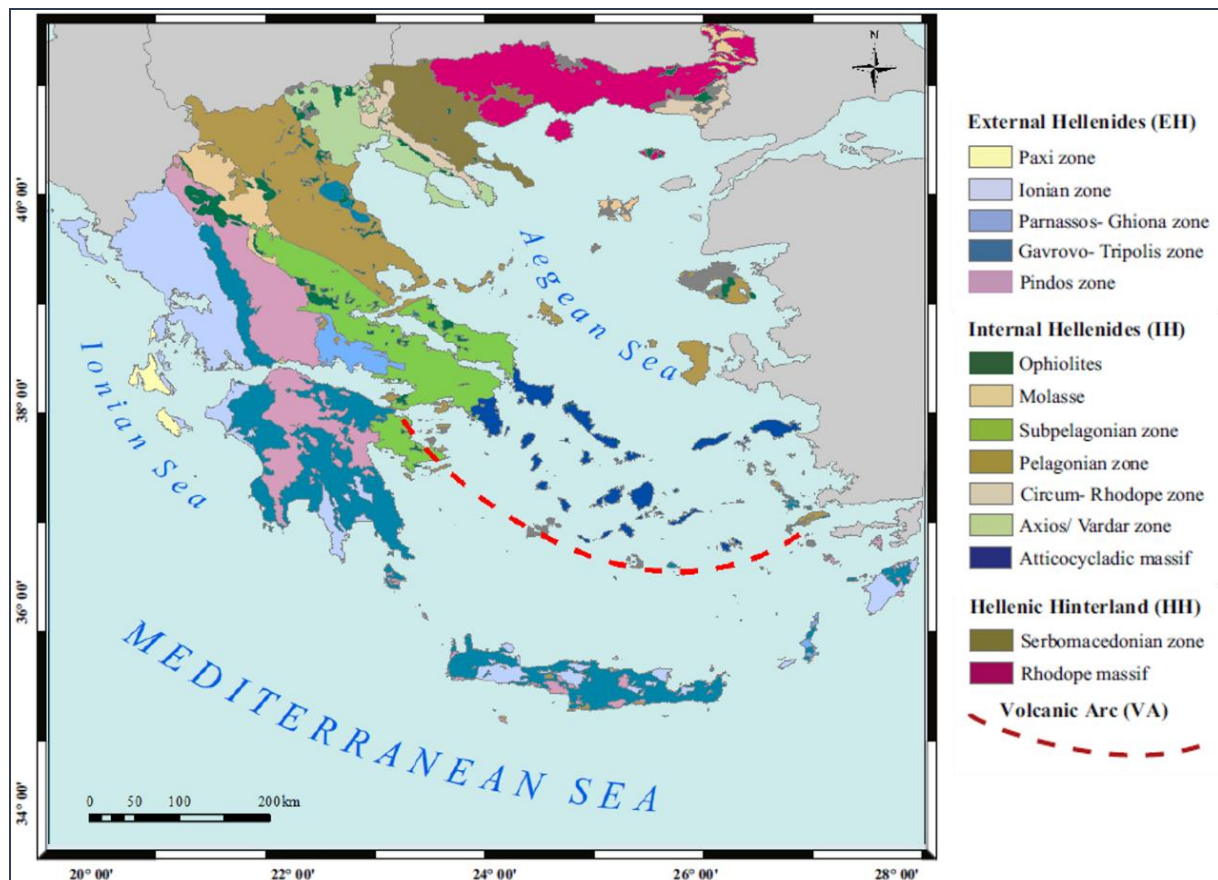


Fig.2.4. Map of the structural zones of the Hellenides (after *Mountrakis, 1986*)

The **External Hellenides** is a part of the Apulian (Adria) microplate, which corresponds to a neritic continental sea depositional environment. It consists of the *Parnassos*, *Gavrovo-Tripolis*, *Ionian* and *Paxos* zones. A palaeogeographic difference of the *Ionian* zone is that, during the Middle-Upper Jurassic, it was an intracontinental basin with pelagic sediments. The **Internal Hellenides** consists of five geotectonic zones. The *Circum-Rhodope* zone represented the continental slope of the Hellenic Hinterland towards the ocean. The general lithostratigraphic succession includes

volcanoclastic deposits, sea deposits ending up in deep-sea sediments westwards, and flysch. The *Vardar zone* corresponds to the Tethys ocean characterised by the presence of deep-sea sediments and obducted ophiolites. The *Pelagonian zone* is envisaged as a fragment of the Cimmerian microcontinent and mainly consists of neritic sediments. The most characteristic lithological units of the Subpelagonian zone are the obducted ophiolites. This zone is considered as the continental slope of the Cimmerian continent towards the ocean, whose sedimentary remnants form the Pindos zone. The *Attico-Cycladic zone*, similar to the Pelagonian, is envisaged as a continental fragment having undergone neritic sedimentation. The ***Hellenic Hinterland*** consists of the *Rhodope* and *Serbo-Macedonian Massifs*, that represent an old continental crust affected by Alpidic metamorphism. Both zones mainly consist of crystalline rocks bearing few neritic deposits and also document Late Eocene–Early Oligocene granitoid intrusions.

2.2.1 Geodynamic setting

The African plate subducts underneath the Eurasian along the Hellenic Arc at a rate of about 10 mm a⁻¹, while the Aegean Sea represents an extensional basin with opening rates in the order of 35-40 mm a⁻¹ (*McClusky et al., 2000*). The plate interactions and the associated crustal deformation taking place in the region, make the Hellenic area one of the most seismically active and rapidly deforming areas worldwide (e.g., *Tsokas and Hansen, 1997*; *Taymaz et al., 2007*; *Le Pichon et al. 2001*). The Hellenic Arc is bounded at its northwestern and eastern ends by two major transform faults, known as the Cephalonia (right lateral) and the Rhodes (left lateral) transform faults (*Yolsal et al. 2009*). Tectonic evolution of the Hellenic Arc is dominated by the effects of the northward subduction of the African under the Eurasian plate. The thinner oceanic lithosphere is currently subducting under Crete and is causing extension of the continental crust and volcanism in the overlying Aegean extensional province (*Fig.2.5*).

Schematically, the present-day shape, topography and bathymetry of the region are the result of three main relief-forming geotectonic processes, which were or are still active within the last 10-15

million years: (i) the Middle to Late Miocene post-orogenic extension and exhumation of the alpine mountain belts; (ii) the migration of the North Anatolian Fault (NAF) westwards into the north Aegean Sea in Late Miocene - Early Pliocene and the westward motion of the Anatolian continental block; (iii) the northward subduction of the eastern Mediterranean crust below the Aegean microplate and the resulting stretching of the latter in a north-northeast - south-southwest direction.

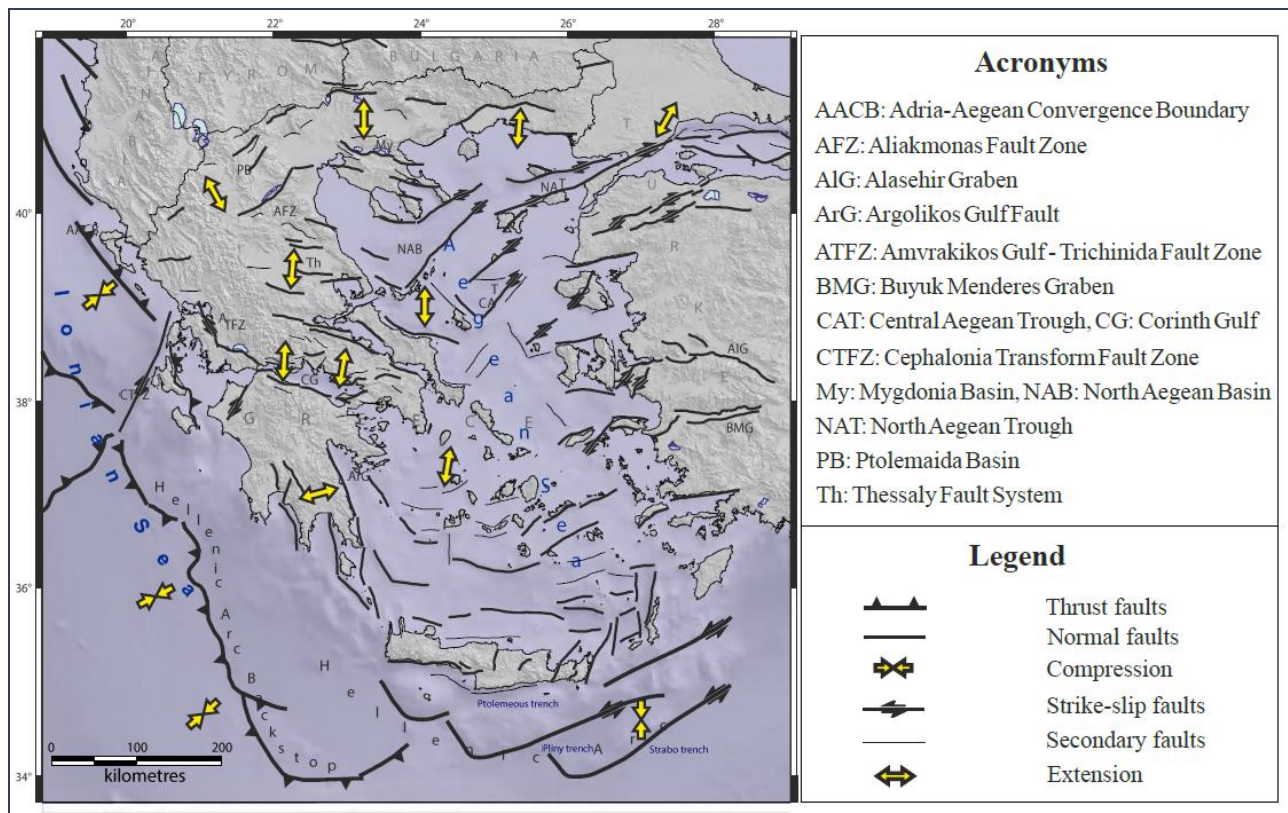


Fig.2.5. Map of the major tectonic structures and the current horizontal stress field main axes. Fault lines derive from the CSSs upper edge of *GreDaSS* (2014).

2.3 North Macedonia

North Macedonia belongs to the Southern Balkan region and together to the bordering countries is among the most seismically active regions of the Balkan Peninsula. According to *Dumurdjanov et al.* (2005), the basement is divided by five major tectonic units (*Fig.2.6*) from west to east: (i) the Chukali-Kasta zone, (ii) the West Macedonian zone, (iii) the Pelagonian massif, (iv) the Vardar zone, and (v) the Serbo-Macedonian massif. The boundaries between the geotectonic units are outlined by NW-SE pre-neotectonic faults (*Dumurdjanov et al.*, 2020). Pre-Cenozoic basement tectonic units have a N-NW trending structure, except in north-central Macedonia where foliations and structures curve around the north plunging Pelagonian anticlinorium (*Dumurdjanov et al.*, 2005). The Serbo-Macedonian zone and Pelagonian massif represent the Precambrian crystalline basement composed of high-grade metamorphic rocks and products of two granitic intrusions (*Dumurdjanov et al.*, 2020).

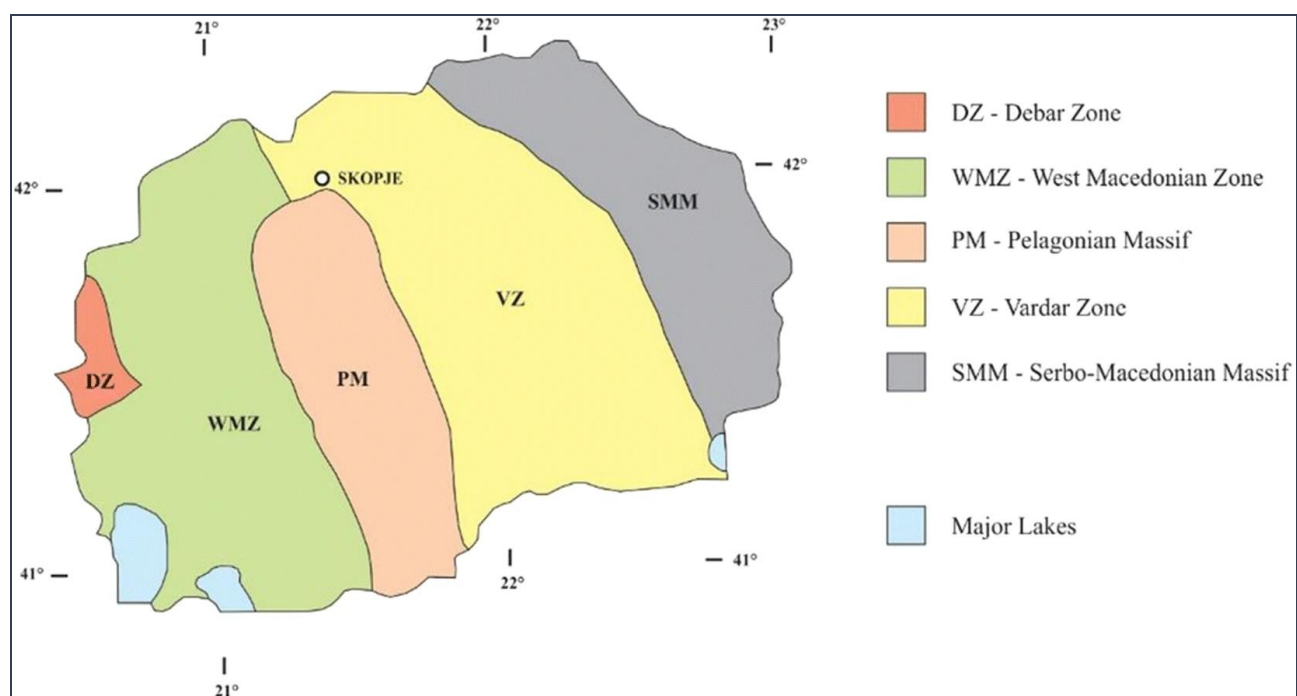


Fig.2.6. Schematic map of major geotectonic units of North Macedonia (*Dumurdjanov et al.*, 2020).

The **Chukali-Kasta zone**, or Debar zone, is part of extensive N-S trending belt of rocks in Albania, with a small part found in Macedonia, close to Debar. This zone is characterized by sheared very low-grade metamorphosed sedimentary rocks of Late Cretaceous (*Dumurdjanov et al., 2005*), that consist of terrigenous and limestone sediments and Triassic diapirs of anhydrite-gypsum masses present on Deshat and Stogovo mountains near Debar. These rocks form a tectonic half-window around the town of Debar, where they are tectonically overlain by rocks of the Western Macedonian zone (*Dumurdjanov et al., 2020*).

The **West Macedonian zone** consists of low- to medium grade metamorphosed Paleozoic sedimentary and igneous rocks and Mesozoic sedimentary rocks (*Dumurdjanov et al., 2005*). The **Pelagonian massif** forms the Precambrian high-grade metamorphic core of a large NW-trending anticlinorium (*Dumurdjanov et al., 2005*). The **Vardar zone** represents a Triassic to early Cretaceous lithologies of the Vardar-Tethys Ocean and consists of highly heterogeneous associations of ocean-derived rocks, represented primarily by ophiolites and mélanges (*Cvetković et al., 2016*). The **Serbo-Macedonian Massif** consists of Cambrian mafic plutonic and volcanic rocks and Early Paleozoic schist all intruded by large bodies of Paleozoic granite (*Dumurdjanov et al., 2005*). This large and heterogeneous geotectonic unit extends from the Aegean Sea to the Pannonian Basin in Serbia.

Above the basement tectonic units, there are two main groups of sedimentary basins that formed in late Eocene to recent time and reflect two major periods of extensional deformation, in Paleogene and Neogene times, separated by a short period of shortening (*Dumurdjanov et al., 2005*). The Paleogene basins trend generally NW-SE and were formed mainly within the Vardar zone and Serbo-Macedonian tectonic units (*Dumurdjanov et al., 2004*). Several basins are present in eastern Macedonia bounded by faults along their eastern side and represent the formation of extensional E-tilted half grabens. The second period of extension deformation began in the middle Miocene and has continued to the present and was dominated by NNE-SSW-directed extension (*Fig.2.7 - Dumurdjanov et al., 2005*).

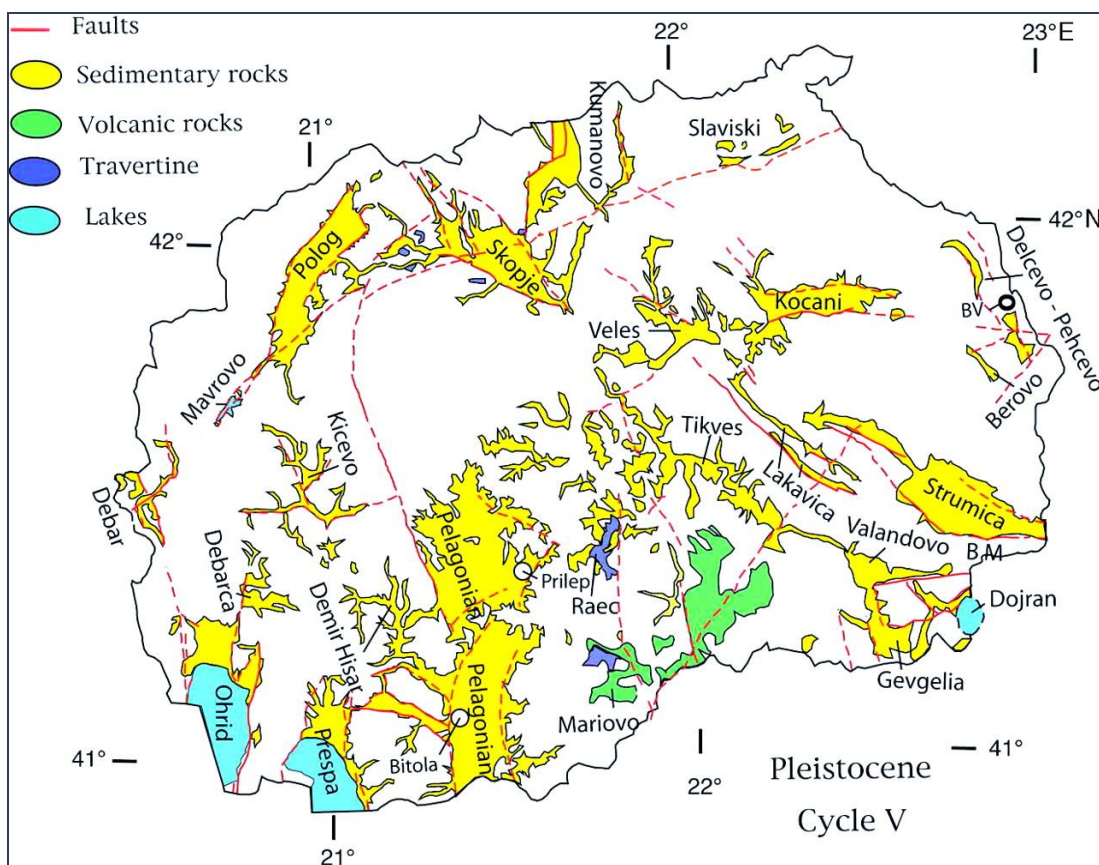


Fig.2.7. Distribution of sedimentary basins in Macedonia (Dumurdjanov *et al.*, 2005). Red lines indicate established active faults active; red dashed lines indicate the inferred faults. **BV** - Bukovik volcanic center; **BM** - Belasica Mountains.

The westernmost part of Macedonia and adjacent Albania is a highly seismic zone associated with recent extensional tectonic movement along normal faults (Fig.2.8). The results of GPS study of Quaternary active faults in Macedonia show that the whole territory is moving uniform toward the S-SE with a speed of 2 to 4 mm a⁻¹ (Burchfiel *et al.*, 2006; Dumurdjanov *et al.*, 2020).

Several Macedonian geologists (Arsovski & Petkovski, 1975; Jancevski, 1987; Dumurdjanov *et al.*, 2005; Burchfiel *et al.*, 2006) postulated the existence a regional fault zone, known as Kjustendil-Kriva Palanka-Skopje-Debar-Elbasan fault zone. This regional transverse extensional fault zone has a length of about 200km; to the east, it has an ENE-WSW orientation, whilst from Gostivar to the west and in Albania it stretches in the SW direction. This zone is characterized by several “en echelon” normal faults from Kjustendil, through the Slaviski graben, to Skopje basin (Dumurdjanov *et al.*, 2005; Dumurdjanov *et al.*, 2020).

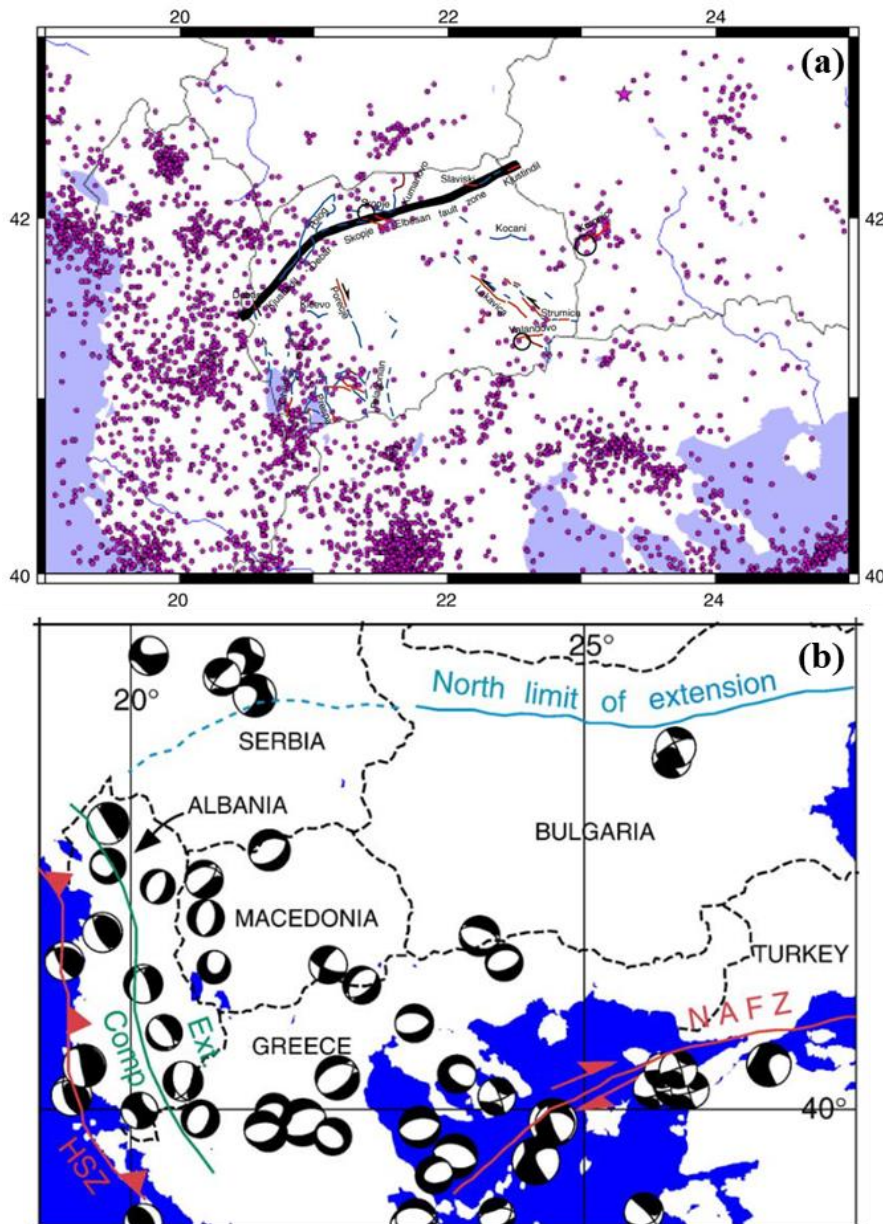


Fig.2.8. (a) Location of earthquakes of $M > 3.0$ in Macedonia and surrounding region for the period 1976 to 2004 (from Burchfield *et al.*, 2006). Three large earthquakes that occurred in the last century are shown by the black circles: Krupnik in Bulgaria [1904] $M = 6.9$; Valandovo [1932] $M = 6.5 - 6.8$; Skopje [1963] $M = 6.1$. (b) Earthquake focal mechanisms for Macedonia and surrounding region (from Burchfield *et al.*, 2006). The northern limit of extension within the SBER and the boundary between extensional and compressional faults in Albania as determined from active faulting are shown. HSZ - Northern Hellenic subduction zone; NAFZ - North Anatolian fault zone.

Neotectonic regional faults (*Fig.2.9*) are mostly created as new fractures along old faults, that transversally intersect different geotectonic units. The orientation of horsts, grabens and regional faults are of EW and NE-SW direction in eastern, central and part of western Macedonia, whereas they are NS to NW-SE-oriented in the west part of Prespa-Ohrid-Debar (*Dumurdjanov et al., 2020*). According to *Durmurdjanov et al. (2005)*, three categories of Quaternary faults are recognized: (i)

faults with evidence of active faulting, (ii) faults with well-developed morphological expression for active faulting, (iii) faults with well-developed morphological expression for the modern topography and suspected active.

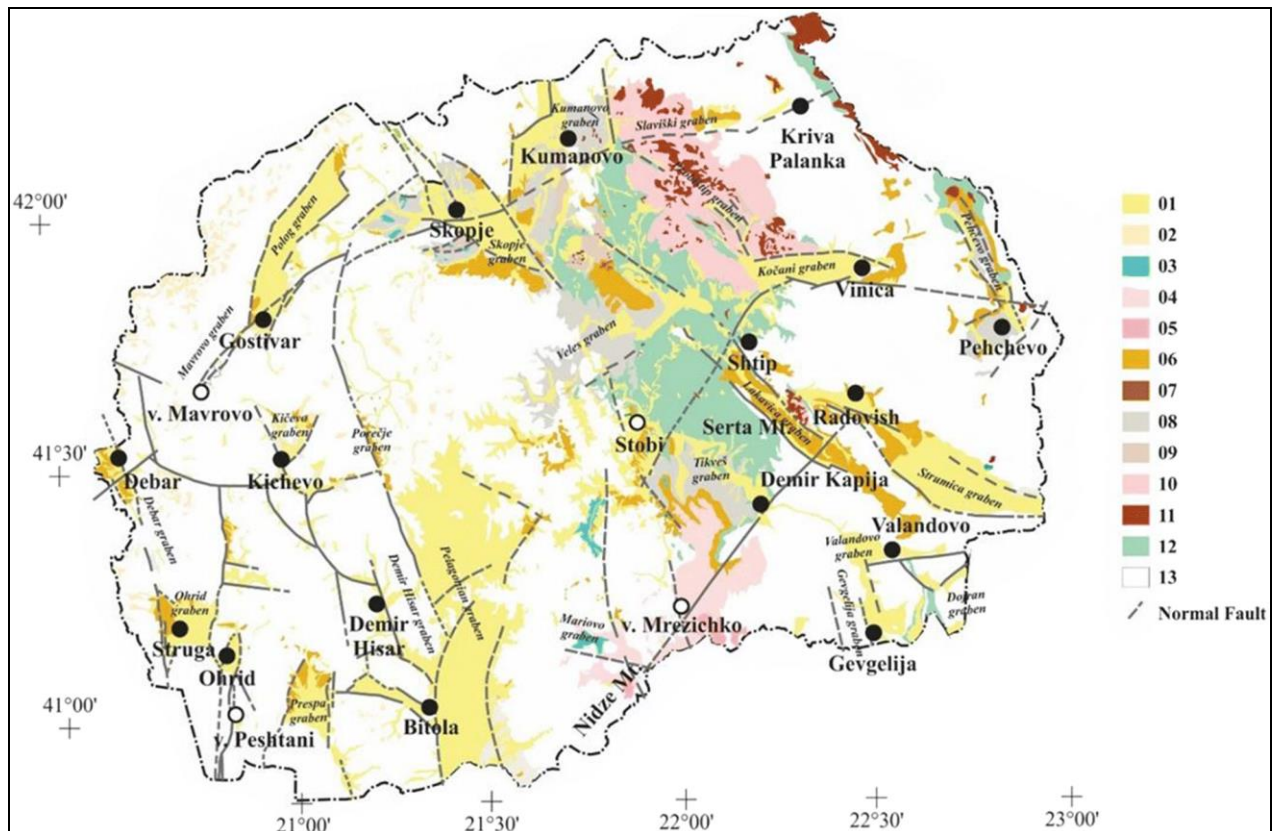


Fig.2.9. Map of neotectonic grabens and main active faults in North Macedonia (Dumurdjanov et al., 2020). Quaternary: 01 – alluvial, proluvial and limnic sediments, 02 – glacial sediments, 03 – travertine deposits; Pliocene – Quaternary: 04 – agglomerats, tuff, sandstones and travertine; Pliocene: 05 – volcanic rocks, 06 – continental sediments; Miocene Pliocene: 07 – calcalkaline basalts; Miocene: 08 – Late Miocene freshwater sediments, 09 – Middle Miocene freshwater sediments; Oligocene – Miocene: 10 – pyroclastic rocks, 11 – volcanic rocks; Late Eocene – Oligocene: 12 – flysch sediments; 13 – Pre-Eocene complex rocks.

2.3.1 Geothermal fields

North Macedonia is one of the richest regions in low-temperature geothermal resources (Popovska-Vasilevska & Armenski, 2016). Indeed, the Macedonian region is characterized by positive geothermal anomalies, which mainly relate to Vardar zone (Georgieva et al., 2000). The regional thermal flow is about $100\text{-}120 \text{ mW m}^{-2}$ along the Vardar zone, whilst it is about $60\text{-}80 \text{ mW m}^{-2}$ in other part of the country (Milivojevic, 1993). Moreover, the Vardar zone is characterized by a reduced thickness of crust, that is about 32 km (Dragasevic, 1974).

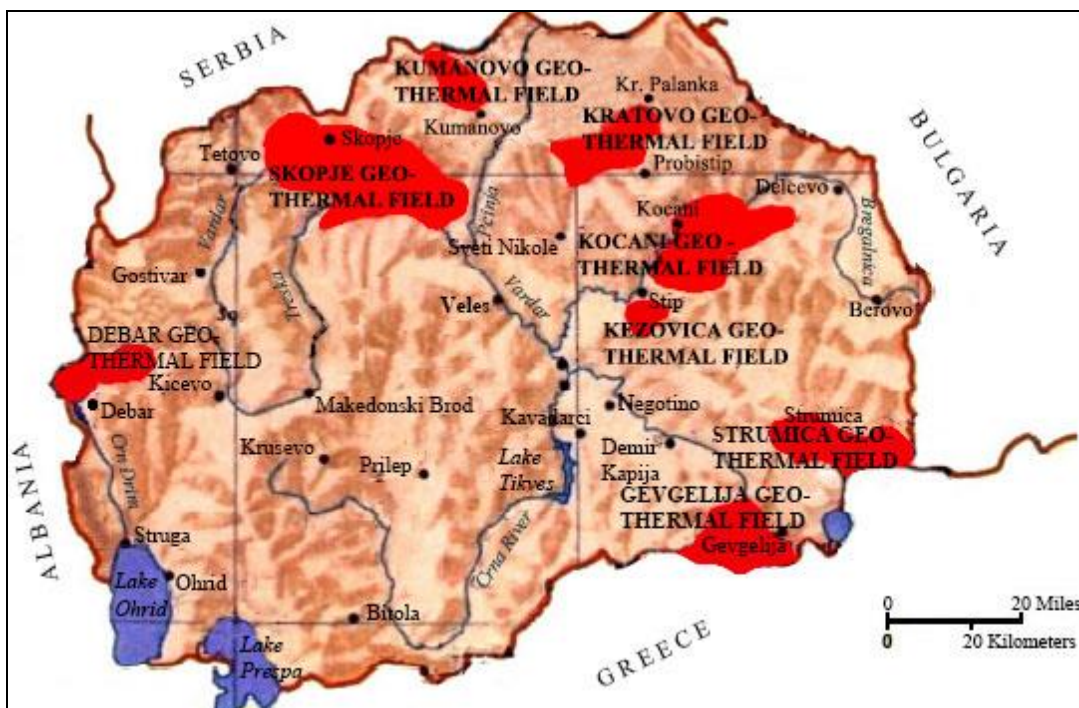


Fig.2.10. Main geothermal fields in Macedonia (Popovski & Micevski, 2005).

The high heat flux and the low thickness of the crust favored the occurrence of 18 geothermal fields in the Macedonian country (*Fig.2.10*), which are situated in Central Serbo-Macedonian Massif, Central and Eastern Macedonia. Exception is the Debar geothermal field, that is located in the West Serbo-Macedonian geothermal zone (Popovski, 2002). The biggest potential and best investigated is the Kochani geothermal system, in Eastern Serbo-Macedonian Massif, with a total maximum flow of 350 l s^{-1} (Popovski, 2002). This system is characterized by two low-temperature geothermal fields: Istibanja (65°C) and Dolni Podlog ($75\text{-}78^\circ\text{C}$). Twenty-five boreholes and wells with depth of 100-1170 m are present (Popovski, 2002). All Macedonian geothermal systems are used for balneology purposes, as spa, for heating of hotels and greenhouses, CO₂ extraction, industrial utilization, or some discharge without any use.

Chapter 3 - Karst hydrosystems in Greece

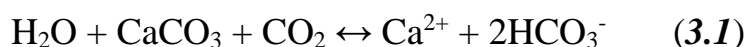
3.1 General information about the karst environment

Climate change has a severe impact on water availability, demand and quality (*Hoegh-Guldberg et al., 2018*), and it will reduce groundwater resources in most dry subtropical regions (*Jiménez Cisneros et al., 2014*). The stress on water resources is due to the increase in water demand for industrial and agricultural activities, and population growth, producing depletion both in quantity and quality of groundwater resources (*Kalhor et al., 2019*). Furthermore, climate change impacts also on coastal groundwater; the rising of sea level, together with the over-pumping of coastal aquifers, produces a dislocation of the saltwater-freshwater interface towards inland (*Jiménez Cisneros et al., 2014*).

Karst aquifers belong to the main freshwater resources. They occur both in sedimentary carbonate rocks (limestone, dolomite) and metamorphic carbonate rocks (marble), which cover about 12% of the global land surface (*Ford & William, 1989*). Moreover, karst aquifers are present also in evaporite formations (gypsum and anhydrite) (*Bakalowicz, 2005*). Thanks to the capacity of storing and transmitting huge amount of good quality freshwater, karst hydro-systems are of worldwide economic interest, representing an important drinking water supply for about 25% of the world's population (*Ford & Williams, 2007*).

Karst hydro-systems are the result of intense water-rock interactions, called karstification process, that involves two groups of processes: one refers to the chemical dissolution of the rock-forming minerals and the other to the mechanical-physical erosion. Initially, the former is the dominant process but, as fractures and conduits are created, the latter becomes more extensive than chemical process (*Pulido-Bosch, 2021*).

The dissolution of carbonate rocks occurs by water containing dissolved carbon dioxide, according to a set of equilibrium equation simplified as follows:



The concentration of dissolved CO₂ in groundwater is controlled by temperature and partial pressure of CO₂ in atmosphere. Carbon dioxide comes from the atmosphere through meteoric recharge, from organic processes within the soils (root respiration, microbial activity, biodegradation of organic matter, etc.) or from depth by geological processes (*Bakalowicz, 1992, Dreybrodt, 2000*).

Unfortunately, karst hydro-systems are particularly vulnerable to chemical and microbial contamination from several sources, climate change and deterioration from overexploitation (*Bakalowicz, 2005*), thus their protection and management are of critical importance. The main sources of karst groundwater pollution, in the last decades, come from agricultural, industrial, residential and commercial activities, such as nitrate pollution from wastewater and fertilizer, heavy metals from mining operations, elevated chloride content due to seawater intrusion (*Fetter, 2001; Wakida & Lerner, 2005; Kalhor et al., 2019*). The high vulnerability of karst aquifers is due to hydrogeological and hydrodynamic features of the system. Karst systems are characterized by strong hydraulic gradient and high flow rate, that confer a short residence time (*Bakalowicz, 2005*). The main features of these aquifers are heterogeneity and anisotropy, which make hard to develop a model of the systems in order to adapt its management. The heterogeneity is due to a diversified network of high-permeability conduits and fractures where water follows preferential paths, which are anisotropic, directionally dependent on fractures geometry (*Ford & Williams, 2007; Goldscheider & Drew, 2007, Kalhor et al., 2019*).

3.2. Karst hydrosystems in Greece

Karst systems represent a strategic resource for Hellenic territory and preserving its quantity and quality is of the utmost importance. Indeed, in Greece, starting from 1970s, research interest about karst systems has considerably increased, because of the increasing water demand. At first, the exploitation was limited to discharge of springs, but the socio-economic development of the country resulted in the expansion of population, agricultural and industrial activities and land use changes in

the karst aquifer boundaries (*Kazakis et al., 2018, Voudouris & Kazakis, 2018*). The main source of quality deterioration of groundwater resources comes from the intensive exploitation in coastal areas, due to the intense urbanization and tourist development, causing the salinization of aquifers (*Daskalaki & Voudouris, 2008*). This is the case of Malia town (Crete) where the over-exploitation since the 1960s, depressed the groundwater level and caused an important quality deterioration of water due to the seawater intrusion in the aquifer (*Steikakis et al., 2016*). Agricultural activities represent the main use of water resources, with over 80% of total consumption (*Mimikou, 2005*); therefore, the second source of pollution in Greece, after the seawater intrusion, comes from fertilizer use in agriculture, as well as disposal of untreated wastewater (*Daskalaki & Voudouris, 2008*).

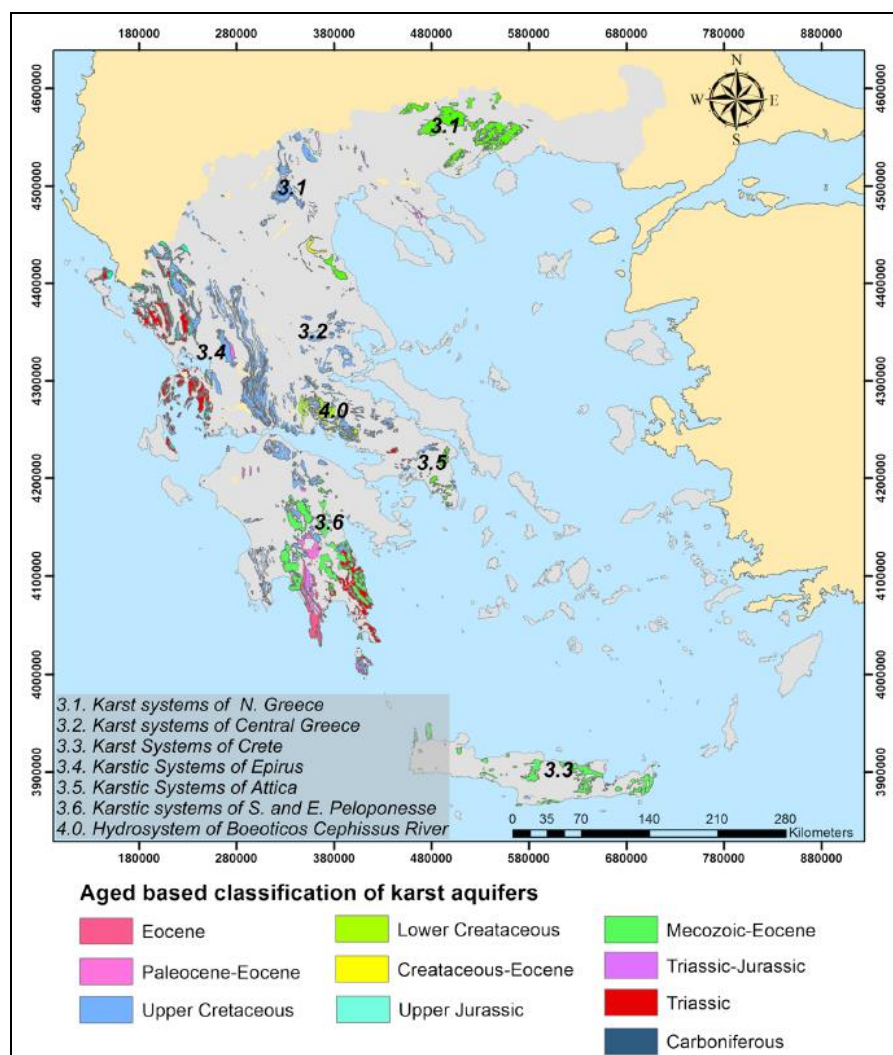


Fig.3.1. Map of spatial distribution of major karst hydrosystems in Greece (*Kallioras & Marinos, 2015*)

The main Hellenic aquifers are hosted in clastic Quaternary and Neogene deposits and in carbonate rocks, in which the groundwaters are extracted via several wells and boreholes (about 300,000 for the whole Greek territory - *Daskalaki & Voudouris, 2008*).

Carbonate formations cover about 35% of the country and are mainly located in Western, Central, and Southern Greece (*Daskalaki & Voudouris, 2008*). Most of them (55% of karst aquifers) reach coastal areas and often extend below sea level. Examples can be found in Central Greece (South Parnassos and Ghiona aquifers), in Eastern Peloponnese (Tripolis and East Argolis aquifers), and in Crete Island (the famous Almyros spring) (*Kallioras & Marinos, 2015; Voudouris & Kazakis, 2018*). The Mediterranean area is known for its widespread presence of coastal and submarine karstic springs, which were estimated to represent about 90% of the whole world (*Bakalowicz, 2015*). The formation of karstic systems below the present sea level is generally attributed to tectonic movements or/and sea level drop during glacial periods (*Fleury et al., 2007*).

Karst aquifers are developed both in carbonate sedimentary rocks, limestones and dolomites (Triassic – Cretaceous), and in carbonate metamorphic rocks, Paleozoic – Mesozoic marbles (*Voudouris & Kazakis, 2018*). Furthermore, some karst hydro-systems are developed in evaporitic formation; high-sulfate karst springs are found in western Greece within the Ionian zone, which can be associated with the dissolution of gypsum (*Rigakis & Karakitsios, 1998; Katsanou et al., 2011; Nikolaou et al., 2011; Katsanou et al., 2017*).

The karst systems in Greece were developed during the Alpine orogeny (Jurassic – Miocene) (*Kallergis, 2001*). The karstification process of the carbonate formations was a result of lateral movements in the upper Eocene, intense tectonism at the end of upper Miocene and eustatic movements of the Mediterranean Sea during glacial and interglacial periods (*Katsanou, 2018*). According to *Papadopoulou-Vrinioti (1993)*, the Hellenic karst systems is distinguished into three groups: (i) “*paleokarst*”, developed during warm-wet climates (upper Cretaceous; upper-lower Miocene) and is considered as fossilized; (ii) “*younger karst*”, developed during the interglacial periods (Pleistocene-Holocene); (iii) “*recent karst*”, developed under the current climatic

conditions. The majority of karst hydrosystems in Greece was formed during the second karstification stage and is characterized by mature features (dolines, poljes and cave). Furthermore, the karst features were determined by three factors: (i) Messinian salinity crisis that caused karstification at great depth below the present sea level; (ii) Quaternary cold periods that caused weathering of the epikarst; (iii) post-Miocene tectonics that created horst and graben structures and produced the filling of large basins (*Bakalowicz, 2015*).

Most of the country's karst aquifers have a holokarst type shape, which are characterized by well-developed karst features extended below base levels and high hydraulic conductivity; holokarst are very common in the limestones of the Ionian, Gavrovo-Tripolis, Parnassos-Giona, and Pelagonian zones that outcrop in Western and Central Greece and Crete Island (*Katsanou & Lambrakis, 2017*). The hydrogeological behaviour is controlled by intense tectonic deformation, which favours infiltration and karstification processes (*Kallioras & Marinos, 2015*). According to *Voudouris & Kazakis (2018)*, the hydraulic conductivity of karst aquifers ranges from 10^{-2} m s⁻¹ to 10^{-6} m s⁻¹, the permeability is medium to high, the transmissivity varies between 0.01 m² s⁻¹ and 0.1 m² s⁻¹, whereas the maximum groundwater velocity is about 0.3 m s⁻¹.

Chapter 4 - Materials & Methods

In the period from October 2016 to October 2022, 202 water samples and 230 gas samples were collected from the main karst springs of Greece and, in the period from August 2019 to October 2022, 68 gas samples were collected from the main geothermal fields of Republic of North Macedonia. My personal involvement includes 8 field campaigns from 2018 to 2022.

Analysis of chemical and isotopic composition of water and gas samples were carried out at the laboratories of Istituto Nazionale di Geofisica e Vulcanologia of Palermo (INGV sez. Pa).

Names, sampling date, coordinates, chemical and isotopic compositions of all the collected samples can be found in Appendix and published as databases in public repositories (*Li Vigni et al.*, 2022a; *Li Vigni et al.*, 2022b; *Li Vigni et al.*; 2023a). The Chapter 5, about the hydrogeochemistry of karst waters in Greece is a submitted paper (*Li Vigni et al.*, 2023b). The Chapter 9, about the gas geochemistry of Duvalo area (Republic of North Macedonia) is already published (*Li Vigni et al.*, 2022c).

4.1 Water sampling and analytical methods

The physico-chemical parameters of sampled water (temperature, pH, Electric Conductivity (EC) and redox potential (Eh)) were measured *in situ* by portable instruments, which were previously calibrated using standard solutions. The total alkalinity was determined *in situ* by titration with Hydrochloric acid (HCl) = 0.1 mol L⁻¹ (0.1 N) on unfiltered samples (expressed as mgHCO₃⁻ L⁻¹).

The water samples collected to determine major anions composition were filtered with 0.45 µm MF_Millipore cellulose acetate filters and stored in LDPE bottles, whilst the aliquot for determination of major cation contents was stored in Polypropylene (PP) bottles and acidified with ultrapure concentrated HNO₃. For trace element analysis, filtered samples were stored in 50 ml PP bottles, and acidified to a pH of ~ 2 with ultrapure concentrated HNO₃.

Water chemistry was analysed using standard methods (APHA, 2005): major cations (Na⁺, K⁺,

Mg^{2+} , Ca^{2+}) and major anions (F^- , Cl^- , NO_3^- , SO_4^{2-}) were determined by Ionic Chromatography (IC; ICS-1100, Dionex), using a Dionex CS-12A column for cations and a Dionex AS14A column for anions. Silica (SiO_2) was determined by Inductively Coupled Plasma-Optic Emission Spectrometry (ICP-OES; Jobin Yvon Ultima 2). For all these analytical methodologies, precision was always better than $\pm 3\%$.

Twenty-five trace elements (Li, Be, B, Al, Ti, V, Cr, Mn, Fe, Co, Ni, Cu, Zn, As, Se, Br, Rb, Sr, Mo, Cd, Cs, Ba, Tl, Pb and U) were analysed by Inductively Coupled Plasma Mass Spectrometry (ICP-MS) using the following instruments: Agilent 7500 for samples collected until 2018 and Agilent 7800 since then. Calibration solutions for all the investigated elements were prepared daily using an appropriate dilution of 100 mg L^{-1} and 1000 mg L^{-1} of stock standard solutions (Merck) with 0.14 mol L^{-1} high purity nitric acid. The accuracy of the method was checked analysing certified reference materials of natural waters (Nist 1643e, Environment Canada TM-24.3 and TM-61.2, Spectrapure Standards SW1 and SW2) at regular intervals during sample analysis. The experimental concentrations determined in this study are in accordance with these certified values (within $\pm 5\%$).

Total dissolved solids (TDS) are here intended as the sum of all determined major ions plus silica. Speciation of solutions, saturation index of the relevant mineral phases, total dissolved inorganic carbon (TDIC) and pCO_2 for each sampled water were calculated using the aqueous speciation PHREEQC code (Parkust & Appelo, 1999). The results of chemical composition of water samples were also compared with the limits set by the European Council (*Directive 98/83/EC; Directive 20/483/EC*) that fixes quality standards for water suitable to human consumption and spring waters. The oxygen and hydrogen isotope compositions of water were determined by using, respectively, Analytical Precision AP 2003 and FinniganMAT Delta Plus IR-Mass Spectrometer devices. The isotope ratios are expressed in delta notation (\textperthousand) with respect to the international standard V-SMOW (Vienna Standard Mean Ocean Water). The uncertainties are $\pm 0.1\text{\textperthousand}$ for $\delta^{18}\text{O}$ and $\pm 1\text{\textperthousand}$ for $\delta^2\text{H}$ ($\pm 1 \sigma$).

4.2 Gas sampling and analytical methods

4.2.1 Gas sampling

Samples for dissolved gas analyses were collected in glass bottles sealed underwater by gastight rubber/teflon plugs. The flask had to be totally filled with water sample to be analysed, taking care not to include air bubbles. Vials of 150 ml of volume were used for the analyses of the chemical composition of the gases (and occasionally for He isotope composition) and of 50 ml of volume for the analysis of $\delta^{13}\text{C}_{\text{TDIC}}$.

Bubbling gases were collected by using an inverted funnel positioned above the bubbles and stored in borosilicate glass flasks equipped with two stopcocks to avoid air contamination and/or in 12 ml Exetainer®. The gas made flow through the sample holder for as long as was necessary to flush it out thoroughly; the volume of the flushed gas must be at least ten times the volume of the bottles. When the gas flux was very low all the system was filled with water before putting the funnel above the bubbling site and the sampler was closed as soon as the gases displaced all the water inside.

Soil gases were collected through a probe inserted in the soil at 50 cm depth and stored in glass vessel with two vacuum stopcocks and Exetainer® Labco vials (12 ml of volume). The sample was collected slowly sucking with a syringe connected through three-way valve to a sample holder.

An evacuated glass vessel filled with a 4M soda solution, which blocked CO₂ and H₂S as dissolved ions, was used to concentrate the minor gases in order to obtain the CH₄/C₂H₆ ratio or the isotope composition of CH₄ when the concentrations were too low.

4.2.2 Analytical methods

Dissolved gas samples were analyzed with the “headspace technique” following the method of *Capasso & Inguaggiato (1998)* and *Liotta & Martelli (2012)* for the chemical composition and *Inguaggiato & Rizzo (2004)* for the He isotope analysis. Dissolved gases were extracted after equilibrium was reached at constant temperature with a host-gas (high-purity argon) being injected in the sample bottle. To allow rapid comparison, starting from the total amount of dissolved gases

(ccSTP L⁻¹), the relative abundances for every single gas species was recalculated as free gas phase in equilibrium with the sampled water. These, expressed in $\mu\text{mol mol}^{-1}$, were obtained from the partial pressure values considering the solubility coefficients (Bunsen coefficient “ β ”, cc_{gas} L_{water}⁻¹ STP) of each gas species, the volume of gas extracted and the volume of the water sample at laboratory temperature (*Capasso & Inguaggiato, 1998*).

The chemical composition (He, H₂, H₂S, O₂, N₂, CH₄, CO₂ and C₂H₆) of sampled dissolved and free gases was analyzed by an Agilent 7890B gas-chromatograph system, using Argon as carrier gas, and equipped with 4-m Carbosieve S II and PoraPlot-U columns. A Thermal Conductivity Detector (TCD) was used to measure the concentration of He, O₂, N₂ and CO₂ and a Flame Ionization Detector (FID) for CH₄ and C₂H₆. The analytical errors were estimated as less than 5 % for He, H₂, H₂S and C₂H₆ and 3 % for O₂, N₂, CH₄ and CO₂. Hydrocarbon analyses were performed with a Shimadzu 14a gas-chromatograph equipped with a Flame Ionization Detector (FID) using He as the carrier gas (*Vaselli et al., 2006*). The analytical error was $\leq 5 \%$.

Carbon isotope composition of carbon dioxide was measured using a Finnigan Delta S mass spectrometer after purification of the gas mixture by standard procedures using cryogenic traps with precision $\pm 0.1 \text{ ‰}$. The ¹³C/¹²C ratios of CO₂ were expressed as $\delta^{13}\text{C}_{\text{CO}_2} \text{ ‰}$ vs. V-PDB (Vienna-Pee-Dee Belemnite). The $\delta^{13}\text{C}$ of Total Dissolved Inorganic Carbon (TDIC) of waters, expressed in δ notation vs V-PDB standard ($\pm 0.2 \text{ ‰}$), was analysed by Analytical Precision 2003 (AP2003) mass spectrometer following the methodology of *Capasso et al. (2005)*. Carbon and hydrogen isotope compositions of CH₄ were measured using a Thermo TRACE GC interfaced with a Delta Plus XP gas source mass spectrometer, equipped with a Thermo GC/C III (for carbon) and with a GC/TC peripherals (for hydrogen). ¹³C/¹²C ratios are reported here as $\delta^{13}\text{C}_{\text{CH}_4}$ values (precision $\pm 0.2 \text{ ‰}$) with respect to the V-PDB standard, while ¹H/²H ratios are reported here as $\delta^2\text{H}_{\text{CH}_4}$ values (precision $\pm 2 \text{ ‰}$) with respect to the V-SMOW standard.

The abundance and isotope composition of He and ⁴He/²⁰Ne ratios were determined by separately admitting He and Ne into a split flight tube mass spectrometer (GVI Helix SFT). Helium isotope

composition is expressed as R/R_A , where R is the ($^3\text{He}/^4\text{He}$) ratio of the sample and R_A is the atmospheric ratio ($R_A = 1.386 * 10^{-6}$; *Ozima & Podosek, 2002*). The analytical errors were generally $< 1\%$.

Argon concentrations and its isotope compositions (^{40}Ar , ^{39}Ar and ^{36}Ar) were analyzed by multicollector Helix MC-GVI mass spectrometer with analytical uncertainty (1σ) for single $^{40}\text{Ar}/^{36}\text{Ar}$ measurements of $< 0.1\%$.

4.3 Carbon dioxide flux maps

In some degassing system of North Macedonia, the carbon dioxide flux was measured using the accumulation chamber method (*Chiodini et al., 1998*) with a portable fluxmeter (WEST Systems, Italy). Two detailed CO₂ flux campaigns were carried out in August 2019 and March 2020 at the site of Duvalo Kosel (Chapter 9) using a regular grid, whilst preliminary measurements at the sites of Botun and Petkoniva (Chapter 8) were carried out in October 2022, focusing only areas with strong alteration. During the measurement campaigns, the meteorological conditions were sunny and stable. At Duvalo Kosel, an easy recognizable site was used as control point and the flux measurements were carried out for each campaign, obtaining values within the error range of this technique. Flux values were determined at each measurement site from the rate of CO₂ concentration increase in the chamber and are expressed as grams per square meter per day ($\text{g m}^{-2} \text{ d}^{-1}$) after conversion from the volumetric to mass concentration considering the measured atmospheric pressure and the temperature values. The portable soil fluxmeter is equipped with a Licor LI820 IR spectrometer characterized by a reproducibility better than 20% in the measuring range 10-20,000 ppm. The accumulation chamber had an area of 0.031 m^2 and a volume 0.0028 m^3 . Instrument calibration, flux measurement and data elaboration were carried out as proposed by *Lewicki et al. (2005)*.

The CO₂ flux data were derived using statistical and geostatistical tools. In order to characterize the CO₂ flux, the GSA method (*Chiodini et al., 1998*), based on Sinclair's partitioning method (*Sinclair,*

1974), was used. This method allows the partitioning of a polymodal statistical distribution into individual populations, the definition of the parameters of statistical populations and relative proportions. Because the gas flux data resulted a combination of log-normal distributed populations, the computed mean and standard deviation of the partitioned populations refer to the logarithm of CO₂ flux values. The mean of the CO₂ flux and the 95% confidence interval of the mean were, thus, estimated by the Sichel's t-estimator (*David, 1977*).

In study-case of Duvalo Kosel, a map of the CO₂ fluxes was drawn using the sequential Gaussian simulations (sGs method; *Cardellini et al., 2003*). The sGs method consists of the production of numerous (usually 100) equiprobable realizations of the spatial distribution of the CO₂ flux using the sgsim algorithm of the GSLIB software library (*Deutsch & Journel, 1998*) according to the variogram model of the normal score of the CO₂ flux derived from the experimental variogram. One hundred equiprobable realizations were computed for the area using a computational grid of 2 x 2 m. The CO₂ flux map is then reported as map of the “expected” values at any cell (E-type estimates), obtained through a pointwise linear average of all the realizations (*Deutsch & Journel, 1998*). The results of the sGs were also used to estimate the total CO₂ output, summing the products of simulated value at each grid cell by the cell surface. The mean and the standard deviation of the 100 simulated values of total CO₂ output, computed for the 100 realizations, were assumed to be the characteristic values of the CO₂ output of its uncertainty for the area.

In the case-study of the geogenic carbon degassing from the big karst systems of Greece, a probability map of endogenous carbon concentration was drawn using the sGs method (*Cardellini et al., 2003*), computing 200 equiprobable realizations with the use of a computational grid of 4 x 4 km.

Part II

Chapter 5 - Hellenic karst hydroystems: geogenic and anthropogenic processes affecting their geochemistry and water quality

This chapter is a submitted paper (*Li Vigni et al., 2023b*), the physico-chemical parameters and the chemistry of the waters are published in repositories (*Li Vigni et al., 2023a*)

From May 2016 to October 2022, 202 karst water samples were collected along the Hellenic territory (*Fig.5.1*), including also the islands of Crete and Euboea. Samples were taken almost exclusively from natural springs. Only two samples (Mavrosoulava and Kaissarianis) were taken from drillings tapping karst aquifers. Sampling sites were selected mostly based on the spring mean flow rates ($> 50 \text{ L s}^{-1}$). Only 23 samples were collected from springs with mean flow rate between 18 and 50 L s^{-1} . Approximate position and flow rate data were taken prevailingly from the catalogue of Hellenic karst springs made by HSGME (Hellenic Survey of Geology and Mineral Exploration - former IGME) in the 1970s and 1980s (*Kakavas, 1984; Kallergis & Skayias, 1980; Knithakis, 1983; Kourmoulis, 1979, 1984, 1987; Skayias, 1978, 1986; Stamos & Manakos, 1986; Vergis, 1985*). Unfortunately, this catalogue does not cover the whole Greek territory, not comprising a few important areas (Attica, Epirus, Central Macedonia, Chalkidiki, and the Aegean islands). For these areas information was obtained from different publications (e.g., *Christodoulou et al., 1993; Leontiadis et al., 1997; Leontiadis & Nikolaou, 1999; Nikolaou, 2010; Nikolaou et al., 2011; Katsanou et al., 2017*). Additional information for Crete were taken from *Kourmoulis, 1979* and *Malagò et al., 2016*. We are aware that mean flow rates could have changed significantly since the time of measurements. Indeed, we found some of the springs, included in the catalogue with high measured flows at the time of the compilation of the catalogue, which are at present completely dry. Our sampling is not complete and many big springs in remote areas, due to the lack of precise geographic indications, have not been sampled and only a few springs were not sampled due to inaccessibility. Nevertheless, we are confident that most of the springs with the highest water flow in the country were sampled.

The physico-chemical parameters as well as the chemical composition in terms of major ions and trace elements, and the results of aqueous speciation calculations are reported in Table A1, A2, A3 and A4, found in Appendix.

Results were compared with the limits set by the Directive 98/83/EC and the Directive 2020/2184/EC that fix quality standards for waters suitable for human consumption.

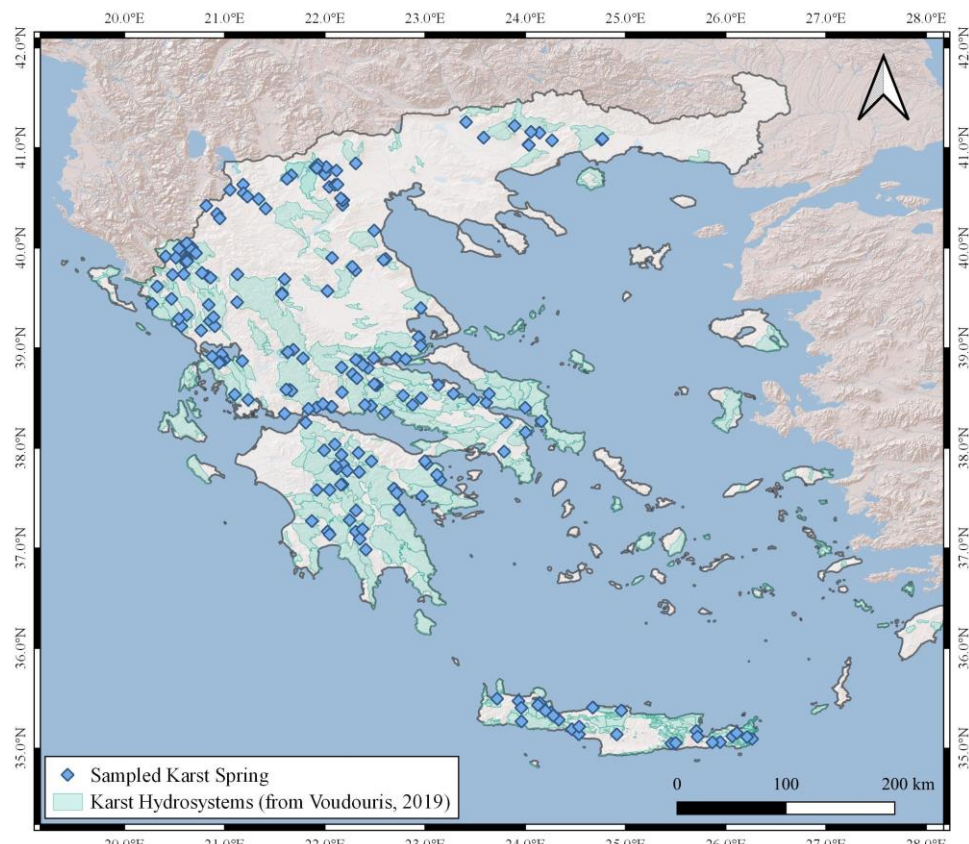


Fig.5.1. Geographic distributions of collected karst springs. Karst hydroystems (green areas) from *Voudouris (2019)*. Basemap by *ESRI* maps.

5.1. Results

5.1.1 Major ions

Temperature values range between 5.6 and 33.5 °C. The highest values were measured in Glyfa, Gouvo, and Kalamos Tsirioneri karst springs; sampling of these springs occurred during the summer period at the first accessible point where the water had a very low flow; indeed, the main emission points in these springs are surrounded by reeds that make them inaccessible to sampling. For these springs the measured temperature was not considered representative of the groundwater

conditions before emergence. The pH values vary from 6.5 to 8.5, whereas Electrical Conductivity ranges from $174 \mu\text{S cm}^{-1}$ to $31,400 \mu\text{S cm}^{-1}$ and Eh from -38 mV to 399 mV.

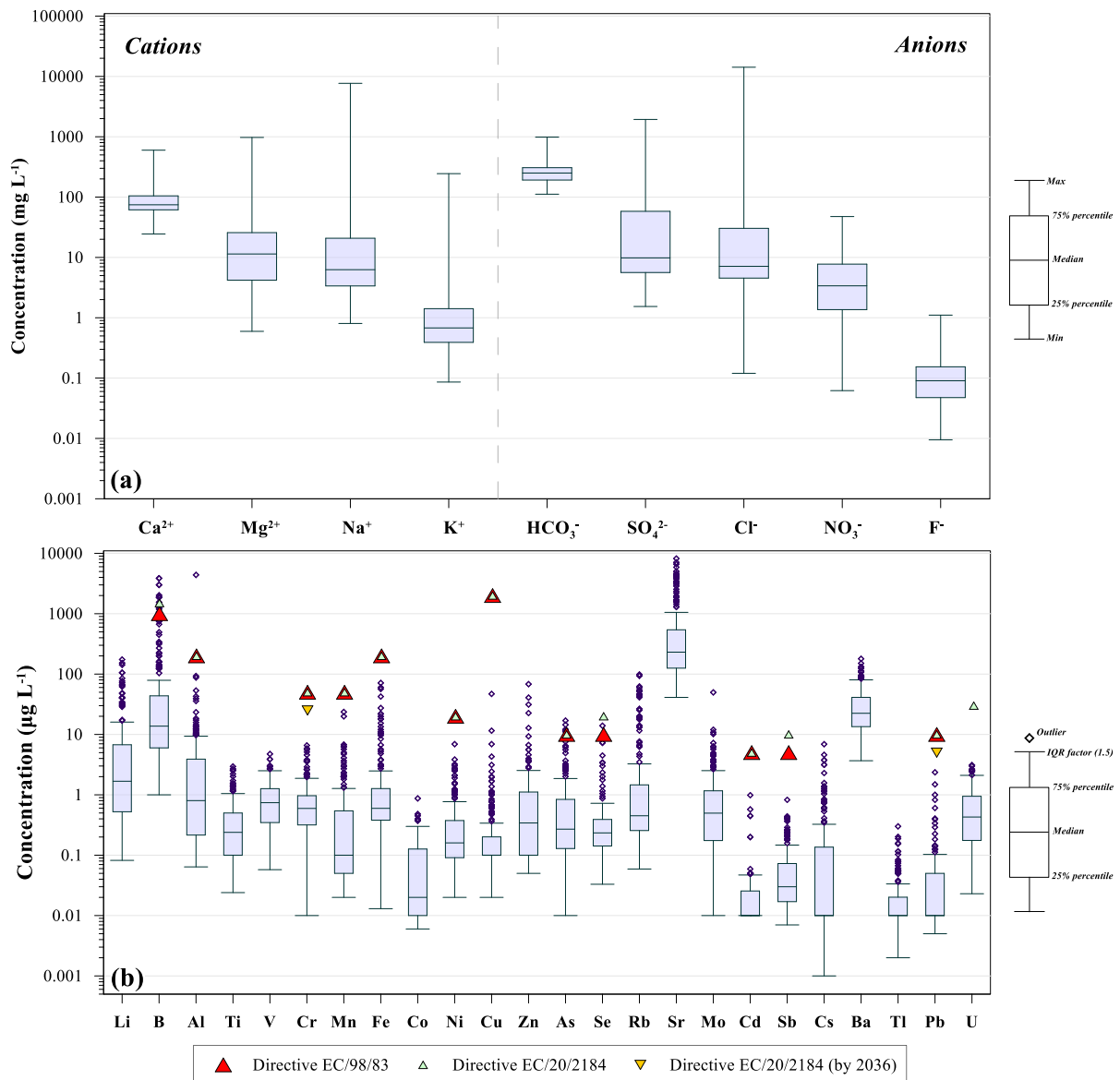


Fig.5.2. Boxplots of (a) major ions and (b) trace elements of the collected karst springs.

The major ions show a large range of concentrations, sometimes four orders of magnitude. According to the median value, the concentration of cations and anions decreases in order to abundance $\text{Ca}^{2+} > \text{Mg}^{2+} > \text{Na}^+ > \text{K}^+$ and $\text{HCO}_3^- > \text{SO}_4^{2-} > \text{Cl}^- > \text{NO}_3^- > \text{F}^-$, respectively (Fig.5.2a).

All water samples were plotted in a Langelier-Ludwig diagram (Fig.5.3), where three groups with different geochemical compositions can be recognised: (**group a**) characterised by Ca-HCO₃ composition and low salinity (165 mg L⁻¹ – 1343 mg L⁻¹ of TDS); (**group b**) characterised by Na-Cl

composition and high saline content (up to $25,760 \text{ mg L}^{-1}$ of TDS); (**group c**) characterised by a sulfate enrichment ($< 70 \text{ mg L}^{-1}$) and low to medium salinity ($336 \text{ mg L}^{-1} – 2425 \text{ mg L}^{-1}$ of TDS). The remaining samples have intermediate compositions often following mixing trends between the three groups.

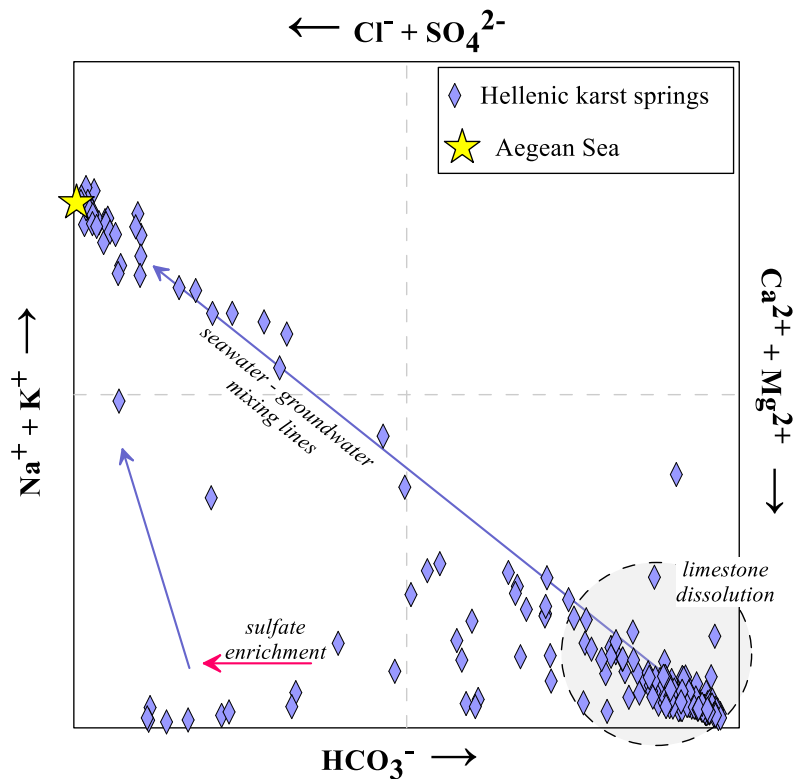


Fig.5.3. Langlier-Ludwig classification diagram.

5.1.2 Trace elements

The collected karst waters were analysed also for trace elements determination (Table A3). They show a wide range of concentration, generally, more than two orders of magnitude (Fig.5.2b). Trace elements can be subdivided into elements never exceeding $1 \mu\text{g L}^{-1}$ (Be, Co, Cd, Sb, Tl), $10 \mu\text{g L}^{-1}$ (Ti, V, Cr, Ni, Cs, Pb, U), $100 \mu\text{g L}^{-1}$ (Mn, Fe, Cu, Zn, As, Se, Rb, Mo), $1000 \mu\text{g L}^{-1}$ (Li, Ba) and $10,000 \mu\text{g L}^{-1}$ (B, Al, Sr). Sometimes the concentration was below the detection limit. Considering the concentration below the detection limit as a missing value, only four elements (Rb, Sr, Ba, U) show no missing data whilst five elements (Mn, Cu, Cd, Tl, Pb) had less than 60% of determined values. Furthermore, Be shows values always below the detection limit.

5.2. Discussion

5.1.1. Geogenic processes

In order to better discriminate saline and non-saline karst springs, samples were subdivided into two groups, characterized by low ($< 100 \text{ mg L}^{-1}$) and high ($> 100 \text{ mg L}^{-1}$) chloride content. Furthermore, based on their sulfate composition, an additional group, that includes 14 karst springs was added (Acheron, Archon, Bobos, Doliana, Gorgogouqli, Gouvo, Kefalovryso Agia Marina, Kourtalioti, Mana Nerou, Nelles, Pantaleiomona, Rogozi, Vathy, and Zavarina Limni).

According to *Voudouris (2019)*, low chloride waters (group a) show the typical bicarbonate-alkaline-earth composition of groundwater circulating in carbonate aquifers. The carbonate dissolution process within the aquifers is confirmed by a good positive correlation between $\text{Ca}^{2+} + \text{Mg}^{2+}$ and HCO_3^- along the 1:1 equivalent ratio line (*Fig.5.4a*). Saline and sulfate waters (groups b and c), instead, have an excess of Ca^{2+} and Mg^{2+} respect to the 1:1 equivalent ratio line; for the former the excess can be explained with a seawater influence and is generally associated with a higher $\text{Mg}^{2+}/\text{Ca}^{2+}$ ratio tending towards that of seawater (*Fig.5.4b*). The low salinity waters display on the same graph (*Fig.5.4b*) a large range in $\text{Mg}^{2+}/\text{Ca}^{2+}$ ratios not related to their Cl^- content. For these waters the $\text{Mg}^{2+}/\text{Ca}^{2+}$ ratio depends on the mineralogy of the aquifers, with values tending towards a $\text{Mg}^{2+}/\text{Ca}^{2+}$ ratio of 1 when the prevailing rocks are dolomitic. On the contrary low $\text{Mg}^{2+}/\text{Ca}^{2+}$ values are expected when the aquifers' rocks are made up prevailingly of calcite. In the Na^+ versus Cl^- binary diagram (*Fig.5.4c*), the most saline waters fall along the seawater dilution line, confirming significant marine contamination of the aquifers. This is consistent with their coastal location. In the same diagram, some low saline waters show an excess of Na^+ with respect to the seawater ratio line, suggesting that water-rock interactions within the aquifer may modify this ratio. The ionic exchange process between Ca^{2+} in water and Na^+ in clay minerals may justify this pattern (*Appelo & Postma, 1993*).

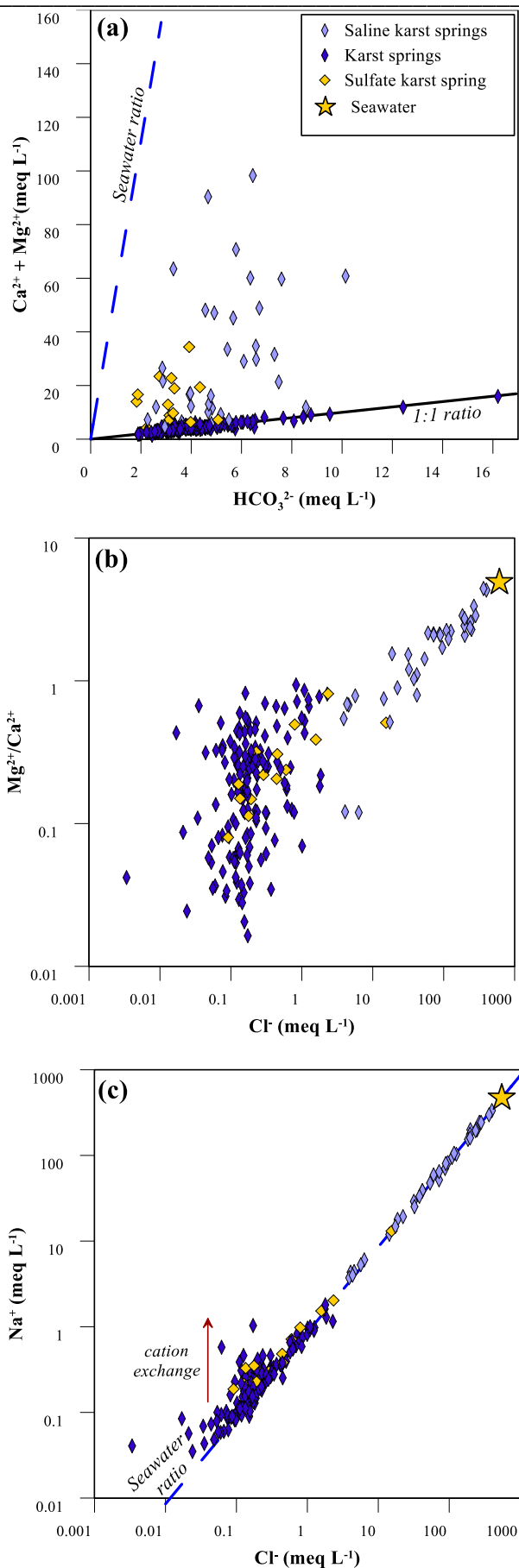


Fig.5.4. Binary correlation plots. (a) $\text{Ca}^{2+} + \text{Mg}^{2+}$ vs. alkalinity; (b) $\text{Mg}^{2+}/\text{Ca}^{2+}$ ratio vs. Cl^- ; (c) Na^+ versus Cl^- .

In a Ca^{2+} vs. SO_4^{2-} binary diagram (Fig.5.5a), some samples belonging to group c plot along the 1:1 equivalent ratio line suggesting gypsum or anhydrite dissolution within their aquifer. To discriminate which sulfate-minerals have undergone dissolution, the saturation index of gypsum (Fig.5.5b) and anhydrite were calculated; karst waters circulating in carbonate aquifers are all undersaturated both in gypsum and anhydrite, whilst the most sulfate-rich waters of group c reach saturation in gypsum but remain undersaturated in anhydrite (Table A4).

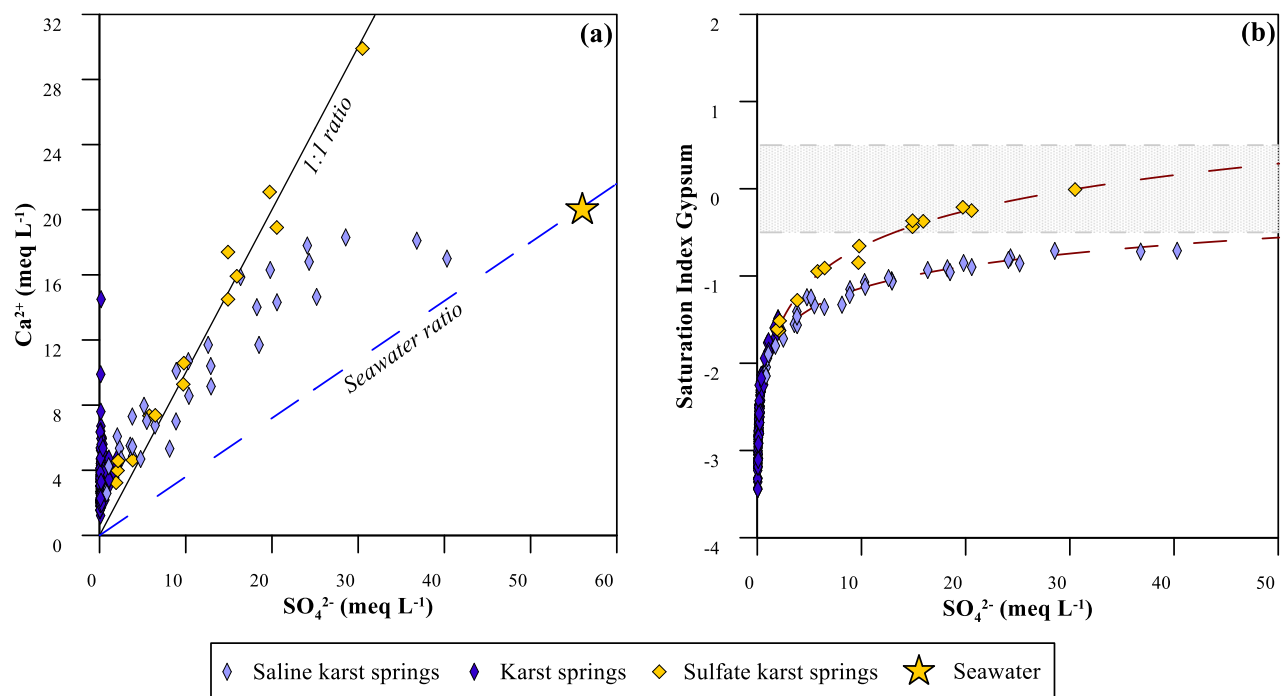


Fig.5.5. Binary correlation plots of sulfate karst springs. (a) Ca^{2+} vs. SO_4^{2-} ; (b) saturation index of gypsum vs. SO_4^{2-} .

The sulfate-composition of these waters is consistent with their geological environment. Springs with high sulfate content are located in Epirus (Fig.5.6). Their waters circulate within the Triassic pre-rift sequence of the Ionian zone (Karakitsios, 1995), which mainly consist of alternating gypsum formations and carbonate breccias cropping out close to major faults. According to previous studies (Nikolaou *et al.*, 2011; Katsanou *et al.*, 2017), the composition of sulfate springs is consistent with gypsum dissolution. On the other hand, for those samples collected near the shoreline, SO_4^{2-} content mostly derives from seawater intrusion although some contribution from gypsum dissolution may in some cases not be excluded (Fig.5.5a,b).

The remaining sulfate karst springs (Archon, Kefalovryso Agia Marina, Kourtalioti, and Pantaleiomana) are located, instead, on Crete Island. Their aquifers are hosted in limestone of Gavrovo-Tripoli Unit at the contact with Phyllite-Quartzite Unit (*Kourmoulis*, 1979). The latter unit is widespread throughout Crete and consists of Carboniferous-Triassic quartz-rich siliciclastic sediments, phyllite, with minor marble, conglomerate, volcanic rocks and evaporitic deposits (gypsum and dolomite) (*Krahl et al.*, 1983; *Ring et al.*, 2022). Thus, although under-saturated in gypsum minerals but following the fitting curve (*Fig.5.5*), the sulfate enrichment of Cretan springs may derive from evaporitic body within the Phyllite-Quartzite unit.

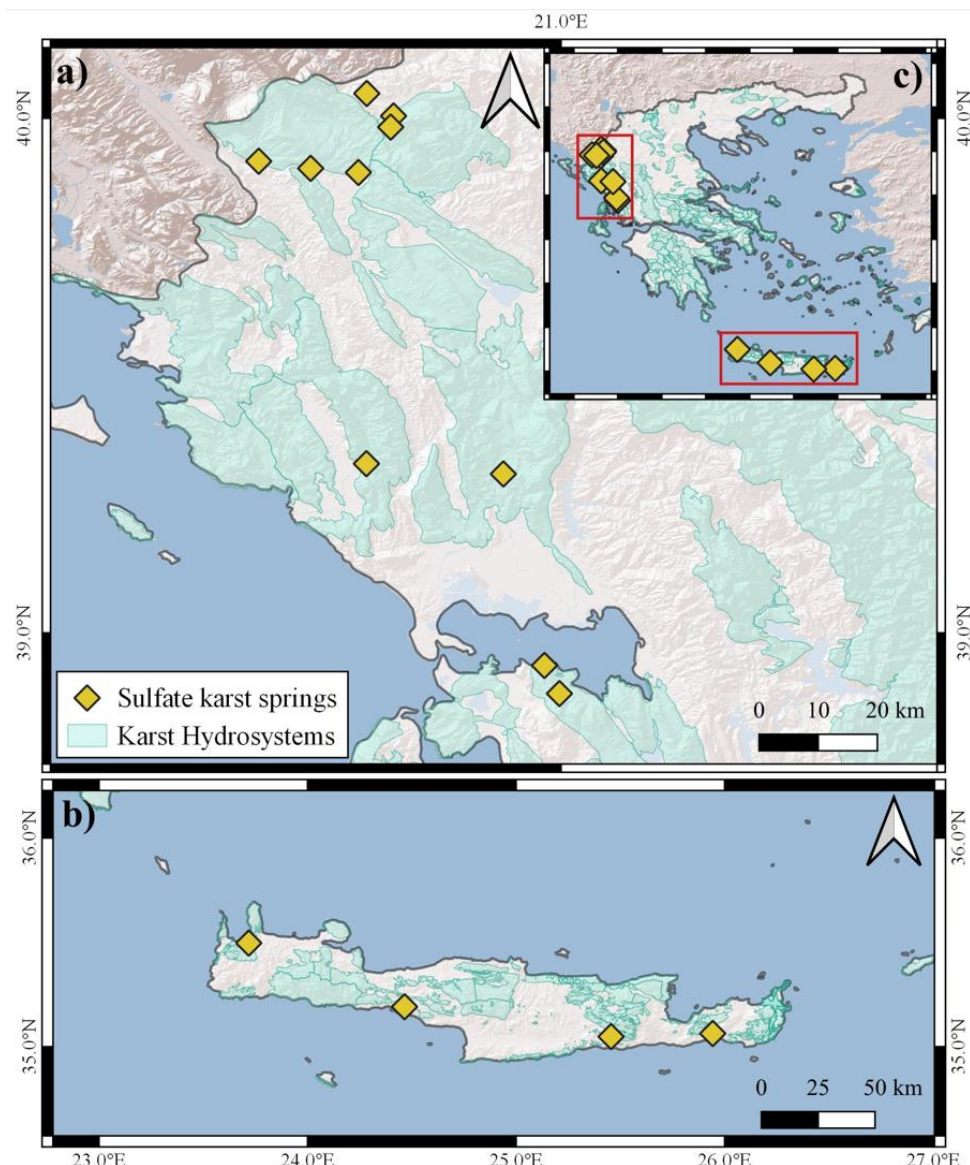


Fig.5.6. Geographical distribution of sulfate karst springs in (a) Epirus and in (b) Crete. Karst hydroystems from Voudouris (2019). Basemap by ESRI maps.

5.2.2 Quality issues

Water resources, in particular karst systems, are essential for the development of life. Thus, their management and protection are of crucial importance not only for human health but also for the correct balance of all terrestrial and marine ecosystems. Unfortunately, overexploitation and human activities (industry, agriculture, tourism) are the major causes of the deterioration of water resources, in terms of quantity and, especially, quality.

Higher trace element concentrations are related to both natural and anthropogenic sources. In this respect, in order to recognize any anthropogenic impact on the aquifer systems, the knowledge of the hydrogeological setting together with the geological and structural features of the region is essential to discriminate the natural baseline (*Morgantini et al., 2009*).

5.2.2.1 Salinity issues

The very great length of the Greek coastline, both absolute and relative to the extension of its territory, explains the high percentage of coastal karst aquifers feeding springs both at and under the sea level. The peculiarity of the Mediterranean area, which explains also the frequent occurrence of submarine karstic springs, derives from the important sea level drop that took place from 5.9 to 5.3 Ma before present during the Messinian Salinity Crisis (*Cita & Ryan, 1978*). If not isolated from the sea by impermeable sediments, these karst systems, which extend deep below sea level, may represent an easy inland access to contaminating seawater (*Fleury et al., 2007*). According to *Voudouris (2019)*, about 5% of the Greek karst hydroystems is of poor quality due to seawater intrusion in coastal aquifers as a consequence of overexploitation. In this study, most of the sampled karst springs have water of good quality for human consumption and are often used as drinking water. About 20% of the sampled springs have a high concentration of Chloride and Boron, often above the limits set by European Council for drinking water ($\text{Cl}^- = 250 \text{ mg L}^{-1}$; $\text{B} = 1000 \mu\text{g L}^{-1}$), making them not suitable for human consumption. An example is the case of Almyri, Orea Elenis, and Selontas, in East Corinth, three springs of the same aquifer under strong anthropogenic stress;

about twenty boreholes extract water from the aquifer, with a rate of $40\text{--}70 \text{ m}^3 \text{ h}^{-1}$, causing different degrees of salinization of groundwater, highlighted from high chloride content ($280\text{--}1250 \text{ mg L}^{-1}$) (Markantonis & Koumantakis, 2011). One of the most studied karst springs is Almyros, a coastal brackish spring close to Heraklion (Crete) (e.g., Maramathas et al., 2003; Monopolis et al., 2005; Maramathas & Gailamas, 2011; Archontelis & Ganoulis, 2015; Steiakakis et al., 2016), where more than 500 shallow wells and more than 50 deeper boreholes are spread in the whole aquifer (Steiakakis et al., 2016). The intensive exploitation, due to the population growth, the development of tourism and the climate change, has led a significant deterioration of the ground water quality due to salinisation effects (Monopolis et al., 2005; Steiakakis et al., 2016). Indeed, the monitoring of groundwater quality, by local Municipalities, indicates an increasing trend of the chloride contents (Steiakakis et al., 2016).

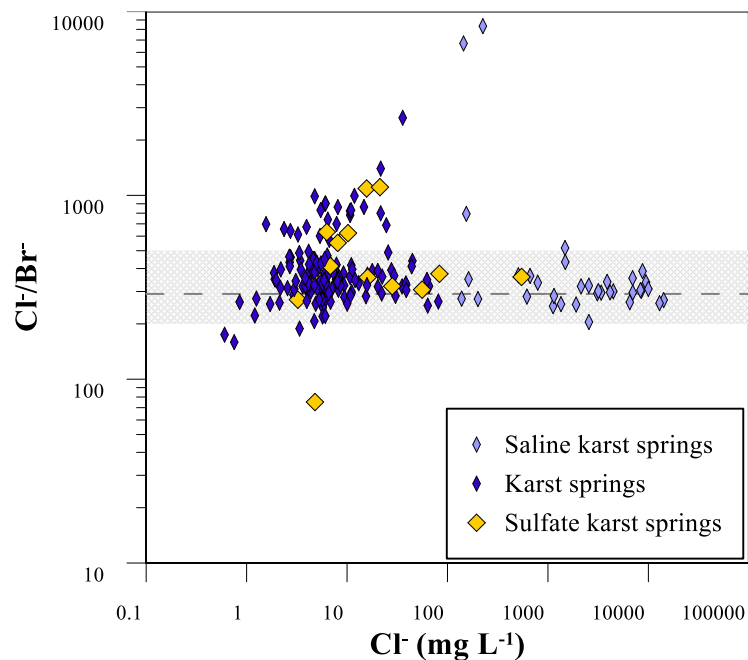


Fig.5.7. Binary correlation plot of Cl/Br^- ratio vs. Cl^- .

In order to better discriminate the possible sources of chloride, the Cl^-/Br^- ratio was calculated (Fig.5.7). Most of the samples show a narrow range of values (200-500) similar to the seawater ratio (291 – Davis et al., 1998). The most saline ones ($\text{Cl}^- > 100 \text{ mg L}^{-1}$), as evidenced before, denote a clear influence from seawater intrusion, while those with lower salinity reflect the Cl^-/Br^-

ratio of the meteoric recharge. Some low-salinity karst samples located in the Epirus area show higher chloride content than other nearby karst springs. Due to the great distance from the coast, the elevated chloride concentration cannot be related to present seawater intrusion. These samples show Cl^-/Br^- ratio > 800 and belong to waters circulating within the Ionian zone sequences, where evaporite outcrops are present. In this respect, these Cl^-/Br^- values may be ascribed to the dissolution of halite salt domes in the cores of anticlines (Nikolaou *et al.*, 2011). Samples of Krya and Perama, situated near Ioannina city, show the highest values of Cl^-/Br^- ratio, 2642 and 8329 respectively: these values may be alternatively ascribed to the use of road salts ($\text{Cl}^-/\text{Br}^- > 5000$; Panno *et al.*, 2006; Mullaney *et al.*, 2009). Indeed, the two springs are located in an area where winter temperatures often drop below zero and are very close to main roads where salts are used for de-icing purposes. Resampling of the spring of Perama at the end of the summer season revealed a similar high Cl^-/Br^- ratio (6707) indicating that a natural origin from evaporite dissolution is probably the best explanation.

Comparatively, fewer water samples show Cl^-/Br^- ratios below that of seawater. These are generally waters with low salinity (Cl^- generally below 10 mg L^{-1}) and their Cl^-/Br^- ratios may in some cases reflect lower values of their meteoric recharge. Alcalà & Custodio (2008) found that rainwater at high altitudes and/or inland areas are characterised by Cl^-/Br^- ratios lower than that of seawater (down to < 100). Indeed, most of these samples were taken at high altitudes and far away from the coast. This situation does not apply to the sample of Gorgogouli (low altitude and close to the coast) where Br^- excess may be ascribed to anthropogenic sources, probably agrochemicals (Alcalà & Custodio, 2008).

According to Mimikou (2005), the 80% of the total consumption of water resources in Greece is used in agricultural activities. The growth and yield of crops are strongly related to the quantity of dissolved salt in the soil waters. Although some plant species can grow in highly saline soils (e.g. halophytes), chloride, sodium and boron have generally toxic effects on the growth of plants and

may reduce the permeability of the soil (*Hanson et al.* 2006). In order to evaluate the salinity effects of soil water, salinity and sodium hazard index are used. The former considers the electrical conductivity of waters, indicating the value of $2250 \mu\text{S cm}^{-1}$ as the maximum salinity level in water for use in irrigation (*Hanson et al.*, 2006). The potential sodium hazard is quantified using the Sodium Adsorption Ratio (SAR), defined by the following equation:

$$\text{SAR} = \frac{\text{Na}^+}{\sqrt{(\text{Ca}^{2+} + \text{Mg}^{2+})/2}} \quad (5.1)$$

where the ion concentrations are expressed in milliequivalents per litre (*Richards, 1954*).

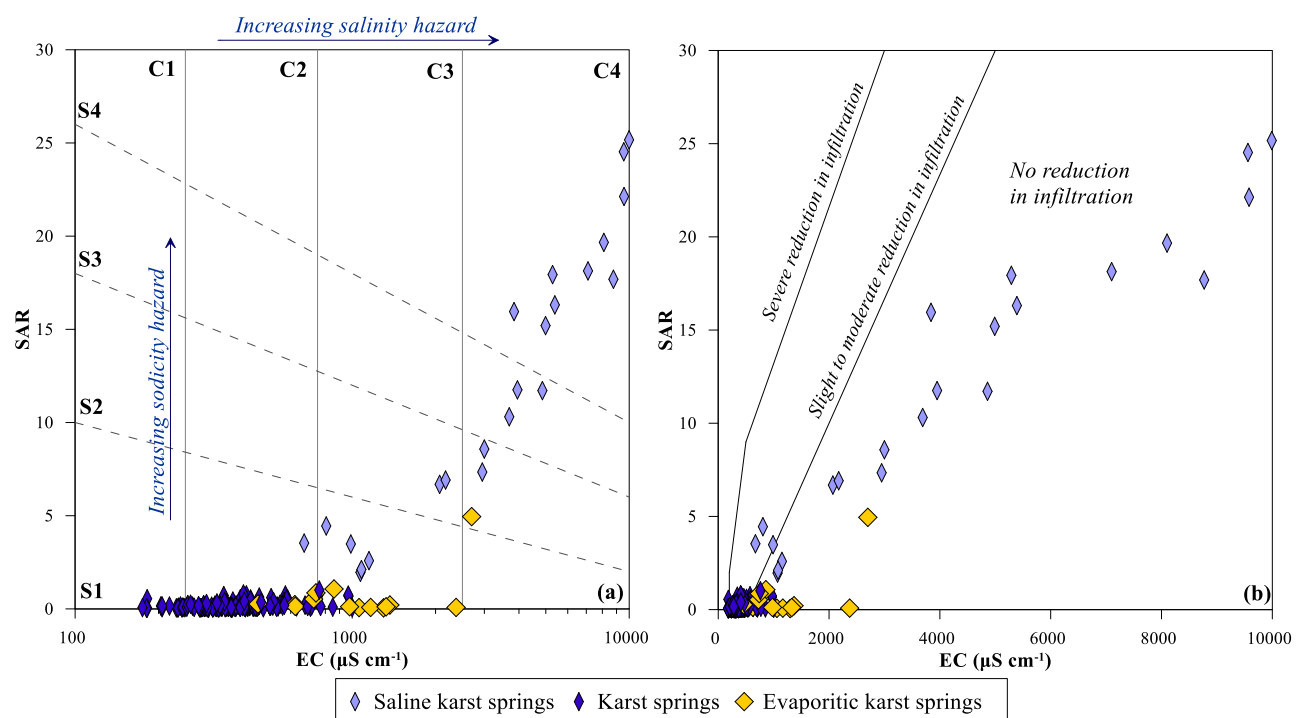


Fig.5.8. Binary plots Sodium Adsorption Ratio vs. Electrical Conductivity, indicating plant toxicity classes (a) and soil permeability classes (b) (*Hanson et al.*, 2006). Thirteen samples with $\text{EC} > 10,000 \mu\text{S cm}^{-1}$ fall outside the graphs. C1 = low; C2 = medium; C3 = high; C4 = very high salinity hazard. S1 = low; S2 = medium; S3 = high; S4 = very high sodicity hazard.

The EC values of karst springs of this study ranges from $174 \mu\text{S cm}^{-1}$ to $31,400 \mu\text{S cm}^{-1}$, with the 15% of the samples, almost all belonging to the saline group, showing values falling in the high or very high salinity hazard fields. The highest EC values are associated with the karst springs located in coastal areas and affected by seawater intrusion into the aquifers. Moreover, nearly all these waters show also highest SAR values, indicating an elevated potential for toxicity to plants

(*Fig.5.8a*). On the contrary, most of the saline waters do not create permeability problems to the soil due to the high sodium contents (*Fig.5.8b*). Only the spring of Perama (Epirus), whose salinity is likely derived from evaporite dissolution, shows a moderate risk of soil permeability reduction (*Fig.5.8b*). The low chloride karst springs group fall almost all in the low and medium salinity hazard classes (*Fig.5.8a*) with a low sodicity hazard (< 2). Only few low chloride karst springs fall in the high salinity hazard class. Almost all the sulfate karst springs are also included in this class (*Fig.5.8a*), being their salinity derived from the dissolution of evaporite rocks, mainly gypsum, but their sodicity hazard remains negligible. All these waters, falling in the high salinity hazard field, can still be used for irrigation provided that the irrigated soils are well drained preventing salt accumulation (*Hanson et al., 2006*). Moreover, the cultivation of salt-tolerant plant varieties allows often the use also of waters belonging to the class of very high salinity hazard if no salt accumulation occurs in the soil. Especially in the areas of Greece characterised by semi-arid climate, the use of salt-tolerant varieties has long been introduced, allowing the cultivation of vegetables sometimes with water conductivity up to nearly 10,000 $\mu\text{S cm}^{-1}$ (*D'Alessandro et al., 2017*).

5.2.2.2 Nitrate

Nitrate is the most abundant nutrient, but it is considered also the most widespread pollutant. Although it may have a natural origin, such as atmospheric deposition or decay of organic matter, the main contribution derives from the increase of anthropogenic activities. The main anthropogenic sources are N-based fertilizers, untreated domestic and industrial wastewater, old septic systems, or leachate from landfill sites (*Abascal et al., 2022; Kalhor et al., 2019*). Nitrate is, often, added in excess to the soil to increase its productivity and most of it is leached to the aquifers below. Although there is no general consensus on the danger to human health represented by nitrate itself (*L'hirondel & L'hirondel 2002*), it remains an undesirable constituent generally accompanied by dangerous components (i.e., toxic agrochemicals or harmful microorganisms).

According to *Daskalaki & Voudouris* (2008), nitrate pollution is, after seawater contamination, the second major source of groundwater degradation in Greece. Many aquifers in Greece display high nitrate content, exceeding the European maximum admissible concentration (50 mg L^{-1}) for drinking water (*Daskalaki & Voudouris*, 2008; *Dokou et al.*, 2015), making them non-suitable for human consumption. The most affected aquifers, with values exceeding the European limits, are the Boeoticos Cephissos hydroystems in Central Greece (*Tziritis*, 2010), the Vocha plain in Korinthos prefecture (*Voudouris et al.*, 2004), Thessaly district (*Daskalaki & Voudouris*, 2008). The main source of nitrate is the excessive application of fertilizers (NH_4NO_3 , $(\text{NH}_4)_2\text{SO}_4$, and Nitrogen Phosphate Potassium) in intensively cultivated lands (such as cotton, tobacco, and olive). Other sources of nitrate are septic tanks and untreated domestic effluent from abandoned wells in urban areas (*Voudouris et al.*, 2004).

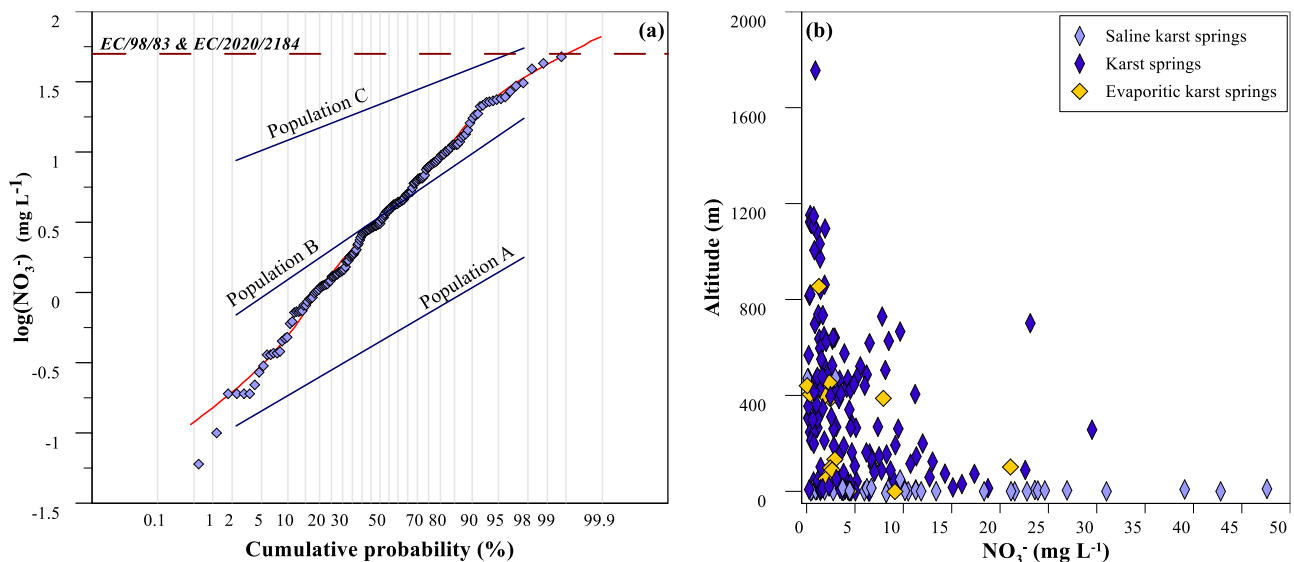


Fig.5.9. (a) Probability plot of NO_3^- concentration. The red dashed line represents the NO_3^- limit fixed by the European Directives (50 mg L^{-1}). (b) Binary correlation plot of altitude vs. NO_3^- .

In this study, nitrate concentration in karst springs never exceeds the European limit for drinking water (50 mg L^{-1} ; 98/83/EC and 2020/2184/EC), suggesting good quality of most sampled karst groundwater. Nevertheless, high NO_3^- content was found in some springs, with values up to 47.6 mg L^{-1} (Fig.5.9a). Three main log-normal populations were recognised from the probability plot (Fig.5.9b). The population A comprises waters with the lowest NO_3^- concentrations ($< 1 \text{ mg L}^{-1}$),

with no evidence of pollution and representing background values. The population B shows a mean NO_3^- value of 4.28 mg L^{-1} , suggesting only limited input from external sources. The third population (C) shows the highest nitrate concentrations (up to 47.6 mg L^{-1}). These springs are located close to urban centres, farmland, or highly touristic coastal areas, clearly evidencing pollution issues. Indeed, in a correlation with the altitude (*Fig.5.9b*), the lowest nitrate concentrations were found in mountain areas, whilst the most polluted springs are located in coastal areas, which are heavily exploited for agriculture and tourism and where urban centres are widely present. Exceptionally, some springs (Kefalovryso Karpenisi, Petres, Tria Piagadia, Santovou, and Xino Nero), although located at about 600-800 m of altitude, display elevated nitrate values. These derive from high altitude, urbanized, and intensively cultivated intramountain basins.

5.2.2.3 Strontium

Strontium is a lithophile metallic element and a common trace element in groundwater. Because of a similar ionic ratio and charge to calcium, Sr behaves similarly in the environment and can replace it. Indeed, intake of high Sr quantities can have negative effects on human health, such as abnormal bone development in young people (ATSDR, 2004). Although the WHO has not set a maximum admissible concentration in drinking water, the USEPA has set a non-regulatory benchmark, a health-based screening level (HBSL), of $4000 \mu\text{g L}^{-1}$ to indicate a potential human-health concern (Norman *et al.*, 2018). Strontium derives from several sources, both natural and anthropogenic. It derives from weathering of some Sr-bearing minerals, as well as carbonates, evaporites, and granites. The main Sr-bearing minerals are celestite (SrSO_4) and strontianite (SrCO_3). In addition, strontium may have a marine source due to seawater-groundwater mixing. Moreover, Sr can be associated with industrial waste, mining, or landfill leachate (Musgrove, 2021 and references therein).

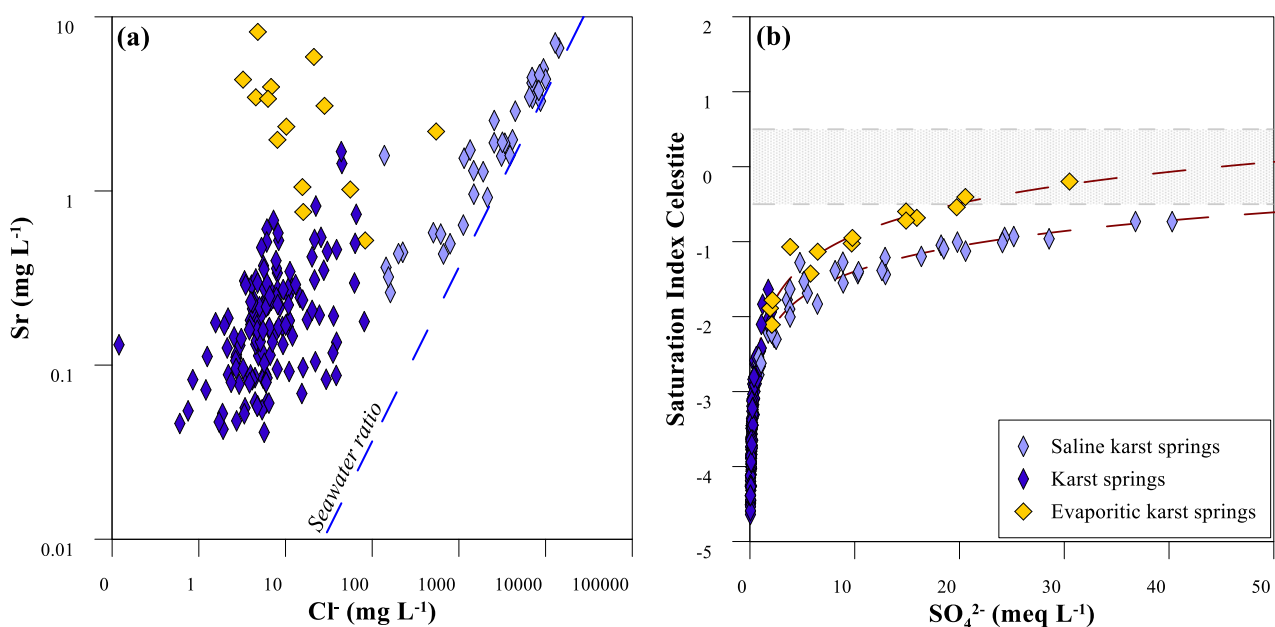


Fig.5.10. Binary correlation plots of sulfate karst springs. (a) Sr vs. Cl^- . (b) Saturation index of celestite vs. SO_4^{2-} (the shaded stripe is the ± 0.5 range of values in which the waters are considered at saturation with respect to the solid phase).

In the present study, Strontium concentration in karst springs ranges between $41.1 \mu\text{g L}^{-1}$ and $8200 \mu\text{g L}^{-1}$ (Fig.2b). The highest concentrations are found in some karst springs located in coastal areas or in Epirus, where evaporite outcrops are present (Fig.5.10a). Strontium of the former springs derives from the mixing between karst groundwater and seawater, whilst the strontium concentration of Epirus springs derives from the dissolution of celestite and strontianite minerals hosted in evaporite formations. While both water types show Sr/SO_4 ratios higher than that of seawater, the waters that interacted with evaporites show generally the highest ratios. In Epirus, Triassic gypsum-rich evaporites include celestite minerals, whose precipitation is favoured by the dissolution of Ca-sulfate. The samples reach even saturation in celestite (Fig.5.10b). Strontium concentrations in Greek evaporites vary from 1100 ppm to 64,270 ppm (Badouna *et al.*, 2021), being sometimes very high and, therefore, justifying the Strontium values found in the sampled karst springs. Some of the sampled waters exceed the above-mentioned USEPA limit, but these are all saline waters anyway not suitable for human consumption.

5.2.2.4 Chromium and Nickel

Chromium appears in the natural environment in trivalent [Cr(III)] and hexavalent [Cr(VI)] oxidation states. Cr(III) is considered an essential element for human physiology; on the contrary, Cr(VI) is highly soluble in water and is considered an extremely toxic form (*Apollaro et al., 2019*). Nickel is a mobile metallic element and in natural water exists in the oxidation states, Ni(II), Ni(III), and Ni(IV), and, like chromium, is considered a toxic element (*Das et al., 2019*).

Chromium and Nickel pollution may derive from both natural and anthropogenic sources. A natural source is the weathering of Cr-Ni-rich minerals in ultramafic and ophiolitic complexes (*Salminen et al. 2005; De Vos et al. 2006*), whilst anthropogenic pollution derives from extensive use of Cr-based chemicals in industrial activities (*Reimann & de Caritat, 1998*).

In Greece, natural Cr and Ni contaminations are observed in areas where the aquifer is hosted in the ophiolitic belts of Pindos and Vardar (*Li Vigni et al, 2021; Vasileiou et al., 2019*). High levels of Cr(VI) were observed in the drinking waters of Central Macedonia, Thessaly, Attica, Lesvos, and Rhodes Islands (*Kaprara et al., 2015*).

In the present study, only total chromium was measured, but Cr(VI) is likely the dominant form, due to its great mobility with respect to Cr(III). In the analysed karst springs (*Fig.2b*), both Cr (up to $6.58 \mu\text{g L}^{-1}$) and Ni (up to $6.91 \mu\text{g L}^{-1}$) show values far from the limits set by the European Council ($50 \mu\text{g L}^{-1}$ for Cr and $20 \mu\text{g L}^{-1}$ for Ni). The Hellenic karst water, like most freshwater worldwide (*Reimann & de Caritat, 1998*), shows low Cr and Ni concentrations, not evidencing contaminations either of anthropogenic or natural origin. Although in Greece many studies evidenced Cr and Ni contaminations deriving from the leaching of widespread ophiolitic sequences in the country (*Dermatas et al., 2015; Economou-Eliopoulos et al., 2017; Tziritis et al., 2012*) or lateritic horizons (*Tziritis, 2014*), no similar impact has been evidenced on the presently studied karstic waters.

5.2.2.5 Arsenic

Arsenic is considered a highly toxic metalloid, which has harmful effects on human health, classified as a class1 carcinogen by the International Agency for Research on Cancer. The European Council has established the value of $10 \mu\text{g L}^{-1}$ as the maximum contaminant level for drinking water. Arsenic contamination may have both natural and anthropogenic sources: it can be naturally derived from the chemical weathering of sulfide ore deposits or transported by geothermal waters, whilst the main anthropogenic sources are mining activity, coal combustion, and As-pesticides (*Fitzmaurice et al., 2009; Shaji et al., 2021*).

Many regions of Greece, especially in the northern part, are affected by elevated concentrations of groundwater (*Gamaletsos et al., 2013*). The highest As concentration was found in the groundwater of the geothermal area of Chalkidiki, in northern Greece, with values up to $1000 \mu\text{g L}^{-1}$ (*Kouras et al., 2007*). The main sources of As in Greece are geothermal fluids arising from active tectonic and volcanic areas (*Gamaletsos et al., 2013; Li Vigni et al. 2023c*).

Data on arsenic in Hellenic karst water are very scarce (*Panagopoulos, 2009; Petalas, 2017; Petalas & Moutsopoulos, 2018; Petalas et al., 2019*). However, in the present study values exceeding the European limit were found in three karst springs (*Fig.5.2b*): Tempi (up to $17.0 \mu\text{g L}^{-1}$), Potamos ($12.1 \mu\text{g L}^{-1}$), and Paleomylos ($12.0 \mu\text{g L}^{-1}$). The three springs are found in the eastern part of Thessaly and Central Greece and the arsenic contamination can be related to the geological conditions. Indeed, the involved karstic systems that were developed within carbonate formations at the contact with metamorphic and metavolcanic formations of the Ampelakia Unit (Blueschist unit) and Pelagonian Unit (*Stamatis, 2010*). Many occurrences of As-rich mineralizations have been found in the area mainly related to the metamorphic rocks (*Keleperidis et al., 2006; Gamaletsos et al., 2013*).

Although not showing extreme As concentrations like some geothermal waters in Greece (*Katsoyiannis et al., 2015; Li Vigni et al., 2023c*), the impact of these waters should not be

disregarded. Because of these As-rich karstic waters were sampled from springs with large flows (up to more than 2000 L s^{-1}), even concentrations not strongly exceeding the maximum allowed level correspond to large As fluxes that may have an adverse influence on the ecosystems fed by these waters.

5.2.2.6 Lead

Lead is a toxic heavy metal element, forming minerals like galena (PbS) and cerussite (PbCO_3). In groundwaters, Pb derives naturally from the leaching of minerals associated with ore deposits. Among anthropogenic sources, mining activities, leaded gasoline, batteries, paints, and water-plumbing systems are considered the primary lead pollutants for groundwater. According to *WHO* (2022), lead was recognised as one of the ten chemicals of major concern to public health, due to its widespread use. The major risk is the neurotoxic effect on children (*WHO*, 2016). The 98/83 European Directive set the limit for drinking water to $10 \mu\text{g L}^{-1}$, but the new directive (2020/2184/EC) lowered the limit to $5 \mu\text{g L}^{-1}$, which must be reached by 2036.

In Greece, elevated Pb concentrations in groundwater (up to $2700 \mu\text{g L}^{-1}$ in Eastern Central Greece) were observed in the whole country, except in Epirus and Central Macedonia (*Dokou et al.*, 2015). In the karst springs collected for this study, Pb concentrations reached up to $2.36 \mu\text{g L}^{-1}$, not exceeding the European Directive. The highest values ($> 0.1 \mu\text{g L}^{-1}$) were found in the karst springs of Euboea Island, West Central Greece, Crete Island. In the same areas, *Dokou et al.* (2015), who did not consider only karstic groundwater, estimated Pb concentration ranges of $10\text{-}50 \mu\text{g L}^{-1}$, $7.5\text{-}10 \mu\text{g L}^{-1}$ and $10\text{-}195 \mu\text{g L}^{-1}$, respectively, higher values than those found in this study.

5.3 Conclusion

As already shown by previous authors (*Daskalaki & Voudouris, 2008; Kallioras & Marinos, 2015; Voudouris & Kazakis, 2018; Kazakis et al., 2018; Voudouris, 2019*), the main hydrogeochemical types of karst water in Greece are calcium-bicarbonate for hinterland springs and sodium-chloride for coastal karst aquifers. Furthermore, a third hydrogeochemical group of waters whose calcium-sulfate composition derives from the dissolution of gypsum within their aquifers has been recognised. Trace elements contents are generally low except for elements associated to carbonate or sulfate minerals dissolution (B, Sr and Ba). Drinking water limits are rarely exceeded except for parameters related to seawater contamination in the coastal aquifers (EC, Na, Cl, B). In these areas most of the human population and activities are concentrated and, therefore, also the highest nitrate levels are found, though always below the drinking water limit. Among the remaining elements only As and Se exceed in few cases their maximum admitted contaminant limits. Such exceedance could not be related to anthropogenic activities and probably derives from present or past hydrothermal activities. Excluding those waters with $EC > 10 \text{ mS cm}^{-1}$, most of the waters unsuitable for drinking purposes due to high salinity may still be used in agriculture to irrigate salinity- and boron-tolerant plant varieties on well drained soils that do not allow salt accumulation.

From a quality point of view, the Greek karstic hydroystems, at least those located far from the coast, have to be considered a still intact water resource of national interest. These systems, being generally prone to contaminant infiltration, have to be carefully protected. Most of the population and human activities are still concentrated in coastal areas where the karstic aquifers are often naturally contaminated by seawater intrusion, although sometimes salinity is increased by over-pumping. But in recent times human activities, that have the potential to contaminate precious water resources, are extending also towards mountainous areas. Luckily many recharge areas of important karstic aquifers are included within natural reserve areas, but it is of utmost importance to preserve also those outside these areas.

Chapter 6 - Impact of geogenic degassing on C-isotopic composition of dissolved carbon in karst systems of Greece

In the period from 2016 to 2018, 193 dissolved gas samples and 37 free gas samples were collected from the big karst hydrosystems of Greece. The chemical composition (CO_2 , H_2S , CH_4 , N_2 , O_2 , He and H_2) of the collected gases analyzed in the present study, together with the isotopic composition of He and CO_2 -C in free gas samples ($\delta^{13}\text{C}_{\text{CO}_2}$) and of Total Dissolved Inorganic Carbon ($\delta^{13}\text{C}_{\text{TDIC}}$), are reported in Table A6, A7 and A8, whilst the computed TDIC (Total Dissolved Inorganic Carbon) and $p\text{CO}_2$ values are listed in Table A4, found in the Appendix.

The dataset was compared with data from the Hellenic thermal karst springs and some thermo-mineral spring (*Daskalopoulou et al., 2019a*).

6.1 Gas Geochemistry

Nitrogen is the dominant component (*Fig.6.1*) of both dissolved (N_2 concentration from 559,900 $\mu\text{mol mol}^{-1}$ to 985,300 $\mu\text{mol mol}^{-1}$) and free (N_2 concentration from 634,800 $\mu\text{mol mol}^{-1}$ to 872,000 $\mu\text{mol mol}^{-1}$) gas samples collected from the Hellenic karst springs. Carbon dioxide varies from 941 $\mu\text{mol mol}^{-1}$ to 292,000 $\mu\text{mol mol}^{-1}$ and from 534 $\mu\text{mol mol}^{-1}$ to 233,400 $\mu\text{mol mol}^{-1}$, for dissolved and free samples, respectively. The highest concentrations are found at Petres and Xino Nero springs, two sites located close to the Florina basin, a well-known area for its several CO_2 -rich gas manifestations (*Pearce et al., 2004; Karakatsanis et al., 2007; D'Alessandro et al., 2011; Ziogou et al., 2013; Gemeni et al., 2015*). Oxygen concentrations arrive up to 286,400 $\mu\text{mol mol}^{-1}$ in dissolved samples and 203,200 $\mu\text{mol mol}^{-1}$ in free samples, indicating an important atmospheric component. Methane ranges between 0.1 $\mu\text{mol mol}^{-1}$ and 29,536 $\mu\text{mol mol}^{-1}$ in dissolved samples and between 0.1 $\mu\text{mol mol}^{-1}$ and 236 $\mu\text{mol mol}^{-1}$ in free gases. Lastly, helium concentrations arrive up to 272 $\mu\text{mol mol}^{-1}$ and to 394 $\mu\text{mol mol}^{-1}$, for dissolved and free samples, respectively.

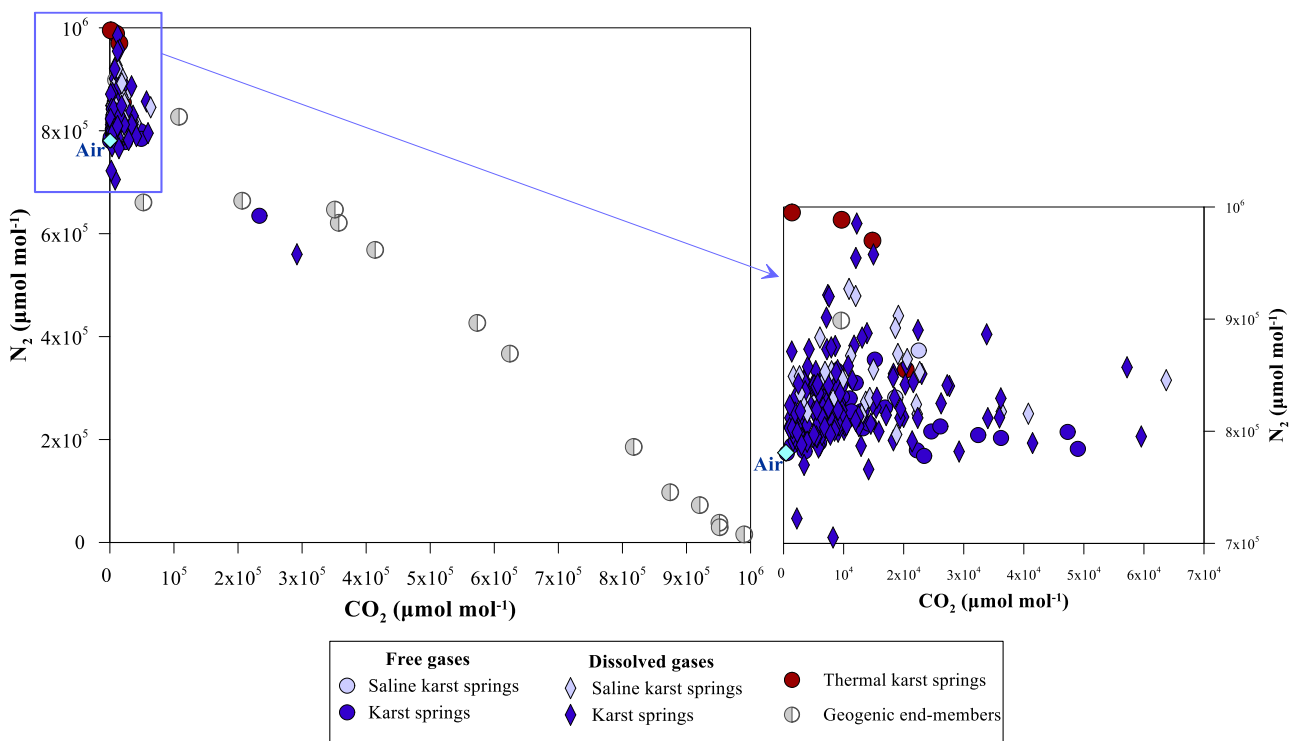


Fig.6.1. Binary plot of CO₂ concentrations vs. N₂ concentrations.

Comparing the free and dissolved phases (*Fig. 6.2*), it is noticeable that the collected gases are not at chemical equilibrium, likely due to the different solubilities of each gaseous species. Indeed, species with low solubility, such as nitrogen, are enriched in the free phase (*Fig. 6.2a*), whilst more soluble species, like CO₂, are favoured in the dissolved phase (*Fig. 6.2b*).

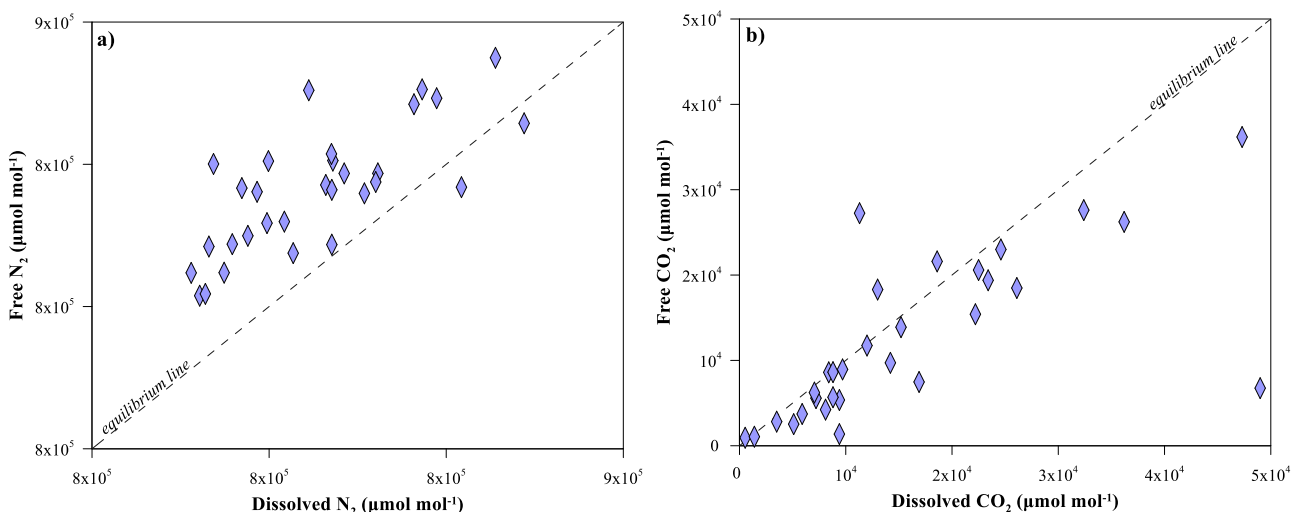


Fig. 6.2. Binary plot of (a) free N₂ concentrations *vs.* dissolved N₂ concentrations and of (b) free CO₂ concentrations *vs.* dissolved CO₂ concentrations. Chemical equilibrium lines are also plotted.

In the N₂-O₂-CO₂ ternary plot (Fig.6.3a), the samples fall almost all in the space delimited by the N₂ and CO₂ vertexes and atmospheric air composition. Most of the samples show compositions close to the latter end-member confirming an important contribution of atmospheric air through the meteoric recharge. Few samples show significant CO₂ enrichments while many display a virtually enrichment in N₂ due to a loss of oxygen by organic and/or inorganic reactions occurring along the groundwater circulation path within the aquifers. In the N₂-He-CO₂ ternary plot (Fig.6.3b), the karstic samples show He enrichment with respect to the atmospheric source sometimes reaching high values. The highest values are found in the thermal samples which presumably have deeper circuits and get more enriched in a He-rich geogenic source.

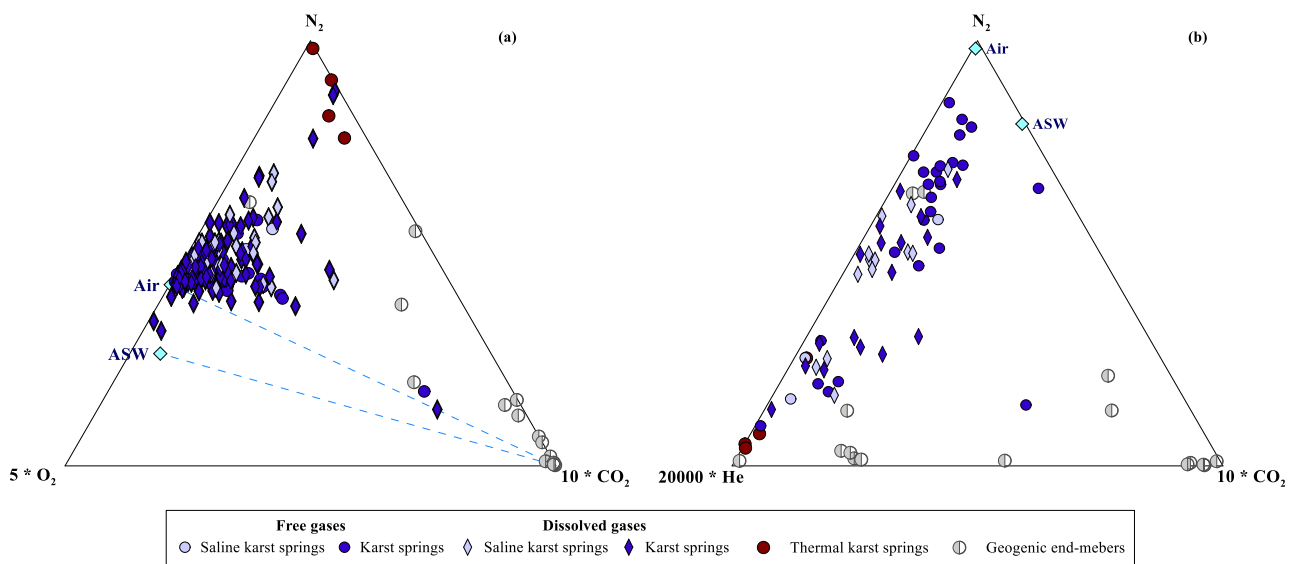


Fig.6.3. (a) N₂-O₂-CO₂ ternary plot. (b) N₂-He-CO₂ ternary plot. Air and ASW compositions are also plotted.

The isotopic composition of helium, expressed as R/R_A ratio, was measured only in few samples: the dissolved samples of Orea Elenis and Voda springs and the free samples of Almyri, Petres and Tempi springs. The R/R_A ratios range from 0.20 to 0.33, whilst the ⁴He/²⁰Ne ratios vary between 3.85 and 13.4, showing higher values than those of atmosphere (0.318, Sano *et al.*, 1985) and suggesting a prevailing crustal source of helium for these springs, derived from radiogenic decay of U and Th, along with a small mantle contribution (up to 4%).

Regarding the isotopic composition of carbon, $\delta^{13}\text{C}_{\text{TDIC}}$ values were measured in dissolved samples, whereas the $\delta^{13}\text{C}_{\text{CO}_2}$ in free samples. The $\delta^{13}\text{C}_{\text{TDIC}}$ varies between -16.6 ‰ and -0.10 ‰ (vs. V-PDB), whereas the $\delta^{13}\text{C}_{\text{CO}_2}$ ranged from -29.9 ‰ to -7.41 ‰ (vs. V-PDB). *Figure 6.4a* compares the $\delta^{13}\text{C}_{\text{CO}_2}$ values with those of $\delta^{13}\text{C}_{\text{TDIC}}$, where two groups can be differentiated. The first group is characterised by low values of both $\delta^{13}\text{C}_{\text{CO}_2}$ (< -12.5 ‰) and $\delta^{13}\text{C}_{\text{TDIC}}$ (< -5 ‰), indicating a mainly biogenic origin of the carbon (*Fig.6.4b*). On the other hand, the second one shows more positive values, falling within the magmatic/marine limestone fields (*Fig.6.4b*). Moreover, carbon is at or close to isotopic equilibrium between the dissolved and free phases in most of the samples, with a few exceptions. For instance, the Arapi and Voidomatis springs, in Epirus, are located along rivers, where a possible continuous mixing with riverine waters may be present, not permitting an equilibrium between the dissolved and the free phases.

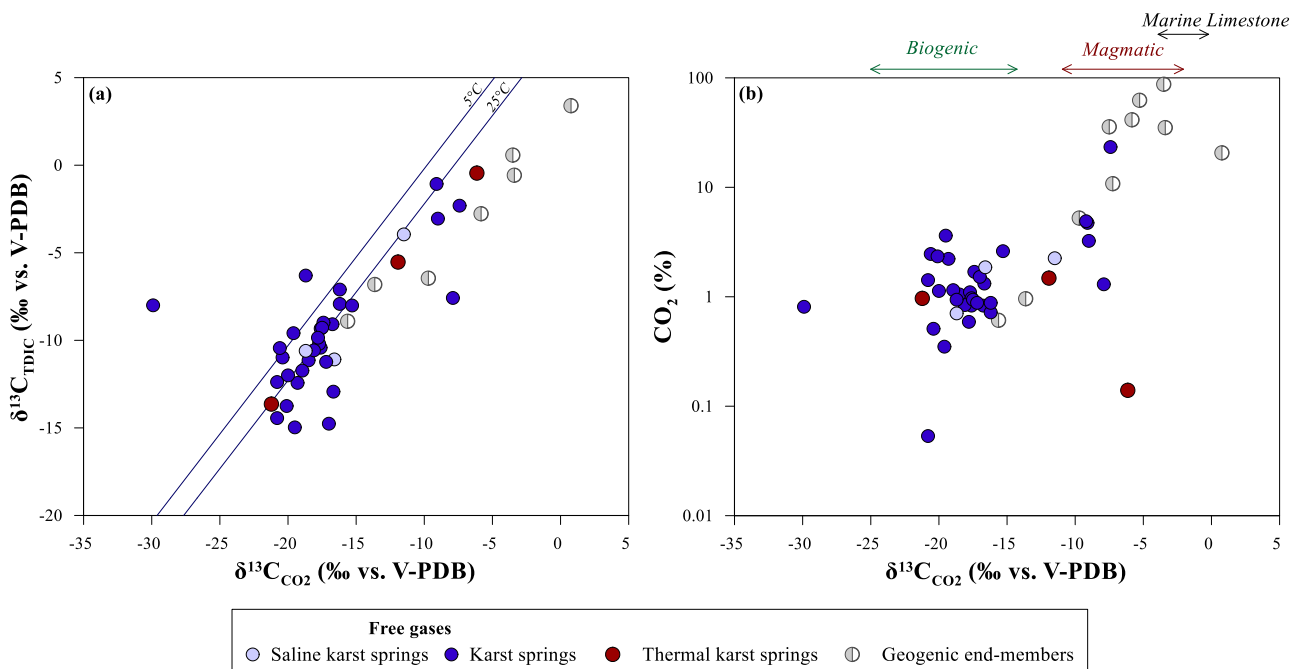


Fig.6.4. (a) Binary plot of $\delta^{13}\text{C}_{\text{CO}_2}$ values vs. $\delta^{13}\text{C}_{\text{TDIC}}$ values. Theoretical curves (blue) of equilibrium isotope fractionation between DIC and gaseous CO_2 at different temperatures are plotted (from Zhang *et al.*, 1995 and Myrttinen *et al.*, 2012). (b) Binary plot of $\delta^{13}\text{C}_{\text{CO}_2}$ values vs. CO_2 concentrations; the three colored arrows represent the $\delta^{13}\text{C}_{\text{CO}_2}$ ranges of the three different sources: biogenic (green), magmatic (red), marine limestone (black).

6.2 Carbon mass balance of the aquifers

The estimation of carbon release from karst hydro-systems correspond to about 15% (*Frondini et al., 2019*) of that estimated present-day CO₂ fluxes from active volcanoes (*Burton et al., 2013; Aiuppa et al., 2017, 2019; Fischer et al., 2019*), suggesting a significant impact on the global carbon budget estimation of the geogenic CO₂ output from regional diffuse degassing structure.

In order to quantify the flux of geogenic CO₂ transported and released by groundwater hosted in carbonate-evaporite aquifers, it is necessary to discriminate the different sources of dissolved carbon dioxide and to characterise their isotopic composition. According to *Wigley et al. (1978)*, the evolution of the total dissolved inorganic carbon (TDIC) and isotopic compositions of carbon in natural water systems is determined by multiple sources and sinks of carbon. In order to estimate the flux of geogenic CO₂ dissolved and transported by groundwaters circulating within regional carbonate aquifers, it is necessary to discriminate the different carbon sources. In the model proposed by *Chiodini et al., (1999, 2000)*, four carbon sources are considered: (i) the atmospheric CO₂ dissolved by rainwater (C_{atm}), (ii) the biogenic carbon produced in the soil (C_{bio}), (iii) the carbon derived from the dissolution of carbonate minerals during water-rocks interactions (C_{carb}), and (iv) the deeply derived carbon (C_{deep}).

The total carbon (TDIC) is given by the sum of dissolved carbonate species, expressed as mol L⁻¹, derived from the carbonate minerals dissolution process within the aquifer (C_{carb}) and the contribution of carbon from external sources to the aquifer (C_{ext}).

$$\text{TDIC} = \text{C}_{\text{carb}} + \text{C}_{\text{ext}} \quad (6.1)$$

If Ca, Mg and SO₄ concentrations in groundwater are, entirely, derived from dissolution of calcium-magnesium carbonate and gypsum (or anhydrite), the amount of carbon from carbonate dissolution can be computed as:

$$\text{C}_{\text{carb}} = \text{Ca} + \text{Mg} - \text{SO}_4 \quad (6.2)$$

where the chemical symbols refer to concentrations in molar units.

In order to investigate the origin of C_{ext} , the effects of carbonate dissolution were eliminated recalculating the values of TDIC and $\delta^{13}C_{TDIC}$ as C_{ext} , using equation (6.1), and $\delta^{13}C_{ext}$ by the following equation:

$$\delta^{13}C_{ext} = \frac{TDIC * \delta^{13}C_{TDIC} - C_{carb} * \delta^{13}C_{carb}}{C_{ext}} \quad (6.3)$$

where TDIC value is computed using the aqueous speciation model of PHREEQC software, $\delta^{13}C_{TDIC}$ is analytically determined and $\delta^{13}C_{carb}$ is set considering the average value of local carbonate rocks. If the water is affected by CO₂ degassing and/or calcite precipitation, these equations underestimate C_{ext} and overestimate $\delta^{13}C_{ext}$ because of isotopic fractionation.

C_{ext} is given by the sum of the carbon originally dissolved in infiltration waters (C_{inf} which corresponds to the sum of the atmospheric content (C_{atm}) plus carbon derived from biogenic activity in the soil (C_{bio}) during infiltration) and different amounts of deeply-derived CO₂ (C_{deep})

$$C_{ext} = C_{deep} + C_{inf} \quad (6.4)$$

Once all the terms of the carbon budget are determined (C_i), the total output of CO₂ ($Q_{CO2,i}$) can be computed for each carbon source, knowing the flow rate of the spring (q - Frondini *et al.*, 2019).

$$Q_{CO2,i} = C_i \times q \quad (6.5)$$

6.3 Carbon balance of the Hellenic karst aquifers

The TDIC and pCO_2 values were computed considering the chemical composition, pH and temperature, at field conditions, of the collected karst springs by means of the PHREEQC software package. The TDIC data range from 1.79 mmol L⁻¹ to 28 mmol L⁻¹, whereas the computed log(pCO_2) values vary between -3.43 bar and -0.58 bar. If plotted on a log(pCO_2) *versus* HCO₃⁻ binary diagram (Fig.6.5a), the collected samples show a good correlation between the bicarbonate concentration and the partial pressure of carbon dioxide, following the theoretical equilibrium

curves for temperatures between 10 and 25 °C almost corresponding to the measured temperatures. A similar trend can be also seen in a TDIC *versus* log($p\text{CO}_2$) diagram (Fig.6.5b), suggesting that most of the carbon is dissolved as HCO_3^- ion, the dominant species in a carbonate system at equilibrium, in a pH range between 6.4 and 10.3 (Drever, 1997).

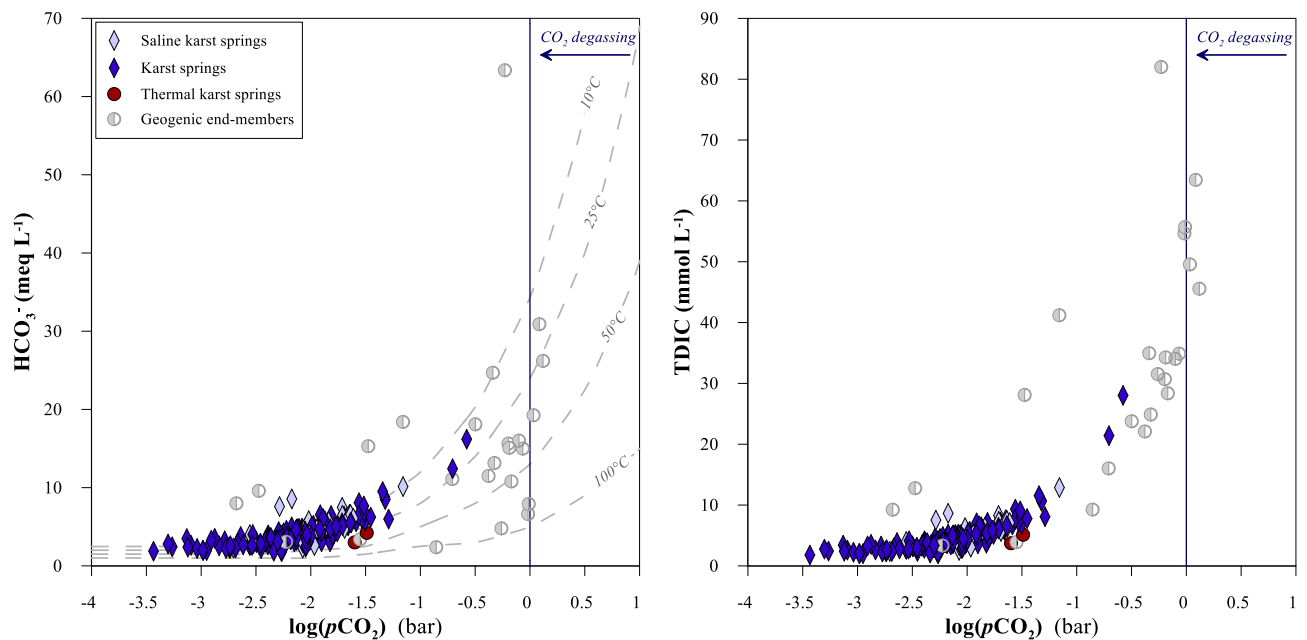


Fig.6.5. Binary diagram of $\log(p\text{CO}_2)$ *vs.* HCO_3^- . The data are compared to the theoretical curves, at different temperatures, computed for a system in equilibrium with calcite, dolomite and gypsum, according to the model proposed by Chiadini *et al.* (1995).

Based on the concentration of TDIC and its isotopic composition (Fig.6.6), the springs of the study area can be divided into two groups. The first group is characterised by more negative $\delta^{13}\text{C}_{\text{TDIC}}$ values (from -17 ‰ to -7 ‰), compatible with dissolved carbon from both dissolution of carbonate minerals and from dissolution of different amounts of biogenic CO_2 during the infiltration of meteoric waters into the soil (from -30 ‰ to -15 ‰; Deines *et al.*, 1974). The second group, instead, is characterised by heavier carbon isotope composition (from -6.5 ‰ to 0 ‰), ascribable to addition of an inorganic deeply-derived source of dissolved carbon. The samples of Tempi and Xino Nero show the more positive $\delta^{13}\text{C}_{\text{TDIC}}$ values, likely owing to a carbon fractionation because of a CO_2 degassing before the emergence of the groundwater from the spring.

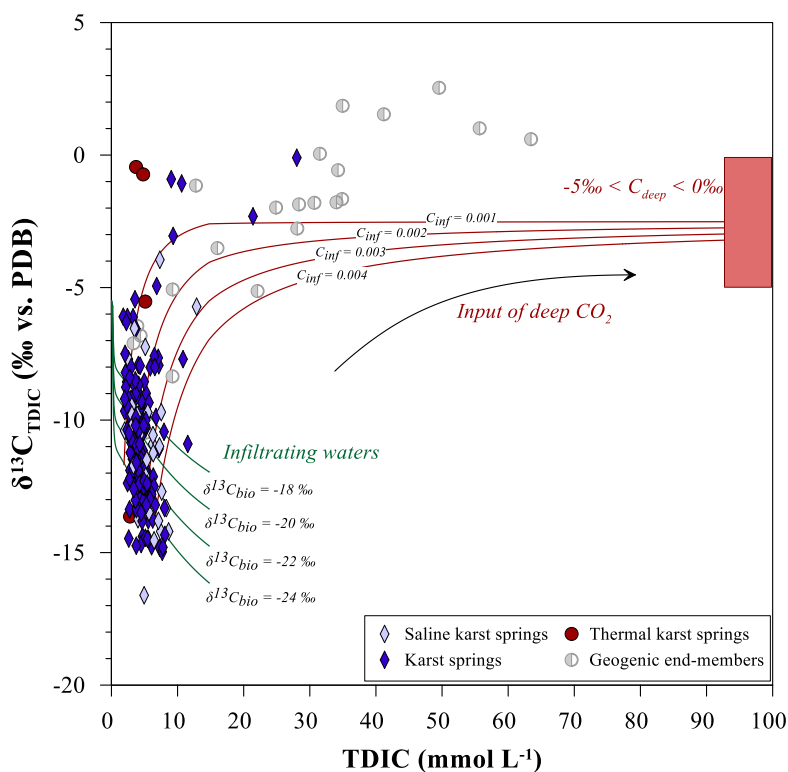


Fig.6.6. Binary diagram of TDIC vs. δ¹³C_{TDIC}. The theoretical curves represent the evolution of groundwater infiltrating through carbonate terrain in absence (green lines) and presence (red lines) of deep CO₂ flux (from Chiodini *et al.*, 2000).

About the 20% of the collected springs are located in coastal areas, where the aquifers are affected by strong mixing with the seawater. Hence, a contribution of dissolved carbon from seawater is also present in these aquifers. On the other hand, the marine carbon source is not considered in the external dissolved carbon computation developed by Chiodini *et al.* (2000). Therefore, to estimate the contribution of the marine source to the saline karst springs, the non-sea-salt fractions of the major ionic species, [X]_{nss}, were calculated using the following equation (Loye-Pilot & Martin, 1996)

$$[X]_{nss} = [X]_{spring} - ([Cl^-]_{spring} \times [X/Cl^-]_{seawater}) \quad (6.6)$$

where the [X]_{spring} and [Cl⁻]_{spring} are, respectively, the concentration of species X and of Cl⁻ in the spring, expressed in mmol L⁻¹, whereas the [X/Cl⁻]_{seawater} is the seawater molar ratio. The so-calculated non-sea-salt major ions are used in the computation of the carbon mass balance (Chiodini *et al.*, 2000). If the no-sea-salt fractions result in negative values, it is assumed that these species are

entirely derived from the marine source and considered as zero in the calculation.

The processes identified in the *Figure 6.6* are better highlighted considering the calculated C_{ext} (*equation 6.4*) and its carbon isotope composition ($\delta^{13}C_{ext}$ (*equation 6.3*) – *Fig.6.7*), where the dissolved carbon contribution does not come from the carbonate dissolution, and also from marine dissolved carbon in saline karst springs, with the advantage of accurately distinguishing between the biological and the endogenous sources (*Chiodini et al., 2000*). Most of the karst samples are characterised by light C_{ext} isotope composition, from -33 ‰ to -10 ‰, and fall along the trends ascribable to the addition of biogenic carbon to infiltrating waters in equilibrium with the atmospheric CO₂. For these springs, the C_{deep} can be considered absent or negligible, thus their computed external dissolved carbon coincides with the dissolved carbon of infiltrating waters, C_{inf} . Conversely, a small group shows a heavier $\delta^{13}C_{ext}$, ranging between -7 ‰ and 0 ‰, indicative of addition of variable amounts of geogenic carbon to the infiltrating waters.

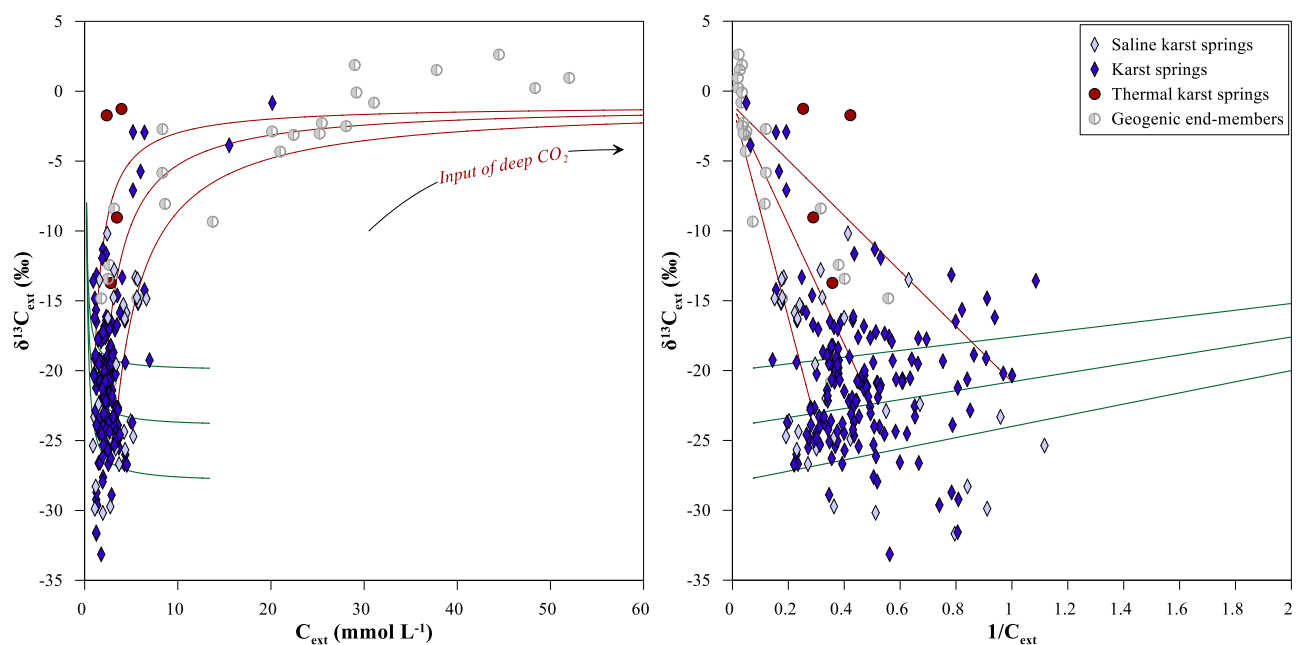


Fig.6.7. (a) Binary diagram of C_{ext} vs. $\delta^{13}C_{ext}$ and (b) binary diagram of $1/C_{ext}$ vs. $\delta^{13}C_{ext}$. The theoretical curves have been computed considering carbon isotopic composition for organic end-member (green lines) of -20 ‰, -24 ‰ and -28 ‰, and carbon isotopic composition for deep end-member of -1 ‰ (red lines).

The obtained C_{inf} values, as suggested by *figure 6.7*, for the former group show an average value of 2.53 ± 0.98 mmol L⁻¹ and a mean $\delta^{13}C_{inf}$ value of -21.1 ± 4.4 ‰, which are assumed as

representative of infiltrating waters. This average C_{inf} value is used to the computation of C_{deep} for each karst springs (*equation 6.4*). In the case samples have C_{ext} less than C_{inf} , the C_{deep} is assumed to be zero. It is noteworthy that karst springs with a $C_{\text{deep}} > 3 \text{ mmol L}^{-1}$ are located close to the Quaternary magmatism areas (*Fig.6.8*). The geogenic carbon may be derived from the thermo-metamorphism of buried carbonates, associated to the heat released by Quaternary volcanic bodies. Important contributions may derived also from regional tectonic structures (*Daskalopoulou et al., 2019*). The different carbon contributions for each collected spring are obtained multiplying their flow rate by each computed carbon source (*equation 6.5*). An estimation of the total amount for each carbon source, transported by Hellenic karst groundwater toward the surface, is calculated by summing the different carbon contributions of each collected spring, as follow: $Q_{\text{CO}_2,\text{TDIC}} 1.75 \times 10^{10} \text{ mol a}^{-1}$, $Q_{\text{CO}_2,\text{carb}} 7.82 \times 10^9 \text{ mol a}^{-1}$, $Q_{\text{CO}_2,\text{inf}} 8.23 \times 10^9 \text{ mol a}^{-1}$, $Q_{\text{CO}_2,\text{deep}} 1.43 \times 10^9 \text{ mol a}^{-1}$. Due to the similar geotectonic setting, the obtained deeply-derived carbon release from the collected karst spring has been compared with the values estimated from Italian karst hydro-systems. The estimate of the deep CO_2 flux obtained in this work is one order of magnitude higher than that obtained for Calabria ($6.1 \times 10^8 \text{ mol a}^{-1}$, *Randazzo et al., 2022*) and one order of magnitude lower than that obtained in Central Apennine ($2.9 \times 10^{10} \text{ mol a}^{-1}$, *Frondini et al., 2019*). Considering the geogenic carbon output from the main thermal and cold gas manifestation of Greece, the estimated deep carbon from karst hydro-systems is the same order of magnitude. Indeed, *Daskalopoulou et al. (2019a)* estimates a geogenic carbon release for SAAVA (South Active Aegean Volcanic Arc) about $3 \times 10^9 \text{ mol a}^{-1}$ and a same order of magnitude for eastern-central and northern part of continental Greece, whilst *D'Alessandro et al. (2020)* estimates for Sperchios Basin, Central Greece, a CO_2 flux of $2.2 \times 10^8 \text{ mol a}^{-1}$.

Although the springs under investigation are widespread across the whole Hellenic territory, the deeply-derived carbon estimation from karst hydrosystems is not representative of the flux from the

entire region and represents a minimum value. On the other hand, this obtained carbon estimation confirms the importance of endogenous carbon release from non-volcanic degassing structures on the global carbon cycle.

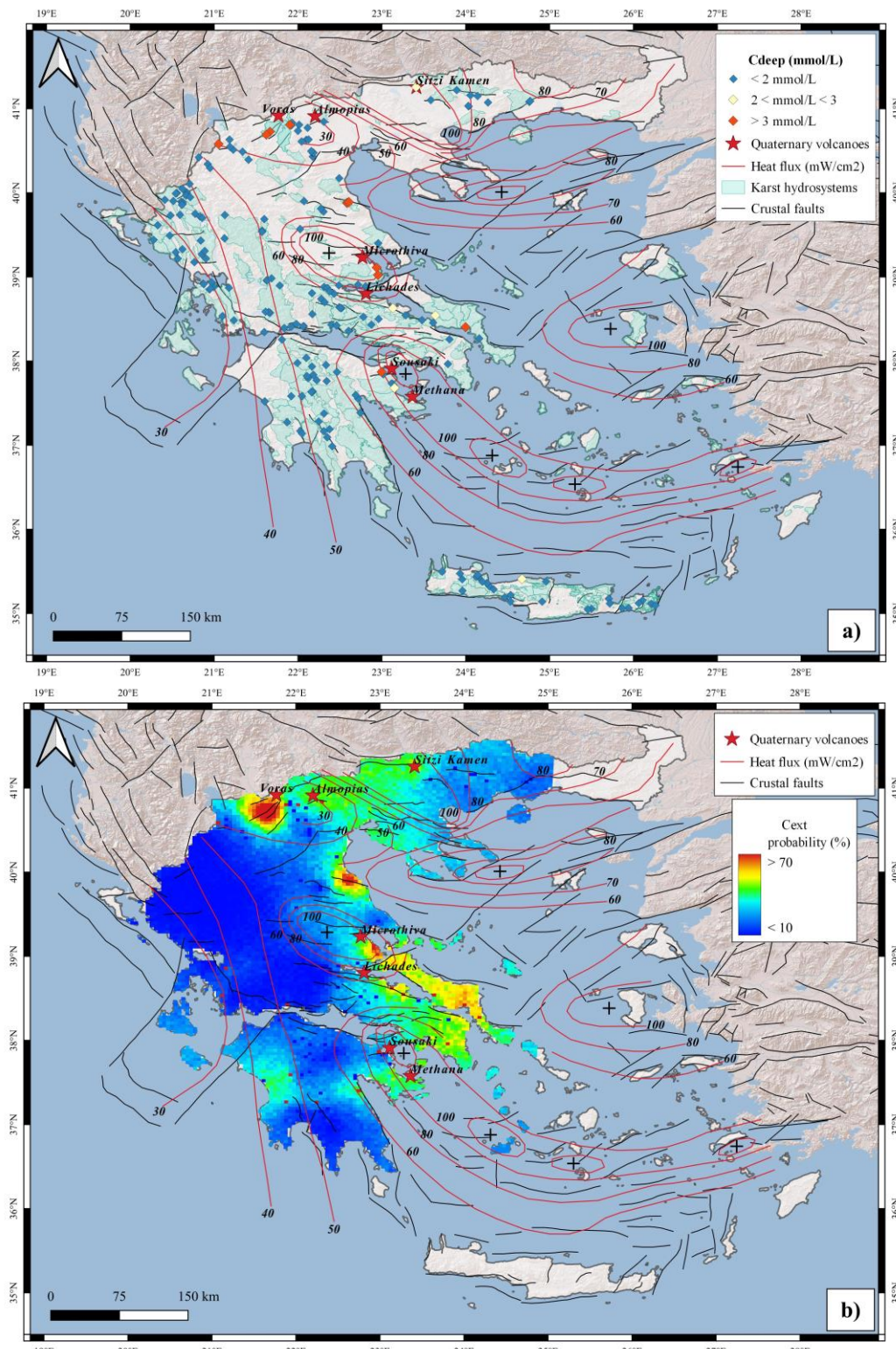


Fig.6.8. (a) Geographic distributions of C_{deep} in the collected karst springs. Heat flux (red lines) from Fytikas & Kolios (1979); karst hydroystems (green areas) from Voudouris (2019). Tectonic structures from DISS Working Group (2021). (b) Probability map of the spatial distribution of C_{ext} concentrations. Base map by ESRI maps.

6.4 Conclusions

In this work, a carbon isotope-mass balance was applied to the main karst hydro-systems of Greece in order to estimate the total amount of gas dissolved and released by these aquifers. The chemical composition of collected karst springs was dominated by nitrogen, indicating a significant contribution of atmospheric air deriving from the meteoric recharge. Only in few samples, the isotope signature of carbon and helium indicated a crustal and/or magmatic gas input.

About of 20% of sampled springs were located in coastal areas, where the aquifers were affected by significant marine intrusion. For these springs, the marine contribution to the carbon mass balance was estimated from the chemical compositions of the water.

The external carbon derived mostly from infiltrating processes, whilst the endogenous carbon release was estimated in about 1.43×10^9 mol a⁻¹. The geogenic source of carbon may be derived from multiple sources, such as thermo-metamorphism of buried carbonates associated to the intrusions of Quaternary magmatic bodies and/or regional tectonic structures. The estimated deep carbon output is comparable with other active tectonic areas, confirming the importance of CO₂ release from regional diffuse degassing within the computation of the global carbon cycle.

Part III

Chapter 7 - Geochemistry of gas manifestations of North Macedonia

In August 2019, March 2020 and October 2022, three sampling campaign were carried out in North Macedonia (MK). Sixty-eight samples of free and dissolved gases were collected from cold ($T < 28^{\circ}\text{C}$) and thermal manifestations (up to 74°C) of the country (Fig. 7.1). The chemical composition (CO_2 , H_2S , CH_4 , N_2 , O_2 , Ar , He and H_2) of the sampled gases analyzed in the present study, together with the isotopic composition of CO_2 , CH_4 , He and Ar , are reported in Table A8 and A9, and can be found in the Appendix.

The dataset was compared with data from the neighbor countries of Greece (*Daskalopoulou et al., 2019a*) and Serbia (*Randazzo et al., 2021*).

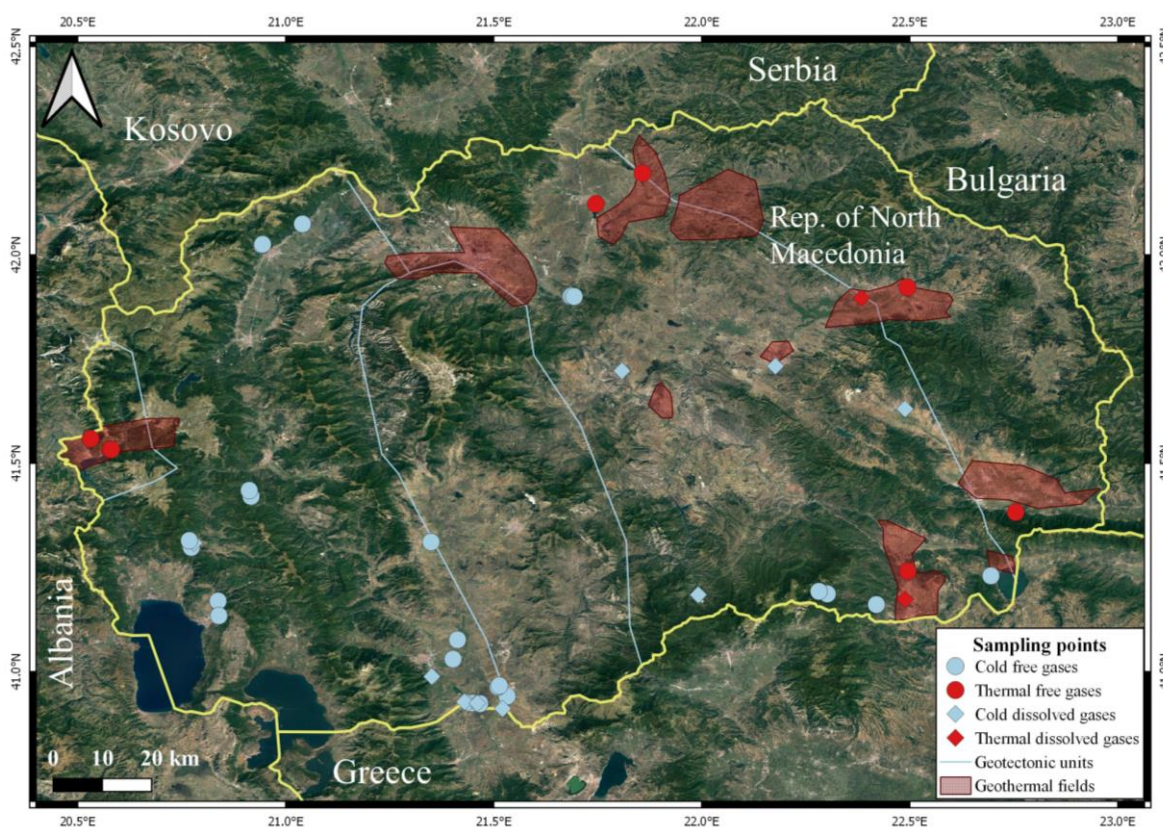


Fig. 7.1. Geographical distribution of sampled sites. Base map from Google.

7.1 Results

7.1.1 Chemical composition of the gases

The main gas components were discriminated with the use of CO₂-CH₄-N₂ ternary diagram (*Fig. 7.2a*), showing that CO₂ and N₂ were the most abundant components. On the basis of their chemical composition (*Fig. 7.2b*), the dataset was subdivided into three categories: (i) N₂-dominated (N₂ concentrations from 822,800 μmol mol⁻¹ to 989,200 μmol mol⁻¹), (ii) CO₂-dominated (CO₂ concentrations from 474,200 μmol mol⁻¹ to 999,000 μmol mol⁻¹), and (iii) H₂S-rich (H₂S concentrations from 11 μmol mol⁻¹ to 12,800 μmol mol⁻¹). The latter consisted of N₂- or CO₂-dominated samples whose chemical composition comprised H₂S (*Fig. 7.2b*). It is noteworthy that the N₂-dominated gases of this group correspond to dissolved samples, whilst the CO₂-dominated gases correspond to free samples. Although H₂S was not present in their gas composition, the dissolved gas samples of Botun 1 and Kiselo Klajnche were included in this group, because they were collected very close to H₂S-rich free gas samples collected in the same areas.

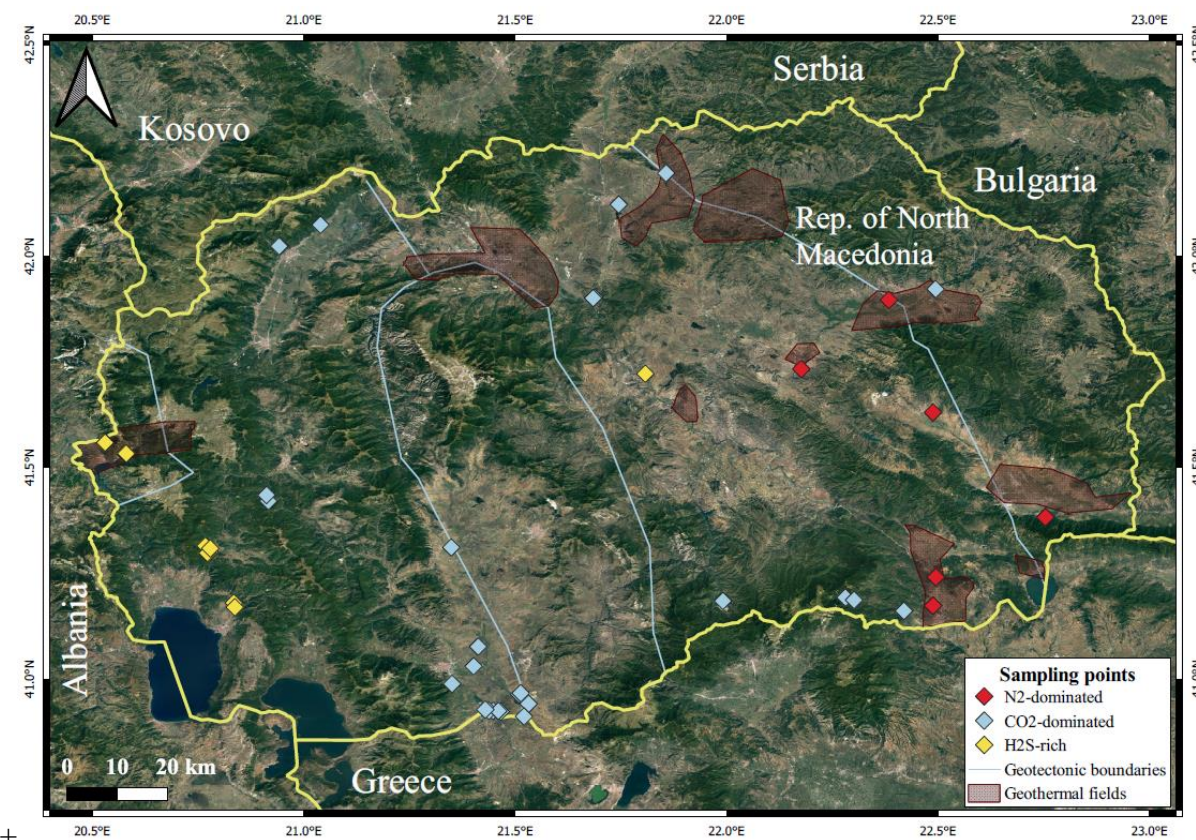


Fig. 7.3. Geographical distribution of three groups. Base map from *Google*.

The gas samples of the H₂S-rich group come all from a narrow area (Debar geothermal field, Botun and Kosel) in the westernmost part of the country with the only exception being the gas sample of Sabotna Voda, close to Veles town (*Fig.7.3*). The N₂-dominated group included the gas samples from sites in Kezhovica, Gevgelija and Strumica geothermal fields, as well as Dobra borehole in Kochani geothermal field, and the cold gas manifestation of Raklisch, in the eastern part of the country (*Fig.7.3*). The CO₂-dominated group consisted of the gas samples taken from the thermal springs of Kumanovo and Katlanovo, in Kumanovo and Skopje geothermal fields, of Istibanja spring in Kochani geothermal field, and the cold gas manifestations: (*i*) Smrdliva Voda, Gornichet, Makedonka Cheshma, and Topli Dol in the mountainous border of Kožuf Mts, west of the Gevgelija basin; (*ii*) Leshok and Banjiche, close to Tetovo town; (*iii*) Bitola basin, in south-east of the country.

Samples	Date	C₂H₆	C₃H₈	C₃H₆	<i>i</i> - C ₄ H ₁₀	<i>n</i> - C ₄ H ₁₀	<i>i</i> - C ₄ H ₈	<i>i</i> - C ₅ H ₁₂	<i>n</i> - C ₅ H ₁₂	C₆H₆
		μmol mol ⁻¹	μmol mol ⁻¹	μmol mol ⁻¹	μmol mol ⁻¹	μmol mol ⁻¹	μmol mol ⁻¹	μmol mol ⁻¹	μmol mol ⁻¹	μmol mol ⁻¹
Smirdliva Voda	02.10.2022	6.1	1.3	0.005	0.6	0.7	0.9	0.2	0.3	0.5
Smokvica	02.10.2022	25.3	5.8	0.02	2.1	1.9	3.2	0.8	1.1	2.3
Bansko	03.10.2022	7.2	1.9	0.008	0.7	0.5	1.5	0.3	0.3	0.9
Krusheani	04.10.2022	0.06	0.02	<i>b.d.l.</i>	<i>b.d.l.</i>	<i>b.d.l.</i>	<i>b.d.l.</i>	<i>b.d.l.</i>	<i>b.d.l.</i>	0.01
Gneotino 1	04.10.2022	0.04	0.01	<i>b.d.l.</i>	<i>b.d.l.</i>	<i>b.d.l.</i>	<i>b.d.l.</i>	<i>b.d.l.</i>	<i>b.d.l.</i>	0.01
Gneotino 2	04.10.2022	3.6	1.2	0.004	0.6	0.9	1.1	0.2	0.3	0.5
Logovardi	04.10.2022	0.08	0.02	<i>b.d.l.</i>	0.01	<i>b.d.l.</i>	<i>b.d.l.</i>	<i>b.d.l.</i>	<i>b.d.l.</i>	0.01
Kozica 1	05.10.2022	0.09	0.04	<i>b.d.l.</i>	0.02	0.02	0.03	<i>b.d.l.</i>	<i>b.d.l.</i>	0.02
Petkoniva	05.10.2022	6.5	1.9	0.008	1.1	1.1	1.4	0.4	0.6	0.8
Botun	06.10.2022	11	3.1	0.011	1.6	1.3	1.6	0.4	0.9	1.9
Kosovrasti	07.10.2022	4.1	0.9	0.003	0.4	0.3	0.5	0.1	0.2	0.7
Banjiche	08.10.2022	1.8	0.6	<i>b.d.l.</i>	0.2	0.2	0.5	0.1	0.1	0.4
Banjiche fountain	08.10.2022	1.4	0.4	<i>b.d.l.</i>	0.1	0.2	0.2	<i>b.d.l.</i>	<i>b.d.l.</i>	0.2

Table 7.1. Concentration of light hydrocarbons. *b.d.l.* = below detection limit.

Methane concentration varied from 2 μmol mol⁻¹ to 7100 μmol mol⁻¹. Only the samples collected at Smokvica presented a slight enrichment in CH₄, with values up to 22,500 μmol mol⁻¹ (*Fig.7.2a*). Ethane was always below the detection limit (< 10 μmol mol⁻¹), with the exception of Smokvica that showed values up to 44 μmol mol⁻¹. The concentration of ethane in the samples of Banjishte, Kosovrasti, both belonged to the Debar geothermal field, Botun and Kosel was obtained analysing

the enriched gas phase in Giggenbach bottles. Samples collected in October 2022 were analysed for C₂-C₅ alkanes and for propene, butene and benzene at the University of Florence; results are reported in *Table 7.1*. The concentration of ΣC₂-C₅ alkanes range from 0.12 μmol mol⁻¹ to 42.5 μmol mol⁻¹, where the ethane is the most abundant species.

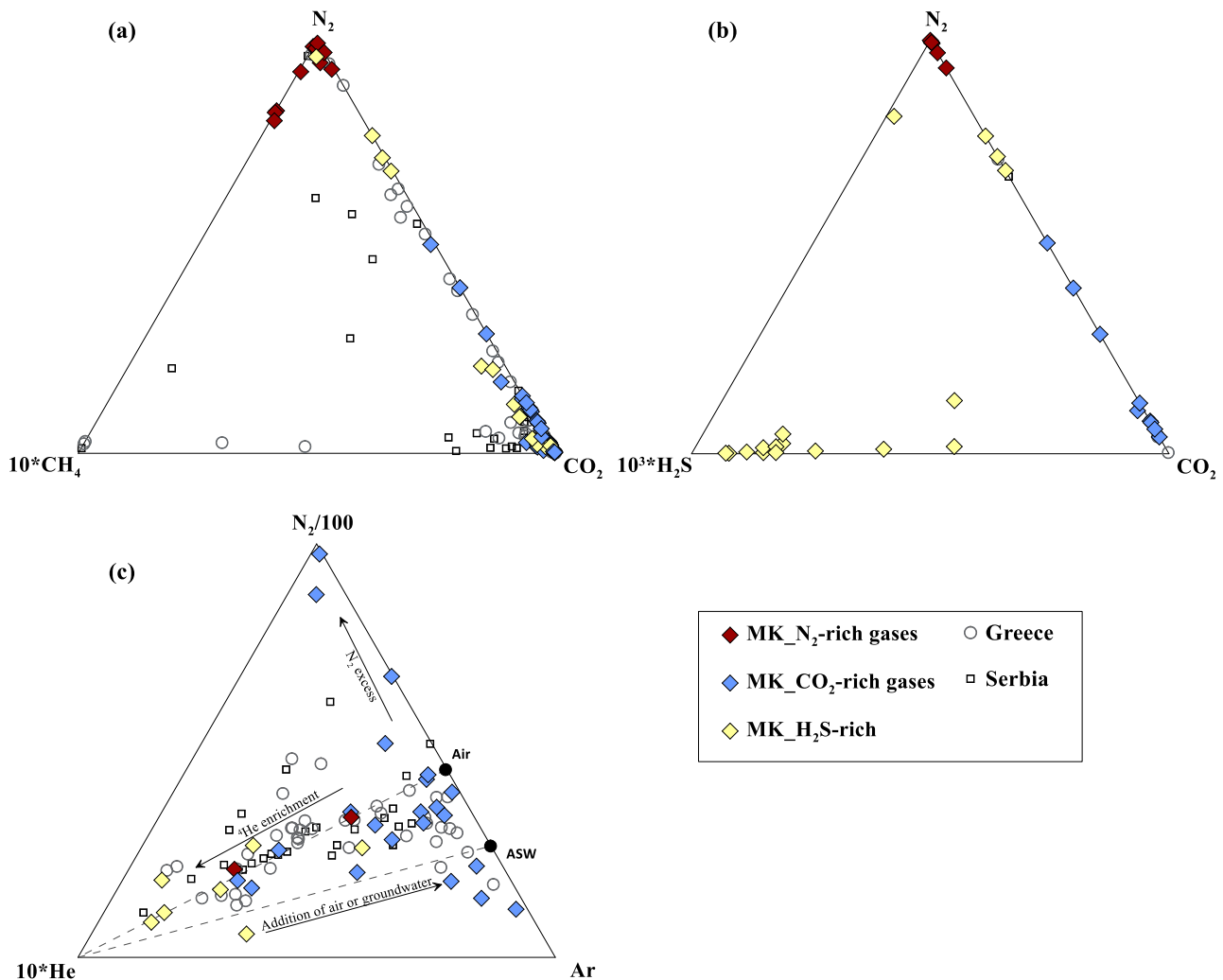


Fig.7.2. Chemical composition of the sampled gases. (a) CO₂-CH₄-N₂, (b) H₂S-CO₂-N₂ and (c) He-Ar-N₂ ternary diagram. The atmospheric air (N₂/Ar = 83) and air saturated water (ASW; N₂/Ar = 38) compositions are also plotted (Giggenbach *et al.*, 1983).

Argon and O₂ showed concentration up to 11,100 μmol mol⁻¹ and 205,700 μmol mol⁻¹, respectively. Helium values were up to 3,552 μmol mol⁻¹. The He-Ar-N₂ ternary diagram (*Fig.7.2b*) describes some mixing processes between crustal, mantle and atmospheric components (Giggenbach *et al.*, 1983). Most of CO₂-dominated samples showed N₂/Ar ratio values between those of air and ASW points (N₂/Ar = 83.6 and 36.9, respectively, at 20°C, Kipfer *et al.*, 2002), suggesting a prevailing

atmospheric origin of these gases, and mixed to the uprising gases by meteoric recharge. For soil gases the atmospheric component derives from diffusion into the soil. Four CO₂-dominated samples (Busemak, Geogas, Pela Rosa and Kozica 1, in Bitola basin) showing a high N₂/Ar ratio (from 134 to 5383), indicate a possible addition of non-atmospheric nitrogen. H₂S-rich samples fall on the theoretical mixing line between Air and deep He-sources and are generally the most enriched in He.

7.1.2 Isotopic composition of the gases

The $\delta^{13}\text{C}_{\text{CO}_2}$ values ranged between -15.7 ‰ and +1.0 ‰. The N₂-dominated gases showed the more negative values (from -15.7 ‰ to -3.2 ‰); the CO₂-dominated and H₂S-rich groups showed similar $\delta^{13}\text{C}_{\text{CO}_2}$ ranges, from -7.7 ‰ to +1.0 ‰ and between -1.7 ‰ and +0.70 ‰, respectively, falling in the magmatic-marine limestone fields (*Fig.7.4*).

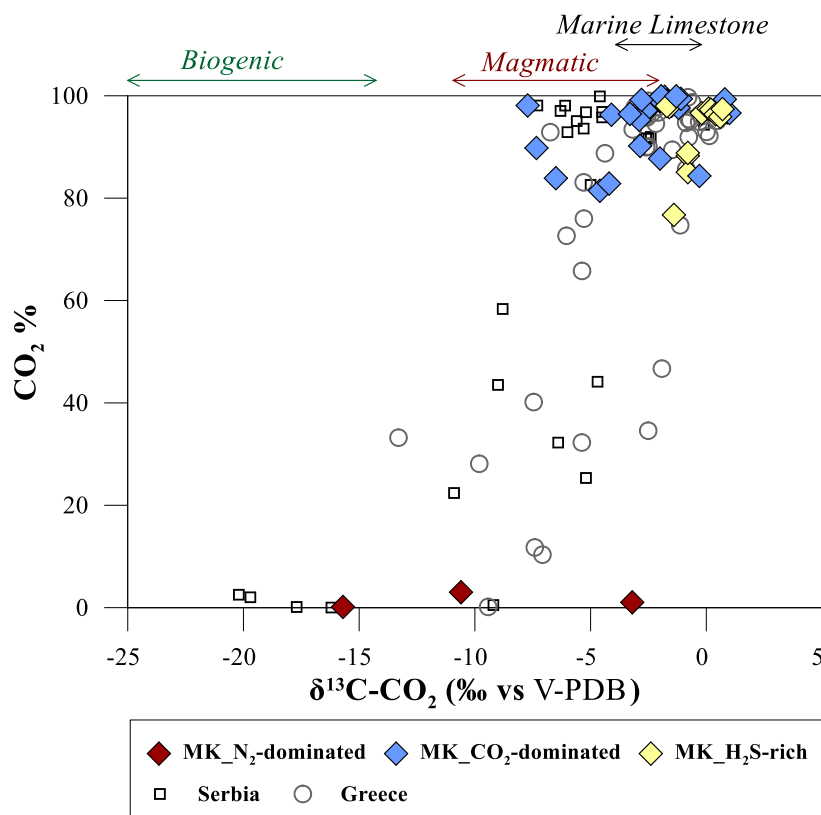


Fig.7.4. Binary plot of CO₂ concentrations vs. $\delta^{13}\text{C}_{\text{CO}_2}$. The three colored arrows represent the $\delta^{13}\text{C}_{\text{CO}_2}$ ranges of the three different sources: biogenic (green), magmatic (red), marine limestone (black).

The isotopic composition of helium, expressed as R/R_A ratio, varied from 0.1 to 1.8, whilst ⁴He/²⁰Ne ranged between 0.5 and 2066, showing higher values than those of atmosphere (0.318,

Sano *et al.*, 1985). Samples of N₂-dominated group had R/R_A and ⁴He/²⁰Ne ranging from 0.15 to 1.09 and from 1.25 to 203, respectively. The gases of CO₂-dominated group showed R/R_A values varying from 0.1 to 1.8 and ⁴He/²⁰Ne values between 0.5 and 473. In the H₂S-rich group, the values of R/R_A varied between 0.08 and 0.36, whereas ⁴He/²⁰Ne values ranged between 11.2 and 2066. The isotope composition of methane showed δ¹³C_{CH4} values ranging between -57.8 ‰ and -7.2 ‰ and δ²H_{CH4} varying from -303 ‰ to -80 ‰. In the N₂-dominated group, δ¹³C_{CH4} values ranged between -8.3 ‰ and -7.2 ‰, whereas δ²H_{CH4} ranged from -116 ‰ to -80 ‰. The samples of CO₂-dominated group had δ¹³C_{CH4} and δ²H_{CH4} values varying from -57.8 ‰ to -19.7 ‰ and from -146 ‰ to -84 ‰, respectively. The gases of H₂S-rich group showed δ¹³C_{CH4} values ranging from -52.8 ‰ to -30.2 ‰ and δ²H_{CH4} values varying between -303 ‰ and -163 ‰.

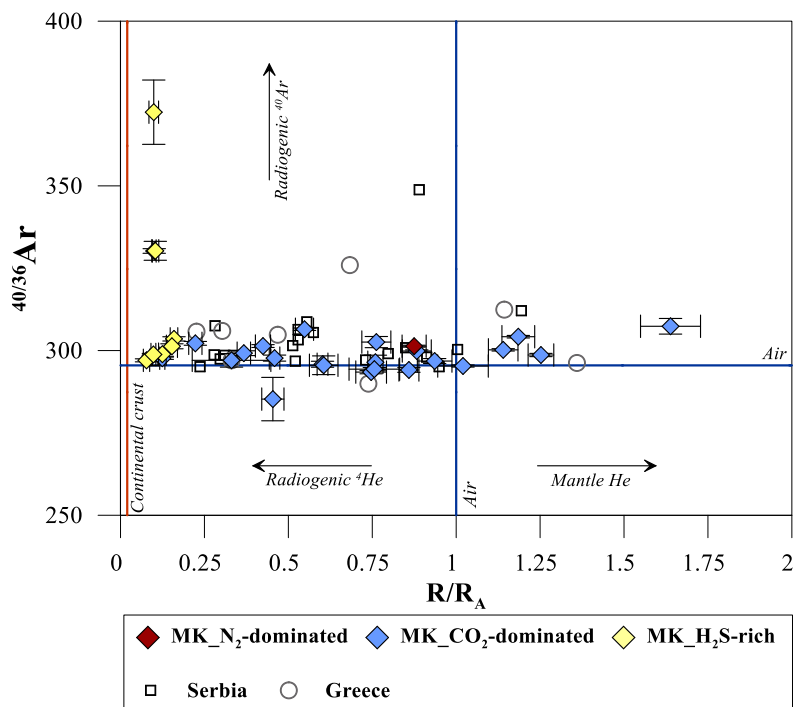


Fig.7.5. Binary plot ^{40/36}Ar versus R/R_A. Isotopic values of helium (R/R_A = 1; Ozima & Podosek, 2002) and argon (^{40/36}Ar = 295.5; Steiger & Jäger, 1977) in air and isotopic value of helium in continental crust (R/R_A = 0.02; Ballentine & Burnard, 2002) was plotted.

Lastly, the isotopic compositions of argon, ^{40/36}Ar and ^{38/36}Ar, were also measured and compared with atmospheric values (^{40/36}Ar = 295.5 and ^{38/36}Ar = 0.188; Steiger & Jäger, 1977; Ozima & Podosek, 2002). Despite the atmospheric mixture is composed mainly of ⁴⁰Ar, the ³⁶Ar is

considered exclusively of atmospheric origin, whilst the ^{40}Ar is the results of radiogenic decay of ^{40}K (*Holland & Gilfillan, 2013*).

In the N_2 -dominated group, the isotopic compositions of argon were measured only in Smokvica sample, which $^{40/36}\text{Ar}$ was 301, whereas $^{38/36}\text{Ar}$ was 0.189. The $^{40/36}\text{Ar}$ of CO_2 -dominated samples ranged between 285 and 307; whilst the $^{38/36}\text{Ar}$ varied from 0.186 to 0.198; lastly, the gases of H_2S -rich group showed a wide range of $^{40/36}\text{Ar}$ values, that varying from 297 to 372, whereas the $^{38/36}\text{Ar}$ ranged between 0.186 and 0.190. Generally, the isotopic compositions of argon in Macedonian gases showed values close to the typical atmospheric signature, with the exception being the samples of Botun and Kose, that show higher $^{40/36}\text{Ar}$ (330 and 372, respectively) than those of air. This slight enrichment in ^{40}Ar , together with high ^4He contents, suggests a mainly crustal source of these gases (*Fig.7.5*).

7.2. Discussion

7.2.1 Origin of CO_2 and He

Carbon dioxide is the carrier phase for mantle-derived fluids. Because of its multiple sources, such as hydrocarbon oxidation, organic matter decay, respiration, decarbonation of marine carbonates and degassing of magmatic bodies (*Jenden et al. 1993; Wycheley et al. 1999*), the interpretation of $\delta^{13}\text{C}_{\text{CO}_2}$ values alone does not provide a clear discrimination of the origin of the fluids. The comparison of the carbon isotope composition with the isotope ratio of noble gases (He, Ne and Ar) is a useful tool to distinguish the origin of the fluids, because of their isotopic signature is well distinct in three main reservoirs (atmosphere, mantle and crust - *Holland & Gilfillan, 2013*).

The coupled R/R_A and $^4\text{He}/^{20}\text{Ne}$ ratios (*Fig.7.6a*) can be used to distinguish the possible source of helium (i.e., MORB ($8 \pm 1 \text{ R}_A$, *Ozima & Podosek, 2002*; $^4\text{He}/^{20}\text{Ne} > 1000$, *Sano & Wakita, 1985*), crustal fluids (0.01-0.02 R_A , *Ballentine & Burnard, 2002*; $^4\text{He}/^{20}\text{Ne} > 1000$, *Sano et al., 1985*), and atmosphere (1R_A , *Ozima & Podosek, 2002*; $^4\text{He}/^{20}\text{Ne} = 0.318$, *Sano et al., 1985*)). The majority of the collected gas samples (CO_2 - and N_2 -dominated) show a mixed crustal-mantle contribution of

helium, with a mantle component between 1 % and 20 %. Some samples fall, mostly among the CO₂-dominated, close to the mixing line with the atmospheric end-member, indicating a possible atmospheric contamination due to the dissolved component in waters in which they bubble or to a mixing between the deep-circulating fluids and shallower air-saturated waters. The gas samples of the H₂S-rich group have R/R_A values (0.08 - 0.36) indicating a main crustal origin of the helium, although sometimes a mantle contribution of up to 5% is also present.

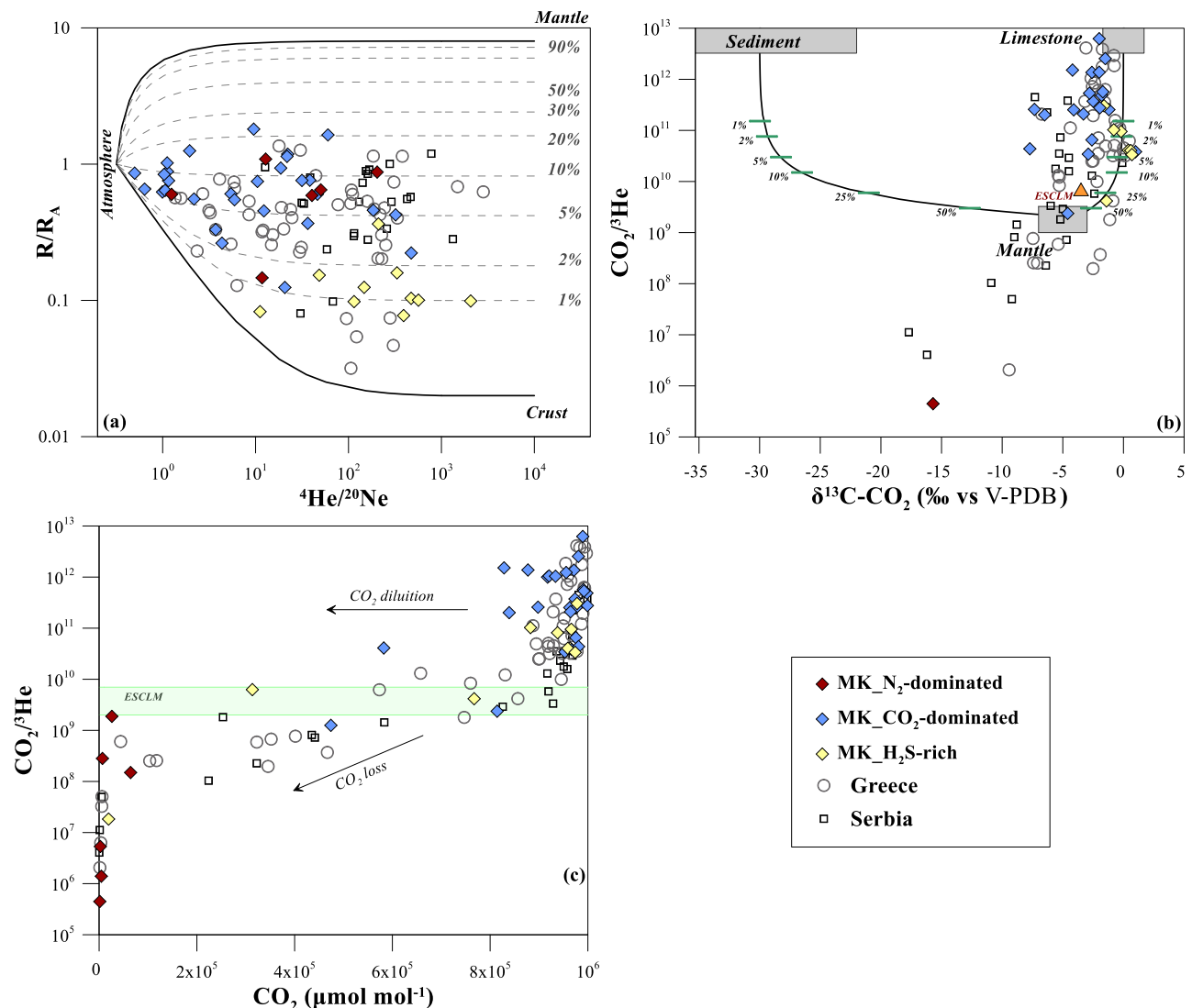


Fig.7.6. (a) Binary plot of R/R_A ratio vs. ⁴He/²⁰Ne ratio. The dashed lines represent the mixing between atmosphere, crust and mantle at different percentages (Sano & Wakita, 1985). (b) Binary plot of CO₂/³He vs. δ¹³C_{CO₂}. The composition for Sediments, MORB and Limestones end-members are: δ¹³C_{CO₂} = -30 ‰, -5 ‰ and 0 ‰ and CO₂/³He = 1 × 10¹³, 2 × 10⁹ and 1 × 10¹³, respectively (Sano and Marty, 1995). Percent of mantle contribution is shown along the mixing line between mantle and, respectively, limestone and sediments. ESCL mantle end-member (orange triangle) is also reported (Bräuer et al., 2016). (c) Binary plot of CO₂ concentration (μmol mol⁻¹) vs. CO₂/³He ratio. The shaded region highlighted the CO₂/³He values of ESCLM (CO₂/³He from 2 to 7 × 10⁹; Bräuer et al., 2016; Marty et al., 2020).

The combination of CO₂ and ³He, expressed as CO₂/³He ratio, is used to evaluate any depletion or enrichment relative to a mantle signature of the fluids (*Fig. 7.6b,c*). As North Macedonia is located in a continental environment, subjected to an extensive tectonic regime, the European Subcontinental Lithospheric Mantle (ESCLM - CO₂/³He from 2 to 7×10^9 ; *Bräuer et al., 2016; Marty et al., 2020*) could be considered as mantle end-member instead of MORB and its composition has been added to *Fig. 7.6b*.

The $\delta^{13}\text{C}_{\text{CO}_2}$ values of collected gases is compared with their CO₂/³He ratios in *Figure 7.6b* (*Ballentine et al. 2001, 2002; Sano & Marty, 1995; Sherwood Lollar et al. 1999*). The gas samples of CO₂-dominated and H₂S-rich groups plot close to the mixing line between mantle and marine limestone end-members, indicating that contributions from organic sediments to fluids deriving from a descending slab are limited. Only the Smokvica sample falls far below the mantle field, indicating a strong CO₂ loss. *Figure 7.6c* compares, instead, the CO₂/³He ratio with the CO₂ concentration of the collected gases. Any samples plotting above the ESCLM range, independently from their CO₂ concentration, contained very low ³He concentrations, indicating a prevailing crustal source of CO₂. The collected gas samples of the CO₂-dominated and H₂S-rich groups mostly fall in this part of the plot. The samples plotting within or below ESCLM range, contain a significant amount of ³He, suggesting either a higher mantle contribution or loss of CO₂ during gas-water-rock interactions. The gases of the N₂-dominated group and Sabotna Voda (H₂S-rich group) belonged to this low CO₂/³He group. One of the processes that account for preferential CO₂ loss is calcite deposition within the hydrothermal circuit (*Stefánsson et al., 2017*), a widespread phenomenon in geothermal aquifers. Indeed, the gases of N₂-dominated group are located in geothermal systems and are characterized by travertine deposition. This process involves deprotonation of CO₂ (aq) to HCO₃⁻ and CO₃²⁻ and formation of calcite, resulting in a decrease of the $\delta^{13}\text{C}$ values of the residual CO₂. The Sabotna Voda sample shows a CO₂/³He value of 1.84×10^7 and low CO₂ concentration (19,300 μmol mol⁻¹), likely due to a CO₂ loss deriving from interaction with shallow aquifers. In this case, due to the higher solubility of CO₂ with respect to helium in aquatic systems, the latter gas

species becomes virtually enriched. Finally, in few samples the low CO₂ contents may be justified by dilution from other gas species, like CH₄ or N₂, without a noticeable change in the CO₂/³He ratio (*Fig. 7.6c*).

7.2.2 Origin of methane and light hydrocarbons

Hydrocarbons with low molecular weight are known as light hydrocarbons (LHs), which include, among the alkanes, methane (CH₄), ethane (C₂H₆), propane (C₃H₈), butane (C₄H₁₀) and pentane (C₅H₁₂) and, among the alkenes, propene (C₂H₆) and butene (C₄H₈) and the aromatic benzene (C₆H₆).

Light hydrocarbons may derive from different sources. **Primary microbial gases** have only methane, ethane and propane (CH₄ >> C₂H₆ > C₃H₈) as hydrocarbon gases and have methane enriched in ¹²C. **Secondary microbial gases** are produced by microbes during petroleum biodegradation and dominated by methane. The microbial methane is produced at temperature up to 80°C. **Thermogenic** methane is produced at higher temperature (> 150 °C) by thermal cracking of organic matter or oil. Thermogenic gases are recognized based on the presence of all methane homologues from methane to pentanes (*Chung et al., 1988*) and are, often, mixed with microbial or/and abiotic gases. Methane is the dominant **abiotic gas** (> 50 vol%, often together with H₂) in ultramafic rocks and Precambrian crystalline shields (*Etiope and Schoell, 2014; McCollom & Seewald, 2007*), produced by Fischer-Tropsch reactions at different temperatures. Geochemical evidence for abiotic origin includes: (i) a specific combination of δ¹³C_{CH4} and δ²H_{CH4}, partially overlapping the thermogenic field (*Etiope et al. 2017*); (ii) an inverse isotopic trend of normal alkanes (δ¹³C_{CH4} > δ¹³C_{C2H6} > δ¹³C_{C3H8}; *Sherwood Lollar et al., 2008*); (iii) considerable amounts of hydrogen gas (H₂), typically produced by serpentinization of olivine-rich rocks and radiolysis (*Etiope and Sherwood Lollar, 2013*).

Bernard and Schoell diagrams (i.e., δ¹³C_{CH4} versus CH₄/(C₂H₆ + C₃H₈) plot proposed by *Bernard et al., 1977*; δ¹³C_{CH4} versus δ²H_{CH4} plot proposed by *Schoell, 1983* and *Whiticar et al., 1986*; and

$\delta^{13}\text{C}_{\text{CH}_4}$ versus $\delta^{13}\text{C}_{\text{CO}_2}$ plot proposed by Gutsalo & Plotnikov, 1981) are the commonly used plots to discriminate the genetic and secondary processes of natural gases containing methane. High $\text{CH}_4/(\text{C}_2\text{H}_6 + \text{C}_3\text{H}_8)$ ratios (> 1000) are, generally, ascribed to an exclusive “microbial” source, whereas lower values (< 100) indicates either loss of methane due to oxidation processes or the production of low-molecular-weight hydrocarbons through thermal ($T > 150$ °C) degradation of organic matter. These genetic diagrams were recently updated by Milkov & Etiope (2018), considering widespread geochemical and geological data from a variety of worldwide distributed areas.

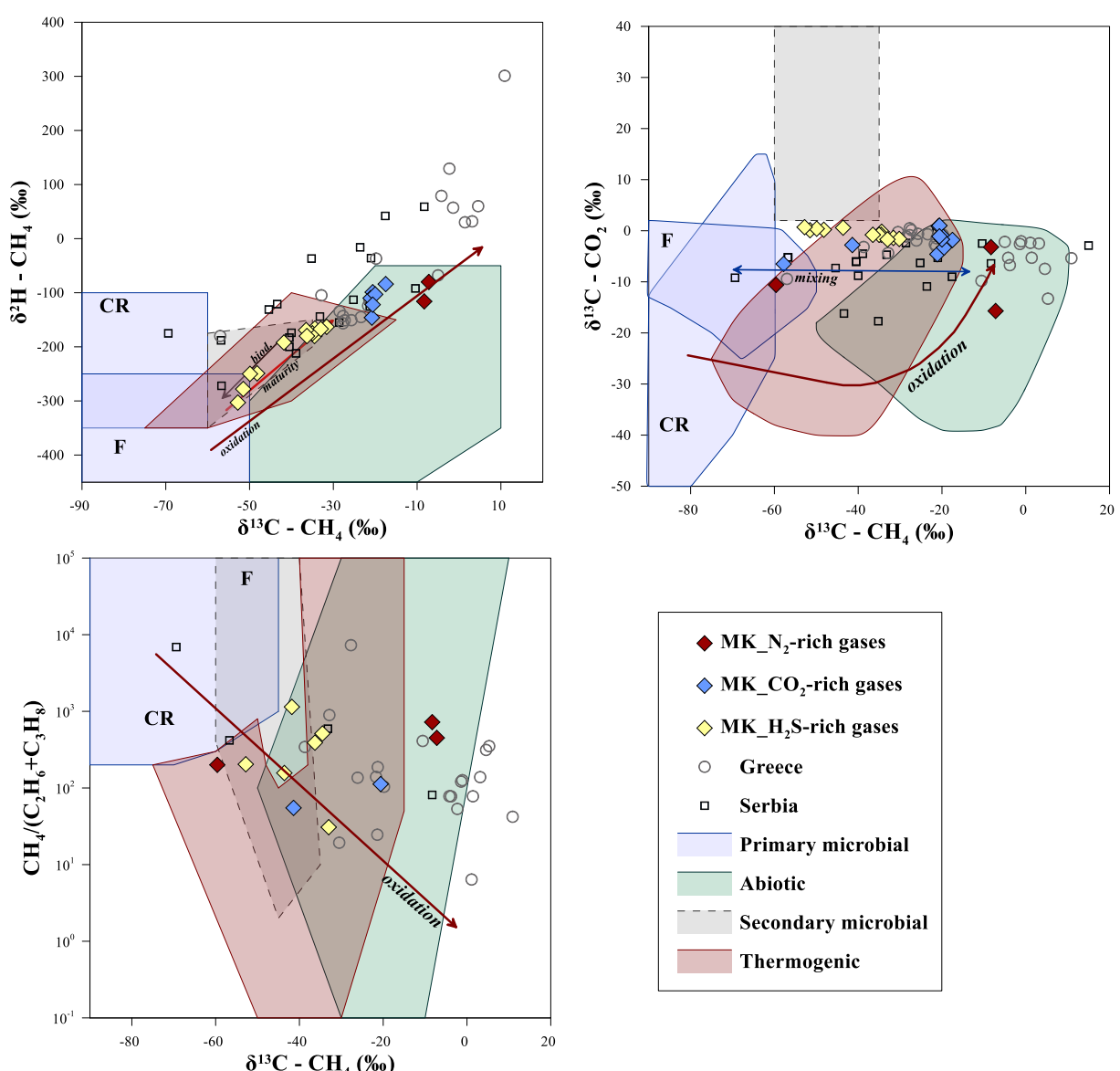


Fig.7.7. (a) Binary plot $\delta^{13}\text{C}_{\text{CH}_4}$ versus $\delta^{2}\text{H}_{\text{CH}_4}$ (Schoell, 1983; Whiticar et al., 1986); (b) binary plot $\delta^{13}\text{C}_{\text{CH}_4}$ versus $\delta^{13}\text{C}_{\text{CO}_2}$ (Gutsalo & Plotnikov, 1981); (c) binary plot $\delta^{13}\text{C}_{\text{CH}_4}$ versus $\text{CH}_4/(\text{C}_2\text{H}_6 + \text{C}_3\text{H}_8)$ (Bernard et al., 1977). Modified genetic fields of Milkov & Etiope, 2018. F – methyl-type fermentation; CR – CO₂ reduction.

Isotopic composition of carbon and hydrogen of methane were measured for the gases collected in Macedonian territory and plotted in the three above-mentioned genetic diagrams (*Fig.7.7a,b,c*). Among the N₂-dominated gases, the isotope composition of methane was measured only in the Smokvica and Bansko hydro-systems. The Smokvica samples fall in the abiotic field, an origin consistent with the hydro-geological background of the area and ascribable to the Fischer-Tropsch reactions at low temperatures. Indeed, according to *Popovska-Vasilevska & Armenski, 2016*, Smokvica geothermal field is located in the Gevgelija geothermal field, a fault zone bounded by Jurassic mafic rocks (diabase and spilites), that includes 3 exploited wells with temperatures at discharge ranging between 63.9 °C and 68.5 °C, and predicted reservoir temperatures of about 75 - 100 °C (*Gorgieva, 1999*). Methane in the Bansko sample seems to be related to a mixing process between biotic and thermogenic end-members.

Among the CO₂-rich samples, only that of Geogas (Bitola plain) plots close to the primary microbial field (*Fig.7.7a*), whilst the thermal gases of Katlanovo and Istibanja and the cold gases of Smrdliva Voda and Gornichet, show δ¹³C_{CH4} values around -20 ‰ and δ²H_{CH4} values around -150 ‰, which are considered typical of geothermal systems (*Etiope & Schoell, 2014*). The origin of methane in these gases is still debated being compatible both with thermogenic or abiotic processes (*Fig.7.7a,b*) or to a mixing of the two sources. The CH₄/(C₂H₆+C₃H₈) ratio calculated in samples of Polog basin (Banjiche) and Bitola basin (Krusheani, Gneotino 1 and 2, Logovardi, Kozica 1) ranges between 41 and 113, suggesting a mainly thermogenic origin of hydrocarbons. On the other hand, according to *Gorgieva (1989)*, the reservoirs of the Katlanovo, Istibanja and Gevgeljia (Smrdliva Voda and Gornichet) hydrothermal systems are composed of Precambrian gneiss and Paleozoic carbonated schist. Hence, a geothermal abiotic source might be ascribed to hydrocarbon production that occurs in these hydrothermal systems within the metamorphic rocks of the Precambrian shield (*McCollom & Seewald, 2007*); moreover, the presence of volcanic-geothermal systems at depth is not excluded (e.g., *Molnár et al. 2022*). These hypotheses are consistent with those suggested by *Daskalopoulou et al. (2018)*, in which the authors relate the gases of Vardar zone to abiogenic

hydrocarbons emitted from volcanic-geothermal systems and the gases of Pelagonian zone and Rhodope Massif to abiogenic hydrocarbons released from hydrothermal systems in the Precambrian shield. Furthermore, the authors do not exclude aerobic or anaerobic oxidation of methane (*Murrell & Jetten, 2009*).

Regarding the samples of the H₂S-rich group, the highest CH₄/(C₂H₆ + C₃H₈) ratio was found at the thermal spring of Banjishte (1142), a value indicative of a microbial origin of CH₄ and H₂S, which might be produced via a microbially sulfate reduction process (MSR; *Machel, 2001*), although a mixing with the thermogenic source is not excluded. On the other hand, the isotopic composition of methane and the CH₄/(C₂H₆ + C₃H₈) ratio (from 31 to 390) of Botun, Duvalo, Kosovrasti, and Petkoniva suggest a thermogenic origin. Two hypotheses can be presented. The first, according to *Li Vigni et al. (2022c)* (see Chapter 9 for further details), CH₄ and H₂S might be produced during thermochemically sulfate reduction (TSR) process (*Milkov & Etiopic, 2018*) occurring in evaporite deposits. Evaporite outcrops of supposedly Upper Cretaceous age (gypsum, anhydrides, salts, multicolored clays and breccias with interbedded dolomite and thin organic-rich shales) are present on the mountains near Debar (*Jančev et al., 1999; Dumurdjanov et al., 2020*), whilst Triassic evaporate presence at depth (Ionian unit; *Schmid et al. 2020*) is at present only hypothesized at Duvalo Kosel, Botun and Petkoniva areas. On the other hand, due to the closeness of Botun samples to the secondary microbial field in δ¹³C_{CH4} *versus* δ¹³C_{CO2} diagram (*Fig.7.7b*), and their plotting in the overlapping zones of the thermogenic, primary and secondary microbial fields in the δ¹³C_{CH4} *versus* δ²H_{CH4} (*Fig.7.7a*) and δ¹³C_{CH4} *versus* CH₄/(C₂H₆ + C₃H₈) diagrams (*Fig.7.7c*), the origin of methane in the west side of the country might be associated, instead, to the production of small quantities of oil and its subsequent biodegradation. This hypothesis can be supported by the presence of oil and gas reservoirs in the close by countries of Albania and Greece (*Bega & Soto, 2017; Zelilidis et al; 2015*). Albania is recognized as an oil and gas province, where several oil reservoirs are found and exploited, (*Nieuwland et al., 2001; Velaj, 2015*), whereas several oil seeps are found in Western Greece (*Etiopic et al., 2013; Zelilidis et al; 2015*). The Albanian hydrocarbon

fields belong to the carbonate reservoirs of the Ionian fold-and-trust belt and are related to the presence of Triassic evaporitic rocks, which provided an efficient seal for the oil and gas migration (*Bega & Soto, 2015 and references therein*). Although the evaporites at Debar are considered as Upper Cretaceous (Jančev et al., 1999), just across the border in Albania, the evaporites at Peshkopia tectonic window are identified as Triassic, part of the Ionian unit (e.g., *Bortolotti et al., 2005*). Although unproven, the evaporites at Debar may, therefore, represent the same Triassic evaporitic unit, and seal a potential oil reservoir.

7.2.3 Geological implication in a regional context

The three identified groups are, generally, geographically well separated (*Fig.7.3*); the N₂-dominated group is sited in the easternmost part of the country, the CO₂-dominated group in the central part, and the H₂S-rich group in the westernmost part. Considering the geological setting of the Macedonian country, the gas manifestations are mainly related to the extensional tectonic regime of the area and, sometimes, associated to boundaries between the major geotectonic units (*Fig.7.8*).

It is noteworthy that all geothermal fields, except Debar, are located in the easternmost part of the country and seem to be connected to the Vardar zone. This zone is characterized by a positive geothermal anomaly (*Gorgieva et al., 2000*), associated, likely, to recent volcanic activity. Indeed, in the Late Miocene – Pliocene period, volcanism occurred within the Vardar zone, developing small-volume centers along faults lines and/or boundaries of geotectonic units (*Fig.2.3 - Molnár et al., 2022*). Hence, considering the overlapping of the geographical distributions of geothermal fields and volcanic products, it can be assumed that the heat anomaly may be related to such volcanic activity. On the other hand, the Debar geothermal field is linked to the Peshkopia zone in the neighbor country of Albania (*Frashëri et al., 2004*), where several thermal springs are present (up to 45 °C) and associated to deep faults at the periphery of a Triassic gypsum diapir, which represents a high thermal conductivity body (*Kodhelaj, 2018*).

The gas manifestations that belong to the geothermal fields connected to the Vardar zone are characterized by a N₂-dominant composition and by the highest helium contents together with low CO₂/³He ratios. These features can be ascribable to the lithology of their reservoirs, which are mainly associated with granites (*Popovska-Vasilevska & Armenski, 2016*). Granites, being enriched in U and Th, produce abundant helium by radiogenic decay, increasing ⁴He in the fluids circulating within the aquifer. The same process was suggested by *Randazzo et al., 2021* for the N₂-rich gas manifestations, with low helium isotope signature, of the Vardar zone in Serbia.

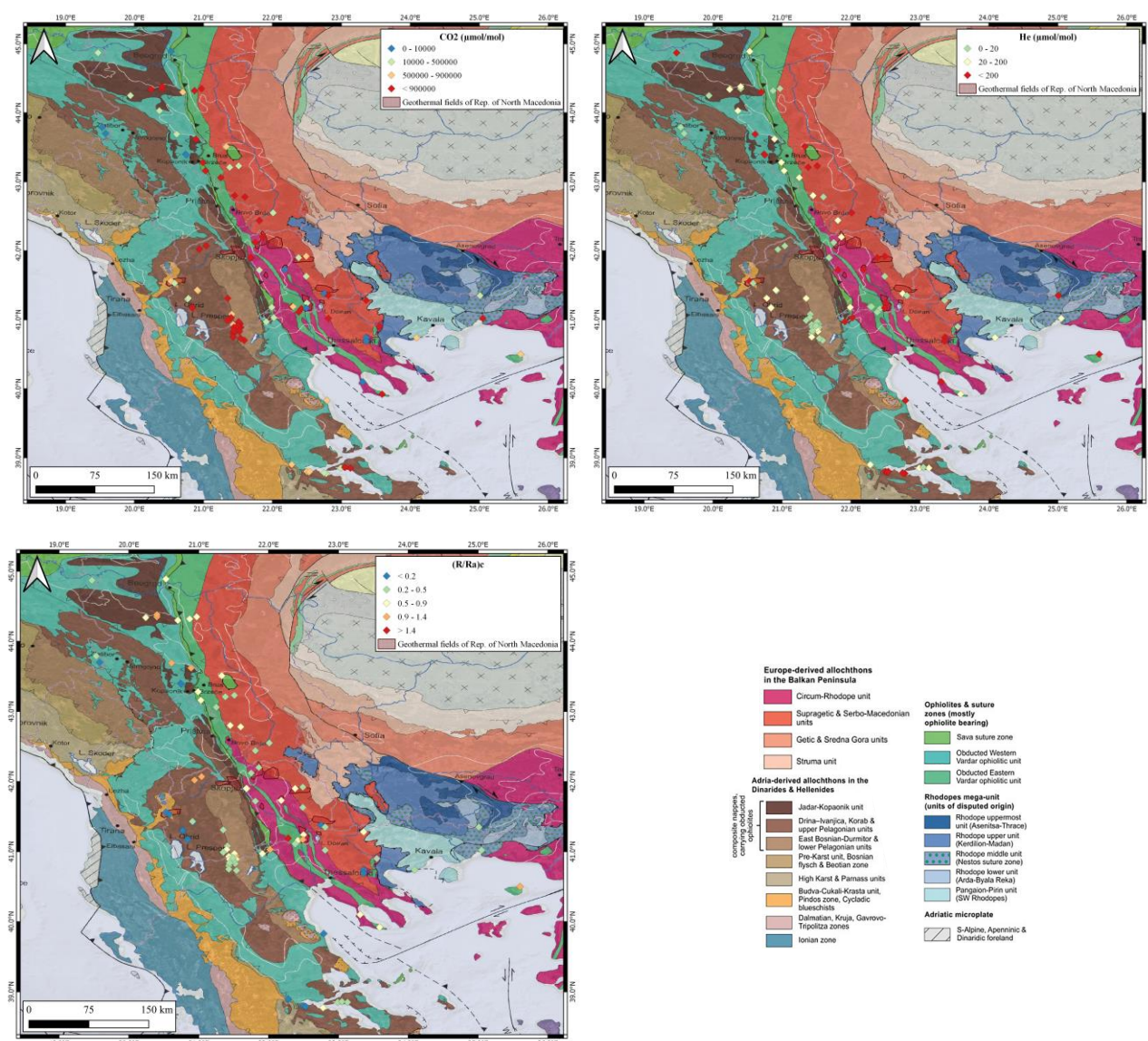


Fig.7.8. Geographical distribution of (a) CO₂ and (b) helium concentrations, (c) corrected R/R_A of the collected gas manifestations. Geological map from *Schmid et al. (2020)*

CO₂-dominated gas samples are widespread in the country (*Fig.7.8a*), comprising both thermal and cold gas manifestations, and their geographical distribution can be related to the extensional tectonic regime of the country. The isotopic composition of carbon dioxide and the high CO₂/³He ratio suggest an endogenous, marine limestone and/or mantellic, origin of the carbon (*Fig.7.4*). In the case of the thermal hydro-systems of Katlanovo and Kumanovo, the reservoirs are hosted in Paleozoic marbles (*Popovska-Vasilevska & Armenski, 2016*), where decarbonation reaction, favored by high temperatures, can occur. Relatively high CO₂ concentrations, derived mainly from a limestone carbon source, were also found in the Axios-Vardar and the Serbo-Macedonian zone of Greece (*Daskalopoulou et al., 2019a*).

The CO₂-dominated gas manifestations are characterized by R/R_A values indicating a prevailing crustal origin with a mantle contribution up to 20% (*Fig.7.5*). The highest mantle He contribution is found in two areas (*Fig.7.8c*). The first one is situated in the southern part of the country, in the Nidze-Kozuf mountains, between Mariovo and Gevgelija grabens, and may be related to the activity of the Quaternary Kozuf-Voras volcanic system (*Kolios et al., 1980; Molnár et al., 2022*). Studies about hypogene karst systems of this area indicate a circulation of the groundwater along deep fault systems and an interaction with the rocks of Kozuf-Voras volcanic system, with presence of metamorphic-derived CO₂ and up to 10% mantle helium (*Temovski et al., 2021*). The second area, instead, is located in the northern part of the country, in Polog graben, close to Tetovo town, and may be associated to the regional ENE-WSW strike-slip fault system, known as Kjustendil-Kriva Palanka-Skopje-Debar-Elbasan fault zone (*Dumurdjanov et al., 2020*), and/or to the secondary normal faults bordering the basin, which may act as preferential escape pathways for mantle fluids. Until now, the type of mantle beneath the Macedonian region has still not been defined. Due to the geodynamic history of the area, characterized by repeated subduction episodes, the presence of a MORB type mantle seems to be improbable. Although non confirmed by data from fluid inclusions hosted in mantle minerals, the presence of a subcontinental lithospheric mantle (ESCLM) type (*Gautheron & Moreira, 2002*) may be hypothesized. Recently, *Molnár et al.*

(2021) measured R/R_A values between 3.1 and 4.5 in He from fluid inclusions in the olivine phenocrystals hosted in the Late Miocene – Pleistocene (1.8 ± 0.1 Ma) lavas of Mlado Nagoričane volcanic center in North Macedonia. Such values may suggest the presence of a strongly metasomatized mantle beneath this area. If this hypothesis is confirmed for the wider area of North Macedonia, the mantle contribution to gas manifestations would be affected by an important underestimation.

Among the H₂S-rich samples, the dissolved sample of Sabotna Voda is the only one outside the western part of the country. It was collected in the central part, close to the town of Veles, in an area pertaining to the Vardar zone. Although containing some H₂S, it shows some differences with respect to the remaining H₂S-rich samples being characterized by a small but significant mantle contribution (0.36 R/R_A) and lower CO₂/³He ratio, likely due to a CO₂ loss due to dissolution within shallow aquifers. East of Sabotna Voda, close to village of Kishino, calc-alkaline basalts of the youngest volcanic site in Macedonia (1.5 Ma – Yanev *et al.* 2008; Molnár *et al.*, 2022) are present, possibly justifying the mantle He contribution (up to 5 %) in this spring. The presence of H₂S might derive from reduction processes of sulfate coming from either Triassic limestone-bound sulfate/evaporite beds or coal beds within the Veles basin. On the other hand, the carbon and helium isotopic compositions of the remaining H₂S-rich gas manifestations reveal a prevailing crustal origin of the gases with a mantle contribution always lower than 2%.

Although the mainly crustal source of the gas manifestations of the Macedonian country, it is noteworthy that while the geothermal fields in the eastern part of the country seem to have a connection with Quaternary volcanism, the gas manifestations in the western part of the country are associated, instead, with active deep fault systems. Historically, Macedonia has been affected by several moderate to strong earthquakes, sometimes with destructive character (Dumurdjaov *et al.* 2020), such as the 6.1M earthquakes in 1963 at Skopje, generated from an intra-basin WNW-oriented fault within the city (Dumurdjanov *et al.*, 2005). Seismicity, associated to the Southern Balkan Extensional Regime, is variable in its distribution within Macedonia. Indeed, earthquakes

are more frequent in western part of the country and in adjacent Albania (*Fig.2.8a*), less frequent in the eastern part and nearly absent in the south-central area (*Burchfield et al., 2006*). This distribution is consistent with the distribution of active neotectonic faulting (*Fig.2.2; Fig.2.9*), created as new ruptures along old structures, as superimposed faults with EW to NE-SW orientation, excluding the Prespa-Ohrid-Debar area, where the faults are oriented in NS to NW-SE directions (*Dumurdjanov et al., 2020*).

7.3 Conclusions

This study represents the first catalogue, although still incomplete, about the gas manifestations in North Macedonia. The collected gas manifestations, comprising both thermal and cold systems, can be subdivided in three groups, based on their chemical composition: (i) N₂-dominated group, located in the eastern part of the country; (ii) CO₂-dominated group, sited in the central part of the country; (iii) H₂S-rich group, found in the western part of the territory. The three above-mentioned categories are geographically well separated, mainly, related to the extensional tectonic regime of the area and, sometimes, associated with boundaries between the major geotectonic units.

On the whole, the gas manifestations collected to the eastern and southern parts of the country, where several geothermal fields are present, are related to the lithology of the reservoirs and may be connected also to the presence of Quaternary volcanic areas, whilst the gas manifestations sampled in northern and western side of the territory may be related to major active tectonic structures, generating earthquakes.

Generally, moving from west to east, it is noteworthy an increment of helium content and a decrement of the CO₂/³He ratio, associated to the presence of granitic lithologies in the eastern part of the country, where the ⁴He is widely produced by the radiogenic decay of U and Th. The C-isotopic composition of carbon dioxide and the R/R_A values of the gas manifestations indicate a prevailing crustal origin with a mantle contribution up to 20%. Moreover, the isotopic composition of methane suggests a likely abiogenic origin of hydrocarbons released from hydrothermal systems

hosted in the Precambrian shield or ultramafic rocks, although a thermogenic source or a mixing of the two sources are not excluded, whilst for the remaining samples suggests mixing processes between thermogenic and microbial sources.

Chapter 8 - Degassing areas of North Macedonia

Even if there are still places to be investigated, some degassing areas were identified in the westernmost part of the country (*Fig.8.1*), including the Bitola-Florina basin, the Polog graben, the Duvalo Kosel and the gas manifestations of Botun and Petkoniva.

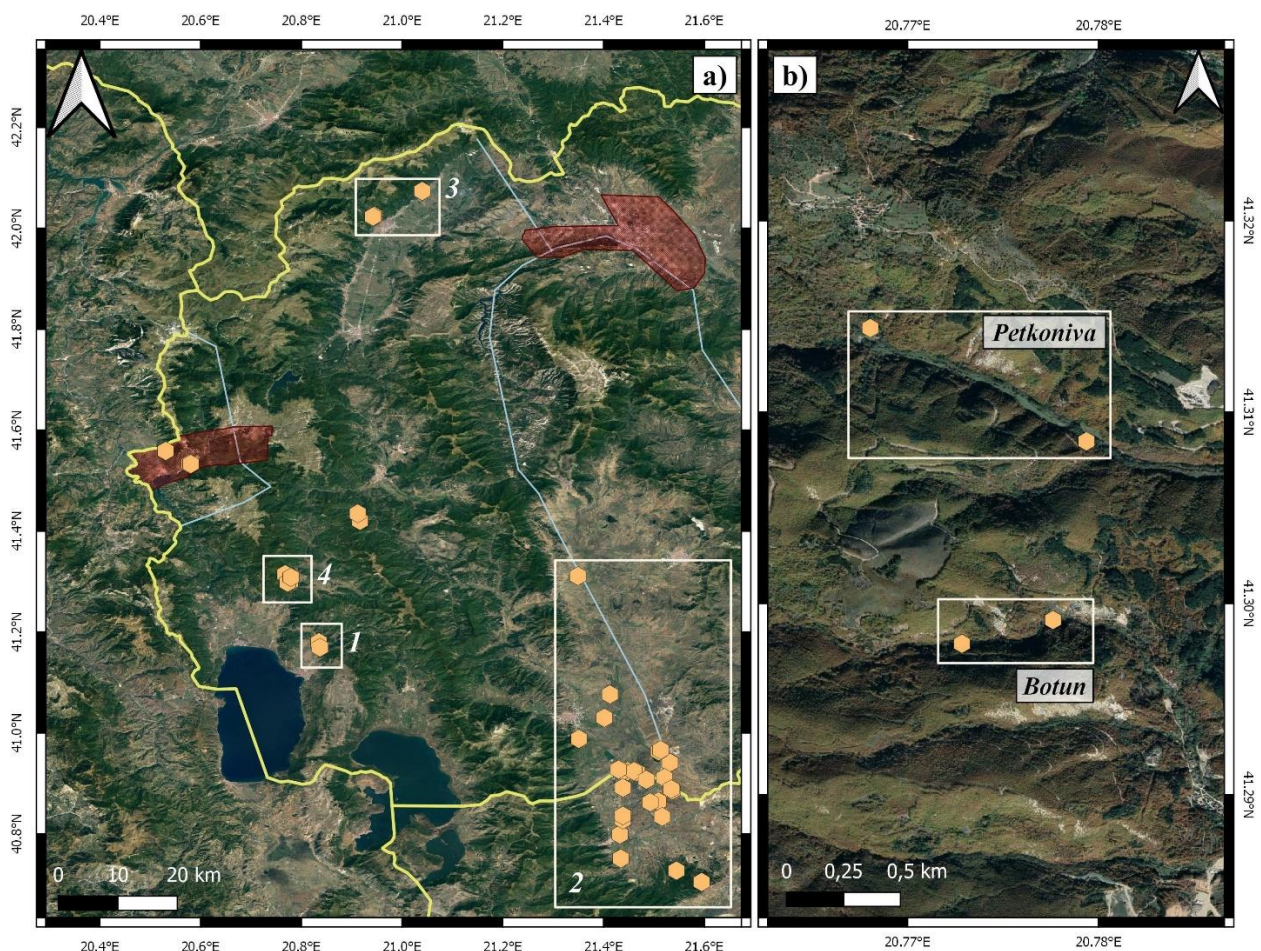


Fig.8.1. (a) Geographical distribution of main degassing area in the westernmost part of North Macedonia. 1 – Duvalo Kosel; 2 – Bitola-Florina basin; 3 – Polog graben; 4 – Botun and Petkoniva. (b) Enlarged area comprising Botun and Petkoniva. Based map from *Google*.

8.1 Gas manifestations of Bitola basin

Bitola basin, together with the Florina basin on the other side of the Greek-Macedonian border, is an NNW-SSE oriented intra-montane graben, part of the larger Pelagonian graben, that belongs to the Pelagonian tectonic zone, and West Macedonian zone, which border running within the basin (*Arsovski, 1997*), and extends for more than 100 km from Prilep in North Macedonia to Kozani in

Greece. It was formed during Middle to Late Miocene (*Dumurdzanov et al.* 2004, 2005), as the result of an extensional phase of Alpine orogenesis, that created the major fault systems of this area (*Metaxas et al.*, 2007; *Gemeni et al.*, 2015). The basin is filled up by terrestrial, fluvial and limnic sediments of Neogene and Quaternary age, whilst the basement consists of metamorphic rocks and Triassic-Jurassic crystalline limestones (*Ivanov & Slavomira*, 2002, *Ziogou et al.*, 2013; *Gemeni et al.*, 2015). Several CO₂-rich mineral springs and wells are found in the basin, resulting from a migration of carbon dioxide from depth to the surface along permeable faults and fracture zones, used as preferential pathways (*Koukouzas et al.*, 2015). The presence of extensive natural CO₂ accumulations on the Greek side (Florina area) is well documented (*Pearce et al.*, 2004; *Karakatsanis et al.*, 2007; *D'Alessandro et al.*, 2011; *Ziogou et al.*, 2013, *Gemeni et al.*, 2015), whilst no data have been published for the North Macedonian side (Bitola area). In the Florina area, and probably also in Bitola, extensive natural CO₂ accumulations occur in the Miocene sand layers, alternating with silt and clay layers, and up to five lignite seams, overlying Mesozoic crystalline limestones (*Karakatsanis et al.*, 2007; *Ziogou et al.*, 2013). Huge amounts of carbon dioxide are extracted from the companies of both parts of the basin; for example, the company of *Air Liquide Greece* extracts 30,000 t a⁻¹ from a reservoir in Florina (*Pearce et al.*, 2004). Moreover, extensive research in Florina basin evidenced areas with CO₂ fluxes from the soil of up to 10,000 g m⁻² d⁻¹ (*Ziogou et al.*, 2013). The gas manifestations collected in Bitola basin during this work represent the first (incomplete) geochemical catalogue for this area and reveal the carbon dioxide (from 83 % to ~100 %) as dominant component of the mixture, whereas the high CO₂/³He ratio indicates a crustal origin of the carbon, although a mantle component is also present (up to 10%), which can be related to the Quaternary volcanic activity of Kozuf-Voras system (*Kolios et al.*, 1980; *Molnár et al.*, 2022). According to *D'Alessandro et al.* (2011), the gas samples of Florina basin show similar characteristics.

Contrarily to the Greek part, where only one company exploits industrially the extracted CO₂, in the Macedonian part many companies extract the gas while other bottle natural sparkling water. Not all the Macedonian companies authorised us to take samples from their drillings. Notwithstanding the extensive research in the Florina area, a quantification of the total carbon dioxide outgassing of the basin has not yet made. Nevertheless, the CO₂ output of the entire area is probably huge, accounting for at least the amount extracted by *Air Liquide Greece* without apparently reducing the output from natural gas emissions in the area.

The study of the total CO₂ output of the area is still underway and, in both Macedonian and Greek parts of the basin, local people indicate the presence of areas with diffuse degassing from the soils not yet measured. Exception is one area close to Florina where CO₂ flux measurements revealed a total CO₂ output of 1.34 t × d⁻¹ (*Daskalopoulou et al., 2019b*). Furthermore, drillings did sometime intercept some pressurised gas reservoir, occasionally ending up in strong uncontrolled degassing. This is the case, for example, of an explorative drilling bored in 1993 close to the village of Neo Kafkasos on the Greek side close to the border that caused the uncontrolled release of abundant water and gas for almost one decade (*Pearce, 2004; D'Alessandro & Kyriakopoulos, 2013*). Similarly, on the Macedonian side close to Gneotino village (*Fig.8.2*), the drilling operations of two piezometers for the observation of the groundwater level ended also in an uncontrolled water and gas eruption, together to a strong travertine deposition.

Leshok and Banjche are the CO₂-dominated gas manifestations collected in Polog graben, in the northern part of the country, likely related to a regional ENE-WSW strike-slip fault system (*Dumurdjanov et al., 2020*) and/or its secondary fault systems bordering the graben. Some local people indicate the presence of degassing and iron incrustations in other parts of this area. Future perspectives are looking for these manifestations in order to estimate the CO₂ release into the atmosphere from this system.



Fig.8.2. Photos of erupting drillings close to Gneotino village. (a & b) Gneotino; (c) Gneotino 2; (d) particular of carbonate incrustations in Gneotino 2.

8.2 Gas manifestations of the southwestern region

The Duvalo Kosel area is a natural phenomenon of intense soil degassing, located in the Ohrid region, in the south-western part of the country. Among the degassing areas, Duvalo is the most studied area, which is described in detail in Chapter 9.

Petkoniva and Botun are two soil degassing areas, located in two adjacent valleys, in the southwest region of the country and about 16 km away from Duvalo in NNW direction. Both sites are characterized by spots with alteration of the soil and of the surrounding vegetations, sometimes blowing sounds are also present. As well as Duvalo Kosel, Petkoniva and Botun belong to the Western Macedonian geotectonic zone. The stratigraphy consists of Paleozoic metamorphic rocks (metasandstones and phyllitic shales) and of Mesozoic rocks, which consists of clastic-carbonate formation with some rhyolite lava flows and diabase intrusions, and cherty-carbonate formation (dolomite and limestone – *Dumurdjanov & Ivanovski, 1978*). The two sites are situated within the

Paleozoic formations; in particular, Petkoniva is located within the metasandstones, whereas Botun is situated within phyllitic shales, both fall along the same NW-SE fault system (*Fig.8.3*).

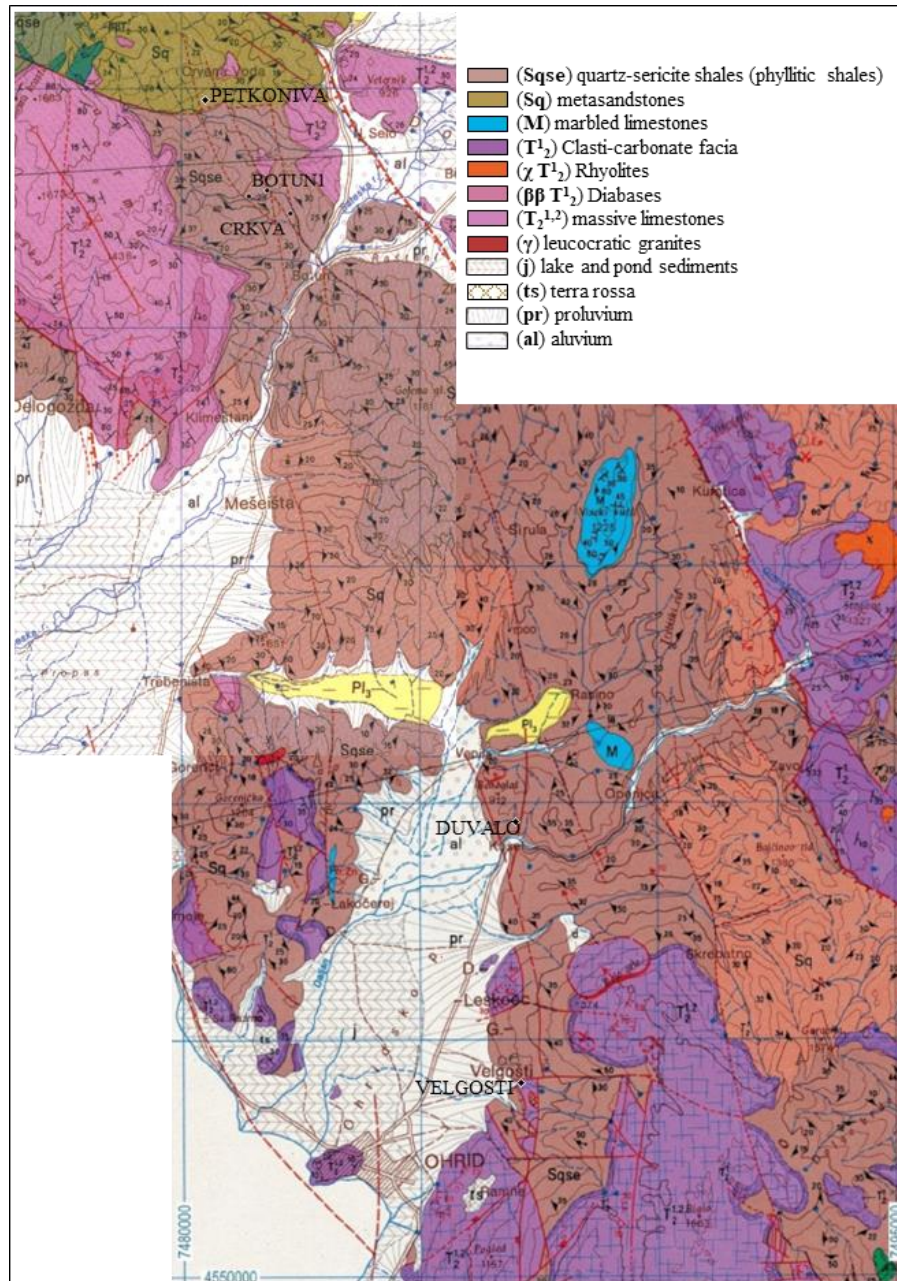


Fig.8.3. Geological map of the area comprising Petkoniva, Botun, Duvalo and Velgosti. Geological map from *BGI* (1975-1980).

8.3 Carbon dioxide output estimation of Petkoniva and Botun

In October 2022, the soil CO₂ fluxes were measured in the two areas under investigation, using the accumulation chamber method (see Chapter 4 for details), and expressed in grams per square meter per day. Such investigation has to be considered only preliminary because, due to time limitations,

measurements were limited to areas of heavy alteration and devoid of vegetation and a small, vegetated stripe around them. The CO₂ output was estimated with 40 measurements over an area of about 600 m² at Petkoniva, giving values that range from 20.2 g × m⁻² × d⁻¹ to 6918 g × m⁻² × d⁻¹, whilst the CO₂ release at Botun was estimated with 44 measurements over an area of about 1600 m², showing values comprised between 3.60 g × m⁻² × d⁻¹ and 12,245 g × m⁻² × d⁻¹.

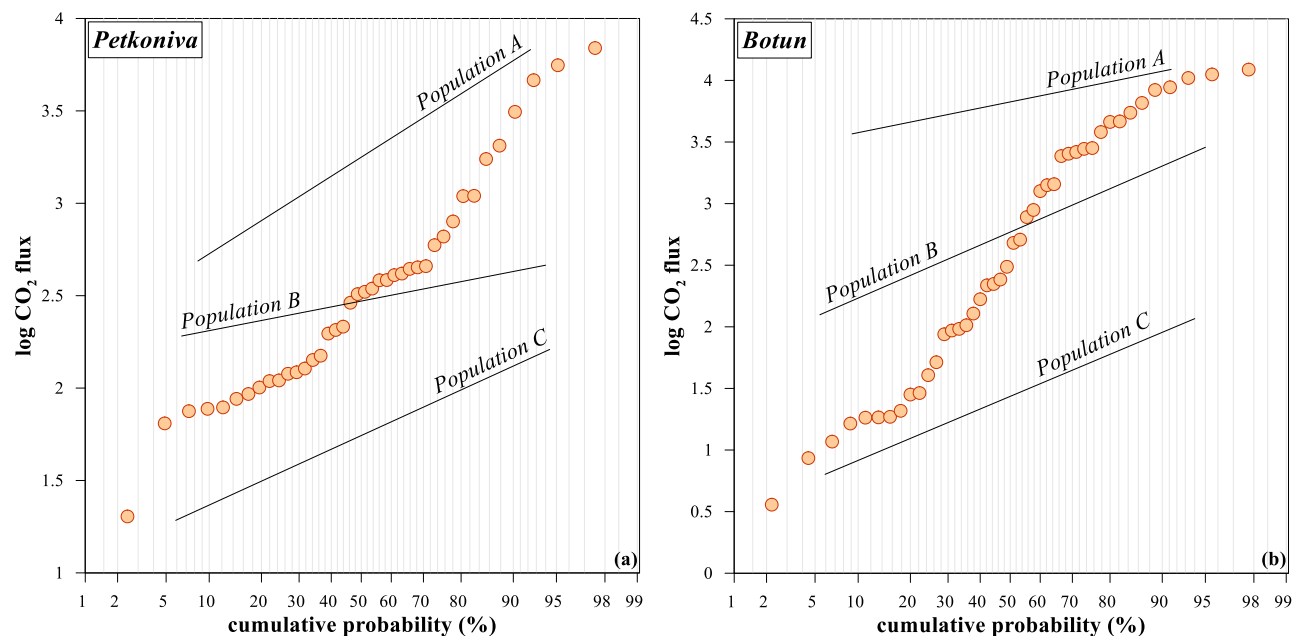


Fig.8.4. Probability plots of the CO₂ fluxes from (a) Petkoniva area and (b) Botun area. The black lines represent the partitioned populations.

Using the Sinclair's partitioning method (Sinclair, 1974), three main log-normal populations were identified (Fig.8.4) for each site, whose statistical parameters refer to the logarithm of CO₂ flux values are shown in *Table 8.1*.

Sites	Populations	Min	Max	Mean	σ	Proportion
		log CO ₂ flux (g × m ⁻² × d ⁻¹)				(%)
<i>Petkoniva</i>	<i>A</i>	2.77	3.84	3.24	0.38	28
	<i>B</i>	2.31	2.66	2.54	0.11	33
	<i>C</i>	1.31	2.18	1.94	0.21	40
<i>Botun</i>	<i>A</i>	3.58	4.09	3.85	0.18	23
	<i>B</i>	2.11	3.45	2.83	0.47	41
	<i>C</i>	0.56	2.01	1.37	0.42	36

Table 8.1. Statistical parameters of CO₂ flux populations, refer to the logarithm.

The population A was characterized by elevated CO₂ flux values and may be considered as representative of a geogenic source of CO₂ degassing. Petkoniva area showed values comprises between 593 g × m⁻² × d⁻¹ and 6918 g × m⁻² × d⁻¹, while CO₂ flux at Botun ranged from 3810 g × m⁻² × d⁻¹ to 12,145 g × m⁻² × d⁻¹. The population B showed the intermediate values. The average CO₂ flux at Petkoniva was 334 g × m⁻² × d⁻¹, whereas at Botun was 738 g × m⁻² × d⁻¹. Lastly, the population C included the lowest CO₂ flux from soil, that ranged from 20.2 g × m⁻² × d⁻¹ to 149 g × m⁻² × d⁻¹ at Petkoniva and from 3.60 g × m⁻² × d⁻¹ to 103 g × m⁻² × d⁻¹ at Botun.

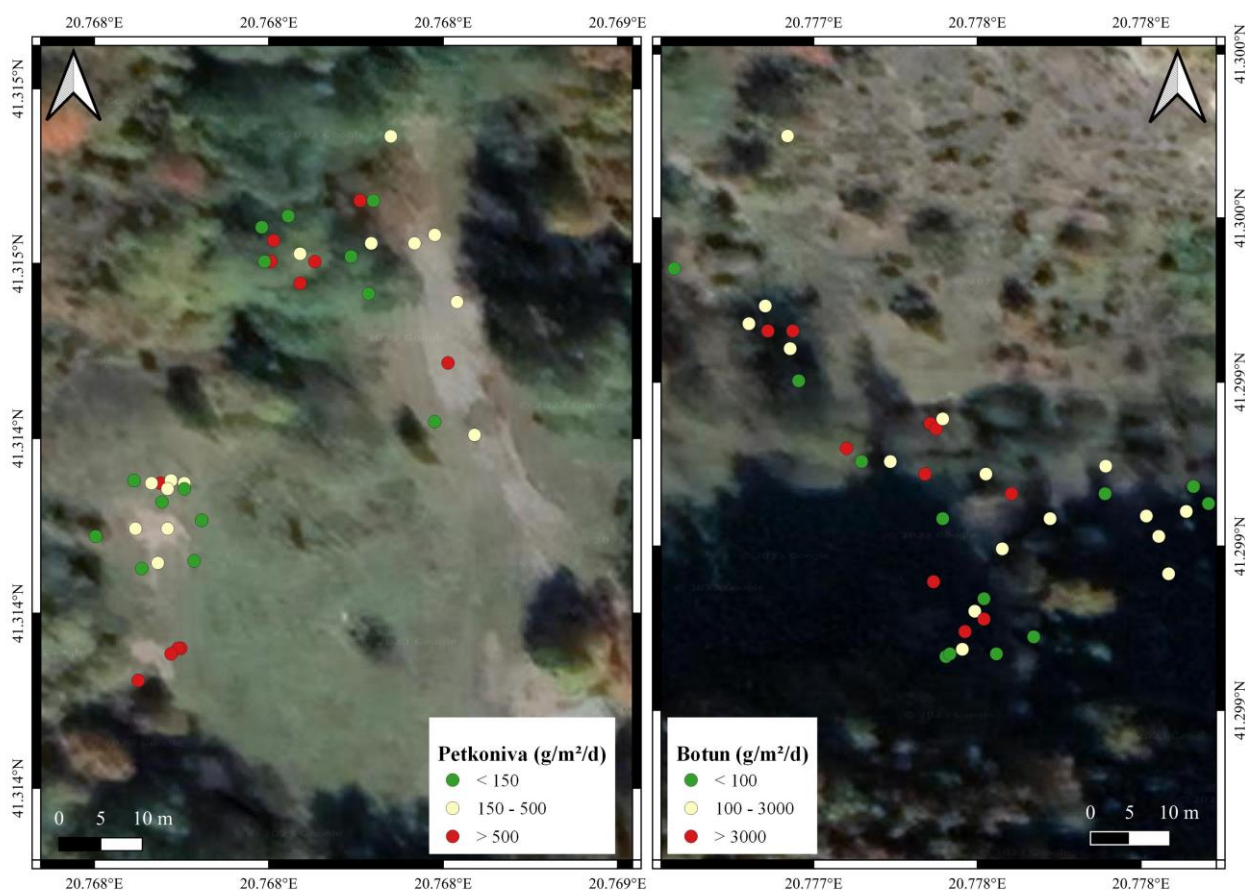


Fig.8.5. Dots maps of CO₂ flux at (a) Petkoniva and (b) Botun and Petkoniva. Based map from Google.

Generally, low CO₂ flux from soil is associated with a biogenic source, showing mean value that varies between 0.2 g × m⁻² × d⁻¹ and 21 g × m⁻² × d⁻¹ (*Chiodini et al., 2008 and references therein*) in several variety of ecosystems. It is noticeable Petkoniva area showed a higher background value (average value of 90.7 g × m⁻² × d⁻¹) respect to Botun, which has an average value of 27.5 g × m⁻² ×

d^{-1} . Although slightly high, the mean CO_2 flux at Botun may be compatible with the carbon dioxide produced by biological activity. On the other hand, the investigation at Petkoniva was only limited to altered spots of the area and their vegetated borders, explaining the elevated values of population C (*Fig.8.5*).

The total amount of released CO_2 at both areas was estimated simply multiplying the geometric average flux value by the degassing surface only to obtain a preliminary order of magnitude output estimation (*Table 8.2*). The estimated CO_2 diffuse degassing at Petkoniva was $0.20 \text{ t} \times \text{d}^{-1}$, whilst at Botun was $0.59 \text{ t} \times \text{d}^{-1}$. This estimation may be assumed mainly to a geogenic source of CO_2 , considering the lack of background measurements at Petkoniva and a maximum biogenic CO_2 flux of $0.04 \text{ t} \times \text{d}^{-1}$ at Botun. Patches of strong soil alteration aligned along preferential directions appeared in both areas, likely connected to main tectonic features of the areas. New measurement campaigns and flux mapping will be carried out to better investigated the CO_2 output of the two areas.

Site	Area km^2	Total output	
		$\text{t} \times \text{d}^{-1}$	$\text{t} \times \text{km}^{-2} \times \text{d}^{-1}$
<i>Duvalo</i>	54.6	66.9	1.23
<i>Botun</i>	1.6	0.59	0.37
<i>Petkoniva</i>	0.6	0.20	0.33

Table 8.2. CO_2 output estimations.

If compared per unit area, the estimated CO_2 release at Petkoniva and Botun are about 3 times less ($0.33 \text{ t} \times \text{km}^{-2} \times \text{d}^{-1}$ and $0.37 \text{ t} \times \text{km}^{-2} \times \text{d}^{-1}$, respectively) than that estimated at Duvalo Kosel ($1.23 \text{ t} \times \text{km}^{-2} \times \text{d}^{-1}$ - *Li Vigni et al., 2022c*). The difference may be partially related to the two different approaches used to estimate the total CO_2 flux. Indeed, the GSA method was used at Petkoniva and Botun, whilst the estimated CO_2 flux at Duvalo Kosel was based on the sGs approach. Albeit this difference the three systems can be considered mutually comparable. One explanation takes into account the difference between the chemical composition of the free-soil gas samples and the dissolved gas samples collected at Petkoniva and Botun (see Chapter 7). Indeed, the composition of

free gas samples was CO₂-dominated and contained H₂S, whilst in the dissolved gas samples (Botun1 and Kiselo Klajnche) N₂ resulted the dominant species and H₂S was absent. The different compositions may be associated with the loss of H₂S and CO₂ by dissolution processes in a shallow aquifer due to their higher solubility in the water (solubility of H₂S > CO₂ >> N₂). Therefore, the loss of CO₂ due to the above-mentioned process may lead to underestimation of the total output from these systems. Lastly, considering the isotopic compositions of the soil gas collected at Duvalo Kosel, Petkoniva and Botun (see Chapter 7), these gas manifestations can be associated to a tectonic degassing almost exclusively related to crustal source, with absent or trivial mantle contribution.

8.4 Conclusions

Some CO₂ degassing areas were identified in the western part of Macedonian territory belonging to the West Macedonian tectonic zone. The study about the quantification of the total amount of CO₂ release from Bitola-Florina basin and from the Polog graben is still ongoing and it is not yet possible to make an estimation.

Soil CO₂ flux measurements were carried out at Duvalo Kosel, Petkoniva and Botun. Regarding the former, a detailed investigation was carried out and described in Chapter 9. On the other hand, only a preliminary investigation could be done at Petkoniva and Botun, limited only to patches with heavy soil alteration and devoid of vegetation. The preliminary estimations reveal a CO₂ flux of 0.20 t × d⁻¹ at Petkoniva and of 0.59 t × d⁻¹ at Botun, mainly related to a shallow crustal source and, likely, connected to main tectonic features of the areas.

Chapter 9 - Duvalo “volcano”: A purely tectonic related CO₂ degassing system

This chapter is already published in *Li Vigni et al. (2022c)*, the chemical and isotopic composition of the gas emissions and the CO₂ flux measurements are published in repositories (*Li Vigni et al., 2022a,b*)

9.1 Introduction

The Duvalo “volcano” is a site of anomalous geogenic degassing close to Ohrid (South-western part of the Republic of North Macedonia) not related to volcanic activity, despite its name. Duvalo area is located close to the village of Kosel, in the North-Eastern part of the Ohrid Basin, that hosts one of the oldest lakes in Europe, Lake Ohrid (*Wagner et al. 2008*) (*Fig.9.1a, b*). It is a natural phenomenon of intense soil degassing (in Macedonian, Duvalo literally means a place where it blows), which is responsible for the intense soil alteration (*Fig.9.1c*), that has damaged vegetation over a large area (many thousands of m²), and the deposition of elemental sulfur and sulfate minerals.

Between the 16th and 19th centuries, during the Ottoman Empire, Duvalo was mined for sulfur, producing about 1700 kg a⁻¹ that was transported to the gunpowder magazines in Thessaloniki, nowadays in Greece, and Istanbul in Turkey (*Serif, 2001*). In 1979, the City Council of Ohrid Municipality declared the Duvalo site a natural rarity with unique features, falling under category III as a Monument of Nature (*Markoski et al., 2019*).

The Duvalo locality is considered to be a volcanic area by local people, due to the “rotten eggs” smell, sulfur exhalations, strong soil degassing and “eruptions” from “craters”, which are considered a trace of extinct volcanic activity. The presence of “craters”, the biggest has a diameter of 50 cm and a depth of 30 cm (*Fig.9.1d*), considered a sign of “volcanic” activity, are instead remnants of the past mining activity. Although the phenomenon was marked as a volcanic solfatara in the local geological literature (e.g. *Kotevski, 1987*), no volcanic rocks or volcanic activity has

been documented in the recent geologic history of the Kosel area (*Dumurdjanov & Ivanovski, 1978; Markoski et al., 2019*). To support the “volcanic” assumption, during dry periods stronger sulfur smell and whistling sound are present, whilst during wet periods bubbling is the dominant sound (*Trojanović, 1925*).

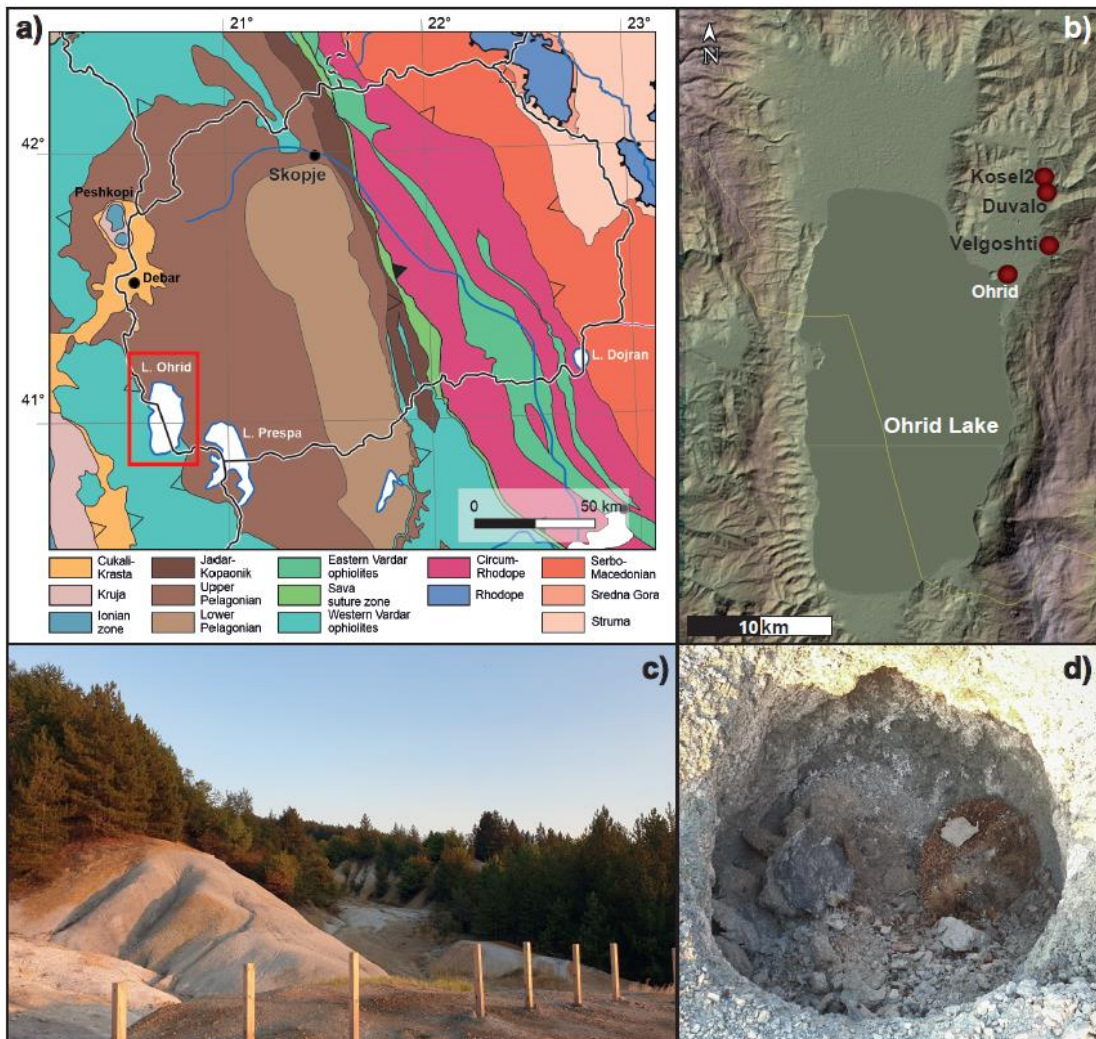


Fig.9.1. (a) Major tectonic units of Republic of North Macedonia, adapted from *Schmid et al. (2020)*. (b) Elevation map of Ohrid Lake Basin with the geographic setting of Duvalo and Velgoshti sites; political border with Albania is shown in yellow line; (c) panoramic photo of Duvalo area; (d) dead hedgehog inside a hole with strong gas exhalation.

Furthermore, the area was affected by an increase in its activity with a significant emission of dense smoke, in May 2014. This increase was interpreted as not related to volcanic activity but as the result of filling of the cracks by rainwater, which increased the gas pressure in the subsurface and generated the emission of water vapour mixed with other gases (*Markoski et al., 2019*). The characteristic alterations of the surface are due to the reactions between the exhalations of H₂S and

the oxygen dissolved in rainwater, forming sulfuric acid which alters the phyllite rocks, leading to their kaolinitization (*Markoski et al., 2019*). According to *Hoffmann et al. (2010)*, the phenomenon is related to an active fault system present in the area.

Few scientific research concerning the geochemical characterization of the gas manifestation of the area were conducted (*Trojanović, 1925; Iloski et al., 1957*, as cited by *Markoski et al. 2019; Dumurdjanov & Ivanovski, 1978*), showing that the gases consist of CO₂ (98 %), H₂S (0.8 %) and inert gases (1 %), with a flux rate of 0.2 l s⁻¹. Between 1956 and 1957, in order to ascertain the sulfur reserves of the Duvalo area, the Office for Geological Research – Ohrid drilled two boreholes. An explosion occurred near one of the two boreholes and the analysis of the emitted gases were carried out, showing an increase of H₂S, up to 2 % (*Iloski et al., 1957*, as cited by *Markoski et al. 2019*).

With the aim to better characterize the source of the Duvalo gas manifestation, the present study reports on new chemical and, for the first time, isotope data of the gas emissions. Furthermore, we present the first map of CO₂ soil diffuse degassing and estimate of the total CO₂ output for the area.

9.2 Geological settings

The Ohrid Basin is a graben structure, part of the Cenozoic South-Balkan Extensional Regime (*Dumurdjanov et al. 2005; Burchfiel et al. 2008*), that is flanked by active N-S striking normal faults, controlled by E-W extension since Pliocene (*Dumurdjanov et al. 2005; Hoffmann et al. 2010*), after initial opening as a pull-apart basin in Late Miocene (*Lindhorst et al. 2015*). The Ohrid Basin is situated along the contact of two major tectonic units: Mirdita Ophiolite Zone in the west, and the Western Macedonian Zone to the east (*Dumurdjanov et al. 2005; Robertson & Shallo, 2000*).

In the area around Kosel village, mostly rocks of the phyllite formation outcrop, composed of quartz-sericite schist, with lenses of quartz-sericite-graphitic schists, with also small intrusions of granitoids and diabase. To the southeast, Triassic marbleized limestone is topping Galichica

Mountain. Duvalo is situated within the quartz-sericite schists, along an intersection of NNW and NNE striking faults (*Fig. 9.2*). The latter follows the direction of an active fault registered within the sediments of Ohrid Lake (*Lindhorst et al. 2015*). The area is seismically active (*Arsovsky & Hadžievsky, 1970; Dumurdjanov et al. 2016*), with the most recent significant earthquake, with a magnitude of M_L = 4.9, registered nearby in 2017 (*Bojadjieva et al. 2019*).

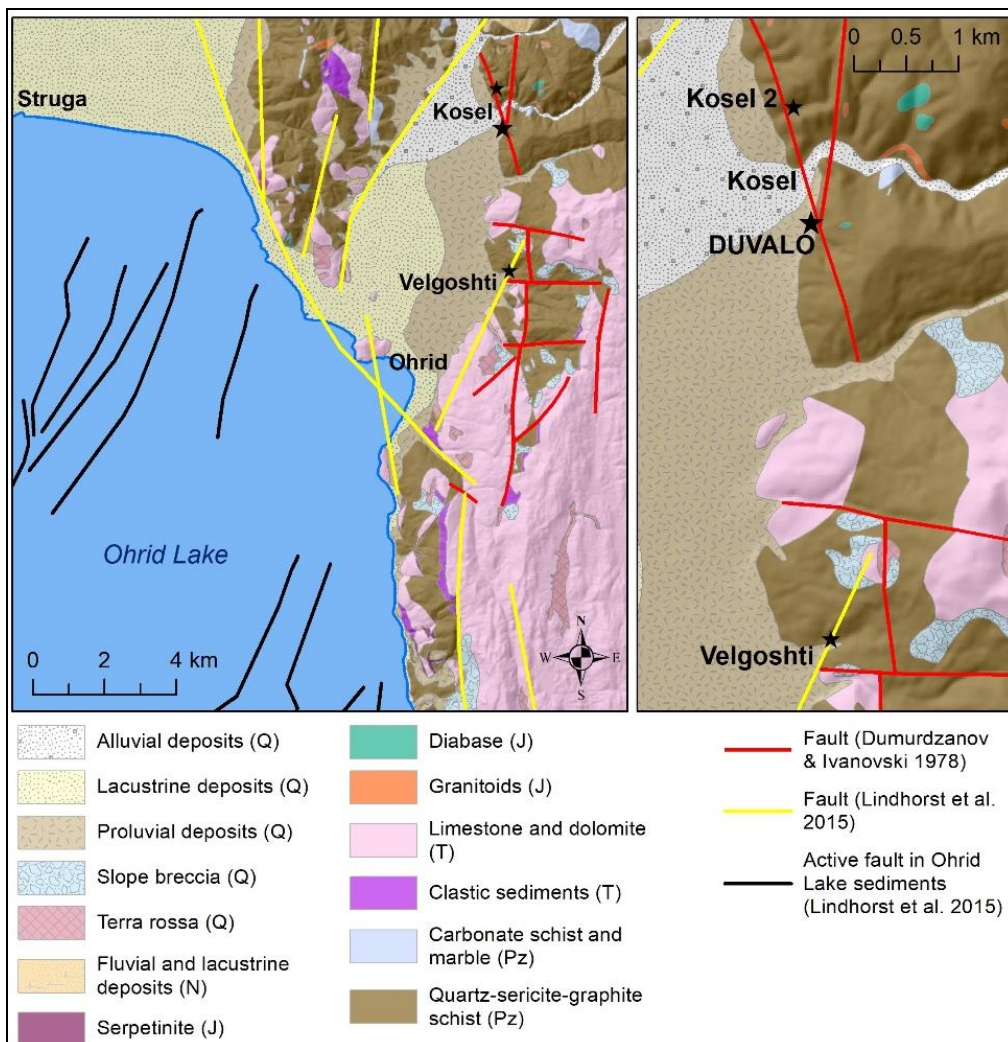


Fig.9.2. Geological settings of Duvalo site. Map compiled from geological data of *Dumurdjanov & Ivanovski (1978)* and *Lindhorst et al. (2015)*. The geographical position of the sampling sites is evidenced by a star.

The gas exhalation area at Duvalo is easily recognised by the large zone devoid of vegetation and covered by light coloured alteration products and bordered by a dense forest area. The trees at the limit of the exhaling area show chlorotic or necrotic leaves or needles especially on their lower branches. This area is elongated in NNW-SSE direction on the hillside bordering the Ohrid Plain

and comprises also some minor areas separated by forest.

At about one km north of Duvalo, along the NNW-striking fault, another area devoid of vegetation can be recognised (Kosel 2). Here, only a few alteration areas may be found, with quartz-sericite-graphitic schists also exposed, while most of the area is extensively eroded and shows a very steep relief because of the highly erodible rocks. Similarly, the exposed parts of the quartz-sericite-graphitic schists can be found at about 4 km south of Duvalo, at the north-eastern outskirt of Velgoshti village, on a hill (thousands of m²) covered by sparse stunted vegetation. Here, sulfur and sulfate efflorescence's and incrustations can be recognised along a 50 m stretch at the southern foot of the hill.

9.3 Results

In August 2019 and March 2020, two sampling campaigns were carried out. Nine gas samples have been collected in the study area: seven samples have been collected along Duvalo area and one sample in each of the other two sites with evident alteration signs, Kosel 2 and Velgoshti (*Fig.9.1, 9.2*).

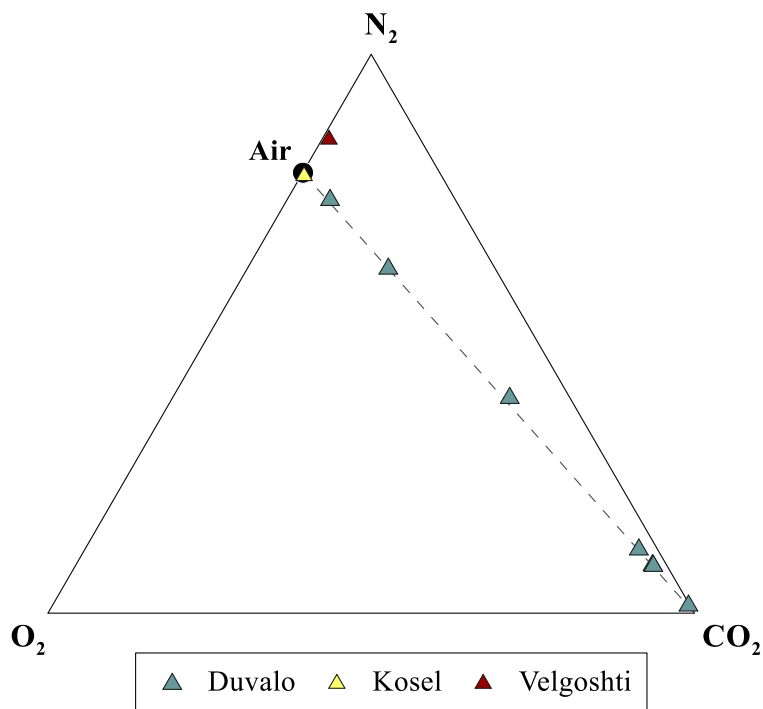


Fig.9.3. CO₂-N₂-O₂ triangular plot. The atmospheric air composition is also plotted.

Generally, carbon dioxide, in four samples, and nitrogen and oxygen, in three samples, are the dominant components of the gas samples from Duvalo area (*Fig.9.3*). Carbon dioxide arrives up to 966,100 µmol mol⁻¹, N₂ ranges from 17,900 µmol mol⁻¹ to 736,100 µmol mol⁻¹, whereas O₂ concentrations varies between 128 µmol mol⁻¹ and 189,700 µmol mol⁻¹, indicating sometimes an important air component. The gases collected at Kosel 2 and Velgoshti are dominated by the atmospheric component (N₂ and O₂), while CO₂ concentrations range from values of 2,900 µmol mol⁻¹ to 8,700 µmol mol⁻¹, respectively.

For all samples, hydrogen sulfide concentrations show a wide spectrum of values between < 10 µmol mol⁻¹ and 5500 µmol mol⁻¹. Methane concentrations display also a large range, that varies between 11 µmol mol⁻¹ and 3250 µmol mol⁻¹. Minor compounds, hydrogen and helium, are also found, with concentrations of < 3 µmol mol⁻¹ - 1010 µmol mol⁻¹ for the former and < 3 µmol mol⁻¹ - 70 µmol mol⁻¹ for the latter. Ethane is always below the detection limit (< 10 µmol mol⁻¹) but the CH₄/C₂H₆ ratio (513) was measured in one sample in the enriched headspace gas of a soda ampule. Argon was measured only in few samples and showed absolute values and N₂/Ar ratios close to the atmospheric ones in the samples of Kosel 2 and Velgoshti. On the contrary, Duvalo showed very low concentrations of argon (61 µmol mol⁻¹ and 79 µmol mol⁻¹) and N₂/Ar ratios (> 200) higher than the atmospheric values.

The $\delta^{13}\text{C}_{\text{CO}_2}$ at Duvalo presents values from -0.2 ‰ to 2.7 ‰ vs. V-PDB, whilst Kosel 2 and Velgoshti have values of -13.7 ‰ and -0.8 ‰, respectively. The isotope composition of He has been determined only in two samples from Duvalo, both showing the value of 0.10 R/R_A. The isotope composition of CH₄ has also been determined showing $\delta^{13}\text{C}_{\text{CH}_4}$ values that range from -36.8 ‰ to -34.4 ‰ V-PDB and $\delta^2\text{H}_{\text{CH}_4}$ values that vary between -180 ‰ and -158 ‰ vs. V-SMOW.

Soil CO₂ fluxes measured at Duvalo area range from 1.34 g m⁻² d⁻¹ to 59,300 g m⁻² d⁻¹ and were modelled as the combination of three log-normal populations (*Fig.9.4*), for which statistical parameters are reported in *Table 9.1*.

Populations	Mean	σ	Propotions	Mean CO₂ flux	95% confidence interval
	log CO₂ flux		(%)	(g m ⁻² d ⁻¹)	
A	1.32	0.54	30	45	35-62
B	2.71	0.46	59	897	746-1,128
C	3.65	0.50	11	8,382	6,289-15,161

Table 9.1. Statistical parameters of CO₂ flux populations.

The population B and C are characterised by elevated mean CO₂ flux values and can be reasonably considered to represent the deep CO₂ degassing. The occurrence of two populations for the deep CO₂ degassing could reflect the relative prevalence of diffusive or advective CO₂ transport mechanisms (e.g., *Chiodini et al.*, 2020). On contrary, population A is characterised by a relatively low mean CO₂ flux and may represent the biological CO₂ background flux for the area. In fact, even if the mean CO₂ flux of population A (45 g m⁻² d⁻¹) is actually slightly higher than the CO₂ fluxes produced by the biological activity for different ecosystems presented in other studies (mean CO₂ flux from 0.2 g m⁻² d⁻¹ to 21 g m⁻² d⁻¹, *Cardellini et al.* 2017, *Viveiros et al.*, 2010 and reference therein) and relatively high with respect to the biological background generally found in numerous hydrothermal sites (*Chiodini et al.*, 2008 and references therein). However, a relatively high biological background CO₂ flux has also been reported for several sites; for example, mean background CO₂ fluxes of 44.8 g m⁻² d⁻¹ and 46.85 g m⁻² d⁻¹ were reported at the Furnas do Enxofre degassing area (Azores; *Viveiros et al.*, 2020) and Horseshoe Lake (Mammoth Mountain, CA, *Cardellini et al.*, 2003) respectively.

Temperatures, measured only at five sites in August 2019, gave values were in the range of 17.2 – 18.5 °C, higher than the mean annual atmospheric temperature of the area (11.1 °C; *Zikov* 1997), but close to the mean summer atmospheric temperature (19.7 °C; *Zikov* 1997) and lower than the atmospheric temperatures during the measurement campaign (from about 20 °C in the early morning up to about 40 °C in the afternoon).

Only two soil CO₂ flux measurements were made at Kosel 2 in areas with some sign of soil alteration, but in this case low CO₂ flux values were found ($4.61 \text{ g m}^{-2} \text{ d}^{-1}$ and $5.23 \text{ g m}^{-2} \text{ d}^{-1}$). No flux measurement was made at the Velgoshti site.

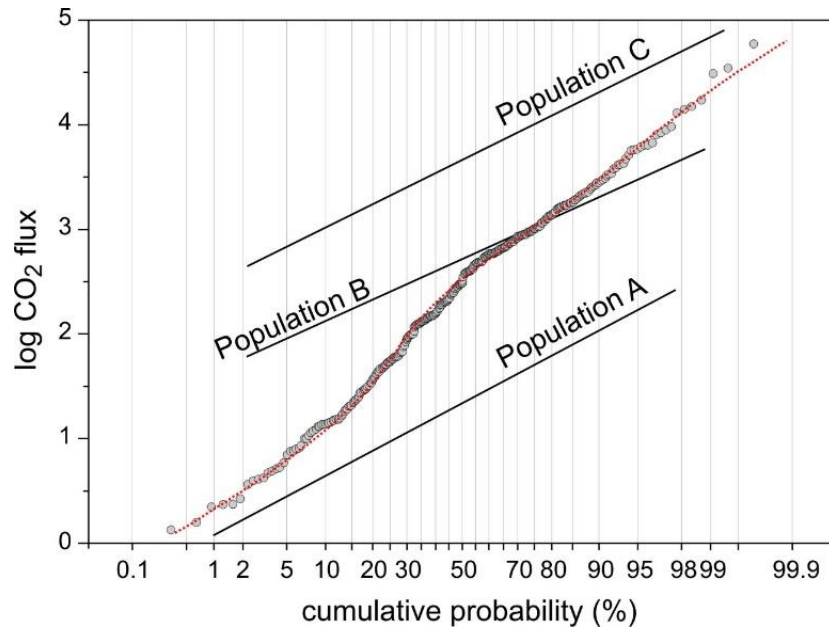


Fig.9.4. Probability plot of CO₂ flux from Duvalo area. The black lines represent the partitioned populations while the dashed red lines represent the combination of the partitioned populations.

9.4 Discussion

9.4.1 Origin of the gases

Results of the most CO₂-rich samples are consistent with previous analyses performed in 1925 (*Trojanović, 1925*), 1957 (*Iloski et al., 1957*; as reported in *Markoski et al. 2019*) and in 1977 (in *Markoski et al., 2019*), when it was reported that the gases were composed mainly of CO₂ (90 % - 98 %) and H₂S (0.8 %). The consistency of the results indicates a certain stability of the exhaling system, at least in the last century.

In the present research, isotope analyses were carried out to deduce the origin of the gas manifestations in Duvalo area. Helium compositions shows a R/R_A ratio of 0.1, which indicates an almost pure crustal origin (*Fig.9.5a*).

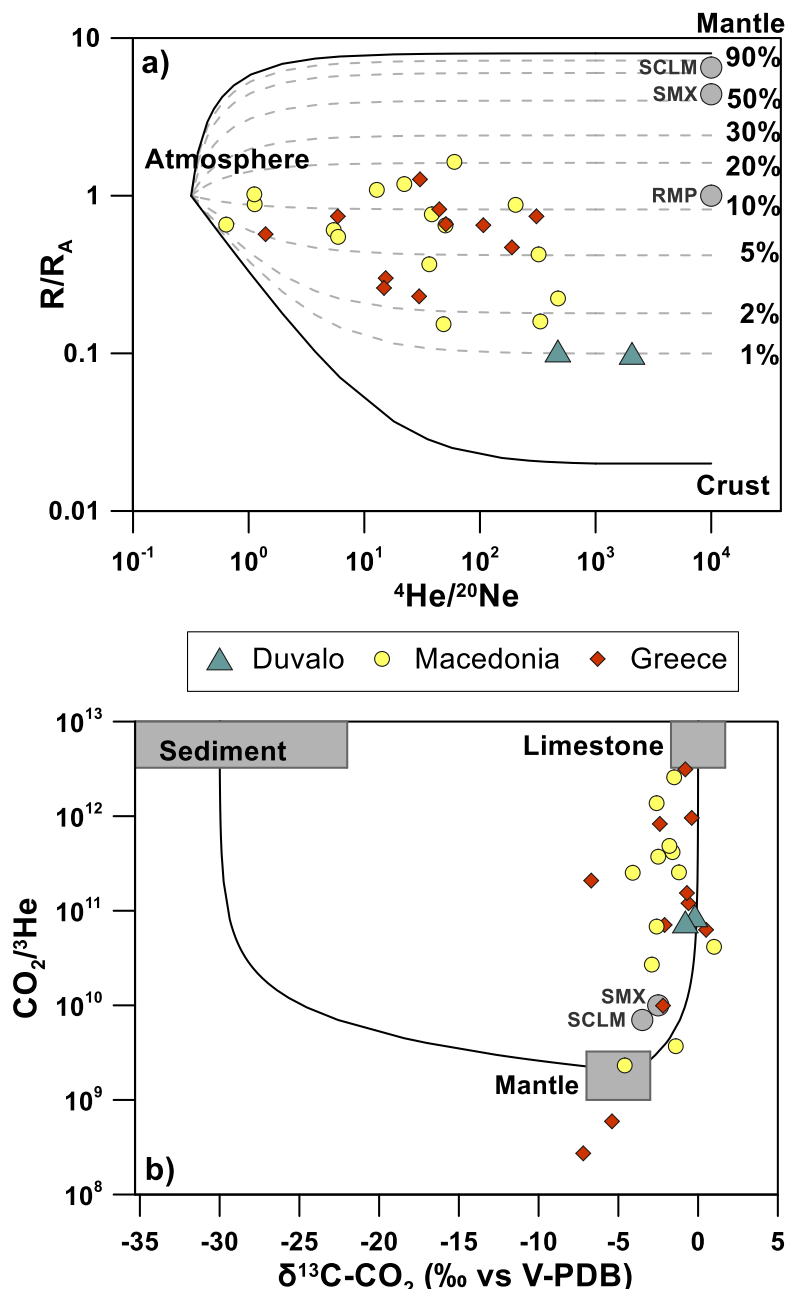


Fig.9.5. Binary plots of: (a) R/R_A vs. $^{4}\text{He}/^{20}\text{Ne}$ of the samples collected at Duvalo. The mixing lines between Atmosphere and a MORB-type Mantle and between Atmosphere and Crust are also plotted. Dashed lines represent mixing between atmosphere and end-members with different percentages of MORB-type mantle contribution (*after Sano & Wakita, 1985*). Three other mantle end-members are also plotted: SMX = Stromboli Mantle Xenoliths – Martelli *et al.*, 2014; SCLM = Sub Continental Lithospheric Mantle – Gautheron & Moreira, 2002; RMP = Roman Magmatic Province - Martelli *et al.*, 2004. (b) $\text{CO}_2/^{3}\text{He}$ vs. $\delta^{13}\text{C}-\text{CO}_2$. The compositions for Sediments, MORB-like Mantle and Limestones end-members are: $\delta^{13}\text{C}-\text{CO}_2 = -30\text{ ‰}$, -5 ‰ and 0 ‰ and $\text{CO}_2/^{3}\text{He} = 1 \times 10^{13}$, 2×10^9 and 1×10^8 , respectively (*after Sano & Marty, 1995*). Percent of mantle contribution is shown along the mixing line between mantle and, respectively, limestones and sediments. SCLM from Brauer *et al.* (2016) and SMX from Martelli *et al.* (2014) and Gennaro *et al.* (2017). Samples from other sites of the Republic of North Macedonia (Temovski *et al.*, 2020) and of the nearby northern Greece region (Daskalopoulou *et al.*, 2018) are plotted for comparison.

Deep normal or transcurrent faults act sometimes as preferential pathway to the uprise of mantle helium, which can be recognised in R/R_A values tending towards the MORB values ($8 \pm 1 \text{ R}/\text{R}_A$ - Ozima & Podosek, 2002). The area of Ohrid is a seismically active extensional basin and the site of Duvalo corresponds to an active fault system. Such extensional basins are widespread in the neighbouring areas. For the other tectonically similar areas in the south and in the north-west of the country, mantle contributions up to 20 % (R/R_A up to 1.64) have been measured (Fig.9.5a - Temovski et al., 2020). Similarly high R/R_A values (up to 1.27) have been found also in northern Greece (Fig.9.5a - Daskalopoulou et al., 2018). On the contrary, at Duvalo a mantle contribution seems absent or at least trivial (about 1%). Similarly, $\delta^{13}\text{C}_{\text{CO}_2}$ values between -0.8 ‰ and -0.1 ‰ and CO_2/He ratios between 7.6×10^{10} and 8.4×10^{10} point towards an almost pure crustal (marine limestones) source also for CO_2 , with at most 2 % mantle contribution (Fig.9.5b).

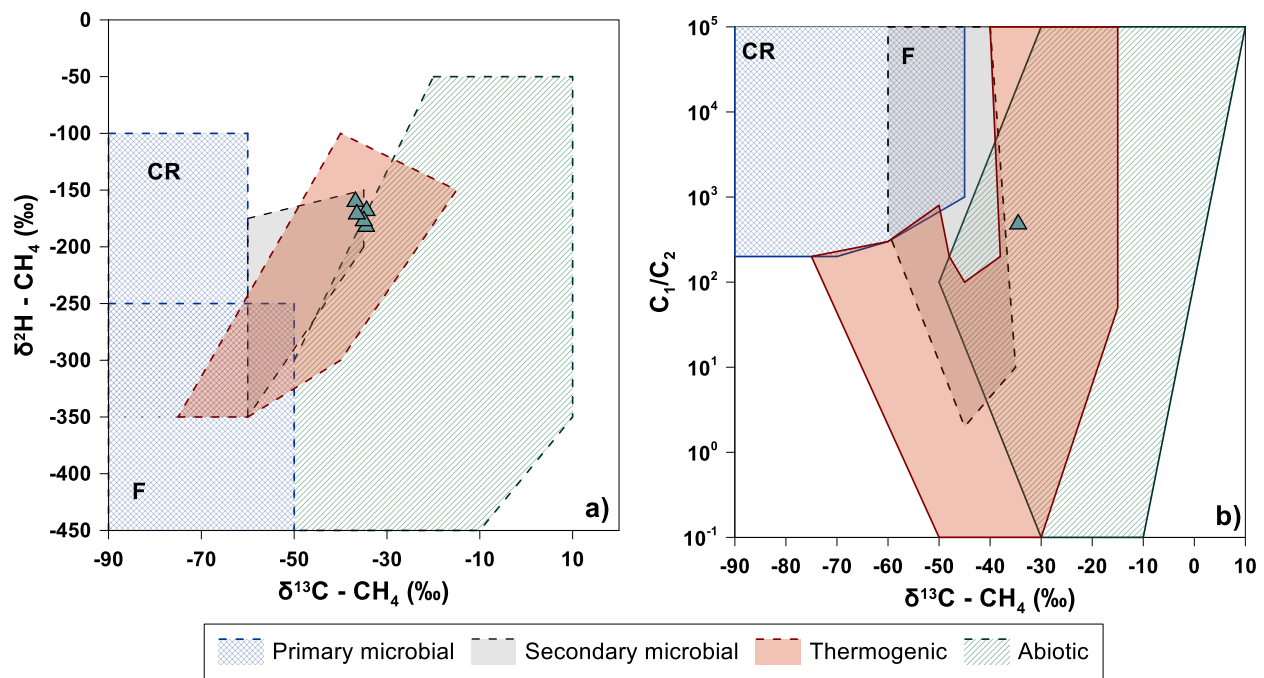
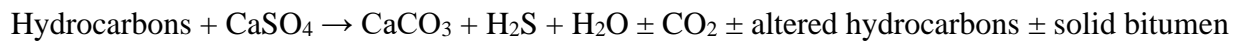


Fig.9.6. $\delta^{13}\text{C}_{\text{CH}_4}$ vs. $\delta^2\text{H}_{\text{CH}_4}$ (a) and $\delta^{13}\text{C}_{\text{CH}_4}$ vs. $\text{C}_1/(\text{C}_2+\text{C}_3)$ (b) binary plots (Milkov & Etiope, 2018). F = fermentation; CR = CO_2 reduction.

Data have been plotted in $\delta^{13}\text{C}_{\text{CH}_4}$ vs. $\delta^2\text{H}_{\text{CH}_4}$ (Schoell, 1983) and $\text{CH}_4/(\text{C}_2+\text{C}_3)$ vs. $\delta^{13}\text{C}_{\text{CH}_4}$ (Bernard et al., 1977) graphs, modified by Milkov & Etiope (2018) in order to discriminate the origin of methane (Fig.9.6). The Duvalo samples fall within the thermogenic range, although secondary

microbial or oxidation processes cannot be excluded (*Milkov & Etiope, 2018* and reference therein). The origin of H₂S in the gases released at Duvalo is somewhat harder to constrain. Unfortunately, no sulfur isotope data are available at present. H₂S is a typical gas of hydrothermal origin but in the present case we have no indication about the presence of a hydrothermal system at depth. No thermal spring is present at Duvalo or in the area around. The closest thermal springs are more than 40 km away in NW direction. No thermal anomaly has been recognised within the soils of Duvalo and at 50 cm depth, even at the sites with the highest measured CO₂ fluxes, the soil temperatures were close to the mean annual atmospheric temperature of the area. The absence of thermal anomalies and the low temperature of the gases is not in itself an indication of absence of any geothermal system at depth. Nevertheless, the south-western part of Macedonia, to which the area belongs, is not considered to have anomalous heat flows (*Popovska-Vasilevska & Armenski, 2016*).

An alternative process that can produce H₂S could be the sulfate reduction (*Machel, 2001*) either microbially (MSR) or thermochemically (TSR). In both cases, the process can be schematized by the following reaction:



MSR is considered to occur at temperatures below 80°C while TSR generally in the 100-140°C range (*Machel, 2001*). TSR is thermodynamically favoured, but kinetically limited, also at temperatures down to 25 °C (*Mougin et al., 2007*).

In the study area, no hydrocarbon, gypsum or anhydrite deposits have been identified, either outcropping or in the subsoil. Nevertheless, organic-rich schists are present in the metamorphic basement part of the Upper Pelagonian in the area (*Dumurdjanov & Ivanovski, 1978*). Shists may be the origin of some hydrocarbons, and the CH₄ found in the gases released at Duvalo. The isotopic composition of CH₄ suggests a thermogenic origin compatible with TSR processes (*Milkov & Etiope, 2018*). Despite their absence at the surface in the area of Duvalo, gypsum or anhydrite deposits may be present at depth. As suggested by *Frasher et al. (1996)*, the Peshkopi tectonic

window in Albania to the north, which is part of the Ionian zone and underlies the Upper Pelagonian (*Robertson & Shallo, 2000; Schmid et al. 2020*), comprises Triassic evaporites in its sequence. Evaporite sulfates are found also south of Peshkopi, on the Macedonian side, near Debar (*Jančev et al. 1999*). Furthermore, sulfates may be contained in small quantities in shallow water carbonates (generally dolomites) of the sedimentary sequence of the Upper Pelagonian. Although still not ascertained, one of these sulfate-containing sequences may be present at some depth beneath Duvalo.

Due to the active tectonic structure, the sulfate-bearing strata may have been put in contact with the organic-rich shales by the fault system along the eastern part of the Ohrid graben. Even without anomalous heat fluxes, the most favorable temperature conditions for TSR may be reached at depths between 3 km and 4 km considering an average geothermal gradient (30°C km⁻¹). The produced H₂S rises towards the surface through the same fault system either in the gas phase or dissolved in water. During transport, H₂S could be oxidized by oxygen-charged meteoric waters producing H₂SO₄. The strongly acidic solutions that will form may react with the limestones of the sedimentary sequence producing abundant CO₂.

Sulfuric acid may also be produced by the oxidative weathering of sulfides. In the geologic succession of the study area, sulfides (mainly pyrite) are found within the phyllite formation, at the contact with the granitoid intrusions (*Dumurdžanov & Ivanovski, 1978*) and may contribute to the production of the CO₂ released at Duvalo. Nevertheless, oxidation of sulfide minerals cannot explain the presence of H₂S in the released gases. Metamorphic reactions producing H₂S from sulfide minerals need high temperatures (> 450 °C) and/or high pressures (*Tomkins, 2010*) and are therefore an improbable H₂S source for this system.

9.4.2 Processes affecting gas composition in the soil

Samples have been plotted in N₂-O₂-CO₂ ternary diagram (*Fig.9.3*) showing a mixing trend between a CO₂-dominated component (CO₂ > 960,000 μmol mol⁻¹) and the atmospheric air

component. Such trend is typical of soil gases where low CO₂ contents correspond to low flux rates of the deep-derived gases. The N₂ excess with respect to the atmospheric air ratio in the soil gas sample of Velgoshti can be attributed to oxygen consumption given that the N₂/Ar ratio of the same sample is nearly identical to the atmospheric one. Helium, CH₄ and H₂S are almost completely related to the deep geogenic member, the highest values being found in the sample with the highest CO₂ concentration.

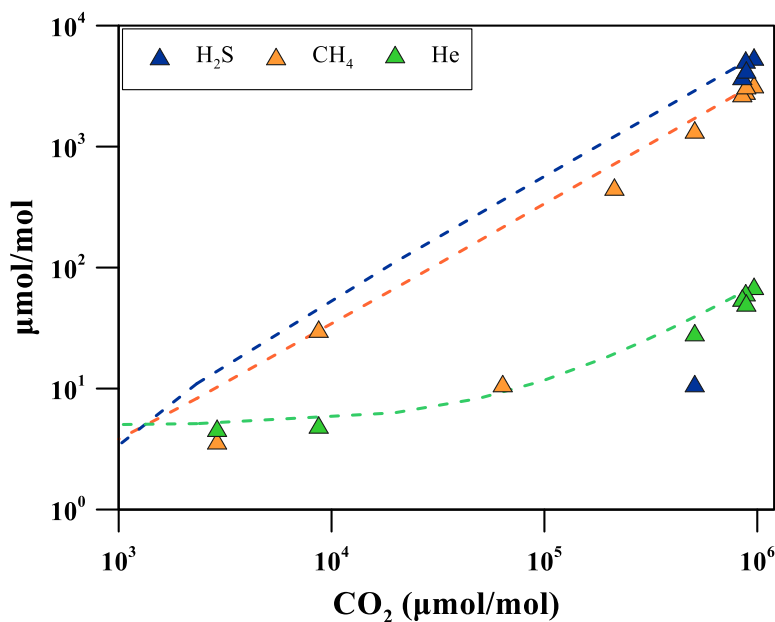


Fig.9.7. H₂S, CH₄ and He vs. CO₂ binary plot. The dashed lines represent the mixing between atmospheric air and the deep geogenic gas.

In a binary plot *versus* CO₂, both CH₄ and He (Fig.9.7) are mostly aligned along a mixing line with atmospheric air. Small deviations from the mixing line may derive from solubility difference when the uprising gases pass through groundwater not saturated in these gases. Few samples have CH₄ well below the mixing line indicating loss by microbial or inorganic oxidation. For H₂S, only the samples with very low air contribution approximately follow the mixing line. Samples with $\leq 50\%$ of air contribution display H₂S values at or below the detection limit ($10 \mu\text{mol mol}^{-1}$), orders of magnitude beneath the mixing line. On its transit toward the soil surface, H₂S can be lost either by dissolution in water (higher solubility with respect to CO₂) or, more probably, by oxidation. A higher contamination of the soil gases by air is, generally, connected with lower fluxes and

therefore to higher permanence time in the soil favouring oxidation processes. The result of H₂S oxidation is the deposition and accumulation of sulfate alteration minerals in the soil (*Alpers et al., 2000*).

Kosel 2 displays a soil gas composition close to that of atmospheric air, indicating the absence of significant deep gas exhalations and the limited alteration of the soil may be related only to the physical-chemical weathering of pyrite in the outcropping black shales (*Dumurdjanov & Ivanovski, 1978*). Pyrite oxidation could be suggested by the low pH (~3) of the water in the small creek draining this area. Like Duvalo, the area of Kosel 2 is also crossed by some active tectonic structures (*Fig.9.2*) and we cannot exclude that it has been the site of geogenic degassing in the past. Nevertheless, the areas devoid of vegetation in this area are all very steep and are probably characterised by strong physical weathering and are not the consequence, like in Duvalo, of the intense chemical alteration.

Velgoshti sample has a higher N₂/O₂ ratio (6.1) with respect to air, which can be attributed to oxygen consumption. Although the altered soil covers a much larger area than in Kosel 2, we have no flux measurement that can indicate that such alteration is linked to high gas fluxes like in Duvalo. Our single soil gas analysis does not indicate geogenic contribution. Nevertheless, the area deserves larger soil CO₂ flux prospection.

9.4.3 CO₂ flux mapping and CO₂ output estimation

An estimation of CO₂ release from soil degassing has been obtained following the sGs method (*Cardellini et al., 2003*). The experimental variogram of the normal scores of CO₂ flux (*Fig.9.8b*) highlights two nested structures: one characterized by a shorter range (30 m) and one by a larger range (90 m), that may reflect the occurrence of a set of spatially organized small scale anomalies. The map of the CO₂ flux shows (*Fig.9.8a*) that the most anomalous degassing areas are aligned along preferential directions following the main tectonic lineament direction of the area. We infer that fracture-zone channel the deep gas, described also as Diffuse Degassing Structures (DDS –

Chiodini et al., 2001). Significant soil CO_2 degassing can help to detect active tectonic features as shown by *Lewicki & Brantley (2000), Kampf et al. (2013), Weinlich (2014), and Kis et al. (2017)*, among others. The inferred features are in concordance with the lineaments shown by *Dumurdjanov & Ivanovski (1978)* mainly in the NNW-SSE direction but also in the NNE-SSW directions.

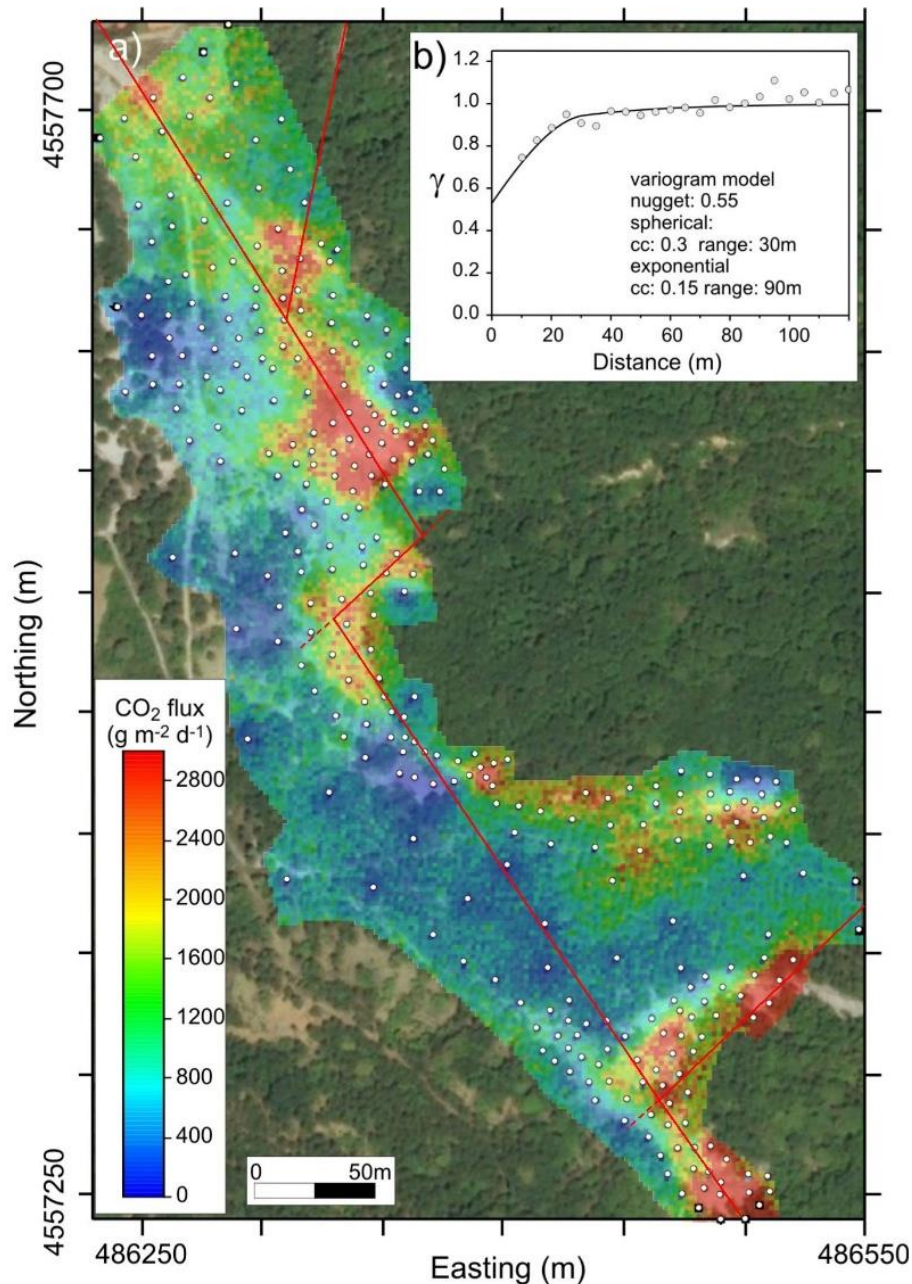


Fig.9.8. (a) Map of the CO_2 flux. White dots refer to measured sites; red lines are inferred diffuse degassing structures which follow the directions of the tectonic lineaments defined by *Dumurdjanov & Ivanovski (1978)*. (b) Experimental variogram and variogram model.

The total amount of released CO₂ estimated from the sGs results for the Duvalo site results in 66.9 t d⁻¹ from the mapped area of ~54,550 m². This CO₂ output corresponds mainly to deep CO₂ considering that most of the area is characterised by the absence of vegetation and that a maximum contribution of biogenic CO₂ of 2.4 t d⁻¹ can be estimated assuming a biogenic CO₂ flux of 45 g m⁻² d⁻¹ (i.e. the mean CO₂ flux of population A) constant over all the area.

9.5 Duvalo in the regional context

The Balkan and the nearby Italian peninsulas, due to their intense geodynamic activity, are the sites of widespread geogenic degassing. But while Italy has been widely studied in the last decades (*Frondini et al., 2019*, and references therein), much less information is available for the Balkans. The latter is long known to be the site of countless CO₂-rich gas manifestations but relatively few have been deeply investigated to unravel the origin of the gases (*Piperov et al., 1994; Vaselli et al., 2002; Marinkovic et al., 2012; Italiano et al., 2017*). From this point of view, the most studied part is probably Greece, the southern end of the Balkan Peninsula (*Daskalopoulou et al., 2018; 2019*). Even less studies tried to quantify the CO₂ output of these sites (*Nisi et al., 2013; Kis et al., 2017*) with the exception of those in Greece, which were recently reviewed by *Daskalopoulou et al. (2019)*. The studied degassing systems in Greece are almost all connected to recent (Quaternary) or active volcanic activity. The output obtained for the non-volcanic Duvalo site is comparable to the estimated CO₂ outputs of the active volcanic systems of the Aegean arc, ranging from 2.6 t d⁻¹ at Methana (*D'Alessandro et al., 2008*) to 92 t d⁻¹ at Nisyros (*Bini et al., 2019*). Non-volcanic degassing has been ascertained also in Greece but until now only that of the Sperchios Basin area has been estimated in about 27 t d⁻¹ (*D'Alessandro et al., 2020*). The area of Florina, although still not measured, has probably an even higher total CO₂ output. Clue of this is the fact that the Air Liquide Greece Company extracts daily about 80 t CO₂ from deep wells without apparently affecting the output of the numerous gas manifestations of the area (*Pearce et al., 2004*). Furthermore, the anomalous degassing area of Florina extends beyond the border with North

Macedonia into the Bitola Plain where other companies exploit the CO₂ accumulation in the subsoil (*Mirčovski et al., 2015*).

In Italy many non-volcanic gas manifestations are present and most have been studied both to define the origin of the emitted gases and to quantify their CO₂ output (e.g. *Chiodini et al., 1999; Rogie et al., 2000; Chiodini et al., 2011, 2020; Minissale et al., 1997; Frondini et al., 2008; 2012*).

Many of them have higher CO₂ outputs (e.g. *Chiodini et al 2011, 2020*) with respect to Duvalo, sometimes up to more than one order of magnitude (e.g. Mefite D’Ansanto 2000 t d⁻¹; *Chiodini et al., 2010*). But in both cases, for the Italian sites and for the Greek ones, a direct or indirect connection to the mantle is always hypothesized. In the case of Central Italy helium isotope compositions ranges from values around 2 R/R_A to about 0.02 R/R_A. The highest ³He/⁴He ratios resemble the values measured in the olivine and pyroxenes of the Tuscan–Latium volcanic products (*Martelli et al., 2004*), linked to subduction-related carbon-rich mantle (e.g. *Frezzotti et al., 2009; Martelli et al., 2004; Peccerillo, 1999*), and the lower ones are interpreted as due to variable addition of crustal ⁴He during the gas storage in crustal reservoir (e.g., *Chiodini et al., 2011*). Also in the case of Greece, ³He/⁴He up to 1.3 R/R_A point to substantial gas contributions from the mantle (*Daskalopoulou et al., 2019*).

In the case of Duvalo the contribution from the mantle seems absent or at least very low. This hypothesis has been made considering a MORB-type mantle end-member. A subcontinental lithospheric mantle (SCLM) type (*Gautheron & Moreira, 2002*) has been hypothesized for gas manifestations in two areas at the periphery of the Balkan peninsula: Slovenia (*Bräuer et al., 2016*) and the South Aegean Active Volcanic Arc – SAAVA (*Shimizu et al., 2005*). Nevertheless, these hypotheses have not been confirmed by data on fluid inclusions in mantle minerals and in the second case they have been challenged by recent data from Kolumbo volcano whose gas emissions have He and C isotopic compositions compatible with a MORB-type mantle (*Rizzo et al., 2016*).

Furthermore, widespread mantle metasomatism by fluids released by the subducting slab in the central Mediterranean region has been hypothesized from isotopic composition of gas

manifestations (*Parello et al., 2000; Frondini et al., 2019; Chiodini et al., 2011*), mantle xenoliths' fluid inclusions (*Martelli et al., 2004*) and petrological and geophysical data (*Frezzotti et al., 2009*). One of the best studied systems is the island of Stromboli where fluid inclusions in minerals of mantle xenoliths allowed to define the mantle end-member for both He (*Martelli et al., 2014*) and C (*Gennaro et al., 2017*) isotopes. Even stronger metasomatism has been hypothesized in the Roman Magmatic Province (central Italy) from He isotopic composition (0.44 – 1.73 R/R_A, *Martelli et al. 2004*) measured in fluid inclusions trapped within olivine and pyroxene phenocrysts associated with mantle-derived basic lavas and pyroclastic rocks.

Some evidence of a metasomatised mantle beneath the southern Balkan Peninsula may come from the R/R_A values measured in gas manifestations never exceeding 1.6 in North Macedonia (*Temovski et al., 2020*), 1.3 in continental Greece (*Daskalopoulou et al., 2018*) and 0.8 in Bulgaria (*Piperov et al., 1994*). Furthermore, mantle metasomatism by subducting material was also invoked by *Yanev et al. (2008)* in their petrographic study of the Miocene to Pleistocene volcanic rocks of North Macedonia. Finally, *Molnar et al. (2021)*, analysing fluid inclusions in olivine phenocrysts from the Mlado Nagoricane volcanic center (N. Macedonia), measured R/R_A values in the range of 3.1 - 4.5. These results are well below MORB or SCLM values and may also suggest a metasomatic process within the mantle below Northern Macedonia.

As seen from central Italy, a strongly metasomatised mantle would have He and C-isotopic values very different from a MORB-type mantle leading to a severe underestimation of the mantle contribution in the sampled gases. However, even considering a case like central Italy, the mantle contribution at Duvalo would be still low (< 10 %). Nevertheless, should the low or absent contribution from mantle degassing be confirmed by future studies, this would make Duvalo a very peculiar system: A relatively shallow source within the crust able to sustain fluxes higher than 1,000 t km⁻² d⁻¹.

9.6 Conclusions

The area of Ohrid is a seismically active extensional basin and the site of Duvalo corresponds to an active fault system. Duvalo area is a natural phenomenon of intense soil degassing considered as a volcanic solfatare in the local geological literature, although volcanic rocks or volcanic activity has not been found in the area.

Based on isotope composition of gas manifestations, we propose a tectonic origin of the phenomena. Isotope composition of helium and $\delta^{13}\text{C}_{\text{CO}_2}$ indicate an almost pure crustal (marine limestone) origin of exhalation, whereas mantle contribution seems absent or at least trivial (about 1 %).

The presence of H₂S could be explained by thermochemical sulfate reduction (TSR), that is compatible with the isotope composition of methane that fall within the thermogenic range. Due to the strong displacement of the tectonic structures of the area, the sulfate-bearing strata may have been put in contact with the organic-rich shales of metamorphic basement by the fault system along the eastern part of the Ohrid graben. Part of the uprising H₂S is oxidized by oxygen-charged meteoric waters in the shallower part of the system and the produced sulfuric acid reacts with carbonate rocks producing abundant CO₂ with the isotope composition measured at Duvalo.

A map of CO₂ flux shows that the most anomalous degassing areas are aligned along a NNW-SSE direction following the main tectonic lineament direction of the area. The total amount of released CO₂ for the non-volcanic Duvalo site is estimated at 66.9 t d⁻¹. The CO₂ output obtained is comparable to, albeit slightly less than the volcanic and non-volcanic systems of Greece and Italy. Nevertheless, the peculiarity of the Duvalo system lies in its ability to sustain high CO₂ fluxes ($> 1,000 \text{ t km}^{-2} \text{ d}^{-1}$) with a relatively shallow crustal source.

References

- Abascal E., Gòmez-Coma L., Ortiz I., Ortiz A. (2023). *Global diagnosis of nitrate pollution in groundwater and review of removal technologies*. Sci. Total Environ. 810, 152233.
- Aiuppa A., Fischer T.P., Plank T., Bani P. (2019). *CO₂ flux emissions from the Earth's most actively degassing volcanoes, 2005-2015*. Scientific Reports, 9:5442.
- Aiuppa A., Fischer T.P., Plank T., Robidoux P., Di Napoli R. (2017). *Along-arc, inter-arc and arc-to-arc variations in volcanic gas CO₂/ST ratios reveal dual source of carbon in arc volcanism*. Earth-Science Reviews, 168, 24-47.
- Alcalà F.J., Custodio E. *Using the Cl/Br ratio as a tracer to identify the origin of salinity in aquifers in Spain and Portugal*. J. Hydrol. 359, 189–207 (2008).
- Alpers C.N., Jambor J.L., Nordstrom D.K. (Eds) (2000). *Sulfate Minerals – Crystallography, Geochemistry and Environment Significance*. Rev. Min. Geochem. 40, 608pp.
- APHA, AWWA, WEF, (2005). Standard methods for the examination of water and wastewater. 21st ed., American Public Health Association, Washington D.C., U.S.A.
- Apollaro C., Fuoco I., Brozzo G., De Rosa R. (2019). *Release and fate of Cr(VI) in the ophiolitic aquifers of Italy: the role of Fe(III) as a potential oxidant of Cr(III) supported by reaction path modelling*. Science of the Total Environment, 660 (2019), 1459-1471.
- Appelo C.A.J., Postma D. (1993). *Geochemistry, Groundwater and Pollution*. Balkema, Rotterdam.
- Archontelis A., Ganoulis J. (2015). *Comparison Between Hydrodynamic Simulation and Available Data in a Karst Coastal Aquifer: The Case of Almyros Spring, Crete Island, Greece*. In: Andreo, B., Carrasco, F., Durán, J., Jiménez, P., LaMoreaux, J. (eds) *Hydrogeological and Environmental Investigations in Karst Systems*. Environmental Earth Sciences, vol 1. Springer, Berlin, Heidelberg. https://doi.org/10.1007/978-3-642-17435-3_34
- Arsovski M., Hadžievsky, D. (1970). *Correlation between neotectonics and the seismicity of Macedonia*. Tectonophys. 9, 129-142.
- Arsovski M., Petkovski R. (1975). *Neotectonics of SR Macedonia*. Publication no. 49. IZZIIS, Skopje (*in Macedonian*).
- Arsovski M. (1997). *Tectonic of Macedonia*. Faculty of Geology and Mining. Stip 306 pp. (*in Macedonian*).
- ATSDR (2004). *Toxicological profile for Strontium*. Agency for Toxic Substances and Disease Registry Atlanta, GA: U.S. Department of Health and Human Services, Public Health Service.
- Badouna I., Neokosmidis S., Stamatakis M., Karkalis C., Koukouzas N., Koutsovitis P. (2021). *Mineralogical and Geochemical Properties of Greek Evaporites, Associated with Their Prospects of Industrial Use*. Mater. Proc., 5, 3. <https://doi.org/10.3390/materproc2021005003>
- Bakalowicz M. (1992). *Geochimie des eaux et flux de matières dissoutes. L'approche objective du rôle du climat dans la karstogénèse. Karst et évolutions climatiques*. Hommage à Jean Nicod. Presses Universitaires de Bordeaux, Talence, pp 61–74. (*in French*)
- Bakalowicz M. (2005). *Karst groundwater: a challenge for new resources*. Hydrogeology Journal 13:148-160.
- Bakalowicz M. (2015). *Karst and karst groundwater resources in the Mediterranean*. Environmental Earth Science, 74, 5-14.
- Ballentine C.J., Schoell M., Coleman D., Cain B. (2001). *300-Myr-old magmatic CO₂ in natural gas reservoirs of the west Texas Permian basin*. Nature, 409, 327-331.
- Ballentine C.J. & Burnard P. (2002). *Production, release and transport of noble gases in the continental crust*. Reviews in Mineralogy and Geochemistry, 47(1), 481-538.

- Barnes I., Irwin W.P., White D.E. (1978). *Global Distribution of Carbon Dioxide Discharges and Major Zones of Seismicity*. US Geological Survey, Water Resources Division.
- Bega Z., Soto J.I. (2017). *The Ionian fold-and-thrust belt in Central and Southern Albania: A petroleum province with Triassic evaporites*. In: Soto J.I., Flinch J.F., Tari G.(Eds.). Permo-Triassic Salt Province of Europe, North Africa and the Atlantic Margin. Tectonics and Hydrocarbon Potential. Elsevier, pp. 517-539.
- Bernard B., Brooks J.M., Sackett W.M. (1977). *A geochemical model for characterization of hydrocarbon gas sources in marine sediments*. Offshore Technology Conference, OTC-2934-MS.
- Berner R.A., Lasaga A.C. (1989). *Modelling the geochemical carbon cycle*. Scientific American, 260, 74-81.
- Bini G., Chiodini G., Cardellini C., Vougioukalakis G.E., Bachmann O. (2019). *Diffuse emission of CO₂ and convective heat release at Nisyros caldera (Greece)*. J. Volcanol. Geotherm. Res. 376, 44–53.
- Blundell D., Freeman R., Mueller S. (eds) (1992). *A continent revealed – the European geotraverse*. European Science Foundation. Cambridge University Press, Cambridge.
- Bojadjieva J., Sheshov V., Edip K., Chaneva J., Kitanovski T., Ivanovski D. (2019). *GIS-based assessment of liquefaction potential for selected earthquake scenarios*. In: Silvestri F., Moraci N. (eds). Earthquake Geotechnical Engineering for Protection and Development of Environment and Constructions. Proceedings in Earth and geosciences, vol. 4, 1453-1460.
- Bortolotti V., Marroni M., Pandolfi L., Principi G. (2005). *Mesozoic to Tertiary tectonic history of the Mirdita ophiolites, northern Albania*. The Island Arc, 14(4), 471–493. <https://doi.org/10.1111/j.1440-1738.2005.00479>
- Brantley S.L., Koepenick K.W. (1995). *Measured carbon dioxide emissions from Oldoinyo Lengai and the skewed distribution of passive volcanic fluxes*. Geology, 23, 933-936. [https://doi.org/10.1130/0091-7613\(1995\)023<0933:MCDEFO>2.3.CO;2](https://doi.org/10.1130/0091-7613(1995)023<0933:MCDEFO>2.3.CO;2)
- Bräuer K., Geissler W.H., Kämpf H., Niedermannn S., Rman N. (2016). *Helium and carbon isotope signatures of gas exhalations in the westernmost part of the Pannonian Basin (SE Austria/NE Slovenia): Evidence for active lithospheric mantle degassing*. Chem. Geol. 422, 60–70.
- Brune S., Williams S., Müller D. (2017). *Potential links between continental rifting, CO₂ degassing and climate change through time*. Nature Geoscience, 10, 941-947. <https://doi.org/10.1038/s41561-017-0003-6>
- Burchfiel B.C., Todosov A., King R.W., Kotzev V., Dumurdjanov N., Sarafinovski T., Nurce B. (2006). *GPS results for Macedonia and its importance for the tectonics of the Southern Balkan extensional regime*. Tectonophysics, 413:239-248.
- Burchfiel B.C., Nakov R., Dumurdžanov N., Papanikolaou D., Tzankov T., Serafimovski T., King R.W., Kotzev V., Todosov A., Nurce B. (2008). *Evolution and dynamics of the Cenozoic tectonics of the South Balkan extensional system*. Geosphere 4, 919–938.
- Burton M.R., Sawyer G.M., Granieri D. (2013). *Deep carbon emissions from volcanoes*. In R.M.Hazen, A.P. Jones & J.A. Baross (Eds.). Carbon in Earth. Reviews in mineralogy and Geochemistry (Vol. 75, pp. 323-354) <http://doi.org/10.2138/rmg.2013.75.11>
- Capasso G., Inguaggiato S. (1998). *A simple method for the determination of dissolved gases in natural waters. An application to thermal waters from Vulcano Island*. Appl. Geochem., 13, 631-642.
- Capasso G., Favara R., Grassa F., Inguaggiato S., Longo M. (2005). *On-line technique for preparation and measuring stable carbon isotope of total dissolved inorganic carbon in water samples ($\delta^{13}\text{C}_{\text{TDIC}}$)*. Ann. Geophys. 48, 159-166.
- Caracausi A., Sulli A. (2019). Outgassing of mantle volatiles in compressional tectonic regime awayfrom volcanism: The role of continental delamination. *Geochemistry, Geophysics, Geosystems*, 20, 2007–2020. <https://doi.org/10.1029/2018GC008046>
- Caracausi A., Buttita D., Picozzi M., Paternoster M., Stabile T.A. (2022). *Earthquakes control the impulsive nature of*

- crustal helium degassing to the atmosphere.* Nature Communications, Earth & Environment, 3:224. <https://doi.org/10.1038/s43247-022-00549-9>
- Cardellini C., Chiodini G., Frondini F. (2003). *Application of stochastic simulation to CO₂ flux from soil: Mapping and quantification of gas release.* J. Geophys. Res., 108, 2425. <https://doi.org/10.1029/2002JB002165>
- Cardellini C., Chiodini G., Frondini F., Avino R., Bagnato E., Caliro S., Lelli M., Rosiello A. (2017). *Monitoring diffuse volcanic degassing during volcanic unrest: the case of Campi Flegrei (Italy).* Scientific Report, 7, 6757.
- Chiodini G., Frondini F., Marini L. (1995). *Theoretical geothermometers and P_{CO₂} indicators for aqueous solutions coming from hydrothermal systems of medium-low temperature hosted in carbonate-evaporite rocks. Applications to the thermal springs of the Etruscan Swell, Italy.* Appl. Geochem. 10, 337-346.
- Chiodini G., Cioni R., Guidi M., Raco B., Marini L. (1998). *Soil CO₂ flux measurements in volcanic and geothermal areas.* App. Geochem., 13, 543–552. [https://doi.org/10.1016/S0883-2927\(97\)00076-0](https://doi.org/10.1016/S0883-2927(97)00076-0)
- Chiodini G., Frondini F., Kerrick D.M., Rogie J., Parello F., Peruzzi L., Zanzari A. R. (1999). *Quantification of deep CO₂ fluxes from central Italy: Examples of carbon balance for regional aquifers and soil degassing.* Chem. Geol., 159, 205–222. [https://doi.org/10.1016/S0009-2541\(99\)00030-3](https://doi.org/10.1016/S0009-2541(99)00030-3)
- Chiodini G., Frontini F., Cardellini C., Parello F., Peruzzi L. (2000). *Rate of diffuse carbon dioxide Earth degassing estimated from carbon balance of regional aquifers: The case of central Apennine, Italy.* J. Geophys. Res., 105(B4), 8423–8434. <https://doi.org/10.1029/1999JB900355>
- Chiodini G., Cardellini C., Amato A., Boschi E., Caliro S., Frondini F., Ventura G. (2004). *Carbon dioxide Earth degassing and seismogenesis in central and southern Italy.* Geophysical Research Letters, 31, L07615.
- Chiodini G., Caliro S., Cardellini C., Avino R., Granieri D., Schmidt A. (2008). *Carbon isotopic composition of soil CO₂ efflux, a powerful method to discriminate different sources feeding soil CO₂ degassing in volcanic-hydrothermal areas.* Earth Planet. Sci. Lett., 274, (3–4), 372–379, <https://doi.org/10.1016/j.epsl.2008.07.051>
- Chiodini G., Granieri D., Avino R., Caliro S., Costa A., Minopoli C., Vilardo G. (2010). *Nonvolcanic CO₂ Earth degassing: case of Mefite d'Ansanto (southern Apennines), Italy.* Geophys. Res. Lett. 37, L11303.
- Chiodini G., Caliro S., Cardellini C., Frondini F., Inguaggiato S., Matteucci F. (2011). *Geochemical evidence for and characterization of CO₂ rich gas sources in the epicentral area of the Abruzzo 2009 earthquakes.* Earth and Planetary Science Letters, 274, 372-379. <https://doi.org/10.1016/j.epsl.2011.02.2016>
- Chiodini G., Cardellini C., Di Luccio F., Selva J., Frondini F., Caliro S., Rosiello A., Beddini G., Ventura G. (2020). *Correlation between tectonic CO₂ Earth degassing and seismicity is revealed by a 10-year record in the Apennines, Italy.* Science Advances, 6, eabc2938. <https://doi.org/10.1126/sciadv.abc2938>
- Christodoulou T., Leontiadis I.L., Morfis A., Payne B.R., Tzimourtas S. (1993). *Isotope hydrology study of the Axios River plain in northern Greece.* J. Hydrol. 146, 391-404.
- Chung H.M., Gormly J.R., Squires, R.M. (1988). *Origin of gaseous hydrocarbons in subsurface environments: theoretical considerations of carbon isotope distribution.* Chemical Geology, 71, 97–104.
- Cita M.B., Ryan W.B.F. (1978). *Messinian erosional surfaces in the Mediterranean.* Mar. Geol. 27, 193–366.
- Council Directive 2020/2184/EC of 16 December 2020 on the quality of water intended for human consumption. Official Journal of the European Union, L 435, 23.12.2020, p. 1–62.
- Council Directive 98/83/EC of 3 November 1998 on the quality of water intended for human consumption. Official Journal of the European Union, L 330, 5.12.1998, p. 32.
- Cvetkovic V., Prelevic D., Schmid S. (2016). *Geology of South-Eastern Europe.* In: Papic P. (eds). Mineral and Thermal Waters of Southeastern Europe. Environmental Earth Science, Springer https://doi.org/10.1007/978-3-319-25379-4_1

- D'Alessandro W., Brusca L., Kyriakopoulos K., Michas G., Papadakis G. (2008). *Methana, the westernmost active volcanic system of the south Aegean arc (Greece): insight from fluids geochemistry*. J. Volcanol. Geotherm. Res. 178, 818–828.
- D'Alessandro W., Bellomo S., Brusca L., Karakazanis S., Kyriakopoulos K., Liotta M. (2011). *The impact on water quality of the high carbon dioxide contents of the groundwater in the area of Florina (N. Greece)*. In: Lambrakis N., Stournaras G., Katsanou K. (Eds.), *Advances in the Research of Aquatic Environment*, vol.2 Springer, Berlin, Germany, pp. 135-143.
- D'Alessandro W., Kyriakopoulos K. (2013). *Preliminary Gas Hazard evaluation in Greece*. Natural Hazards 69, 1987-2004, doi: 10.1007/s11069-013-0789-5.
- D'Alessandro, W., et al. (2017). *The impact of natural and anthropogenic factors on groundwater quality in an active volcanic/geothermal system under semi-arid climatic conditions: the case study of Methana peninsula (Greece)*. J. Geochem. Explor. 175, 110–119 (2017). <https://doi.org/10.1016/j.gexplo.2017.01.003>
- D'Alessandro W., Li Vigni L., Gagliano A.L., Calabrese S., Kyriakopoulos K., Daskalopoulou K. (2020). *CO₂ release to the atmosphere from thermal springs of Sperchios Basin and northern Euboea (Greece). The contribution of "hidden" degassing*. Applied Geochemistry, 119, 104660 <https://doi.org/10.1016/j.apgeochem.2020.104660>
- Das K.J., Chandramouli Reddy R., Bagoji I.B., Das S., Bagali S., Mullur L., Khodnapur J.P., Biradar M.S. (2019). *Primary concept of nickel toxicity – an overview*. J Basic Clinic Physiol Pharmacol 30(2):141-152 <https://doi.org/10.1515/jbcpp-2017-0171>
- Daskalaki P., Voudouris K. (2008). *Groundwater quality of porous aquifers in Greece: a synoptic review*. Environ Geol, 54:505-513.
- Daskalopoulou K., Calabrese S., Grassa F., Kyriakopoulos K., Parello F., Tassi F., D'Alessandro W. (2018). *Origin of methane and light hydrocarbons in natural fluid emissions: a key study from Greece*. Chem. Geol. 479, 286-301.
- Daskalopoulou K., Calabrese S., Gagliano A.L., D'Alessandro W. (2019a). *Estimation of the geogenic carbon degassing of Greece*. Applied Geochemistry, 106, 60-74.
- Daskalopoulou K., D'Alessandro W., Calabrese S., Cardellini C., Gagliano A.L., Ionescu A., Karakatsanis S., Kyriakopoulos K., Li Vigni L., Pop C. (2019b). *Gas Geochemistry and Fractionation Processes in Florina Basin, Greece*. Geophysical Research Abstracts, ISSN 1607 – 7962, Vol. 21, EGU2019-8824.
- David M. (1977). *Geostatistical ore reserve estimation* (p. 364). Developments in Geomathematics 2. Elsevier.
- Davis S.N., Whittemore D.O., Fabryka-Martin J.. (1998). *Uses of Chloride/Bromide ratios in studies of potable water*. Groundwater 36, 338-350 (1998). <https://doi.org/10.1111/j.1745-6584.1998.tb01099.x>
- De Vos W, et al., (2006). *Geochemical Atlas of Europe. Part 2 - Interpretation of Geochemical Maps, Additional Tables, Figures, Maps, and Related Publications*. Geological Survey of Finland, ISBN: 951-690-960-4
- Deines P., Langmuir D., Harmon R.S. (1974). *Stable carbon isotope ratios and the existence of a gas phase in the evolution of carbonate ground waters*. Geochim. Cosmochim. Acta, 38, 1147-1164.
- Dermatas, D., Mpouras, T., Chrysochoou, M., Panagiotakis, I., Vatseris, C., Linardos, N., Theologou, E., Boboti, N., Xenidis, A., Papassiopi, N., Sakellariou, L. (2015). *Origin and concentration profile of chromium in a Greek aquifer*. J. Hazard Mater 281, 35-46.
- Deutsch C. V., Journel A.G. (1998). *Gslib: Geostatistical software library and user's guide* (2nd ed.). Oxford University Press.
- Diamantopoulou P. (1999). *Hydrogeological conditions of the island of Zakynthos, Ionian Sea*. Ph.D Thesis., Department of Geology, University of Patra, Greece, p.160 (*in Greek*).
- DISS Working Group (2021). *Database of Individual Seismogenic Sources (DISS), Version 3.3.0: A compilation of potential sources for earthquakes larger than M 5.5 in Italy and surrounding areas*. Istituto Nazionale di Geofisica e

- Vulcanologia (INGV). <https://doi.org/10.13127/diss3.3.0>
- Dokou, Z., Kourgialas, N.N. & Karatzas, G.P. (2015). *Assessing groundwater quality in Greece based on spatial and temporal analysis*. Environ Monit Assess 187, 774, <https://doi.org/10.1007/s10661-015-4998-0>
- Dragasevic T. (1974). *Savremena gradja Zemljine kore i gornjeg omotaca na području Jugoslavije*. Report RGF, Beograd, 31pp. (*in Serbian*).
- Drever J.I. (1997). *The Geochemistry of Natural Waters: Surface and Groundwater Environments*. Prentice Hall, Inc, New Jersey . 436 pp.
- Dreybrodt W. (2000). *Equilibrium chemistry of karst waters in limestone terranes*. In: Klimchouk A., Ford D.C., Palmer A.N., Dreybrodt W. (eds) Speleogenesis, evolution of karst aquifers. National Speleological Society Inc., Huntsville, pp. 126-135.
- Du J., Cheng W., Zhang Y., Jian C., Guan Z. (2006). *Helium and Carbon isotopic compositions of thermal springs in earthquake zone of Sichuan, Southwestern China*. J. Asian Earth Sci. 26, 533-539.
- Dumurdjanov N., Ivanovski T. (1978). *Map and explanatory notes of the basic geological map 1:100000 (map sheets Ohrid and Pogradec) of the Socialist Federal Republic of Yugoslavia*. Federal Geological Survey, Belgrad, 51.
- Dumurdjanov N., Serafinovski T., Burchfiel C.B. (2004). *Evolution of the Neogene-Pleistocene basins of Macedonia*. Geological Society of America, DMC001, p.1-XX.
- Dumurdjanov N., Serafinovski T., Burchfiel C.B. (2005). *Cenozoic tectonics of Macedonia and its relation to the South Balkan extensional regime*. Geosphere 1:1-22. <https://doi.org/10.1130/GES00006.1>
- Dumurdjanov N., Milutinovic Z., Salis R. (2016). *Seismotectonic zones and seismic hazard in the Republic of Macedonia*. In: Lepitkova S., Boev, B. (Eds.), Proceedings of the Third Congress of Geologists of Republic of Macedonia, Geologica Macedonica, Special edition 4, Vol. 1, 477-491.
- Dumurdjanov N., Milutinovic Z., Salic R. (2020). *Seismotectonic model backing the PSHA and seismic zoning of Republic of Macedonia for National Annex to MKS EN 1998-1:2012 Eurocode 8*. J. Seismol. 24:319-341.
- Economou-Eliopoulos M., Megremi I., Vasilatos Ch., Frei R., Mpourodimos I. (2017) *Geochemical constraints on the sources of Cr(VI) contamination in waters of Messapia (Central Evia) Basin*. Applied Geochemistry 84, 13-25.
- Etiope G., Christodoulou D., Kordella S., Marinaro G., Papatheodorou G. (2013). *Offshore and onshore seepage of thermogenic gas at Katakolon Bay (Greece)*. Chem. Geol. 347, 115-126.
- Etiope G., Sherwood Lollar B., (2013). *Abiotic methane on Earth*. Reviews of Geophysics 51, 276–299.
- Etiope G. & Schoell M. (2014). Abiotic gas: atypical but non rare. Elements, 10, 291-296.
- Etiope G., Samardzic N., Grassa F., Hrvatovic H., Miošić N., Skopljak F., (2017). *Methane and hydrogen in hyperalkaline groundwaters of the serpentinized Dinaride ophiolite belt, Bosnia and Herzegovina*. Applied Geochemistry 84, 286–296.
- Faulker D.R., Jackson C.A.L., Lunn R.J., Schlische R.W., Shipton Z.K., Wibberley C.A.J., Withjack M.O. (2010). *A review of recent developments concerning the structure, mechanics and fluid flow properties of fault zones*. J. Struct. Geol., 32, 1557-1575. <https://doi.org/10.1016/j.jsg.2010.06.009>
- Fetter C.W., (2001). *Applied HydroGeology*, 4th edition. Prentice Hall, Inc., Upper Saddle River, NJ, USA.
- Fischer T.P., Arellano S., Carn S., Aiuppa A., Galle B., Allard P., Lopez T., Shinohara H., Kelly P., Werner C., Cardellini C., Chiodini G. (2019). *The emissions of CO₂ and other volatiles from the world's subaerial volcanoes*. Scientific Reports, 9:18716.
- Fitzmaurice A.G., Bilgin A.A.; O'Day P.A., Illera V., Burris D.R., Reisinger H.J., Hering J.G. (2009). Geochemical and hydrologic controls on the mobilization of arsenic derived from herbicide application. Applied Geochemistry, vol.

- 24, 11, pp. 2152-2162.
- Fleury P., Bakalowicz M., de Marsily G. (2007). *Submarine springs and coastal karst aquifers: a review*. J Hydrol 339:79–92.
- Ford D.C., Williams P.W. (1989). *Karst Geomorphology and Hydrology*. Unwin Hyman London (601 pp.).
- Ford D.C., Williams P.W., (2007). *Karst Hydrogeology and Geomorphology*. Wiley, Chichester.
- Foster G., Royer D., Lunt D. (2017). *Future climate forcing potentially without precedent in the last 420 million years*. Nat. Commun. 8, 14845.
- Frashëri A., Nishani P., Bushati S., Hyseni A. (1996). *Relationship between tectonic zone of the Albanides, based on results of geophysical studies*. In: Ziegler, P.A., Horwath, F. (Eds.), Peri-Tethys Memoir 2: Structure and Prospects of Alpine Basins and Forelands. Mem. Musée Hist. Nat., Paris 170, 485–511.
- Frashëri A. & Čermak V., (2004). *The geothermal atlas of Albania*. Sh. B. L. U. Tirana. 65-89.
- Frezzotti M.L., Peccerillo A., Panza G. (2009). *Carbonate metasomatism and CO₂ lithosphere–asthenosphere degassing beneath the Western Mediterranean: an integrated model arising from petrological and geophysical data*. Chem. Geol. 262, 108–120.
- Frondini F., Caliro S., Cardellini C., Chiodini G., Morgantini N., Parella F. (2008). *Carbon dioxide degassing from Tuscany and Northern Latium (Italy)*. Global and Planetary Change, 61, 89–102, <https://doi.org/10.1016/j.gloplacha.2007.08.009>
- Frondini F., Cardellini C., Caliro S., Chiodini G., Morgantini N. (2012). *Regional groundwater flow and interactions with deep fluids in western Apennine: the case of Narni-Amelia chain (Central Italy)*. Geofluids, 12, 182–196.
- Frondini F., Cardellini C., Caliro S., Beddini G., Rosiello A., Chiodini G. (2019). *Measuring and interpreting CO₂ fluxes at regional scale: The case of the Apennines, Italy*. J. Geol. Soc., 176, 408–416. <https://doi.org/10.1144/jgs2017-169>
- Fytikas M., Kolios N. (1979). *Preliminary heat flow map of Greece*. In: Čermak V., Rybach L. (Eds.), Terrestrial Heat Flow in Europe. Springer-Verlag, Berlin Heidelberg, New York, pp. 197-205.
- Gamaletsos P., Godelitsas A., Dotsik, E., Tzamos E., Göttlicher J., Filippidis A. (2013). *Geological sources of As in the environment of Greece: A review*. In: Threats to the Quality of Groundwater Resources: Prevention and Control; Scozzari, A., Dotsika, E., Eds.; Hdb. Env. Chem. 40, 77–113.
- Gautheron C., Moreira M. (2002). *Helium signature of the subcontinental lithospheric mantle*. Earth and Planetary Science Letters, 199(1-2), 39-47.
- Gemeni V., Vasilatos C., Koukouzas N., Kanellopoulos C. (2015). *Geochemical consequences in shallow aquifers from the long-term presence of CO₂ in a natural field: The case of Florina Basin, W. Macedonia, Greece*. Greenhouse Gases: Science and Technology, vol. 6(4), 450-469.
- Gennaro M.E., Grassa F., Martelli M., Renzulli A., Rizzo A.L. (2017). *Carbon isotope composition of CO₂-rich inclusions in cumulate-forming mantle minerals from Stromboli volcano (Italy)*. J. Volcanol. Geotherm. Res. 346, 95–103.
- Giggenbach W.F., Gonfiantini R., Jangi B.L., Truesdell A.H. (1983). *Isotopic and chemical composition of Parbaty Valley geothermal discharges, NW-Himalaya*. Geothermics, 12, 199–222.
- Goldscheider N., Drew D. (2007). *Methods in Karst Hydrogeology*. Taylor & Francis, London.
- Gorgieva M. (1989). *Chemical geothermometers and mineral equilibria of some hot waters in Yugoslavia*. Report UNU Geothermal Training Programme, Reykjavik, 61pp.
- Gorgieva M. (1999). *Summary of fundamentals for evaluation of the geothermal potential of the Vardar zone and Serbo-*

- Macedonian mass in the territory of the Republic of Macedonia.* Macedonian/U.S.A. scientific project: Evaluation of reserves and technical feasibility of geothermal energy in Macedonia, Skopje, pp. 63-110.
- Gorgieva M., Gorgiev D., Popovski K., Dimitov K., Manasov S. (2000). *Inferred section of the main (low-temperature) geothermal systems in the Republic of Macedonia.* Proceedings World Geothermal Congress 2000, Kyushu – Tohoku, Japan, May 28 – June 10, 2000.
- Gutsalo L.K., Plotnikov A.M. (1981). *Carbon isotopic composition in the CH₄-CO₂ system as a criterion for the origin of methane and carbon dioxide in Earth natural gases.* Doklady Akademii Nauk SSSR 259, 470–473. (in Russian)
- Hanson, B.R., Grattan, S.R., Fulton, A. Agricultural salinity and drainage. Division of Agriculture and Natural Resources Publication 3375, University of California Irrigation Program. University of California, Davis, U.S.A., p. 164 (2006).
- Hoegh-Guldberg O.D. et al. (2018). *Impacts of 1.5°C Global Warming on Natural and Human Systems.* In: Global Warming of 1.5°C. An IPCC Special Report on the impacts of global warming of 1.5°C above pre-industrial levels and related global greenhouse gas emission pathways, in the context of strengthening the global response to the threat of climate change, sustainable development, and efforts to eradicate poverty [Masson-Delmotte, V., P. Zhai, H.-O. Pörtner, D. Roberts, J. Skea, P.R. Shukla, A. Pirani, W. Moufouma-Okia, C. Péan, R. Pidcock, S. Connors, J.B.R. Matthews, Y. Chen, X. Zhou, M.I. Gomis, E. Lonnoy, T. Maycock, M. Tignor, and T. Waterfield (eds.)].
- Hoffmann N., Reicherter K., Fernández-Steeger T., Grützner C. (2010). *Evolution of ancient Lake Ohrid: a tectonic perspective.* Biogeosciences 7, 3377-3386.
- Holland G., Gilfillan S. (2013). *Application of noble gases to the viability of CO₂ storage.* In P. Burnard (Ed.), The noble gases as geochemical tracers. Advances in isotope geochemistry (pp. 177-223), Springer.
- Hunt J.A., Zafu A., Mather T.A., Pyle D.M., Barry P.H. (2017). *Spatially variable CO₂ degassing in the main Ethiopian rift: Implications for magma storage, volatile transport, and rift-related emissions.* Geochemistry, Geophysics, Geosystems, 18, 3714-3737 <https://doi.org/10.1002/2017GC006975>
- Inguaggiato S., Rizzo A. (2004). *Dissolved helium isotope ratios in ground-waters: a new technique based on gas–water re-equilibration and its application to Stromboli volcanic system.* App. Geochem. 19, 5, 665-673. <https://doi.org/10.1016/j.apgeochem.2003.10.009>
- Irwin W.P., Barnes I. (1980). *Tectonic relations of carbon dioxide discharges and earthquakes.* Journal of Geophysical Research 85, 3115-3121.
- Italiano F., Kis B.M., Baciu C., Ionescu A., Harangi S., Palcsu L. (2017). *Geochemistry of dissolved gases from the Eastern Carpathians - Transylvanian Basin boundary.* Chem. Geol. 469, 117–128
- Ivanov D.A., Slavomira E. (2002). *Preliminary palynological data on Neogene flora from Bitola Basin (F.Y.R.O.M.).* Comptes rendus de l'Academie bulgare des Sciences, vol. 55(4), 81-86
- Jančev S., Pezdič J., Szaran J., Halas S. (1999). *Characteristics of sulphate occurrences near Kosovrasti, Macedonia.* RMZ 46(3), 501–508.
- Jancevski J. (1987). *Classification of fault structures according to genesis, age and morphology, with review to their seismicity on the territory of Macedonia.* Institute of Earthquake Engineering and Engineering Seismology (UKIM-IZIIS), Ss. Cyril and Methodius University in Skopje. Doctoral dissertation. Skopje, R. Macedonia, 247 p. (in Macedonian)
- Jenden P.D., Hilton D.R., Kaplan I.R., Craig H. (1993). *Abiogenic hydrocarbons and mantle helium in oil and gas fields.* In: Howell D.G. (Eds.), The future of Energy Gases: US Geol. Surv. Profes. Paper, vol. 1570, pp. 31-56
- Jiménez Cisneros B.E. et al. (2014). *Freshwater resources.* In: Climate Change 2014: Impacts, Adaptation, and Vulnerability. Part A: Global and Sectoral Aspects. Contribution of Working Group II to the Fifth Assessment Report of the Intergovernmental Panel on Climate Change [Field, C.B., V.R. Barros, D.J. Dokken, K.J. Mach, M.D. Mastrandrea, T.E. Bilir, M. Chatterjee, K.L. Ebi, Y.O. Estrada, R.C. Genova, B. Girma, E.S. Kissel, A.N. Levy, S. MacCracken, P.R. Mastrandrea, and L.L. White (eds.)]. Cambridge University Press, Cambridge, United Kingdom

- and New York, NY, USA, pp. 229-269.
- Jolivet L., Brun J.P. (2010). *Cenozoic geodynamic evolution of the Aegean*. Int. J. Earth. Sci (Geol. Rundsch), 99:109-138. <https://doi.org/10.1007/s00531-008-0366-4>
- Kakavas N.J. (1984). *Inventory of karstic springs of Greece. VI – East Central Greece*. Institute of Geological and Mining Research, Athens (1984).
- Kalhor K., Ghasemizadeh R., Rajic L., Alshawadkeh A. (2019). *Assessment of groundwater quality and remediation in karst aquifer: A review*. Groundwater for Sustainable Development vol.8, pp. 104-121.
- Kallergis G. (2001). *Applied-Environmental Hydrogeology*, 2nd eds; TEE: Athens, Greece, 2001; ISBN 978-960-7018-73-1.
- Kallergis G.A., Skayias, S.D. (1980). *Inventory of karstic springs of Greece. III – Thessaly*. Institute of Geological and Mining Research, Athens (1980).
- Kallioras A., Marinos P. (2015). *Water resources assessment and management of karst aquifer systems in Greece*. Environ Earth Sci 74:83-100.
- Kämpf H., Brauer K., Schumann J., Hahne K., Strauch G. (2013). *CO₂ discharge in an active, non-volcanic continental rift area (Czech Republic): characterization ($\delta^{13}\text{C}$, $^3\text{He}/^4\text{He}$) and quantification of diffuse and vent CO₂ emissions*. Chemical Geology, 339, 71-83.
- Kaprara E., Kazakis N., Simeonidis K., Coles S., Zouboulis A.I., Samaras P., Mitrakas M. (2015). *Occurrence of Cr(VI) in drinking water of Greece and relation to the geological background*. Journal of Hazardous Materials 281, 2-11.
- Karakatsanis S., Koukouzas N., Pagonas M., Zelilidis A. (2007). *Preliminary sedimentological results indicate a new detailed stratigraphy for the Florina sedimentary basin and relate them with CO₂ presence*. Bull. Geol. Soc. Greece 40, Proc. 11th Internat. Congr. Athens, May 2007.
- Karakitsios V. (1995). *The Influence of Preexisting Structure and Halokinesis on Organic Matter Preservation and Thrust System Evolution in the Ionian Basin, Northwest Greece*. Am. Assoc. Petrol. Geologists Bull. 79, 960-980.
- Katsanou K., Siavalas G., Lambrakis N. (2011). *The thermal and mineral springs of Aitoloakarnania Prefecture: function mechanism and origin of groundwater*. Environmental Earth Sciences 65, 2351-2364.
- Katsanou K., Lambrakis N. (2017). *Modeling the Hellenic karst catchments with the Sacramento Soil Moisture Accounting model*. Hydrogeol Journal 25, pages757–769.
- Katsanou K., Lambrakis N., D'Alessandro W., Siavalas G. (2017). *Chemical parameters as natural tracers in hydrogeology: A case study of Louros Karst System, Greece*. Hydrogeology Journal 25, 487-499.
- Katsanou K. (2018). *Hellenic Karst Aquifers Vulnerability Approach Using Factor Analysis: The Example of the Louros Karst Aquifers*. Geosciences, 8, 417.
- Katsoyiannis I.A., Mitrakas M., Zouboulis A.I. (2015). *Arsenic occurrence in Europe: Emphasis in Greece and description of the applied full-scale treatment plants*. Desalin. Water Treat. 54, 2100–2107.
- Kazakis N., Chalikakis K., Mazzilli N., Olliver C., Manakos A., Voudouris K. (2018). *Management and research strategies of karst aquifers in Greece: Literature overview and exemplification based on hydrodynamic modelling and vulnerability assessment of a strategic karst aquifer*. Science of Total Environment 643, 592-609.
- Kelepertsis A., Alexakis D., Skordas K. (2006). *Arsenic, antimony and other toxic elements in the drinking water of Eastern Thessaly in Greece and its possible effects on human health*. Environ. Geol. 50, 76–84.
- Kerrick D.M., McKibben M.A., Seward T.M., Caldeira K. (1995). *Convective hydrothermal CO₂ emission from high heat flow regions*. Chemical Geology 121, 285– 293.
- Kerrick D.M. (2001). *Present and past nonanthropogenic CO₂ degassing from the solid earth*. Reviews of Geophysics,

- 39, 565-585. <https://doi.org/10.1029/2001RG000105>
- King C.Y. (1986). *Gas geochemistry applied to earthquakes prediction: An overview*. Journal of Geophysical Research, 91, B12, 12269-12281. <https://doi.org/10.1029/JB091iB12p12269>
- Kipfer R., Aeschbach-Hertig W., Peeters F., Stute M. (2002). *Noble gases in lakes and ground waters*. Rev. Mineral. Geochem., 47, 615-700.
- Kis B.M., Ionescu A., Cardellini C., Harangi S., Baciu C., Caracausi A., Viveiros F. (2017). *Quantification of carbon dioxide emissions of Ciomadul, the youngest volcano of the Carpathian-Pannonian Region (Eastern-Central Europe, Romania)*. Journal of Volcanology and Geothermal Research, 341, 119-130. <https://doi.org/10.1016/j.jvolgeores.2017.05025>
- Kis B.M., Caracausi A., Palcsu L., Baciu C., Ionescu A., Futò I., et al. (2019). *Noble gas and carbon isotope systematics at the seemingly inactive Ciomadul volcano (Eastern-Central Europe, Romania): Evidence for volcanic degassing*. Geochemistry, Geophysics, Geosystems, 20, 3019-3043. <https://doi.org/10.1029/2018GC008153>
- Knithakis M.A. (1983). *Inventory of karstic springs of Greece. IV – Hydrological basin of Strimonas River*. Institute of Geological and Mining Research, Athens.
- Kodhelaj N., (2018). *Geothermal Energy and its use in Albania*. LAMBERT Academic Publishing.
- Kolios N., Innocenti F., Manetti P., Peccerrillo A., Giuliani O. (1980). *The Pliocene volcanism of the Voras mts (Central Macedonia, Greece)*. Bull. Volcanol., 43, 553-568.
- Kotevski G. (1987). *Hidrogeologija na mineralnite, termalnite i termomineralnите води на територијата на Социјалистичка Република Македонија (Hydrogeology of the mineral, thermal and thermomineral waters in the territory of the Socialist Republic of Macedonia)*. Samupravna praktika, Skopje, 352. (**in Macedonian**)
- Kourmoulis N.E. (1979). *Inventory of karstic springs of Greece. II – Crete*. Institute of Geological and Mining Research, Athens.
- Kourmoulis, N.E. (1984). *Inventory of karstic springs of Greece. V – Western Central Greece*. Institute of Geological and Mining Research, Athens.
- Kourmoulis, N.E. (1987). *Inventory of karstic springs of Greece. IX – Eastern Central Greece (Phocis - Boeotia)*. Institute of Geological and Mining Research, Athens.
- L'hirondel J., L'hirondel J.L. (2002). *Nitrate and man: Toxic, harmless, or beneficial?* Oxfordshire: CABI.
- Langelier W., Ludwig H. (1942). *Graphical methods for indicating the mineral character of natural waters*. JWWA, 34, 335–352.
- Le Pichon X., Sengor A.M.C., Demirbag E., Rangin C., Imren C., Armijo R., Gorur N., Cagatay N., Mercier de Lépinay M., Meyer B., Saatcilar B., Tok, B. (2001). *The active Main Marmara fault*. Earth Planet. Sci. Lett., 192, 595–616.
- Lee C.A., Jiang H., Dasgupta R., Torres M., (2019). *A Framework for Understanding Whole-Earth Carbon Cycling*. In: Orcutt B., Daniel I., Dasgupta R. (eds), Deep Carbon: Past to Present. Cambridge University Press, pp. 313-357.
- Leontiadis I.L., Nikolaou E. (1999). *Environmental isotopes in determining groundwater flow systems, northern part of Epirus, Greece*. Hydrogeol. J. 7, 219-226.
- Leontiadis I.L., Smyrniotis C.H., Nikolaou E., Georgiadis P. (1997). *Isotope hydrology study of the major areas of Paramythia and Koroni, Epirus, Greece*. In: Karst Waters and Environmental Impacts (Günay and Johnson Eds.), Balkema, Rotterdam.
- Lewicki J., Brantley S.L. (2000). *CO₂ degassing along the San Andreas Fault, Parkfield, California*. Geophys. Res. Lett. 27(1), 5-8
- Lewicki J.L., Bergfeld D., Cardellini C., Chiodini G., Granieri D., Varley N., Werner C. (2005). *Comparative soil CO₂*

- flux measurements and geostatistical estimation methods on Masaya volcano, Nicaragua.* Bull. Volcan., 68, 76–90. <https://doi.org/10.1007/s00445-005-0423-9>
- Li Vigni L., Daskalopoulou K., Calabrese S., Parello F., D'Alessandro W. (2021). *Geochemical characterization of the alkaline and hyperalkaline groundwater in the Othrys Ophiolite Massif, central Greece.* Italian Journal of Geosciences, 140, 42–56.
- Li Vigni L., Cardellini C., Temovski M., Ionescu A., Molnar K., Palcsu L., Gagliano A.L., Cappuzzo S., D'Alessandro W. (2022a). *Location and soil CO₂ flux from Duvalo area, North Macedonia,* Version 1.0. Interdisciplinary Earth Data Alliance (IEDA). <https://doi.org/10.26022/IEDA/112210>
- Li Vigni L., Cardellini C., Temovski M., Ionescu A., Molnar K., Palcsu L., Gagliano A. L., Cappuzzo S., D'Alessandro W. (2022b). *Location, chemical and isotopic composition of soil gases collected in Duvalo area, North Macedonia.* Version 1.0. Interdisciplinary Earth Data Alliance (IEDA). <https://doi.org/10.26022/IEDA/112209>. Accessed 2022-01-11
- Li Vigni L., Cardellini C., Temovski M., Ionescu A., Molnar K., Palcsu L., Gagliano A. L., Cappuzzo S., D'Alessandro W. (2022c). *Duvalo “volcano” (North Macedonia): A purely tectonic-related CO₂ degassing system.* Geochemistry, Geophysics, Geosystems. 23. E2021GC010198. <https://doi.org/10.1029/2021GC010198>
- Li Vigni L., Daskalopoulou K., Calabrese S., Brusca L., Bellomo S., Cardellini C., Kyriakopoulos K., Brugnone F., Parello, F., D'Alessandro W. (2023a). *Chemical-physical parameters, major, minor and trace elements compositions of big karst springs of Greece,* Version 1.0. Interdisciplinary Earth Data Alliance (IEDA). <https://doi.org/10.26022/IEDA/112899>. Accessed 2023-04-04.
- Li Vigni L., Daskalopoulou K., Calabrese S., Brusca L., Bellomo S., Cardellini C., Kyriakopoulos K., Brugnone F., Parello F., D'Alessandro W. (2023b). *Hellenic karst hydrosystems: geogenic and anthropogenic processes affecting their geochemistry and water quality.* Scientific Report (*submitted*)
- Li Vigni L., Daskalopoulou K., Calabrese S., Kyriakopoulos K., Bellomo S., Brusca L., Brugnone F., D'Alessandro W. (2023c). *Characterization of trace elements in thermal and mineral waters of Greece.* Environmental Science and Pollution Research. <https://doi.org/10.1007/s11356-023-27829-x>
- Lindhorst K., Krastel S., Reicherter K., Stipp M., Wagner B., Schwenk T. (2015). *Sedimentary and tectonic evolution of Lake Ohrid (Macedonia/Albania).* Basin Res. 27, 84–101.
- Liotta M., Martelli M. (2012). *Dissolved gases in brackish thermal waters: an improved analytical method.* Geofluids, 12, 236–244. <https://doi.org/10.1111/j.1468-8123.2012.00365.x>
- Loye-Pilot M. D., Martin J. M. (1996). *The Impact of Desert Dust Across the Mediterranean.* Edited by S. Guerzoni and S. Chester, Kluwer Academic Publishers 1996, Dordrecht, The Netherlands.
- Machel H.G. (2001). *Bacterial and thermochemical sulfate reduction in diagenetic settings — old and new insights.* Sediment. Geol. 140, 143–175.
- Malagò A., Efthathiou D., Bouraoui F., Nikolaidis N.P., Franchini M., Bidoglio G., Kritsotakis M. (2016). *Regional scale hydrologic modelling of a karst-dominant geomorphology: the case study of the Island of Crete.* Journal of Hydrology, 540, 64.81.
- Maramathas A., Maroulis Z., Marinos-Kouris D. (2003). *Brackish Karstic Springs Model: Application to Almiros Spring in Crete. Ground water.* Ground Water, 41 (5), 608–19. <https://doi.org/10.1111/j.1745-6584.2003.tb02399.x>
- Maramathas A., Gialamas I. (2011). *Climate change impact on the Almiros brackish karst spring at Heraklion Crete Greece.* In: Lambrakis, N., Stournaras, G., Katsanou, K. (eds) *Advances in the Research of Aquatic Environment. Environmental Earth Sciences.* Springer, Berlin, Heidelberg. https://doi.org/10.1007/978-3-642-19902-8_9
- Marinković G., Papić P., Stojković J., Dragišić, V. (2012). *Factors contributing to the formation of carbonated mineral water systems in Serbia.* Annales Geologiques de la Peninsule Balkanique 73, 117–124.
- Markantonis K., Koumantakis J. (2011). *Contribution on hydrogeological investigation of karstic systems in eastern*

- Korinthia*, In: Advances in the Research of Aquatic Environment (Lambrakis, N., Stournaras, G., Katsanou, K. eds.) Springer, Berlin, Germany, vol. 1, 511-518. <https://doi.org/10.1007/978-3-642-19902-8>
- Markoski B., Jovanovski M., Peshevski I. (2019). *Duvalo - dry mofette, Kosel, Ohrid*. Geomap doo, Skopje. (*in Macedonian with extended summary in English*)
- Martelli M., Nuccio P.M., Stuart F.M., Burgess R., Ellam R.M., Italiano F. (2004). *Helium-strontium isotope constraints on mantle evolution beneath the Roman Comagmatic Province, Italy*. Earth Planet. Sci. Lett., 224, 295–308.
- Martelli M., Rizzo A.L., Renzulli A., Ridolfi F., Arienzio I., Rosciglione A. (2014). *Noble-gas signature of magmas from a heterogeneous mantle wedge: the case of Stromboli volcano (Aeolian Islands, Italy)*. Chem. Geol. 368 (2014), 39–53.
- Marty B., Almeyrac M., Barry P.H., Bekaert D.V., Broadley M.W., Byrne D.J., et al. (2020). *An evaluation of the C/N ratio of the mantle from natural CO₂-rich gases analysis: Geochemical and cosmochemical implications*. Earth and Planetary Science Letters, 551(2020), 116574.
- McClusky S., Balassanian S., Barka A., Demir C., Ergintav S., Georgiev I., Gurkan O., Hamburger M., et al. (2000). *Global Positioning System constraints on plate kinematics and dynamics in the eastern Mediterranean and Caucasus*. Papers on Geodesy and Gravity Tectonophysics, Volume 105, Issue B3, Pages 5695–5719.
- McCollom T.M., Seewald J.S. (2007). *Abiotic synthesis of organic compounds in deep-sea hydrothermal environments*. Chem. Rev., 107, 382-401.
- McKenzie D. (1978). *Active tectonics of the Alpine Himalayan belt: the Aegean Sea and surrounding regions*. Geophys. J. R. Astr. Soc., 55: 217-254.
- Metaxas A., Karageorgiou D. E., Varvarousis G., Kotis T., Ploumidis M., Papanikolaou G. (2007). *Geological evolution - stratigraphy of Florina, Ptolemaida, Kozani and Saradapiro graben*. Bulletin of the Geological Society of Greece, 40(1), 161–172.
- Micevski E., Popovski K., Popovska-Vasilvska S., Kolcakovski Z. (2007). *The hydrogeothermal potential of the Vardar zone and Serbo-Macedonian mass and energetical valorization of the available geothermal resources at the territory of the Republic of Macedonia*. European Geothermal Congress, Unterhaching, Germany, May 30 – June 1, 2007.
- Milivojevic M. (1993). *Geothermal model of Earth's Crust and Lithosphere for the territory of Yugoslavia: Some tectonic implications*. Studia geoph. et geol. No.37, Belgrade, pp.23-31.
- Milkov A.V., Etiope G. (2018). *Revised genetic diagrams for natural gases based on a global dataset of >20,000 samples*. Org. Geochem. 125, 109–120.
- Miller S.A., Ben-Zion Y., Burg J.P. (1999). *A three dimensional fluid controlled earthquake model: behavior and implications*. J.Geophys. Res., 104 (B5), 10621-10638.
- Mimikou M.A. (2005). *Water resources in Greece: present and future*. Glob Nest Int J 7(3):313-322.
- Minissale A., Evans W., Magro G., Vaselli O. (1997). *Multiple source components in gas manifestations from north-central Italy*. Chem. Geol. 142, 175–192.
- Mirčovski V., Boev B., Efremoski Z., Šorša A., Dimov D. (2015). *Hydrochemical data for the ground waters in the Bitola's part of the Pelagonia Valley, Republic of Macedonia*. Geologica Macedonica 29(1), 15-24.
- Molnár K., Temovski M., Palcsu L. (2021). *First noble gas results from fluid inclusions of the Late Miocene-Pleistocene Macedonian volcanics*. EGU General Assembly 2021, online, 19–30 Apr 2021, EGU21-9440, <https://doi.org/10.5194/egusphere-egu21-9440>.
- Molnár K., Lahitte P., Dibato S., Benko Z., Agostini S., Donczo B., Ionescu A., Milevski I., Sziksza Z., Kertesz Z., Temovski M. (2022). *The westernmost Late Miocene-Pliocene volcanic activity in the Vardar zone (North Macedonia)*. International Journal of Earth Science, s00531-021-02153-2.

- Monopolis D., Lambrakis N.J., Perleros B. (2005). *The brackish karstic spring of Almiros of Heraklion, Crete*. EUR 2005, 21366, 321-328.
- Morgantini, N., Frondini, F., Cardellini, C. (2009). *Natural trace elements baselines and dissolved loads in groundwater from carbonate aquifers of central Italy*. Phys. Chem. Earth 34, 520–529.
- Mörner N.K., Etiope G. (2002). *Carbon degassing from the lithosphere*. Global and Planetary Change, 33, 185-203. [https://doi.org/10.1016/S0921-8181\(02\)00070-X](https://doi.org/10.1016/S0921-8181(02)00070-X)
- Mougin P., Lamoureux-Var V., Bariteau A., Huc A.Y. (2007). *Thermodynamic of thermochemical sulphate reduction*. J. Petrol. Sci. Eng. 58, 413–427.
- Mountrakis D.M. (1985). *Geologia tis Elladas*. University Studio Press, Thessaloniki, 207. (in Greek)
- Mountrakis D.M. (2010). *Geologia kai geotektoniki exelixi tis Elladas*. University Studio Press, Thessaloniki, 374. (in Greek)
- Muirhead J.D., Kattenhorn S.A., Lee H., Mana S., Turrin B.D., Fischer T.P., Kianji G., Dindi E., Stamps D.S. (2016). *Evolution of upper crustal faulting assisted by magmatic volatile release during early-stage continental rift development in the East African Rift*. Geosphere, 12, 1670-1700. <https://doi.org/10.1130/GES01375.1>
- Mullaney J.R., Lorenz D.L., Arnston A.D. (2009). *Chloride in Groundwater and Surface Water in Areas Underlain by the Glacial Aquifer System, Northern United States*. US Geological Survey, Reston, VA.
- Murrell C.J., Jetten M.S.M. (2009). *The microbial methane cycle*. Environ. Microbiol. Rep. 1, 279-284.
- Musgrove M. (2021). *The occurrence and distribution of strontium in U.S. groundwater*. Applied Geochemistry 126 (2021) 104867.
- Myrttinens A., Becker V., Barth J.A.C. (2012). *A review of methods used for equilibrium isotope fractionation investigations between dissolved inorganic carbon and CO₂*. Earth-Science Reviews, 115, 192-199.
- Nanou E.A., Zagana E. (2018). *Groundwater vulnerability to pollution map for karst aquifer protection (Ziria karst system, Southern Greece)*. Geosciences 8, 125. <https://doi.org/10.3390/geosciences8040125>
- Nieuwland D.A., Oudmayer B.C., Valbona U. (2001). *The tectonic development of Albania: explanation and prediction of structural styles*. Marine and Petroleum Geology, 18, 161-177.
- Nikolaou E. (2010). *Update of Epirus groundwater data. Hydrogeology Report (V)*. 3rd E.U. Framework project IGME, pp.192. (in Greek)
- Nikolaou E., Pavlidou S., Katsanou K. (2011). *Aquifer systems of Epirus, Greece: An overview*. In: Advances in the Research of Aquatic Environment (Lambrakis, N., Stournaras, G., Katsanou, K. eds.) Springer, Berlin, Germany, vol. 1, 425-433.
- Nisi B., Vaselli O., Marchev P., Tassi F. (2013). *Diffuse CO₂ Soil Flux Measurements at the Youngest Volcanic System in Bulgaria: The 12.2 Ma old Kozhuh Cryptodome*. Acta Vulcanol. 25(1–2), 169–177.
- Norman J.E., Toccalino P.L., Morman S.A. (2018). *Health-based screening levels for evaluating water-quality data*. US Geological Survey web page, <https://water.usgs.gov/nawqa/HBSL> (accessed 18/03/2023), <https://doi.org/10.5066/F71C1TWP>.
- Ozima M., Podosek F.A. (2002). Noble Gas Geochemistry. Cambridge University Press, 2nd, 286 p.
- Panagopoulos G., Lambrakis N., Katagas C., Papoulis D., Tsolis-Katagas P. (2005). *Water–rock interaction induced by contaminated groundwater in a karst aquifer, Greece*. Environ. Geol. 49, 300–313, <https://doi.org/10.1007/s00254-005-0090-3>
- Panagopoulos, G. (2009). *Application of major and trace elements as well as boron isotopes for tracing hydrochemical processes: the case of Trifilia coastal karst aquifer, Greece*. Environ. Geol. 58, 1067–1082.

- Panno S.V. et al. (2006). *Characterization and Identification of Na-Cl Sources in Ground Water*. Groundwater 44, 176–187.
- Papadopoulou-Vrinioti K., (1999). *Hellenic karst and Environment*. In Proceedings of the 3rd Pan-Hellenic Geographical Conference, Athens, Greece, 1-3 April 1999; pp.290-299.
- Parello F., Allard P., D'Alessandro W., Federico C., Jean-Baptiste P., Catani O. (2000). *Isotope geochemistry of Pantelleria volcanic fluids, Sicily Channel rift: A mantle volatile end-member for volcanism in southern Europe*. Earth Planet. Sci. Lett. 180, 325–339.
- Parkhurst D.I., Appelo C.A.J. (1999). *User guide to PHREEQC (version 2) – a computer program for speciation, batch-reaction, one-dimensional transport, and inverse geochemical calculation*. U.S. Geological Survey of Water Resource Investigation Report 99 – 4259, p. 310.
- Pearce J.M., Czernichowski-Lauriol I., Lombardi S., Brune S., Nador A., Baker J., Pauwels H., Hatziyannis G., Beaubien S., Faber E. (2004). *A review of natural CO₂ accumulations in Europe as analogues for geological sequestration*. Geol. Soc. London Spec. Pubbl. 233, 29–41.
- Pearce J.M. (ed) (2004). *Natural analogues for the geological storage of CO₂*. Final report of the Nascent project. British Geological Survey Technical Report, 122pp.
- Peccerillo A. (1999). *Multiple mantle metasomatism in central-southern Italy: geochemical effects, timing and geodynamic implications*. Geology 27, 315–318.
- Pe-Piper G., Piper D.J.W. (2007). *Neogene backarc volcanism of the Aegean: new insights into the relationship between magmatism and tectonics*. Geol. Soc. Am. Spec. Pap 418:17-31. [https://doi.org/10.1130/2007.2418\(02\)](https://doi.org/10.1130/2007.2418(02)).
- Petalas C. (2017). *Analysis of the hydrogeological and hydrochemical characteristics of an immature karst aquifer system*. Environ. Process. 4, 603–624. <https://doi.org/10.1007/s40710-017-0250-y>
- Petalas C.P., Akratos C.S., Tsihrintzis V.A. (2018). *Hydrogeological investigation of a karst aquifer system*. Environ. Process. 5, 155–181. <https://doi.org/10.1007/s40710-017-0277-0>
- Petalas C.P., Moutsopoulos K.N. (2019). *Hydrogeologic behavior of a complex and mature karst aquifer system under drought condition*. Environ. Process. 6, 643–671. <https://doi.org/10.1007/s40710-019-00382-x>
- Piperov N.B., Kamensky I.L., Tolstikhin I.N. (1994). *Isotopes of the light noble gases in mineral waters in the eastern part of the Balkan peninsula, Bulgaria*. Geochim. Cosmochim. Acta 55, 1889–1898.
- Popovska-Vasilevska S. & Armenski S. (2016). *Geothermal conditions in Macedonia*. Technika Poszukiwan Geologicznych, Geotermia, Zrownowazony Rozwoj, 1/2016, 185-195.
- Popovska-Vasilevska S., Armenski S. (2016). *Geothermal Potential of Macedonia and Its Utilization*. In P. Papić (Ed.), Mineral and Thermal Waters of Southeastern Europe. Environmental Earth Science. (p. 131-146). Springer International Publishing Switzerland.
- Popovski K. (2002). *Feasibility Study on possible investments in geothermal projects in Macedonia*. WB study, Skopje.
- Pulido-Bosch A., (2021). *Principles of Karst Hydrogeology*. Springer Textbooks in Earth Sciences, Geography and Environment. https://doi.org/10.1007/978-3-030-55370-8_2
- Randazzo P., Caracausi A., Aiuppa A., Cardellini C., Chiodini G., D'Alessandro W., et al. (2021). *Active degassing of deeply sourced fluids in central Europe: New evidences from a geochemical study in Serbia*. Geochemistry, Geophysics, Geosystems, 22, e2021GC010017. <https://doi.org/10.1029/2021GC010017>
- Randazzo P., Caracausi A., Aiuppa A., Cardellini C., Chiodini G., Apollaro C., Partenoster M., Rosiello A., Vespasiano G. (2022). *Active degassing of crustal CO₂ in areas of tectonic collision: A case study from the Pollino and Calabria sectors (Southern Italy)*. Frontiers in Earth Science, 10: 946707.
- Reimann C. et al. (1998). *Environmental Geochemical Atlas of the Central Barents Region*. ISBN 82-7385-176-1.

- NGU-GTK-CKE Special Publication, Geological Survey of Norway, Trondheim, Norway, 745 pp.
- Richards L.A. *Diagnosis and improvement of saline and alkaline soils*. U.S. Salinity Laboratory Staff, Agricultural Handbook No 60. U.S. Department of Agriculture, p. 160 (1954).
- Rigakis N., Karakitsios V. (1998). *The source rock horizons of the Ionian Basin (NW Greece)*. Marine and Petroleum Geology 15, 593-617.
- Rizzo A.L. et al. (2016). *Kolumbo submarine volcano (Greece): an active window into the Aegean subduction system*. Sci. Rep. 6, 28013.
- Robertson A., Shallo M. (2000). *Mesozoic-Tertiary tectonic evolution of Albania in its regional Eastern Mediterranean context*. Tectonophysics, 316, 197–254.
- Rogie J.D., Kerrick D.M., Chiodini G., Frondini F. (2000). *Flux measurements of nonvolcanic CO₂ emissions from some vents in central Italy*. J. Geophys. Res. 105, 8435–8445.
- Rose T.P., Davisson M.L. (1996). Radiocarbon in hydrologic systems containing dissolved magmatic carbon dioxide. Science, 273, 1367-1370. <https://doi.org/10.1126/science.273.5280.1367>
- Salminen R. et al., (2005) *FOREGS Geochemical Atlas of Europe, Part 1: Background Information, Methodology and Maps*. Geological Survey of Finland, ISBN: 951-690-921-3.
- Sano Y., Wakita H. (1985). *Geographical distribution of ³He/⁴He ratios in Japan: implications for arc tectonics and incipient magmatism*. J. Geophys. Res., 90, 8729-8741.
- Sano Y., Marty B. (1995). *Origin of carbon in fumarolic gas from islands arcs*. Chem. Geol., 119, 265-274.
- Schmid S.M. et al. (2020). *Tectonic units of the Apennine collision zone between Eastern Alps and western Turkey*. Gondwana Res. 78:308-374. <https://doi.org/10.1016/j.gr.2019.07.005>
- Schoell M. (1983). *Genetic characterization of natural gases*. America Association of Petroleum Geologists Bulletin, 67, 2225–2238.
- Scott M., Lindsey R. (2016). *Which emits more carbon dioxide: volcanoes or human activities?* NOAA Climate.gov. Accessed February 22, 2023.
- Šerif A. (2001). *Rudarstvoto vo Makedonija vo vreme na Osmanliskoto vladeenje* (Mining in Macedonia during the Ottoman Rule), INI, Logos-A, Skopje. (**in Macedonian**)
- Seward T.M., Kerrick D.M. (1996). *Hydrothermal CO₂ emissions from the Taupo volcanic zone. New Zealand*. Earth and Planetary Science Letters, 139, 105-113. [https://doi.org/10.1016/0012-821X\(96\)00011-8](https://doi.org/10.1016/0012-821X(96)00011-8)
- Shaji E., Santosh M., Sarath K.V., Prakash P., Deepchand V., Divya B.V. (2021). *Arsenic contamination of groundwater: A global synopsis with focus on the Indian Peninsula*. Geoscience Frontiers, vol. 12, 3, 101079.
- Sherwood Lollar B., Slater G.F., Ahad J., Sleep B., Spivack J., Brennan M., MacKenzie P. (1999). *Contrasting carbon isotope fractionation during biodegradation of trichloroethylene and toluene: Implications for intrinsic bioremediation*. Org Geochem 30:813–820.
- Sherwood Lollar B., Lacrampe-Couloume G., Voglesonger K., Onstott T.C., Pratt L. M., Slater G.F. (2008). *Isotopic signatures of CH₄ and higher hydrocarbon gases from Precambrian Shield sites: a model for abiogenic polymerization of hydrocarbons*. Geochimica et Cosmochimica Acta 72, 4778–4795.
- Shimizu A., Sumino H., Nagao K., Notsu K., Mitropoulos P. (2005). *Variation in noble gas isotopic composition of gas samples from the Aegean arc, Greece*. J. Volcanol. Geotherm. Res. 140, 321–339.
- Sinclair A.J. (1974). *Selection of threshold values in geochemical data using probability graphs*. J. Geochem. Explor., 3, 129–149. [https://doi.org/10.1016/0375-6742\(74\)90030-2](https://doi.org/10.1016/0375-6742(74)90030-2)

- Skayias S.D. (1986). *Inventory of karstic springs of Greece. VIII – Water District of East Central Greece (Euboea Province)*. Institute of Geological and Mining Research, Athens.
- Skayias, S.D. (1978). *Inventory of karstic springs of Greece. I – Peloponnesus, Zakynthos, Kefallinia*. Institute of Geological and Mining Research, Athens.
- Sorey M.L., Evans W.C., Kennedy B.M., Farrar C.D., Hainsworth L.J., Hausback B. (1998). *Carbon dioxide and helium emissions from a reservoir of magmatic gas beneath Mammoth Mountain, California*. J. Geophys. Res.: Solid Earth, 103, 15503-15323. <https://doi.org/10.1029/98JB01389>
- Spasovski O. (2012). *Potential and geochemical characteristics of geothermal resources in Eastern Macedonia*. In Panagiotaras D. (Ed), *Geochemistry – Earth's system processes*. (p. 291-322).
- Stamatis G. (2010). *Groundwater quality of the Ag. Paraskevi/Tempi Valley karstic springs – Application of a tracing test for research of the microbial pollution (Kato Olympos/NE Thessaly)*. Bull. Geol. Soc. Greece 43, 1868-1877. <https://doi.org/10.12681/bgsg.11378>
- Stamos A., Manakos A. (1986). *Inventory of karstic springs of Greece. Water District of Western Macedonia*. Institute of Geological and Mining Research, Athens.
- Stefansson A., Lemke K.H., Benezeth P., Scott J. (2017). *Magnesium bicarbonate and carbonate interactions in aqueous solutions: an infrared spectroscopic and quantum chemical study*. Geochem. Cosmochim. Acta, 198, 271-284.
- Steiakakis E., Vavadakis D., Kritsotakis M., Voudouris K., Anagnostopoulou C. (2016). *Drought impacts in the fresh water potential of a karst aquifer in Crete, Greece*. Environ Earth Sci, 75:507.
- Steiger R.H., Jager E. (1977). *Subcommission on geochronology: convention on the use of decay constants in geo- and cosmochronology*. Earth and Planetary Science Letters, 36, 359-362.
- Suarez C.A., Edmonds M., Jones A.P. (2019). *Earth catastrophes and their Impact on the Carbon Cycle*. Elements, vol. 15, pp. 301-306.
- Tamburello G., Pondrelli S., Chiodini G., Rouwet D. (2018). *Global-scale control of extensional tectonics on CO₂ earth degassing*. Nature Communications, 9, 4608.
- Taymaz T., Yilmaz Y., Dilek Y. (2007). *The geodynamics of the Aegean and Anatolia: Introduction*. Geological Society, London, Special Publications, 291, 1–16.
- Temovski M., D'Alessandro W., Ionescu A., Li Vigni L., Molnár K., Palcsu L., Cardellini C. (2020). *Preliminary geochemical characterization of gas manifestations in North Macedonia*. EGU2020-2763, EGU General Assembly 2020.
- Temovski M., Turi M., Futo I., Braun M., Molnar M., Palcsu L. (2021). *Multi-method geochemical characterization of groundwaters from a hypogene karst system*. Hydrogeology Journal, 29:1129-1152.
- Tomkins A.G. (2010). *Windows of metamorphic sulfur liberation in the crust: Implications for gold deposit genesis*. Geochim. Cosmochim. Acta 74, 3246–59.
- Trojanović S. (1925). *La Solfatare de Kosel*. Annales géologiques de la Peninsule Balkanique, 8(1), 140-146.
- Tsokas G.N., Hansen R.O. (1997). *Study of the crustal thickness and the subducting lithosphere in Greece from gravity data*. J. Geophys. Res., 102 (B9), 585–597.
- Tziritis E.P. (2010). *Assessment of NO₃⁻ contamination in a karstic aquifer, with the use of geochemical data and spatial analysis*. Environ. Earth Sci. 60, 1381–1390. <https://doi.org/10.1007/s12665-009-0274-3>
- Tziritis E.P., Kelepertzis E., Korres G., Perivolaris D., Repani S. (2012). *Hexavalent chromium contamination in groundwaters of Thiva Basin, Central Greece*. Bull. Environ. Contam. Toxicol. 89, 1073-1077.

- Tziritis E.P. (2014). *Environmental monitoring of Micro Prespa Lake basin (Western Macedonia, Greece). Hydrogeochemical characteristics of water resources and quality trends.* Environmental Monitoring and Assessment 186(7): 4553-4568
- Vaselli O., Minissale A., Tassi F., Magro G., Seghedi I., Ioane D., Szakács A. (2002). *A geochemical traverse across the Eastern Carpathians (Romania): Constraints on the origin and evolution of the mineral water and gas discharges.* Chem. Geol. 182, 637–654.
- Vaselli O., Tassi F., Montegrossi G., Capaccioni B., Giannini L. (2006). *Sampling and analysis of volcanic gases.* Acta Vulcanologica, 18, 65-76.
- Vasileiou E., Papazotos P., Dimitrakopoulos D., Perraki M. (2019). *Expounding the origin of chromium in groundwater of the Sarigkiol Basin, Western Macedonia, Greece: A cohesive statistical approach and hydrochemical study.* Environ. Monit. Assess. 191, 509.
- Velaj T. (2015). *The structural style and the hydrocarbon exploration of the subthrust in the Berati Anticlinal Belt, Albania.* Journal of Petroleum Exploration Production Technology, 5, 123–145.
- Vergis S. (1985). *Inventory of karstic springs of Greece. VII – Water District of Thrace.* Institute of Geological and Mining Research, Athens (1985).
- Viveiros F., Cardellini C., Ferreira T., Caliro S., Chiodini G., Silva C. (2010). *Soil CO₂ emissions at Furnas volcano, São Miguel Island, Azores archipelago: Volcano monitoring perspectives, geomorphologic studies and land use planning application.* Journal of Geophysics Research, 115, B12208.
- Viveiros F., Chiodini G., Cardellini C., Caliro S., Zanon V., Silva C., Rizzo A.L., Hipòlitio A., Moreno L. (2020). *Deep CO₂ emitted at Furnas do Enxofre geothermal area (Terceira Island, Azores archipelago). An approach for determining CO₂ sources and total emissions using carbon isotopic data.* Journal of Volcanology and Geothermal Research, 401, 106968.
- Voudouris K., Panagopoulos A., Koumantakis I. (2004). *Nitrate pollution in the coastal aquifer system of the Korinthos prefecture (Greece).* Global Nest: the Int. J. vol.6, No 1, pp. 31-38.
- Voudouris K., Kazakis N. (2018). *General characteristics and classification of karst aquifers in Greece.* Review of the Bulgarian geological Society, vol.79, part 3, p. 159-160.
- Voudouris K. (2019). *Status and codification of karst aquifer systems in Greece.* Bulletin Geological Society of Greece, 57, 23-51.
- Wakida F.T., Lerner D.N. (2005). *Non-agricultural source of groundwater nitrate: a review and case study.* Water Res. 39 (1), 3-16.
- Walker J.C.G., Hays P.B., Kasting J.F. (1981). *A negative feedback mechanism for the long-term stabilization of Earth's surface temperature.* Journal of Geophysical Research, 86, 9776-9782
- Weinlich F.H. (2014). *Carbon dioxide controlled earthquake distribution pattern in the NW Bohemian swarm earthquake region, western Eger Rift, Czech Republic-gas migration in the crystalline basement.* Geofluids, 14, 143–159.
- Werner C., Fischer T.P., Aiuppa A., Edmonds M., Cardellini C., Carn S., et al. (2019). *Carbon dioxide emissions from subaerial volcanic regions: Two decades in review.* In: Deep Carbon past to present (Chap.8, pp. 188-236). Cambridge University Press.
- Whiticar M.J., Faber E., Schoell M., (1986). *Biogenic methane formation in marine and freshwater environments: CO₂ reduction vs. acetate fermentation – isotope evidence.* Geochimica et Cosmochimica Acta 50, 693–709.
- WHO (World Health Organization), (2016). *Lead in drinking water. Background document for development of WHO guidelines for drinking water quality.* Geneva: WHO.
- WHO (World Health Organization), (2022). *Lead in drinking. Health risks, monitoring and corrective actions.*

- Technical brief. Geneva: WHO.
- Wigley T.M.L., Plummer L.N., Pearson F.J. Jr. (1978). *Mass transfer and carbon isotope evolution in natural water system*. Geochim. Cosmochim. Acta, 42, 1117-1139.
- WMO (2019). *The state of greenhouse gases in the atmosphere based on global observations through 2018*. WMO Greenhouse Gas Bulletin, n° 15.
- Wong K., Mason E., Brune S., East M., Edmonds M., Zahirovic S., (2019). *Deep carbon cycling over the past 200 million years: a review of fluxes in different tectonic settings*. Front. Earth Sci. 7:263
- Wycherley H., Fleet A., Shaw H. (1999). *Some observations on the origins of large volumes of carbon dioxide accumulations in sedimentary basins*. Mar Pet Geol 16:489–494
- Yanev Y., Boev B., Doglioni C., Innocenti F., Manetti P., Pecskay Z., Tonarini S., D’Orazio M. (2008). *Late Miocene to Pleistocene potassic volcanism in the Republic of Macedonia*. Miner. Petrol. 94, 45-60.
- Yolsal S., Taymaz T., Yalciner A.C. (2009). *Earthquake source parameters along the Hellenic-Cyprus arcs and simulations of historical tsunamis in the eastern Mediterranean*. Tectonophysics.
- Yuče G., Fu C.C., D’Alessandro W., Gulbay A.H., Lai C.W., Bellomo S., et al. (2017). *Geochemical characteristics of soil radon and carbon dioxide within the Dead Sea Fault and Karasu Fault in the Amik basin (Hatay) Turkey*. Chemical Geology, 469, 129-146. <https://doi.org/10.1016/j.chemgeo.2017.01.003>
- Zelilidis A., Maravelis A.G., Tserolas P. (2015). *An overview of the petroleum systems in the Ionian zone, onshore NW Greece and Albania*. Journal of Petroleum Geology, 38(3), 331–348.
- Zhang J., Quay P.D., Wilbur D.O. (1995). *Carbon isotope fractionation during gas-water exchange and dissolution of CO₂*. Geochimica et Cosmochimica Acta, 59 (1), 107-114.
- Zikov M. (1997). *Temperatura na vozduhot, termički režim i klimatska podelba spored termičkot režim vo Republika Makedonija* (Air temperature, thermal regime and climatic division according to the thermal regime in Republic of Macedonia). In: Zikov M., Georgieva M., Andonovski T., Stojmilov A., Gramatikovski V., Bakeva V., Dimitrievski V. (eds): *Vlijanieto na Sredozemnoto more vrz klimata na Republika Makedonija*. Makedonska riznica, 39-73. (**in Macedonian**)
- Ziogou F., Gemeni V., Koukouzas N., de Angelis D., Libertini S., Beaubien S., Kruger M. (2013). *Potential environmental impacts of CO₂ leakage from the study of natural analogue sites in Europe*. Energy Procedia.
- Илоски Г., Ивановски Г., Орачески С. (1957). *Извештај за сулфурните појави кај с. Косел-Охридско, Биро за геолошки истражувања – Охрид*. Report on sulfur phenomena in the village of Kosel-Ohrid, Bureau for Geological Research – Ohrid (**in Macedonian**)
- ВГИ, (1975-1980) *Топографски карти, листови Охрид*, размер 1:200000, 1:100000, 1:50000 и 1:25000, Белград. (**in Macedonian**)

Appendix

Appendix A1 - The geothermal fields of Republic of North Macedonia

Republic of North Macedonia is one of the richest regions in low-temperature geothermal resources (*Popovska-Vasilevska & Armenski, 2016*). The high heat flux and the low thickness of the crust favored the occurrence of 18 geothermal fields in the Macedonian country (*Fig.2.10*), which are situated in the Central Serbo-Macedonian Massif in Central and Eastern Macedonia. Exception is the Debar geothermal field, that is located in the Western Serbo-Macedonian geothermal zone (*Popovski, 2002*).

A.1 Gevgelija geothermal field

The hydrogeothermal system of Gevgelija Valley (*Fig.A.1*) is discharged through several surface thermal springs near Gornicet village as well as through exploration drillings and wells in Negorska Banja and Smokvica (*Micevski et al., 2007*).

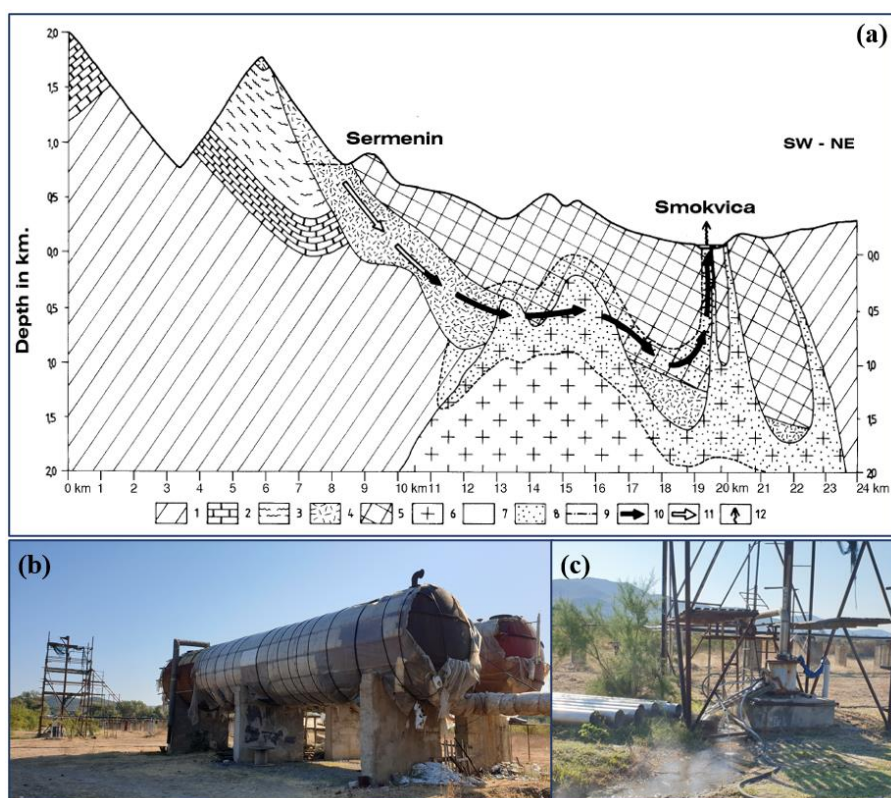


Fig.A.1. (a) Geological section of Smokvica field in Gevgelija geothermal field from *Gorgieva et al. (2000)*. 1- gneiss; 2- marbles; 3- phyllites; 4- limestones; 5- gabbro and diabases; 6- granites; 7- hydrogeothermal isolation; 8- hydrogeothermal reservoir; 10- thermal water flow; 11- cold water flow; 12- thermal spring. (b & c) pictures of Smokvica field.

The discharge occurs through fault systems bounded by Jurassic volcanic rocks, diabases and spilites and Triassic limestone from Kozhuf Mountain and Paleozoic marbles at the border with Valandovo Valley. The hot fluids circulate through the deep fault structures near the Smokvica field and Negorska banja (*Micevski et al., 2007*). According to *Gorgieva et al. (2000)*, the maximum temperature at discharge is 54 °C, and the predicted reservoir temperature is 75 - 100 °C. The geothermal system in the Gevgelia valley has been well studied through 15 boreholes with depths between 100 and 800 m.

A.2 Katlanovo geothermal field

The geothermal system in the Skopje Valley is of karst-fractured type. The substratum has block structure and is covered by thick Tertiary sediments. There are two geothermal fields in the Skopje valley: Volkovo and Katlanovo (*Fig.A.2*), without any hydraulic connection between them. The primary reservoir is composed of Precambrian and Paleozoic marbles.



Fig.A.2. Pictures of sampling sites at Katlanovo system.

The maximum measured temperature at discharge is about 54 °C, whereas the predicted reservoir temperature is about 80 – 115 °C (*Gorgieva, 1989*). The Skopje geothermal system has not been examined in detail. There are only five boreholes with depths of 86m at Katlanovo spa, of 186 and 350 m in Volkovo and of 1654 and 2000 m in the middle part of the valley. The last two boreholes

showed no geothermal anomaly, and no thermal waters were found because they went only through Tertiary sediments (*Gorgieva et al., 2000*).

A.3 Kezovica geothermal field

The hydrogeothermal system Kezhovica - Ldzhi is located near the Kezhovica Spa, in Shtip region. The reservoir is hosted in fractured Jurassic granites (*Fig.A.3*), covered with Tertiary sediments of Ovche Pole and Lakavichki basin (*Spasovski, 2012*). The Kezhovica spa uses water from two wells with capacity of 4.5 L s^{-1} and a measured water temperature of 63°C . The predicted reservoir temperature is about $100 - 115^\circ\text{C}$ (*Gorgieva, 1989*).

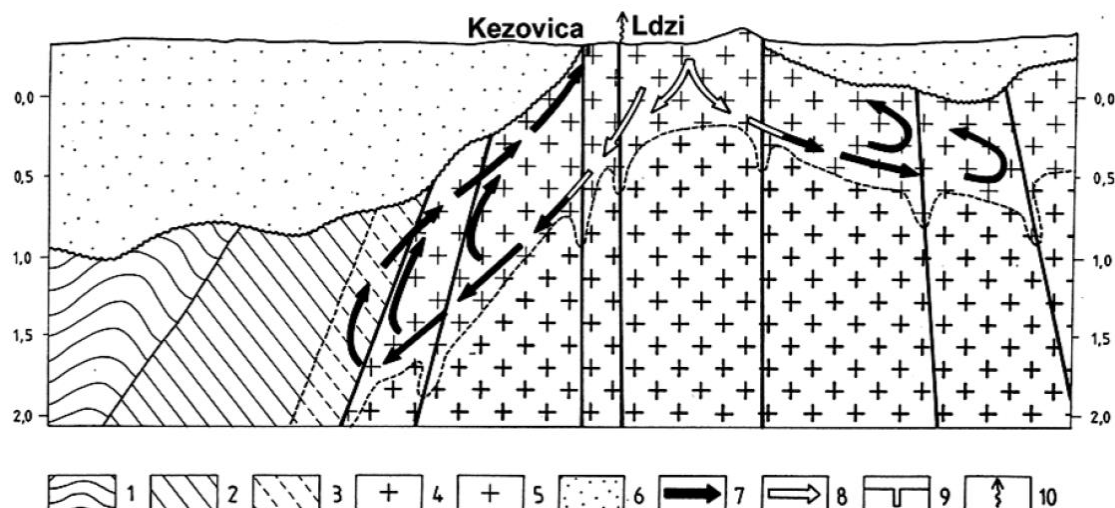


Fig.A.3. (a) Geological section of Kezovica geothermal field from *Spasovski (2012)*. 1- shall; 2- gneiss; 3- reservoir of gneiss; 4- massive granite; 5- cracked granite; 6- tertiary sediments; 7- thermal water flow; 8- cold water flow; 9- constructed boreholes; 10- thermal source.

A.4 Kochani geothermal field

The Kochani geothermal field (*Fig.A.4*) is the best-investigated system and considered the most important geothermal reservoir in Macedonia. It consists of two systems, Podlog and Istibanja, without hydraulic connection. The Istibanja geothermal system lies on the contact between the Serbo-Macedonian and Vardar geo-tectonic units, at the eastern periphery of the Kochani valley (*Spasovski, 2012*). The reservoir is situated in Precambrian gneiss and Paleozoic carbonated schists; it has the highest measured temperature in Macedonia (79°C) obtained by drilling, whilst the predicted maximum reservoir temperature is about 100°C (*Gorgieva et al., 2000*). There are more

than 25 boreholes and wells with depths from 100 to 1170 m (*Popovska-Vasilevska & Armenski, 2016*).

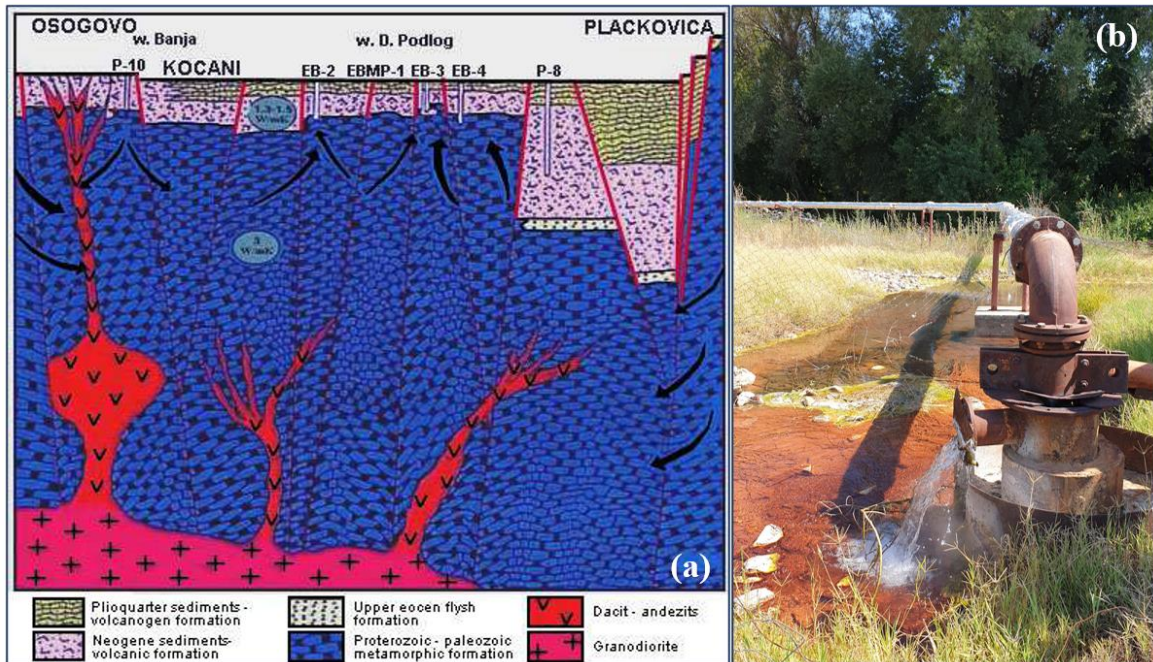


Fig.A.4. (a) Geological section of Kochani geothermal field from *Naunov (2003)*. (b) picture of one of the Istibanja drillings.

A.5 Kumanovo geothermal field

The Kumanovo geothermal field is characterised by relatively low temperatures, up to 40 °C, and low predicted reservoir temperatures because of lack of water-rock equilibrium and mixing of hot and cold water (*Gorgieva et al., 2000*). The reservoir consists of Paleozoic marbles and covers the northwest part of the Kratovo-Zletovo volcanic area (*Micevski et al., 2007*).

A.6 Strumica geothermal field

The reservoir of Strumica geothermal system (*Fig.A.5*) is hosted in Paleozoic fractured granites, covered by Tertiary sediments (thickness up to 1300 m) (*Micevski et al., 2007*). The reservoir is drained through several natural springs and boreholes (i.e., B-1 in Bansko village with water temperature of 70 °C and capacity of 50 L s⁻¹, and D-2 in Drvosh-Baldovci with water temperature of 29 °C and capacity of 51 L s⁻¹; *Micevski et al., 2007*). The maximum measured temperature is about 73 °C, whereas the predicted maximum reservoir temperature is 120 °C (*Gorgieva, 1989*).

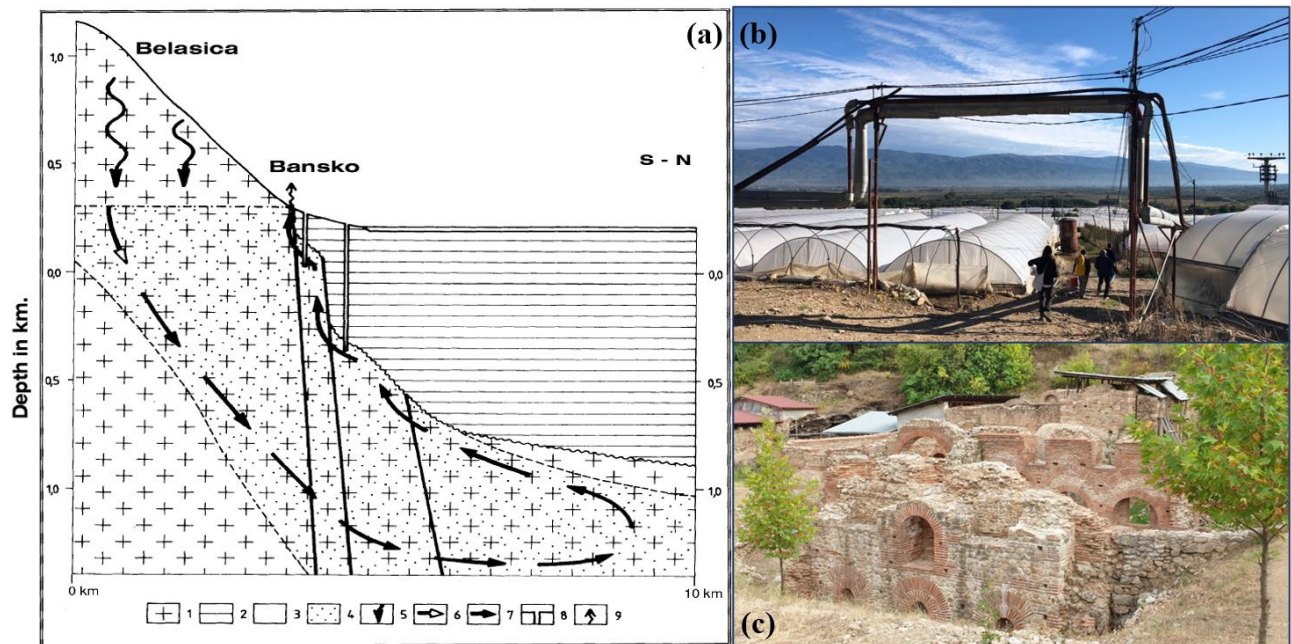


Fig.A.5. (a) Geological section of Bansko drilling in Strumica geothermal field from Gorgieva et al. (2000). 1- granite; 2- Neogene sediments; 3- aluvion; 4- hydrogeothermal reservoir; 5- cold water flow; 6- cold underground flow; 7- thermal water flow; 8- borehole; 10- thermal spring. (b) picture of Bansko. (c) picture of ruins of a Roman thermal bath at Bansko.

Appendix A2
Table A1

Identification number, geographical coordinates and flow rate of the collected Hellenic karst springs.

ID	Name	Date	Latitude	Longitude	Flow rate (L s^{-1})
1	Stratones (vasca)	18/05/2016	41.08881	24.767511	683
2	Agios Ioannis Paradisos	18/05/2016	41.08151	24.758688	533
3	Kefalari	19/05/2016	41.07399	24.265921	1,000
4	Drama	19/05/2016	41.15039	24.141744	2778
5	Milopotamos	19/05/2016	41.15983	24.056483	556
6	Aggitis	19/05/2016	41.22067	23.893010	2,778
7	Symboli	19/05/2016	41.02887	24.035283	278
8	Ano Symboli	19/05/2016	41.03288	24.030773	1,000
9	Eptamylia	20/05/2016	41.10205	23.583489	278
10	Sidirokastro	20/05/2016	41.25739	23.408329	278
11	Petres	21/05/2016	40.72604	21.665075	111
12	Stratopedo (Xanthi)	22/03/2017	41.09036	24.769230	56
13	Mexiates	11/05/2017	38.88218	22.310921	300
14	Kombotades	11/05/2017	38.87020	22.347968	81
15	Mavroneri	11/05/2017	38.80067	22.429668	125
16	Agia Anna	12/05/2017	39.77587	22.304607	153
17	Mati	12/05/2017	39.81190	22.273927	1,631
18	Kefalokryso	12/05/2017	39.90073	22.071745	1,184
19	Voda	15/05/2017	40.80922	21.902661	1,000
20	Nisia	15/05/2017	40.83215	21.930348	333
21	Karkagia	15/05/2017	40.80825	22.013392	1,194
22	Flamouria	15/05/2017	40.73690	21.999048	69
23	Sevastiana	15/05/2017	40.77296	22.114301	403
24	Aristotelis	15/05/2017	40.63005	22.098653	528
25	Agios Nikolaos	15/05/2017	40.60950	22.043057	4,722
26	Kopano	15/05/2017	40.63391	22.125795	153
27	Artemis	16/05/2017	40.42985	22.176380	20
28	Georgianos	16/05/2017	40.47453	22.176208	69
29	Stratopedo	16/05/2017	40.47793	22.177592	389
30	Rachia	16/05/2017	40.47689	22.184236	806
31	Tripotamos	16/05/2017	40.49581	22.158138	1,000
32	Aravissos	14/10/2018	40.84487	22.307440	694
33	Santovou	15/10/2018	40.39307	21.409720	76
34	Istekou	15/10/2018	40.48911	21.338490	148
35	Lefki	15/10/2018	40.51251	21.226930	572
36	Koromilia	15/10/2018	40.54716	21.187880	444
37	Gavros	16/10/2018	40.63248	21.183530	146
38	Ieropigi	16/10/2018	40.57998	21.052480	167
39	Tempi	16/10/2018	39.87940	22.585270	772
40	Anavras est	17/10/2018	39.56950	22.025560	64
41	Voula	17/10/2018	39.56942	22.025554	217

ID	Name	Date	Latitude	Longitude	Flow rate (L s^{-1})
42	Gkouras	17/10/2018	39.68778	21.597500	111
43	Gorgogyrio	17/10/2018	39.55028	21.571667	583
44	Xilopariko	17/10/2018	39.53667	21.571667	265
45	Kaliakuda	17/10/2018	39.40002	22.956808	85
46	Livari	17/10/2018	39.11144	22.938190	20
47	Nerotrovias	18/10/2018	38.82972	22.377500	69
48	Mantania	18/10/2018	38.80722	22.166667	250
49	Belouchi	18/10/2018	38.73833	22.277222	833
50	Kefalovryso	18/10/2018	38.69889	22.318333	178
51	Paleomylos	18/10/2018	38.88921	22.805630	333
52	Ag. Dimitrios	18/10/2018	38.90856	22.716330	250
53	Megali Brisi	18/10/2018	38.89912	22.487110	306
54	Ag. Eleusa	18/10/2018	38.62939	22.519860	154
55	Kefalovryso Lilaia	18/10/2018	38.64050	22.492170	106
56	Ano Kefaloriso	18/10/2018	38.63019	22.504490	331
57	Polystavri	19/10/2018	38.41421	22.068790	157
58	Gouva	19/10/2018	38.40708	21.917620	425
59	Thermo	19/10/2018	38.44146	21.980260	116
60	Fleva	19/10/2018	38.41209	22.059974	118
61	Myloi	19/10/2018	38.43159	22.397993	583
62	Kirras p3	19/10/2018	38.42233	22.460022	1,528
63	Potamos	19/10/2018	38.35869	22.602392	177
64	Almyra Nera	20/10/2018	38.62916	23.131710	756
65	Rema	20/10/2018	38.54324	23.282630	189
66	Mylos Kokkosi	20/10/2018	38.48610	23.478650	97
67	Mavroneri est	20/10/2018	38.52518	22.779784	972
68	Charriton	20/10/2018	38.49965	22.961018	2,778
69	Erkinna Krya	20/10/2018	38.43176	22.875070	611
70	Agios Ioannis	20/10/2018	38.42228	22.459946	101
71	Koprinitsi	18/05/2019	37.27185	21.869910	71
72	Ag. Floros	18/05/2019	37.16790	22.026510	2,600
73	Pidima	18/05/2019	37.13794	22.047270	260
74	Logara	18/05/2019	37.28131	22.246860	138
75	Vivario	18/05/2019	37.18967	22.375630	1,900
76	Methydrio	18/05/2019	37.63777	22.176070	400
77	Pyrgakio	18/05/2019	37.63429	22.158970	250
78	Sintzi	19/05/2019	37.76154	22.341350	128
79	Mpailtsakou	19/05/2019	37.77299	22.221970	200
80	Ladon	19/05/2019	37.83682	22.182590	2,000
81	Planitero	19/05/2019	37.93361	22.166210	3,000
82	Feneos	19/05/2019	37.95261	22.334190	78
83	Triza	19/05/2019	37.86929	22.464250	187
84	Moustos	19/05/2019	37.38507	22.743670	80
85	Lerna	20/05/2019	37.55293	22.717050	2,000
86	Kefalari (Argos)	20/05/2019	37.59610	22.688170	3,333
87	Kantia	20/05/2019	37.51964	22.968420	800
88	Epidavros (Ag. Nikolaos)	20/05/2019	37.68120	23.150500	417
89	Selontas	20/05/2019	37.73413	23.117810	556

ID	Name	Date	Latitude	Longitude	Flow rate (L s ⁻¹)
90	Almyri	20/05/2019	37.84229	23.016200	833
91	Orea Elenis	20/05/2019	37.87030	22.996880	556
92	Mavrosoulava	22/05/2019	38.25802	23.806620	1389
93	Kaissarianis	22/05/2019	37.96548	23.787821	4.44
94	Koroni	27/02/2020	39.29296	20.542060	10,000
95	Skala	27/02/2020	39.17558	20.764580	2,000
96	Agios Georgios	27/02/2020	39.27016	20.851420	3,140
97	Vathy	27/02/2020	39.30888	20.887830	1,890
98	Biros	27/02/2020	39.43226	20.840240	800
99	Likostomo	27/02/2020	39.75034	20.773730	500
100	Krya	27/02/2020	39.71920	20.831390	200
101	Perama	27/02/2020	39.70200	20.857810	300
102	Mana Nerou	28/02/2020	40.04820	20.622100	245
103	Bobos	28/02/2020	40.00453	20.674250	250
104	Nelles	28/02/2020	39.98290	20.668690	160
105	Doliana	28/02/2020	39.89468	20.605910	1,430
106	Kalpaki	28/02/2020	39.88645	20.624130	300
107	Pigi Lithis	29/02/2020	39.02196	22.954650	50
108	Livari 2	29/02/2020	39.10896	22.933070	97
109	Livari	29/02/2020	39.11144	22.938190	20
110	Tempi 2	29/02/2020	39.88082	22.586370	100
111	Tempi	29/02/2020	39.87945	22.585180	772
112	Vryton	07/03/2020	40.79974	21.918361	42
113	Krystallopigi	07/03/2020	39.49172	20.469770	150
114	Petronikos	20/07/2021	38.87061	21.17545	833
115	Kryoneri	20/07/2021	38.34475	21.59736	344
116	Agios Stefanos	21/07/2021	38.45546	23.61104	535
117	Glyfa	21/07/2021	38.54251	23.63823	300
118	Kalam Tsirioneri	21/07/2021	38.40377	23.99841	139
119	Almyropotamos	21/07/2021	38.26894	24.16113	99
120	Astakos	22/07/2021	38.53502	21.10024	181
121	Lambra	22/07/2021	38.48393	21.23443	3,889
122	Anapsades	23/07/2021	38.95836	21.62643	145
123	Sotira	23/07/2021	38.95952	21.6303	19
124	Mega Rema	23/07/2021	38.98303	21.68408	135
125	Kefalovriso Karpenisi	23/07/2021	38.89733	21.782	203
126	Kefalovriso Thermo	23/07/2021	38.57260	21.66633	194
127	Kefalia Agia Sofias	23/07/2021	38.58320	21.64904	184
128	Prophitis Ilias	23/07/2021	38.58570	21.61386	28
129	Gorgogouvli	24/07/2021	38.88204	20.99691	183
130	Gouvo	24/07/2021	38.93666	20.96777	139
131	Vonitsa	24/07/2021	38.91510	20.87498	278
132	Monastiraki	24/07/2021	38.85114	20.94386	157
133	Korpi	24/07/2021	38.86237	20.95509	28
134	Nafpaktos	25/07/2021	38.39344	21.83619	306
135	Kallio	25/07/2021	38.55769	22.17071	833
136	Tempi 2	26/07/2021	39.88082	22.586370	100
137	Ponte	26/07/2021	39.89066	22.60649	100

ID	Name	Date	Latitude	Longitude	Flow rate (L s ⁻¹)
138	Dion	26/07/2021	40.17360	22.49127	50
139	Barouka	28/07/2021	40.42120	20.81678	175
140	Ano Arenes	28/07/2021	40.34093	20.92366	289
141	Kato Arenes	28/07/2021	40.29520	20.95105	710
142	Agios Fanourios	29/07/2021	39.99811	20.55454	120
143	Glavas	29/07/2021	39.99186	20.54221	965
144	Almyros (Agios Nikolaos)	09/06/2022	35.17436	25.70581	2,192
145	Kalo Chorio	09/06/2022	35.11733	25.71862	50
146	Zou	09/06/2022	35.15433	26.1085	21
147	Zakros	09/06/2022	35.11497	26.21175	103
148	Kato Zakros	09/06/2022	35.09526	26.26247	83
149	Ag Georgios	09/06/2022	35.12179	26.06386	18
150	Archon	09/06/2022	35.06309	25.9435	44
151	Psychro	09/06/2022	35.06059	25.86561	100
152	Synoirimos	10/06/2022	35.05519	25.49994	63
153	Kefalovryso Agia Marina	10/06/2022	35.04824	25.45597	57
154	Mati	10/06/2022	35.13990	24.91177	83
155	Spili	10/06/2022	35.21790	24.53618	130
156	Ligres	10/06/2022	35.14160	24.53323	23
157	Kourtalioti	10/06/2022	35.19129	24.46532	804
158	Agia Dynamis	11/06/2022	35.28653	24.33255	141
159	Limni Kourna	11/06/2022	35.32704	24.27874	79
160	Georgiopolis	11/06/2022	35.36048	24.25173	5,556
161	Vryses	11/06/2022	35.37638	24.20025	100
162	Armeni	11/06/2022	35.42960	24.15533	333
163	Stylos	11/06/2022	35.43346	24.12588	143
164	Koiliaris	11/06/2022	35.45530	24.14263	750
165	Meskla	12/06/2022	35.40594	23.95923	139
166	Agia	12/06/2022	35.47371	23.93166	395
167	Pantaleimona	12/06/2022	35.49647	23.71819	194
168	Samaria	12/06/2022	35.26956	23.96091	83
169	Panormos	13/06/2022	35.40850	24.67182	148
170	Geropotamos	13/06/2022	35.40938	24.67451	105
171	Fodele	13/06/2022	35.37821	24.95805	262
172	Almyros	16/06/2022	35.33327	25.04718	2,744
173	Plataria	03/10/2022	39.44032	20.27727	200
174	Foiniki	03/10/2022	39.61465	20.32675	200
175	Xino Nero	10/10/2022	40.69085	21.62150	36.1
176	Anthochori	10/10/2022	39.73630	21.12717	200
177	Perama	10/10/2022	39.70200	20.857810	300
178	Vella	11/10/2022	39.86604	20.62432	500
179	Kastri	11/10/2022	39.85682	20.61400	200
180	Zaravina Limni	11/10/2022	39.90268	20.51300	220
181	Rogozzi	11/10/2022	39.91661	20.41189	700
182	Arapi	11/10/2022	39.96751	20.66476	540
183	Voidomatis	11/10/2022	39.94875	20.71385	1,000
184	Lista	12/10/2022	39.73182	20.48038	1,700
185	Gerolimitsaina	12/10/2022	39.73734	20.59214	100

ID	Name	Date	Latitude	Longitude	Flow rate (L s^{-1})
186	Kabi	12/10/2022	39.21811	20.90188	650
187	Acheron	13/10/2022	39.32879	20.62144	1,500
188	Chohla	13/10/2022	39.21797	20.56580	2,400
189	Krioneri	13/10/2022	39.45793	21.12387	30
190	Makaria	15/10/2022	38.15811	24.00212	500
191	Dimitsana	15/10/2022	37.58315	22.04741	51
192	Kefalari Kakouraiika	15/10/2022	37.58244	21.91908	50
193	Agia Mama	16/10/2022	37.16643	22.30795	37
194	Tripi	16/10/2022	37.09362	22.34800	42
195	Sotiros	16/10/2022	36.98629	22.40815	196
196	Kefalovryso Lianos	17/10/2022	37.37684	22.31037	42
197	Maggani	17/10/2022	37.79661	22.12101	47
198	Mati	17/10/2022	37.82140	22.10626	47
199	Kertezi	17/10/2022	37.97772	21.99292	65
200	Tria Piagadia	17/10/2022	38.03760	22.09863	50
201	Mpala	17/10/2022	38.25498	21.80866	83

Table A2

Physico-chemical parameters, chemical composition of major ions of the collected Hellenic karst springs.

ID	T °C	pH	E.C. μS cm⁻¹	Eh mV	Ca²⁺ mg L⁻¹	Mg²⁺ mg L⁻¹	Na⁺ mg L⁻¹	K⁺ mg L⁻¹	HCO₃⁻ mg L⁻¹	F⁻ mg L⁻¹	Cl⁻ mg L⁻¹	NO₃⁻ mg L⁻¹	SO₄²⁻ mg L⁻¹	SiO₂ mg L⁻¹
1	15.5	7.32	321	399	68.1	7.01	5.11	1.58	249	0.160	4.88	2.81	8.11	7.94
2	15.9	7.22	294	351	74.3	6.68	4.83	1.29	256	0.151	5.18	3.21	8.25	7.66
3	16.7	7.16	351	n.m.	66.1	10.3	5.10	0.930	277	0.210	4.36	4.98	7.09	9.17
4	15.1	7.51	351	258	75.5	7.32	2.96	0.840	289	0.144	3.62	6.84	6.99	6.00
5	16.1	7.19	380	314	79.7	8.83	2.63	0.770	292	0.138	4.45	10.8	7.84	6.19
6	13.0	7.47	266	n.m.	36.9	5.99	3.69	1.18	215	0.143	2.92	3.55	8.78	8.44
7	17.6	7.5	397	n.m.	64.2	14.1	6.53	1.09	284	0.269	5.72	8.93	9.89	10.6
8	17.1	7.43	320	n.m.	55.2	10.6	6.21	1.12	243	0.186	4.68	4.08	6.89	9.24
9	18.2	7.36	353	205	63.2	7.71	8.90	1.19	255	0.136	3.93	2.96	17.5	10.4
10	24.0	7.03	574	207	63.6	8.01	23.8	3.33	351	0.382	6.09	8.27	24.8	18.0
11	14.9	6.49	851	250	198	24.5	5.26	0.780	758	0.177	3.37	8.49	6.61	12.5
12	16.4	7.45	427	182	74.7	8.20	4.35	1.10	252	0.110	5.46	3.35	9.78	8.48
13	14.8	7.35	409	163	73.6	11.2	7.67	0.661	277	0.298	11.8	1.33	6.89	5.60
14	15.1	7.33	381	210	74.2	10.4	7.06	0.676	267	0.192	10.7	4.22	7.31	7.20
15	14.0	7.38	420	190	68.5	18.6	3.37	0.446	292	0.057	6.65	5.18	4.57	8.00
16	16.1	7.57	376	184	62.6	13.0	7.96	1.53	235	0.141	7.85	17.4	14.0	14.9
17	16.0	7.47	390	202	66.5	11.6	6.74	1.35	246	0.124	6.41	14.3	12.0	13.5
18	17.4	7.35	417	225	62.3	19.7	7.79	1.09	276	0.302	6.21	9.48	12.9	14.7
19	16.1	6.97	676	183	121	37.2	9.81	2.50	534	0.217	8.05	6.21	13.1	11.6
20	10.1	7.66	303	232	46.2	18.7	1.00	0.434	232	0.057	1.25	1.31	3.08	4.70
21	13.4	7.32	532	217	86.0	27.9	5.60	1.63	393	0.091	6.08	4.42	14.4	9.90
22	16.6	7.71	328	115	69.8	5.75	2.17	0.543	242	0.038	2.17	0.90	7.67	8.70
23	14.9	7.43	549	163	83.5	35.2	10.6	2.87	399	0.110	10.8	12.7	23.1	16.9
24	12.2	7.46	707	176	69.8	19.9	3.37	1.05	295	0.082	4.64	7.50	11.4	7.19
25	11.0	7.52	366	179	62.2	19.1	2.36	0.680	279	0.068	2.56	2.18	6.23	5.55
26	13.2	7.39	439	177	76.6	20.7	3.51	1.12	316	0.076	4.34	8.67	16.3	9.60
27	12.6	7.33	338	183	74.7	3.81	3.33	0.837	237	0.055	6.04	4.22	7.70	9.90
28	12.8	7.46	367	206	68.4	14.1	1.98	0.559	276	0.213	2.73	2.99	5.02	5.22

Appendix A2 – Table A2

ID	T	pH	E.C.	Eh	Ca ²⁺	Mg ²⁺	Na ⁺	K ⁺	HCO ₃ ⁻	F ⁻	Cl ⁻	NO ₃ ⁻	SO ₄ ²⁻	SiO ₂
29	12.7	7.4	367	179	68.3	14.0	1.97	0.555	276	0.154	2.68	3.01	5.03	5.27
30	12.7	7.43	369	182	68.9	14.7	2.09	0.563	279	0.203	2.72	3.07	5.28	5.42
31	12.5	7.49	368	222	70.3	13.9	1.97	0.555	278	0.162	2.66	3.09	4.87	5.23
32	16.2	7.21	714	306	86.0	9.24	5.93	1.01	348	0.092	4.76	2.87	5.45	9.24
33	14.8	7.46	311	178	64.0	9.89	4.66	0.300	260	0.063	4.53	6.51	10.1	9.81
34	12.3	7.58	339	175	71.8	7.60	3.44	1.04	278	0.063	5.75	2.91	9.87	12.2
35	13.4	7.64	300	180	61.7	10.9	2.30	0.290	267	0.075	3.95	1.80	4.38	6.51
36	12.3	7.51	371	162	57.2	11.3	13.3	1.00	256	0.090	2.19	1.31	3.52	6.73
37	10.9	7.44	240	156	44.1	5.93	4.11	0.420	184	0.073	4.77	0.30	3.08	10.6
38	11.1	7.06	478	166	83.6	4.20	2.11	0.230	397	0.052	2.69	1.40	4.34	10.1
39	14.7	7.17	508	211	104	18.9	6.46	0.480	493	0.190	7.17	0.72	5.63	6.69
40	17.1	7.29	450	158	83.2	12.7	9.60	1.92	333	0.105	7.07	22.6	20.1	19.0
41	16.4	7.29	455	n.m.	61.2	15.2	7.72	0.670	307	0.049	10.7	7.74	9.51	19.4
42	11.6	7.55	294	174	61.2	2.60	2.30	0.210	203	0.029	1.91	1.11	3.78	5.36
43	10.9	7.63	286	214	54.4	1.76	1.82	0.262	213	0.033	1.88	1.09	2.85	6.11
44	10.9	7.34	282	280	53.8	1.50	1.44	0.199	188	0.029	2.73	1.69	2.98	6.13
45	11.1	8.35	182	162	24.5	2.48	10.6	16.1	149	0.113	4.47	0.19	5.80	12.0
46	18.6	7.00	17600	126	318	401	4,590	134	409	0.401	7,042	3.81	786	4.99
47	11.3	7.99	289	180	51.7	2.97	2.06	0.130	196	0.058	3.25	1.83	2.48	4.05
48	9.9	7.94	232	154	42.2	2.04	1.38	0.203	156	0.140	2.36	0.22	1.60	4.82
49	8.7	7.67	323	204	60.4	2.13	2.15	0.260	162	0.027	3.41	0.38	2.90	4.56
50	9.4	7.20	412	175	79.4	1.58	2.07	0.121	279	0.020	5.38	0.36	2.67	4.14
51	20.1	7.14	19400	110	287	398	4,560	137	300	0.662	8,744	1.86	989	9.81
52	15.8	7.30	419	156	81.5	4.58	7.77	0.290	294	0.054	11.0	13.0	4.83	9.99
53	16.5	7.46	514	150	79.0	11.8	13.8	0.950	316	0.088	24.6	18.8	8.71	14.2
54	10.2	7.52	283	155	66.7	3.26	1.89	0.180	266	0.026	3.35	0.19	2.34	3.24
55	11.3	7.57	323	162	68.9	2.44	2.55	0.380	257	0.037	4.15	1.14	4.63	5.61
56	11.8	7.5	364	166	72.3	6.75	2.96	0.297	288	0.026	6.44	0.19	4.03	5.19
57	11.8	7.53	384	n.m.	44.5	3.33	5.05	0.180	165	0.091	7.88	0.36	9.43	8.57
58	17.2	7.06	585	182	90.8	6.91	19.1	0.990	344	0.098	25.7	5.04	12.7	12.5
59	13.0	7.05	469	n.m.	71.0	9.38	10.6	1.30	207	0.105	8.34	0.73	22.7	11.4

Appendix A2 – Table A2

ID	T	pH	E.C.	Eh	Ca ²⁺	Mg ²⁺	Na ⁺	K ⁺	HCO ₃ ⁻	F ⁻	Cl ⁻	NO ₃ ⁻	SO ₄ ²⁻	SiO ₂
60	14.2	7.45	297	170	53.5	2.75	4.95	0.601	188	0.059	6.77	0.19	4.06	7.73
61	17.2	7.51	5290	127	106	138	1,192	541	240	0.178	2,553	2.75	391	3.52
62	16.6	7.30	17900	146	281	414	4,075	147	278	0.340	6,964	0.60	877	4.26
63	16.3	7.48	24500	98	293	593	5,610	204	201	0.065	9,467	0.45	1210	2.78
64	16.8	7.23	7100	n.m.	135	177	1,362	49.6	456	0.055	2,137	8.43	310	24.4
65	17.7	7.22	970	n.m.	64.2	31.4	26.6	1.56	387	0.053	81.1	10.1	7.51	12.2
66	17.4	7.45	1150	n.m.	69.3	28.4	101	4.13	293	0.091	162	5.98	41.2	11.3
67	21.3	7.38	366	n.m.	81.8	12.8	4.02	0.717	342	0.027	5.93	6.52	6.42	7.15
68	18.5	7.60	630	n.m.	69.2	18.4	4.06	0.650	304	0.057	5.54	11.4	6.20	6.75
69	14.6	7.50	364	n.m.	57.1	11.2	5.22	0.711	292	0.099	9.22	2.82	15.4	7.34
70	25.0	7.14	505	n.m.	78.5	11.5	5.20	0.898	313	0.277	6.52	3.77	6.77	10.5
71	16.9	7.03	568	172	112	8.17	16.0	1.00	369	0.114	27.7	6.68	18.8	12.5
72	15.7	7.49	510	156	63.5	25.4	22.5	0.891	231	0.091	44.7	3.96	58.1	8.12
73	16.1	7.43	580	162	70.9	31.7	20.8	0.813	254	0.110	44.0	4.53	84.1	8.46
74	15.3	7.08	536	163	119	8.54	6.44	0.735	394	0.072	11.3	4.14	14.7	10.7
75	13.8	7.38	419	150	71.7	19.8	4.37	0.481	256	0.135	7.77	3.05	48.5	8.04
76	10.6	7.53	236	155	60.7	1.08	2.53	0.223	195	0.034	4.62	1.34	2.45	7.23
77	10.5	7.40	333	172	90.8	2.76	3.49	0.587	288	0.034	6.35	1.03	5.96	7.88
78	11.6	7.30	269	176	64.9	2.26	2.55	0.317	209	0.070	4.05	2.67	5.67	6.58
79	13.6	7.45	370	165	80.2	5.80	3.31	0.481	271	0.080	5.57	5.56	8.79	7.75
80	13.9	7.44	376	164	70.7	12.8	3.54	0.547	262	0.095	5.64	5.21	16.6	6.54
81	11.1	7.43	316	170	60.3	12.5	2.64	0.532	243	0.063	3.98	2.02	6.29	5.93
82	12.4	7.30	364	159	72.1	11.0	2.76	0.446	278	0.065	5.29	1.44	6.29	7.92
83	10.2	7.59	249	170	45.9	10.5	1.89	0.231	185	0.044	3.47	1.40	8.75	4.62
84	17.6	7.08	9990	126	208	281	2368	75.5	332	0.153	4473	21.5	620	22.4
85	17.3	7.10	968	169	100	13.3	29.7	1.02	320	0.084	65.5	11.3	21.1	9.52
86	16.2	7.12	450	161	93.8	9.84	4.60	0.547	325	0.101	8.20	9.61	13.7	8.84
87	19.5	7.01	8770	128	202	261	1616	50.4	446	0.199	3,103	23.6	428	26.2
88	16.1	7.18	16500	109	234	407	3,540	104	346	0.015	6,532	26.9	889	24.0
89	16.0	7.24	31400	98	340	892	7,679	221	285	0.015	14,200	42.8	1936	47.1
90	17.5	7.06	29300	99	362	975	6,851	213	394	0.015	12,922	39.1	1768	48.5

Appendix A2 – Table A2

ID	T	pH	E.C.	Eh	Ca ²⁺	Mg ²⁺	Na ⁺	K ⁺	HCO ₃ ⁻	F ⁻	Cl ⁻	NO ₃ ⁻	SO ₄ ²⁻	SiO ₂
91	19.3	6.76	18300	150	326	541	3,678	115	619	0.638	6,994	22.8	951	29.5
92	16.3	7.17	458	144	88.8	14.6	5.82	0.391	335	0.038	15.9	6.18	6.53	9.65
93	22.4	7.09	760	103	92.0	43.1	37.0	1.21	422	0.219	62.5	29.5	29.0	14.4
94	15.9	7.39	331	180	74.4	12.9	6.16	0.356	265	0.048	9.36	4.59	14.0	6.58
95	15.9	7.41	326	161	78.3	5.74	6.54	0.520	245	0.032	8.33	4.28	15.1	9.73
96	14.0	7.53	432	151	94.8	10.0	14.1	0.481	225	0.087	21.6	1.46	95.9	7.97
97	13.5	7.49	621	191	147	18.4	11.1	0.418	192	0.091	15.7	2.92	278	8.64
98	12.5	7.70	291	291	64.4	4.67	7.15	0.278	192	0.023	11.0	2.78	20.9	8.10
99	12.0	7.91	293	178	71.1	4.59	2.53	2.15	229	0.036	3.84	3.42	9.17	7.22
100	12.2	7.73	344	160	67.4	2.85	22.2	0.203	186	0.030	35.8	4.27	21.5	7.83
101	11.3	7.75	806	168	65.7	4.76	139	0.559	140	0.162	225	0.10	47.4	8.02
102	12.3	7.19	1059	160	319	36.5	4.94	0.317	203	0.422	4.54	0.37	765	9.63
103	11.3	7.32	623	183	147	28.5	6.94	0.606	200	0.186	8.07	2.46	311	8.97
104	11.9	7.39	1368	-38	378	54.6	16.5	0.587	167	0.973	21.3	0.06	988	8.35
105	12.5	7.22	1298	81	422	20.5	4.30	0.469	196	0.300	3.24	1.91	948	10.2
106	12.3	7.42	295	122	79.9	1.35	4.02	1.08	239	0.023	5.13	11.2	6.25	8.94
107	15.5	7.08	9560	168	183	250	2,175	85.6	402	0.015	3,888	23.9	621	25.2
108	13.4	7.32	19930	153	366	637	5,587	245	353	0.015	9,990	1.05	1372	39.8
109	18.6	7.04	17390	102	336	526	4,690	181	387	0.015	8,502	0.92	1168	35.4
110	15.3	6.95	561	125	134	22.5	7.30	0.567	517	0.086	8.61	1.13	7.63	8.34
111	14.7	7.10	517	182	119	23.4	6.98	0.633	467	0.095	6.85	0.27	7.65	8.31
112	13.0	7.33	393	136	80.4	27.0	4.47	1.67	353	0.015	5.70	8.14	11.2	11.2
113	14.0	7.84	219	124	53.1	4.04	4.33	0.184	175	0.032	6.13	0.48	7.07	6.63
114	18.5	7.26	3840	118	110	73.9	882	28.9	295	0.450	1,480	10.5	171	13.1
115	17.1	7.45	2069	99	73.9	33.5	276	12.3	221	0.108	508	6.43	83.6	11.3
116	14.9	7.34	2999	168	107	58.1	444	16.4	286	0.015	792	18.4	111	17.0
117	27.8	7.84	2949	175	93.6	87.8	411	24.8	522	0.333	664	10.2	120	30.4
118	33.5	7.81	21450	114	356	509	4,483	186	463	0.015	8,343	47.6	1,158	44.3
119	20.6	7.09	12950	152	234	279	2,436	80.9	401	0.015	4,154	24.6	605	22.1
120	18.1	7.03	10520	153	214	222	1,894	75.9	372	0.015	3,390	31.0	495	20.4
121	17.0	8.23	395	154	50.5	5.63	15.5	1.36	160	0.129	21.6	1.42	12.9	6.55

Appendix A2 – Table A2

ID	T	pH	E.C.	Eh	Ca ²⁺	Mg ²⁺	Na ⁺	K ⁺	HCO ₃ ⁻	F ⁻	Cl ⁻	NO ₃ ⁻	SO ₄ ²⁻	SiO ₂
122	14.8	8.13	358	140	73.1	1.73	2.57	0.321	215	0.051	4.30	0.86	2.89	8.64
123	12.6	7.40	419	159	74.7	1.91	7.08	0.543	270	0.040	4.15	1.21	2.75	8.72
124	14.1	7.34	403	162	76.7	3.11	4.07	0.536	217	0.082	4.54	1.29	4.58	10.0
125	11.6	7.53	363	201	63.1	4.01	4.18	0.778	204	0.091	8.09	7.81	7.11	9.30
126	13.6	7.49	351	168	69.7	2.64	4.44	0.641	231	0.129	4.76	1.66	6.87	9.13
127	14.2	7.35	442	178	88.6	1.99	3.36	0.450	284	0.110	5.01	2.55	4.49	9.49
128	17.5	8.38	414	161	80.2	3.32	5.47	0.708	213	0.125	6.50	3.82	6.10	11.5
129	15.3	7.35	2372	193	599	54.4	7.56	2.36	239	0.589	4.79	21.1	1,466	21.6
130	29.0	7.28	2700	60	186	57.4	301	14.4	112	0.464	547	4.40	467	6.86
131	16.8	7.28	4990	163	146	70.5	894	31.3	287	0.338	1,487	13.4	183	13.4
132	13.6	7.50	540	165	85.8	13.1	4.23	0.680	205	0.190	7.28	4.72	98.5	9.68
133	13.6	7.68	354	154	62.3	2.27	3.33	0.508	182	0.057	6.00	5.10	16.3	10.6
134	15.1	7.64	351	153	49.1	7.18	9.06	0.868	176	0.068	17.8	3.65	5.96	11.1
135	10.4	7.82	235	199	43.9	1.53	1.11	0.282	145	0.032	1.71	1.01	2.37	5.11
136	15.8	7.06	691	204	128	21.9	6.09	0.817	516	0.179	7.85	1.20	6.68	7.90
137	15.2	7.02	769	209	152	20.8	6.55	0.872	580	0.141	8.13	1.15	7.26	8.85
138	19.2	7.40	534	179	80.0	28.8	3.56	0.891	370	0.143	4.72	16.1	8.26	8.80
139	5.6	7.92	182	176	35.9	0.91	0.93	0.407	119	0.048	0.12	0.91	2.17	5.17
140	14.0	8.45	245	160	36.5	9.56	1.94	0.282	171	0.029	0.60	0.47	4.50	12.9
141	7.2	8.18	243	168	42.9	2.26	1.30	0.278	146	0.038	0.75	0.73	2.44	4.87
142	12.6	7.45	314	196	65.7	1.46	1.34	0.352	214	0.036	2.13	2.64	1.73	8.54
143	11.8	7.63	330	190	60.3	1.29	1.36	0.364	200	0.055	1.97	1.52	1.93	8.21
144	14.9	7.36	9580	112	171	217	1851	70.4	174	0.224	3,174	6.23	498	7.39
145	18.2	7.51	430	143	46.4	20.1	17.2	0.751	222	0.030	30.4	3.45	8.36	8.10
146	16.9	7.70	415	183	42.1	13.4	21.9	0.829	160	0.023	38.8	4.68	10.7	6.55
147	16.5	7.77	411	186	42.6	14.2	18.7	0.712	164	0.051	35.3	4.54	13.8	5.83
148	26.0	7.87	3950	126	97.4	89.9	669	24.2	243	0.042	1,125	8.23	184	4.38
149	17.0	7.65	462	126	45.6	23.7	21.2	0.731	219	0.057	38.5	7.37	12.8	5.35
150	19.8	7.42	860	122	79.8	39.6	46.7	7.55	309	0.091	83.1	2.45	100	7.26
151	14.7	8.13	430	126	34.7	19.7	13.5	2.81	199	0.051	29.5	1.62	10.5	2.66
152	11.6	7.75	255	253	39.3	6.08	6.02	0.645	139	0.027	10.8	1.91	4.49	4.33

Appendix A2 – Table A2

ID	T	pH	E.C.	Eh	Ca ²⁺	Mg ²⁺	Na ⁺	K ⁺	HCO ₃ ⁻	F ⁻	Cl ⁻	NO ₃ ⁻	SO ₄ ²⁻	SiO ₂
153	11.7	7.78	457	123	64.8	12.1	8.77	0.387	136	0.027	16.0	1.27	92.3	3.60
154	15.3	7.39	298	150	35.8	14.4	8.10	0.196	164	0.038	15.4	3.54	7.00	3.65
155	15.0	7.63	469	131	68.8	16.7	12.8	0.665	220	0.163	22.4	2.46	52.4	4.43
156	17.6	7.85	405	130	43.6	11.9	22.9	0.762	136	0.163	38.8	7.01	29.2	8.12
157	17.0	7.03	726	209	92.7	27.8	22.5	0.978	189	0.283	28.2	2.64	185	6.69
158	15.6	7.11	346	130	43.7	17.0	11.7	0.500	187	0.074	20.3	3.84	13.9	5.63
159	25.6	7.19	1071	75	94.0	30.9	85.8	3.245	139	0.188	138	3.73	229	2.42
160	15.5	7.05	3690	232	109	79.5	580	18.3	159	0.154	1,148	21.1	183	4.50
161	12.5	7.22	333	121	49.0	8.13	5.59	0.289	190	0.061	10.0	3.08	5.50	3.20
162	10.8	7.32	204	78	30.7	3.96	3.47	0.168	115	0.036	5.90	1.47	2.12	1.96
163	10.5	7.25	206	113	31.4	3.78	3.51	0.180	115	0.038	5.98	1.66	2.21	1.92
164	15.9	7.25	989	246	51.8	24.7	122	5.07	180	0.249	201	4.46	40.2	4.99
165	12.5	7.14	261	108	38.4	7.21	6.43	0.262	147	0.074	12.03	12.0	4.43	3.59
166	14.5	7.17	325	116	39.1	11.4	8.71	0.317	156	0.171	15.8	2.33	11.4	4.61
167	17.3	7.12	740	254	91.7	21.5	35.2	2.15	243	0.122	55.9	9.13	103	7.35
168	12.5	7.51	279	n.m.	45.5	3.04	4.58	0.266	135	0.040	8.02	0.71	5.19	4.68
169	18.5	6.79	761	110	107	11.9	41.5	1.42	365	0.154	63.6	15.1	18.6	48.4
170	16.0	7.03	4860	70	159	99.8	766	35.7	292	0.124	1,349	6.70	248	9.20
171	18.7	7.09	1080	124	85.0	35.4	91.9	1.88	336	0.063	154	9.67	51.0	23.22
172	15.7	7.61	8100	102	140	177	1,487	43.00	175	0.114	2,557	13.2	426	3.06
173	16.4	7.26	5390	156	140	121	1,094	38.4	242	1.106	1,906	11.3	263	10.9
174	16.5	7.42	380	159	80.2	3.88	5.08	0.626	225	0.097	5.72	2.23	21.6	8.62
175	15.5	6.47	1001	291	290	17.6	5.01	0.821	988	0.346	4.15	9.67	8.60	18.2
176	7.2	7.96	181	145	40.3	0.60	0.80	0.156	120	0.074	0.85	0.81	1.54	3.46
177	13.0	7.94	671	113	53.7	3.94	99.6	0.430	140	0.295	145	2.98	35.5	6.77
178	12.4	7.52	300	155	70.5	1.32	2.00	0.430	209	0.074	2.98	4.53	1.83	7.13
179	12.4	7.83	365	136	82.4	1.69	2.07	0.508	244	0.076	3.09	3.35	2.11	7.44
180	20.1	8.37	1166	126	290	26.1	5.26	0.782	114	0.397	6.82	2.36	716	0.30
181	12.9	7.06	1326	141	348	23.9	8.05	0.626	265	0.637	6.28	7.94	716	8.66
182	11.2	7.60	393	112	79.6	7.61	4.44	0.430	172	0.184	6.11	1.36	77.8	6.19
183	10.4	8.08	206	138	38.1	7.24	1.68	0.274	136	0.173	1.56	0.81	8.70	4.67

Appendix A2 – Table A2

ID	T	pH	E.C.	Eh	Ca ²⁺	Mg ²⁺	Na ⁺	K ⁺	HCO ₃ ⁻	F ⁻	Cl ⁻	NO ₃ ⁻	SO ₄ ²⁻	SiO ₂
184	12.0	7.66	245	218	53.5	1.85	2.60	0.391	160	0.106	3.83	0.74	8.55	5.90
185	12.9	7.41	348	156	80.0	2.58	2.14	0.508	204	0.053	4.19	0.62	33.5	7.13
186	16.0	7.30	435	130	93.4	4.33	8.28	0.704	234	0.089	14.7	6.51	47.6	7.05
187	13.3	7.39	979	130	212	28.2	6.90	0.508	188	0.481	10.2	1.98	470	5.37
188	16.3	7.26	520	154	94.6	11.0	15.1	1.02	265	0.086	20.2	4.40	51.9	7.07
189	6.5	7.97	175	109	37.3	2.47	1.59	0.235	123	0.084	1.21	0.74	3.32	3.40
190	19.2	7.30	2174	90	121	37.9	341	12.0	316	0.015	618	11.8	99.0	9.35
191	12.0	7.50	281	130	61.5	0.77	2.37	0.196	191	0.034	5.50	1.86	3.80	5.68
192	16.1	6.96	569	136	127	2.67	8.37	0.626	380	0.023	13.1	9.18	3.32	8.87
193	12.0	7.26	451	136	86.6	8.90	3.63	0.274	203	0.143	6.07	0.99	95.6	5.73
194	13.2	7.50	409	130	51.9	25.8	3.33	0.196	281	0.127	5.68	1.12	7.21	3.59
195	12.2	7.85	253	128	40.1	10.3	2.57	0.117	157	0.038	4.72	1.67	4.08	3.64
196	15.2	7.21	395	119	94.2	0.94	3.06	0.117	288	0.110	6.14	2.73	4.32	7.48
197	14.1	7.13	455	168	107	2.49	3.61	0.391	315	0.093	6.57	3.91	4.04	7.55
198	14.3	7.18	448	145	101	7.62	4.00	0.508	309	0.095	5.29	4.90	18.9	8.16
199	10.5	7.33	366	35	77.2	2.54	2.53	0.235	244	0.097	3.98	0.37	3.80	7.22
200	13.4	7.08	505	120	112	3.78	6.32	0.391	337	0.084	9.41	23.1	8.84	9.97
201	14.3	7.30	462	156	95.2	3.55	6.78	0.508	288	0.105	11.1	6.01	6.20	10.4

n.m. – not measured

Table A3

Chemical composition of trace elements of the collected Hellenic karst springs.

ID	Li μg L ⁻¹	B μg L ⁻¹	Al μg L ⁻¹	Ti μg L ⁻¹	V μg L ⁻¹	Cr μg L ⁻¹	Mn μg L ⁻¹	Fe μg L ⁻¹	Co μg L ⁻¹	Ni μg L ⁻¹	Cu μg L ⁻¹	Zn μg L ⁻¹	As μg L ⁻¹	Se μg L ⁻¹	Br- μg L ⁻¹	Rb μg L ⁻¹	Sr μg L ⁻¹	Mo μg L ⁻¹	Cd μg L ⁻¹	Sb μg L ⁻¹	Cs μg L ⁻¹	Ba μg L ⁻¹	Tl μg L ⁻¹	Pb μg L ⁻¹	U μg L ⁻¹
1	1.76	9.16	0.621	0.58	0.607	0.454	0.05	0.507	0.127	0.083	0.10	0.100	2.63	0.261	19.0	1.57	113	0.716	0.02	0.099	0.192	17.3	0.02	0.05	1.36
2	1.45	8.53	0.849	0.61	0.642	0.509	0.05	0.682	0.141	0.151	0.25	0.870	3.06	0.263	17.1	1.44	161	0.837	0.01	0.129	0.147	18.5	0.02	0.05	1.39
3	4.95	8.06	0.699	0.67	0.790	0.428	0.05	0.702	0.124	0.126	0.33	0.650	1.71	0.296	14.5	2.18	235	2.02	0.01	0.113	0.548	14.4	0.01	0.05	2.09
4	2.41	6.66	0.797	0.52	0.568	0.367	0.05	0.590	0.145	0.113	0.13	0.480	0.904	0.205	11.3	1.47	85.2	0.515	0.01	0.041	0.346	10.7	0.02	0.13	0.769
5	1.28	6.82	0.960	0.49	0.622	0.289	0.02	0.852	0.155	0.145	0.22	0.707	0.854	0.209	13.0	1.44	84.7	0.472	0.01	0.060	0.188	10.8	0.02	0.05	0.756
6	0.86	11.1	4.20	0.68	0.837	0.237	0.36	3.82	0.131	0.150	0.33	0.100	0.490	0.198	10.2	0.904	77.8	0.697	0.02	0.100	0.026	15.2	0.05	1.00	1.28
7	1.98	9.85	0.748	0.77	1.38	0.738	1.17	0.884	0.124	0.160	0.08	0.100	6.48	0.291	18.6	2.01	231	1.49	0.02	0.265	0.126	22.0	0.01	0.05	2.47
8	1.69	11.3	0.742	1.05	1.07	0.682	1.27	0.481	0.108	0.078	0.10	0.100	5.58	0.267	13.6	1.76	172	1.65	0.02	0.188	0.130	17.5	0.05	0.05	1.77
9	3.09	17.7	0.600	0.70	1.00	0.523	0.05	0.463	0.119	0.142	0.10	0.100	2.45	0.199	12.4	2.17	181	1.17	0.02	0.040	0.187	19.7	0.11	0.05	2.99
10	30.6	138	0.540	1.18	2.41	1.77	0.05	0.595	0.166	0.393	0.10	0.100	3.68	0.228	19.3	13.2	282	1.90	0.03	0.073	3.77	20.5	0.20	0.05	2.56
II	7.49	16.1	0.954	0.94	0.421	0.709	0.17	2.06	0.379	2.50	0.27	0.590	0.267	0.442	17.9	1.49	305	0.774	0.01	0.050	0.083	7.58	0.05	0.05	1.01
12	1.84	30.1	0.500	0.93	0.659	0.453	0.10	1.56	0.182	0.086	0.20	0.200	3.07	0.268	6.57	1.87	117	1.03	0.05	0.143	0.238	17.0	0.02	0.10	0.151
13	9.19	27.0	0.500	0.99	0.790	0.770	0.02	0.960	0.250	0.340	0.10	5.58	1.81	0.300	11.9	1.16	277	0.990	0.01	0.090	0.270	42.2	0.02	0.01	0.550
14	5.92	24.4	0.500	1.24	0.800	3.74	0.66	0.990	0.260	0.210	0.10	2.93	0.290	0.370	13.7	0.664	250	0.670	0.01	0.030	0.010	36.6	0.01	0.04	0.520
15	1.18	8.20	0.500	1.42	1.09	2.00	0.05	2.33	0.240	0.300	0.10	1.80	0.630	0.240	11.6	0.593	114	0.560	0.01	0.020	0.290	19.6	0.01	0.01	0.560
16	1.57	22.1	0.500	2.69	1.62	0.680	0.05	0.620	0.220	0.040	0.10	1.14	0.420	0.230	18.7	0.480	157	0.720	0.01	0.020	0.010	40.8	0.01	0.01	1.01
17	1.34	19.6	0.500	2.22	1.56	0.520	0.02	0.920	0.220	0.130	0.03	2.04	0.390	0.220	16.5	0.450	162	0.610	0.01	0.020	0.010	33.5	0.01	0.01	0.900
18	3.98	47.4	0.500	2.57	1.01	0.350	0.05	0.670	0.210	0.060	0.10	0.980	0.550	0.300	18.5	1.10	220	0.870	0.01	0.030	0.180	41.1	0.01	0.01	0.970
19	12.5	157	0.500	2.01	2.13	1.66	0.04	1.12	0.400	0.680	0.10	2.28	2.91	0.360	22.0	2.32	338	2.48	0.01	0.060	0.260	36.1	0.03	0.01	2.67
20	0.46	4.30	0.500	0.72	0.770	1.67	0.05	0.610	0.150	0.150	0.10	1.17	0.400	0.180	4.56	0.568	112	0.260	0.01	0.060	0.010	8.53	0.01	0.01	0.650
21	4.28	62.6	0.500	1.72	0.490	2.22	0.02	1.09	0.300	0.390	0.47	2.13	0.680	0.230	22.7	1.36	245	0.850	0.01	0.030	0.030	25.1	0.01	0.06	1.45
22	0.62	18.3	0.500	1.41	0.660	5.13	0.02	1.04	0.240	0.270	0.79	2.53	0.840	0.120	6.92	0.774	186	0.080	0.01	0.100	0.030	11.5	0.01	0.05	0.200
23	6.28	104	0.500	2.95	1.62	3.56	0.08	0.980	0.370	1.15	0.09	1.54	0.940	0.330	29.9	3.08	276	0.950	0.01	0.070	0.230	34.9	0.01	0.01	2.10
24	2.10	38.1	0.500	1.15	0.910	3.58	0.05	0.790	0.250	0.430	0.10	1.03	0.470	0.220	11.2	0.570	159	0.460	0.01	0.040	0.010	9.80	0.01	0.01	0.700
25	2.21	36.6	0.500	0.86	0.580	1.84	0.02	0.850	0.210	0.260	0.25	1.48	0.330	0.200	8.17	0.543	145	0.540	0.01	0.030	0.010	7.09	0.01	0.03	0.550
26	1.96	37.8	0.500	1.57	0.650	3.81	0.05	0.930	0.270	3.84	0.10	0.990	0.270	0.150	11.0	0.558	165	0.350	0.01	0.020	0.010	16.3	0.01	0.01	0.760
27	0.71	3.44	0.500	1.52	0.300	0.450	0.02	0.820	0.250	0.080	0.10	1.81	0.170	0.110	6.72	0.352	61	0.550	0.01	0.010	0.010	14.6	0.01	0.01	1.36
28	1.88	30.6	0.500	0.75	0.600	1.58	0.05	0.770	0.230	0.100	0.10	1.23	1.34	0.150	5.92	0.800	110	0.510	0.01	0.030	0.060	7.10	0.01	0.01	1.39

Appendix A2 – Table A3

ID	Li	B	Al	Ti	V	Cr	Mn	Fe	Co	Ni	Cu	Zn	As	Se	Br-	Rb	Sr	Mo	Cd	Sb	Cs	Ba	Tl	Pb	U
29	1.90	30.6	0.500	0.77	0.590	1.59	0.03	0.870	0.240	0.120	0.10	1.69	1.35	0.130	6.20	0.800	111	0.560	0.01	0.040	0.060	7.18	0.01	0.01	1.42
30	1.93	30.8	0.500	0.79	0.590	1.58	0.05	1.09	0.230	0.110	0.10	2.79	1.32	0.170	5.93	0.810	115	0.660	0.01	0.040	0.060	7.88	0.01	0.01	1.40
31	1.76	28.8	0.500	0.71	0.618	1.67	0.05	0.920	0.225	0.100	0.10	0.984	1.38	0.150	5.74	0.748	106	0.460	0.01	0.030	0.060	6.79	0.01	0.01	1.35
32	5.69	78.9	0.100	0.62	0.842	0.430	0.10	2.32	0.183	0.400	0.16	3.54	6.15	0.247	10.6	2.10	181	1.72	0.01	0.369	0.735	43.3	0.19	0.01	1.50
33	0.84	8.26	0.172	0.64	0.100	0.374	0.18	11.0	0.131	2.10	4.29	1.70	0.100	0.237	12.8	0.304	132	0.290	0.01	0.012	0.005	11.6	0.10	0.01	0.381
34	0.33	2.36	0.196	0.80	0.100	0.100	4.10	42.5	0.184	0.229	0.10	1.05	0.100	0.145	23.4	0.987	89.4	0.086	0.01	0.009	0.010	14.5	0.08	0.01	0.369
35	0.58	6.42	0.100	0.41	0.100	0.527	0.10	0.283	0.120	0.172	0.14	1.38	0.193	0.119	5.87	0.468	87.8	0.202	0.01	0.009	0.017	8.67	0.05	0.01	0.298
36	0.61	7.55	0.376	0.42	0.100	0.657	0.10	0.631	0.109	0.164	0.10	1.30	0.230	0.116	5.54	0.469	88.1	0.435	0.01	0.010	0.048	8.40	0.05	0.01	0.305
37	0.31	6.74	0.253	0.70	0.100	0.199	0.12	0.100	0.081	0.082	0.10	0.610	0.054	0.058	4.82	0.406	58.5	0.143	0.01	0.010	0.006	10.5	0.03	0.01	0.419
38	0.63	2.16	0.100	0.68	0.100	0.716	0.10	0.956	0.222	1.16	0.10	1.14	0.100	0.208	6.54	0.551	95.6	0.036	0.01	0.010	0.010	11.1	0.03	0.01	0.172
39	16.0	139	0.100	0.50	1.54	0.815	0.10	0.709	0.202	0.588	0.10	1.10	17.00	0.176	n.m.	2.51	242	2.27	0.01	0.265	1.57	19.9	0.06	0.01	1.10
40	0.76	11.7	0.100	1.33	0.805	3.57	0.10	0.458	0.161	0.249	0.10	0.793	0.189	0.871	22.9	0.617	136	0.508	0.01	0.010	0.010	30.5	0.02	0.01	1.13
41	1.35	17.0	0.100	1.18	1.86	5.60	6.81	22.0	0.173	0.419	0.10	1.80	0.278	0.380	13.0	0.404	167	0.334	0.01	0.011	0.010	19.9	0.02	0.01	0.243
42	0.30	3.53	0.327	0.25	0.100	0.100	0.10	0.402	0.086	0.087	0.10	1.64	0.100	0.133	5.45	0.176	42.8	0.124	0.01	0.010	0.010	5.03	0.01	0.01	0.109
43	0.54	5.14	0.215	0.33	0.100	0.090	0.10	0.491	0.095	0.259	0.39	1.52	0.100	0.087	4.96	0.196	52.7	0.244	0.01	0.010	0.010	4.23	0.02	0.01	0.082
44	0.39	4.05	0.197	0.34	0.100	0.100	0.10	0.121	0.088	0.072	0.10	0.909	0.100	0.086	4.26	0.145	47.8	0.124	0.01	0.010	0.010	4.22	0.02	0.01	0.075
45	7.17	4.83	10.5	0.73	3.89	0.774	3.65	71.3	0.056	0.504	11.6	22.6	0.501	0.100	11.4	54.7	61.3	0.389	0.01	0.075	0.851	4.55	0.01	0.13	0.093
46	61.9	1553	0.100	0.10	0.100	0.100	0.10	11.1	0.481	1.08	0.10	0.100	0.063	0.100	n.m.	43.4	3404	2.97	0.01	0.010	0.731	22.8	0.08	0.01	1.52
47	0.29	2.44	9.36	0.23	0.191	0.588	0.55	17.9	0.123	0.702	0.07	1.52	0.247	0.146	5.30	0.332	95.5	0.478	0.01	0.021	0.010	18.3	0.02	0.01	0.335
48	0.33	1.18	0.483	0.21	0.100	0.347	0.10	0.076	0.065	0.054	0.10	0.249	0.100	0.100	3.60	0.115	79.7	0.056	0.01	0.010	0.010	22.4	0.01	0.01	0.054
49	0.10	2.71	0.092	0.20	0.100	0.185	0.10	0.372	0.110	0.115	0.10	0.099	0.100	0.100	7.72	0.133	56.8	0.020	0.01	0.010	0.010	4.56	0.01	0.01	0.168
50	0.10	1.49	0.100	0.19	0.100	0.069	0.10	0.551	0.131	0.160	0.10	0.728	0.100	0.052	8.94	0.114	55.4	0.060	0.01	0.010	0.010	4.61	0.01	0.01	0.180
51	66.8	1429	0.100	0.10	0.100	2.16	0.10	13.4	0.449	1.90	0.10	0.100	12.05	0.100	22,601	47.0	3280	5.70	0.01	0.010	6.89	23.9	0.12	0.01	3.11
52	1.42	8.87	0.100	0.55	0.100	0.374	0.10	0.437	0.137	0.149	0.10	0.278	0.227	0.138	26.4	0.238	91.9	0.113	0.01	0.010	0.003	8.41	0.01	0.01	0.203
53	2.10	21.7	0.100	0.83	2.67	2.91	0.10	0.380	0.154	0.509	0.10	0.100	0.306	0.427	35.8	0.342	194	0.124	0.01	0.010	0.023	32.6	0.01	0.01	0.414
54	0.10	1.42	0.636	0.17	0.100	0.335	0.10	0.441	0.122	0.399	0.10	0.100	0.100	0.051	6.89	0.112	52.5	0.020	0.01	0.009	0.010	11.1	0.01	0.01	0.064
55	0.10	2.42	0.865	0.31	0.100	0.873	0.10	0.896	0.126	0.526	0.10	0.100	0.087	0.082	8.40	0.177	82.5	0.020	0.01	0.010	0.002	16.8	0.01	0.01	0.091
56	0.10	2.98	0.538	0.28	0.058	0.786	0.10	0.624	0.143	0.766	0.06	0.100	0.093	0.060	8.72	0.169	60.5	0.019	0.01	0.014	0.010	16.9	0.01	0.01	0.142
57	1.91	8.34	0.460	0.41	0.100	0.703	0.10	0.165	0.070	0.180	0.10	0.270	0.374	1.16	11.3	0.408	359	0.764	0.01	0.039	0.003	123	0.01	0.01	0.237
58	2.90	20.2	0.100	0.71	0.076	0.513	0.12	0.746	0.157	0.266	0.10	0.339	0.097	0.542	52.5	0.646	542	0.233	0.01	0.010	0.010	61.4	0.00	0.01	0.196
59	4.56	18.1	0.100	0.73	0.100	0.262	0.10	0.713	0.122	0.163	0.10	0.983	0.076	2.01	15.0	0.722	520	0.487	0.01	0.015	0.005	151	0.01	0.02	0.327
60	0.95	6.27	0.116	0.46	0.100	0.931	0.10	0.169	0.080	0.069	0.10	0.205	0.045	0.526	15.8	0.364	255	0.208	0.01	0.010	0.010	75.1	0.01	0.01	0.127

Appendix A2 – Table A3

ID	Li	B	Al	Ti	V	Cr	Mn	Fe	Co	Ni	Cu	Zn	As	Se	Br-	Rb	Sr	Mo	Cd	Sb	Cs	Ba	Tl	Pb	U
61	48.6	494	0.100	0.10	0.100	0.100	0.10	3.75	0.224	0.216	0.10	0.100	9.21	0.096	7,905	19.2	1890	1.10	0.01	0.010	3.16	22.0	0.01	0.01	0.412
62	65.0	1,193	0.100	0.10	0.100	0.100	0.10	19.8	0.163	0.100	0.10	0.100	3.27	0.100	19,653	41.2	4173	0.468	0.01	0.010	3.74	25.0	0.07	0.01	0.680
63	85.1	1,860	0.100	0.10	0.100	0.100	0.10	27.4	0.230	0.143	0.10	0.100	12.1	0.100	28,122	62.4	5026	2.95	0.01	0.010	2.30	24.5	0.15	0.01	1.35
64	15.7	333	0.100	0.96	0.100	5.87	0.74	8.44	0.205	2.67	0.10	0.351	2.01	0.137	6,679	11.6	918	1.64	0.01	0.010	0.616	19.5	0.16	0.01	1.83
65	1.98	12.7	0.100	0.85	1.71	2.65	1.14	0.881	0.152	0.868	0.10	0.545	2.51	0.232	307	0.805	178	0.562	0.01	0.042	0.092	28.9	0.02	0.01	0.835
66	2.92	35.8	0.481	0.80	0.789	0.868	0.93	1.42	0.143	1.01	0.10	1.02	0.640	0.061	463	1.16	261	0.549	0.01	0.016	0.037	36.2	0.01	0.01	0.679
67	0.26	4.00	0.100	0.42	0.577	1.97	0.10	0.551	0.146	0.671	0.10	0.240	0.089	0.135	16.0	0.266	88.2	0.118	0.01	0.010	0.010	14.4	0.01	0.01	0.409
68	0.42	3.67	0.100	0.46	0.969	2.63	0.10	0.411	0.117	0.424	0.10	0.572	0.242	0.201	16.3	0.284	83.9	0.175	0.01	0.009	0.013	14.4	0.01	0.01	0.455
69	0.43	14.5	0.453	0.47	0.669	1.24	0.10	0.636	0.146	1.02	0.12	1.12	0.208	0.293	24.5	0.268	167	0.438	0.01	0.027	0.010	30.1	0.01	0.01	0.312
70	1.67	8.04	0.153	0.67	1.42	2.62	0.10	0.504	0.130	0.268	0.10	0.312	0.537	0.186	17.5	1.36	164	0.509	0.01	0.010	0.065	15.6	0.03	0.01	0.378
71	2.03	25.5	1.94	0.50	0.302	0.591	0.06	0.142	0.016	0.252	0.34	0.327	0.062	0.454	70.5	0.398	351	0.101	0.03	0.015	0.010	41.2	0.01	0.02	0.236
72	1.80	16.8	2.29	0.50	1.99	0.595	0.05	0.117	0.010	0.145	0.02	0.508	0.538	0.383	102	0.459	1438	2.52	0.03	0.057	0.025	61.2	0.02	0.02	1.41
73	1.92	18.0	2.25	0.50	2.12	0.588	0.05	0.100	0.010	0.172	0.03	0.440	0.496	0.439	107	0.538	1684	2.93	0.03	0.062	0.026	45.7	0.02	0.02	1.55
74	1.39	14.1	4.50	0.50	0.317	0.937	1.25	1.22	0.018	0.252	0.18	0.247	0.051	0.364	28.4	0.229	344	0.091	0.03	0.020	0.010	22.9	0.01	0.02	0.176
75	0.44	7.94	15.8	0.50	1.15	0.453	0.05	0.238	0.009	0.033	0.05	0.111	0.112	0.247	22.3	0.222	398	0.515	0.03	0.025	0.010	9.15	0.01	0.02	0.885
76	0.18	4.45	13.6	0.50	0.252	0.754	0.05	0.202	0.008	0.050	0.05	0.096	0.044	0.200	10.3	0.096	138	0.013	0.03	0.020	0.010	4.91	0.01	0.02	0.053
77	0.38	5.76	10.7	0.50	0.346	0.854	0.05	0.473	0.023	0.062	0.12	0.144	0.076	0.200	13.5	0.186	223	0.031	0.03	0.020	0.010	13.0	0.01	0.02	0.097
78	0.49	4.44	8.90	0.50	0.203	0.465	0.05	0.220	0.009	0.042	0.14	0.242	0.074	0.200	13.1	0.139	288	0.337	0.03	0.020	0.010	17.4	0.01	0.02	0.095
79	0.47	7.18	42.8	0.50	0.472	0.476	0.30	1.03	0.018	0.111	0.20	0.690	0.114	0.401	20.0	0.151	372	0.716	0.03	0.012	0.010	22.2	0.01	0.02	0.243
80	0.59	8.25	7.33	0.50	0.631	0.489	0.30	15.4	0.026	0.256	0.27	0.491	0.372	0.538	20.5	0.177	356	0.549	0.03	0.033	0.010	20.0	0.02	0.02	0.654
81	0.39	5.90	4.84	0.50	1.37	0.511	0.05	0.262	0.013	0.085	0.08	0.611	0.143	0.363	12.5	0.205	171	0.845	0.03	0.022	0.010	27.9	0.01	0.02	0.736
82	0.46	6.13	2.15	0.50	0.805	0.535	0.05	0.164	0.016	0.075	0.06	0.312	0.316	0.313	15.0	0.132	195	0.316	0.03	0.014	0.010	15.1	0.01	0.02	0.491
83	0.22	3.16	3.68	0.50	0.886	0.322	0.06	0.128	0.013	0.033	0.04	0.420	0.395	0.331	8.78	0.123	288	1.17	0.03	0.020	0.010	16.4	0.01	0.02	0.625
84	40.2	1045	2.92	0.50	1.43	0.592	0.05	0.100	0.010	0.206	0.05	0.100	3.05	0.945	14,884	26.6	2872	4.71	0.45	0.113	0.222	55.1	0.07	0.02	1.32
85	2.07	13.7	2.17	0.50	0.717	0.683	0.46	0.595	0.011	0.125	0.11	0.300	0.145	0.235	204	0.576	734	0.774	0.03	0.014	0.027	40.8	0.01	0.02	0.518
86	1.36	9.48	3.66	0.50	0.869	0.794	0.55	0.719	0.019	0.271	0.17	0.374	0.150	0.384	26.8	0.286	574	0.951	0.03	0.017	0.010	30.1	0.02	0.02	0.609
87	34.1	780	4.08	0.50	1.22	0.548	0.57	1.53	0.023	0.770	0.03	0.182	0.399	2.34	10,591	20.1	1587	1.64	0.45	0.106	0.185	25.3	0.02	0.02	0.525
88	71.6	1,847	4.62	0.50	2.75	1.80	2.00	0.217	0.010	1.20	1.00	0.100	1.50	3.43	24,915	46.0	3472	4.97	0.20	0.243	0.765	19.1	0.03	0.02	1.49
89	142	3,859	6.95	0.50	1.39	1.15	2.00	0.309	0.010	0.538	1.00	0.100	2.99	9.71	52,717	93.3	6617	10.1	0.20	0.422	1.35	26.5	0.05	0.02	2.40
90	174	3,871	9.85	0.50	1.28	1.30	2.00	2.05	0.010	0.560	0.05	0.100	7.59	14.0	49,878	98.6	7081	12.0	0.99	0.440	3.14	46.4	0.01	0.02	2.54
91	153	2,020	3.90	0.50	1.14	0.948	2.00	0.228	0.010	2.50	1.00	0.397	4.92	3.000	23,619	59.8	4484	6.12	0.57	0.232	4.60	46.4	0.06	0.02	1.41
92	0.99	8.82	2.16	0.50	0.840	1.43	2.00	0.287	0.011	0.375	0.68	3.66	0.988	0.348	43.0	0.322	96.7	0.062	0.03	0.018	0.054	11.6	0.01	0.02	0.219

Appendix A2 – Table A3

ID	Li	B	Al	Ti	V	Cr	Mn	Fe	Co	Ni	Cu	Zn	As	Se	Br-	Rb	Sr	Mo	Cd	Sb	Cs	Ba	Tl	Pb	U
93	5.75	58.2	2.27	0.50	0.838	2.13	3.38	5.26	0.050	1.51	0.51	68.1	1.50	0.308	180	1.46	296	0.446	0.03	0.049	0.147	31.9	0.03	0.02	1.87
94	1.58	16.2	1.59	0.23	0.983	0.599	0.05	0.056	0.010	0.050	0.05	0.154	0.117	0.323	28.9	0.342	131	0.109	0.05	0.020	0.005	13.2	0.00	0.01	0.321
95	1.29	17.4	1.91	0.25	0.772	0.944	0.05	0.156	0.010	0.061	0.05	0.184	0.164	0.326	23.2	0.280	166	0.223	0.05	0.020	0.005	34.0	0.01	0.01	0.249
96	1.75	15.4	2.12	0.33	1.26	0.656	0.05	0.776	0.008	0.219	0.05	0.178	0.514	0.244	15.5	0.261	527	2.65	0.05	0.089	0.005	41.5	0.01	0.01	0.441
97	2.29	18.1	1.94	0.25	1.72	0.615	0.05	0.434	0.009	0.375	0.08	0.282	0.674	0.523	14.4	0.257	1053	7.23	0.05	0.186	0.005	28.8	0.02	0.01	0.849
98	1.10	9.48	1.74	0.21	0.908	0.698	0.05	0.038	0.010	0.052	0.05	0.444	0.346	0.459	13.2	0.256	181	0.437	0.05	0.029	0.005	91.1	0.00	0.01	0.191
99	0.85	7.78	2.02	0.33	1.45	0.320	0.62	5.67	0.035	0.117	0.12	0.427	0.307	0.421	12.0	0.215	79.1	0.299	0.05	0.042	0.004	32.6	0.01	0.01	0.366
100	1.74	12.0	1.44	0.22	1.05	0.798	0.04	0.426	0.021	0.092	0.14	0.292	0.435	0.410	13.6	0.277	191	0.308	0.05	0.036	0.029	30.4	0.00	0.01	0.163
101	8.66	22.3	1.99	0.29	0.653	0.534	0.05	0.261	0.010	0.033	0.07	0.824	2.82	0.355	27.0	0.614	445	0.260	0.05	0.072	0.239	95.8	0.02	0.01	0.115
102	6.75	29.4	4.19	0.24	0.130	0.265	0.32	1.16	0.020	0.274	0.22	0.232	0.365	0.513	12.2	0.278	3451	4.59	0.05	0.030	0.054	18.1	0.01	0.01	0.226
103	5.51	22.6	1.43	0.24	0.527	0.802	0.05	0.313	0.012	0.286	0.07	0.493	0.522	0.650	14.6	0.407	1967	0.877	0.05	0.087	0.165	18.0	0.01	0.01	0.222
104	14.8	48.7	1.91	0.13	0.077	0.050	1.31	0.654	0.014	0.050	0.05	0.132	0.043	0.430	19.2	0.602	5887	0.190	0.05	0.020	0.362	14.4	0.00	0.01	0.301
105	8.99	43.6	1.28	0.31	2.95	0.285	0.29	0.994	0.021	2.77	0.08	0.726	1.07	1.05	12.0	0.379	4359	10.9	0.05	0.395	0.034	14.9	0.08	0.01	0.750
106	0.57	11.0	1.81	0.21	0.725	0.677	0.70	0.220	0.046	0.158	0.29	0.349	0.268	0.484	12.9	0.355	136	0.092	0.05	0.039	0.005	92.5	0.00	0.01	0.117
107	34.3	1,071	1.69	0.64	1.69	1.88	0.05	0.228	0.016	2.09	0.20	0.050	1.33	3.38	11,480	19.2	1598	3.12	0.05	0.037	0.364	20.9	0.04	0.01	1.83
108	105	2,993	3.19	0.08	1.36	0.981	0.92	3.79	0.062	0.669	0.11	0.224	0.845	7.36	32,224	51.6	4384	3.45	0.05	0.020	0.813	28.4	0.06	0.01	1.68
109	106	3,013	3.89	0.10	1.11	0.670	0.10	0.426	0.015	0.538	0.07	0.530	0.819	7.25	28,084	52.3	4642	2.91	0.05	0.020	0.616	28.6	0.06	0.01	1.31
110	14.4	162	1.25	0.22	1.61	0.917	0.05	0.013	0.010	0.415	0.05	1.16	11.5	0.371	26.7	1.99	217	1.69	0.05	0.240	1.13	19.8	0.03	0.01	0.837
111	17.4	198	1.41	0.32	1.97	1.04	0.05	0.055	0.010	0.465	0.05	0.982	14.5	0.526	26.00	2.33	236	2.27	0.05	0.256	1.36	21.2	0.03	0.01	0.969
112	0.34	19.1	1.47	0.26	0.767	6.58	0.05	0.667	0.015	0.164	0.08	0.247	0.866	0.448	17.2	1.38	102	0.157	0.05	0.019	0.012	18.0	0.00	0.01	0.603
113	0.56	11.0	4.73	0.24	0.484	0.286	0.05	0.522	0.010	0.036	0.13	3.71	0.133	0.377	18.5	0.170	84.4	0.164	0.05	0.020	0.005	18.5	0.00	0.01	0.108
114	40.2	314	3.48	0.16	1.30	0.624	5.03	2.36	0.022	0.151	0.68	12.8	2.86	0.608	2,861	7.66	1307	1.11	0.01	0.211	1.27	59.1	0.02	0.12	0.438
115	7.15	130	1.25	0.10	0.408	0.504	0.31	0.826	0.010	0.020	0.02	0.050	0.152	0.140	1,381	3.02	576	0.481	0.02	0.046	0.136	55.6	0.01	0.01	0.212
116	10.7	125	2.34	0.12	0.923	2.21	0.16	2.72	0.021	1.25	0.26	0.826	1.07	0.457	2,363	3.49	498	0.228	0.02	0.074	0.306	29.3	0.01	0.18	1.12
117	12.2	201	18.4	0.26	3.05	1.43	23.6	60.1	0.872	6.91	1.37	40.8	2.68	0.404	1,822	13.3	435	0.776	0.02	0.411	0.163	18.9	0.01	2.36	0.292
118	76.6	1,920	12.6	0.24	1.89	0.695	20.0	56.5	0.110	3.21	1.95	0.907	1.86	4.48	27,339	46.3	3780	1.39	0.02	0.264	0.325	27.8	0.01	1.49	0.917
119	41.4	986	5.05	0.65	0.680	2.15	0.80	3.17	0.034	0.326	0.26	0.778	2.24	0.653	13,991	25.2	1969	1.87	0.04	0.147	0.160	17.8	0.03	0.23	0.785
120	32.4	742	7.67	0.31	1.18	3.58	0.43	2.95	0.032	0.258	0.64	1.79	0.231	1.39	11,466	17.9	1878	1.43	0.04	0.108	0.072	57.4	0.02	0.34	0.984
121	5.87	21.1	2.57	0.10	0.557	0.264	2.12	3.03	0.023	0.302	1.08	1.31	0.554	0.154	27.1	0.888	309	0.487	0.02	0.086	0.010	35.0	0.01	0.05	0.171
122	0.61	1.69	0.582	0.10	0.415	0.314	1.33	0.444	0.011	0.098	0.23	0.050	0.121	0.139	11.6	0.233	204	0.078	0.02	0.011	0.002	38.6	0.01	0.01	0.096
123	0.67	1.74	0.260	0.10	0.435	0.330	0.02	0.252	0.010	0.101	0.20	0.050	0.140	0.221	10.9	0.245	210	0.084	0.02	0.010	0.002	43.4	0.01	0.01	0.097
124	1.74	9.09	11.4	0.10	0.497	0.299	0.68	1.99	0.014	0.164	0.22	0.579	0.132	0.266	11.8	0.397	312	0.240	0.02	0.064	0.003	80.1	0.01	0.01	0.151

Appendix A2 – Table A3

ID	Li	B	Al	Ti	V	Cr	Mn	Fe	Co	Ni	Cu	Zn	As	Se	Br-	Rb	Sr	Mo	Cd	Sb	Cs	Ba	Tl	Pb	U
I24	1.74	9.09	11.4	0.10	0.497	0.299	0.68	1.99	0.014	0.164	0.22	0.579	0.132	0.266	11.8	0.397	312	0.240	0.02	0.064	0.003	80.1	0.01	0.01	0.151
I25	1.25	8.42	0.326	0.10	0.585	1.61	0.12	0.299	0.020	0.052	0.08	0.050	0.211	0.636	9.38	0.330	270	0.408	0.02	0.020	0.004	53.7	0.01	0.01	0.140
I26	1.46	15.7	0.315	0.10	0.520	0.290	0.09	0.053	0.011	0.125	0.33	0.467	0.193	0.446	12.4	0.391	296	0.357	0.02	0.056	0.002	67.0	0.01	0.01	0.158
I27	0.79	5.02	0.209	0.10	0.479	0.355	0.06	0.050	0.010	0.169	0.22	0.050	0.142	0.263	11.7	0.270	216	0.128	0.02	0.058	0.002	54.8	0.01	0.01	0.137
I28	1.82	14.9	0.398	0.10	0.546	0.292	0.44	0.121	0.012	0.078	0.13	0.050	0.146	0.153	15.8	0.367	278	0.252	0.02	0.019	0.002	51.2	0.01	0.01	0.181
I29	31.7	124	0.560	0.10	1.41	0.605	0.24	0.050	0.035	1.58	0.15	0.050	0.355	0.333	63.8	1.02	8197	3.62	0.02	0.128	0.017	15.1	0.02	0.02	1.48
I30	40.7	122	6.81	0.16	2.29	0.020	2.95	1.79	0.072	0.279	0.14	0.331	1.18	0.136	1,519	4.34	2196	0.297	0.02	0.158	0.015	24.4	0.01	0.82	0.129
I31	12.6	226	5.26	0.30	1.15	0.846	0.28	1.27	0.022	0.279	0.59	4.60	0.216	0.646	3,425	6.54	959	0.564	0.02	0.082	0.119	43.3	0.01	0.41	0.572
I32	4.06	11.9	0.574	0.10	1.27	0.371	0.03	0.048	0.007	0.022	0.03	0.050	0.279	0.250	19.0	0.353	678	0.591	0.02	0.049	0.006	31.8	0.01	0.01	0.429
I33	0.88	3.15	0.172	0.10	0.586	0.391	0.03	0.050	0.009	0.020	0.09	0.100	0.103	0.137	17.3	0.221	216	0.233	0.02	0.040	0.003	62.3	0.01	0.01	0.134
I34	2.23	9.22	0.556	0.10	0.494	0.387	0.71	0.685	0.010	0.068	0.37	0.318	0.219	0.333	46.0	0.365	182	0.337	0.02	0.116	0.003	31.4	0.01	0.01	0.120
I35	0.40	1.00	1.46	0.10	0.232	0.211	0.03	0.046	0.010	0.020	0.04	0.050	0.077	0.154	6.69	0.118	47.1	0.034	0.02	0.039	0.003	8.46	0.01	0.01	0.054
I36	15.2	158	0.292	0.10	1.63	0.833	0.54	0.050	0.010	0.344	0.03	0.979	11.09	0.259	23.0	2.19	244	1.89	0.02	0.289	1.39	17.8	0.03	0.01	1.04
I37	12.7	144	3.82	0.30	1.10	0.914	2.71	3.16	0.019	0.477	0.06	1.11	6.16	0.238	23.2	2.13	223	1.11	0.05	0.365	1.19	19.9	0.03	0.01	0.857
I38	8.93	55.7	1.61	0.10	1.62	2.30	0.69	0.633	0.011	0.304	0.03	0.112	1.70	0.333	22.8	1.29	158	0.337	0.02	0.053	0.587	20.2	0.01	0.01	0.763
I39	0.36	1.00	1.33	0.10	0.328	1.02	0.06	0.295	0.009	0.047	0.27	0.640	0.128	0.111	3.65	0.181	131	0.057	0.02	0.037	0.003	36.8	0.01	0.01	0.047
I40	0.09	4.02	1.61	0.10	0.947	4.58	0.22	0.597	0.018	1.56	0.17	0.050	0.175	0.230	3.46	0.189	46.2	0.150	0.02	0.041	0.003	3.98	0.01	0.01	0.023
I41	0.24	4.83	4.95	0.10	0.304	1.15	0.04	0.916	0.007	0.041	0.04	0.239	0.106	0.080	4.73	0.207	54.6	0.108	0.02	0.042	0.003	3.67	0.01	0.01	0.192
I42	0.20	1.00	0.590	0.10	0.482	0.854	0.03	0.050	0.007	0.020	0.10	0.114	0.224	0.064	8.16	0.209	125	0.025	0.02	0.052	0.016	21.0	0.01	0.01	0.084
I43	0.66	1.00	0.312	0.10	0.397	0.934	0.11	0.050	0.010	0.028	0.02	0.050	0.161	0.142	5.70	0.259	169	0.080	0.02	0.042	0.006	132	0.01	0.01	0.083
I44	29.9	1,246	23.4	0.18	4.75	0.729	0.05	21.9	0.020	0.913	1.67	6.68	0.635	1.77	10,530	17.7	1902	49.7	0.06	0.826	0.607	44.0	0.30	0.61	2.13
I45	0.94	38.8	1.97	0.04	1.61	0.440	0.05	0.539	0.020	0.030	0.04	0.185	0.411	0.318	107	0.327	450	2.13	0.01	0.034	0.057	35.2	0.01	0.01	0.636
I46	0.63	34.4	2.14	0.04	1.38	0.317	0.05	0.616	0.020	0.030	0.04	0.148	0.220	0.262	119	0.338	135	0.582	0.01	0.013	0.005	8.29	0.01	0.01	0.402
I47	0.41	24.9	2.75	0.02	2.09	0.687	0.05	0.245	0.020	0.030	0.05	0.219	0.191	0.470	111	0.313	117	0.374	0.01	0.023	0.002	11.3	0.01	0.01	0.455
I48	10.7	342	12.3	0.08	0.925	0.257	3.07	9.65	0.020	0.308	0.54	1.76	0.250	0.253	4,510	7.45	637	1.45	0.01	0.076	0.017	31.2	0.01	0.14	0.777
I49	0.45	20.8	2.31	0.04	1.63	0.241	0.04	0.594	0.020	0.030	0.11	0.123	0.133	0.164	116	0.322	87.2	0.314	0.01	0.013	0.003	12.3	0.01	0.01	0.493
I50	4.07	41.1	1.90	0.07	0.300	0.063	2.35	2.01	0.020	0.178	0.48	3.98	0.197	0.110	222	1.03	520	0.565	0.01	0.080	0.005	47.0	0.01	0.01	0.661
I51	0.31	10.6	92.9	0.12	1.00	0.147	4.75	4.83	0.020	0.071	1.69	0.550	0.195	0.233	80.6	0.211	82.9	0.154	0.01	0.026	0.002	4.65	0.01	0.01	0.275
I52	0.50	4.94	4,392	2.52	1.28	0.884	50.8	12.0	0.020	0.337	47.0	9.31	0.106	0.269	37.9	0.119	222	0.151	0.01	0.012	0.010	45.7	0.01	0.29	0.163
I53	0.52	5.57	196	0.16	1.63	0.491	2.28	0.586	0.020	0.071	6.91	31.3	0.152	0.271	44.8	0.173	758	0.869	0.01	0.016	0.010	11.0	0.01	0.03	0.410
I54	0.25	6.32	87.6	0.28	1.21	0.281	6.43	18.1	0.020	0.099	2.44	0.120	0.199	0.220	54.6	0.104	68.7	0.305	0.01	0.021	0.010	12.8	0.01	0.01	0.367
I55	0.63	6.47	53.4	0.03	1.21	1.16	0.20	0.193	0.020	0.160	2.01	1.41	0.423	0.130	61.9	0.620	819	2.31	0.01	0.220	0.008	29.3	0.06	0.11	1.14

Appendix A2 – Table A3

ID	Li	B	Al	Ti	V	Cr	Mn	Fe	Co	Ni	Cu	Zn	As	Se	Br-	Rb	Sr	Mo	Cd	Sb	Cs	Ba	Tl	Pb	U
I56	1.72	18.2	11.8	0.02	1.41	0.695	0.05	0.274	0.020	0.312	0.32	0.192	0.654	0.557	127	0.450	461	4.38	0.01	0.142	0.012	60.9	0.03	0.01	0.800
I57	2.01	13.3	7.01	0.05	1.29	0.571	0.05	0.097	0.020	0.179	0.16	0.108	0.324	0.516	88.0	0.713	3084	3.88	0.01	0.074	0.018	23.2	0.03	0.01	0.922
I58	0.52	6.07	5.61	0.05	1.59	0.670	0.04	0.460	0.020	0.051	0.20	0.100	0.258	0.437	63.7	0.263	206	1.58	0.01	0.027	0.009	21.0	0.02	0.01	0.794
I59	3.30	39.9	17.3	0.04	1.26	0.221	1.14	2.49	0.020	0.368	0.77	1.21	0.254	0.513	504	1.33	1597	2.90	0.01	0.046	0.068	11.5	0.01	0.14	1.14
I60	10.1	219	35.8	0.36	1.26	0.405	0.05	1.67	0.020	0.269	0.85	1.17	0.161	0.438	4,047	6.25	1542	2.42	0.01	0.032	0.133	19.7	0.01	0.09	0.938
I61	0.43	1.00	39.2	0.05	0.770	0.249	0.48	1.19	0.020	0.092	1.14	0.387	0.114	0.033	39.0	0.177	170	0.422	0.01	0.021	0.001	27.0	0.01	0.01	0.471
I62	0.24	1.00	14.5	0.10	0.510	0.138	0.04	1.52	0.020	0.036	0.11	0.100	0.058	0.180	17.1	0.099	79.9	0.645	0.01	0.022	0.010	12.3	0.01	0.01	0.206
I63	0.22	1.00	7.85	0.12	0.515	0.127	0.05	1.47	0.020	0.030	0.04	0.100	0.058	0.140	13.3	0.096	79.6	0.266	0.01	0.017	0.010	11.3	0.01	0.01	0.188
I64	2.18	38.1	5.39	0.13	1.81	0.450	0.15	0.940	0.020	0.085	0.17	1.36	0.212	0.124	736	1.26	436	0.860	0.01	0.028	0.031	89.5	0.01	0.15	0.719
I65	0.32	1.00	10.0	0.11	0.955	0.178	0.05	0.827	0.020	0.029	0.05	0.174	0.099	0.088	34.7	0.160	147	0.274	0.01	0.010	0.001	27.6	0.01	0.01	0.393
I66	0.76	1.00	2.02	0.05	1.70	0.270	0.05	0.083	0.020	0.022	0.03	0.135	0.126	0.176	48.6	0.214	236	0.497	0.01	0.018	0.002	108	0.01	0.01	0.642
I67	4.60	36.4	5.4	0.06	0.375	0.331	0.59	0.709	0.020	0.500	0.19	0.195	0.169	0.724	182	0.391	1019	0.795	0.01	0.046	0.001	49.6	0.01	0.01	1.16
I68	0.52	1.00	6.35	0.08	0.213	0.097	0.13	0.687	0.020	0.091	0.28	0.600	0.055	0.302	23.7	0.176	94.8	0.156	0.01	0.022	0.010	37.9	0.01	0.02	0.141
I69	1.68	27.2	2.23	0.12	1.18	0.378	0.30	0.556	0.020	0.162	0.07	0.336	0.361	0.583	253	0.431	500	0.557	0.01	0.026	0.020	32.8	0.01	0.01	0.946
I70	16.9	270	13.5	0.21	0.924	0.483	0.07	1.32	0.020	0.992	1.13	0.286	0.523	0.391	5269	7.31	1718	1.86	0.01	0.073	0.411	88.0	0.01	0.10	1.44
I71	47.5	53.8	6.70	0.07	3.89	0.408	0.05	0.638	0.020	0.115	0.17	1.42	0.294	0.175	194	4.75	320	2.86	0.02	0.066	1.04	13.5	0.02	0.07	1.45
I72	28.7	669	9.77	0.40	1.40	0.732	0.42	10.3	0.020	0.450	0.76	2.39	0.146	0.388	12,494	19.6	2539	6.37	0.01	0.027	0.010	44.6	0.01	0.39	1.24
I73	15.5	448	0.100	0.10	0.947	1.43	0.10	0.500	0.010	0.100	0.10	0.100	0.144	0.100	7,481	14.1	1290	0.846	0.01	0.059	0.028	111	0.03	0.05	0.414
I74	1.34	12.5	0.100	0.10	1.19	0.441	0.10	0.500	0.010	0.100	0.10	0.100	0.177	0.285	26.0	0.456	275	0.383	0.01	0.034	0.010	84.7	0.01	0.05	0.206
I75	4.46	13.4	7.13	0.10	0.614	0.381	0.07	1.52	0.012	3.02	0.63	2.19	0.544	0.100	12.5	3.25	228	0.600	0.04	0.014	0.532	19.8	0.01	0.05	0.939
I76	0.34	3.88	0.157	0.10	0.160	0.243	0.10	0.500	0.010	0.100	0.10	0.100	0.069	0.100	3.24	0.100	82.5	0.040	0.01	0.034	0.010	13.1	0.01	0.05	0.048
I77	5.23	16.3	0.110	0.10	0.741	0.560	0.96	0.510	0.007	0.100	0.10	1.54	2.85	0.234	21.5	0.768	364	0.316	0.01	0.103	0.193	68.1	0.01	0.05	0.121
I78	0.45	5.24	0.100	0.10	0.704	0.967	0.10	0.500	0.010	0.100	0.10	0.100	0.299	0.170	9.64	0.429	130	0.049	0.01	0.032	0.009	112	0.01	0.05	0.105
I79	0.48	5.70	0.138	0.10	0.665	0.754	6.19	6.69	0.037	0.100	0.10	0.100	0.376	0.114	9.03	0.412	142	0.060	0.01	0.035	0.006	80.2	0.01	0.05	0.115
I80	7.93	49.2	2.81	0.10	0.477	0.022	1.50	0.500	0.017	0.271	0.10	0.100	0.990	0.100	16.5	0.971	3958	0.384	0.01	0.182	0.010	17.7	0.01	0.05	0.762
I81	10.7	34.7	0.100	0.10	2.51	0.392	2.02	0.500	0.023	0.274	0.10	0.100	0.421	0.209	9.94	0.527	3384	3.66	0.01	0.117	0.010	10.8	0.01	0.05	1.29
I82	1.94	9.96	0.100	0.10	0.701	0.714	0.10	0.500	0.010	0.100	0.10	0.100	0.337	0.318	6.75	0.428	604	1.44	0.01	0.082	0.024	24.1	0.01	0.05	0.227
I83	0.99	5.65	0.563	0.10	0.482	0.581	0.20	0.500	0.010	0.100	0.10	0.100	0.586	0.230	2.24	0.388	175	1.72	0.01	0.139	0.020	130	0.01	0.05	0.298
I84	1.40	10.7	0.100	0.10	0.359	0.430	0.10	0.500	0.010	0.100	0.10	0.100	1.23	0.165	10.8	0.492	160	0.194	0.01	0.064	0.170	179	0.01	0.05	0.095
I85	1.59	6.32	0.247	0.10	1.02	0.204	5.69	1.92	0.031	0.075	0.10	0.100	0.415	0.301	9.95	0.433	229	0.525	0.01	0.048	0.006	83.6	0.01	0.05	0.213
I86	0.51	7.66	0.100	0.10	0.766	0.709	0.10	0.500	0.008	0.100	0.10	0.100	0.189	0.270	17.0	0.391	244	0.701	0.01	0.032	0.004	49.6	0.01	0.05	0.227
I87	6.69	52.3	0.318	0.10	2.19	0.187	0.10	0.500	0.010	0.290	0.10	0.100	0.610	0.190	16.4	0.565	2341	4.51	0.01	0.178	0.046	16.7	0.02	0.05	1.42

Appendix A2 – Table A3

ID	Li	B	Al	Ti	V	Cr	Mn	Fe	Co	Ni	Cu	Zn	As	Se	Br-	Rb	Sr	Mo	Cd	Sb	Cs	Ba	Tl	Pb	U
188	1.93	18.1	0.100	0.10	1.06	0.614	0.32	0.500	0.010	0.100	0.10	0.100	0.251	0.157	52.1	0.532	418	0.388	0.01	0.017	0.010	41.2	0.01	0.05	0.337
189	0.82	6.32	0.064	0.10	0.192	0.210	0.10	0.500	0.010	0.100	0.10	0.100	0.102	0.174	5.44	0.196	72.0	0.146	0.01	0.022	0.010	10.8	0.01	0.05	0.070
190	9.57	130	0.100	0.10	0.347	0.236	0.10	0.500	0.019	0.100	0.10	0.100	2.68	0.106	21,94	6.64	565	0.231	0.01	0.201	0.294	16.2	0.04	0.05	0.413
191	0.27	5.77	0.602	0.10	0.290	0.986	0.10	0.500	0.010	0.100	0.10	0.345	0.063	0.168	12.9	0.142	158	0.026	0.01	0.012	0.010	6.27	0.01	0.05	0.053
192	0.98	10.1	0.100	0.10	0.358	1.15	0.08	0.500	0.014	0.230	0.10	0.386	0.046	0.166	39.3	0.419	290	0.010	0.01	0.015	0.010	25.1	0.01	0.05	0.117
193	0.35	5.99	0.100	0.10	0.276	0.120	0.16	0.500	0.010	0.100	0.10	0.828	0.248	0.110	27.5	0.244	509	0.657	0.01	0.146	0.010	48.8	0.03	0.05	1.37
194	0.20	4.54	0.100	0.10	0.958	0.137	0.10	0.500	0.012	0.100	0.10	0.489	0.129	0.092	21.0	0.178	41.1	0.601	0.01	0.033	0.010	5.67	0.01	0.05	0.742
195	0.08	2.98	0.802	0.10	0.423	0.198	0.10	0.500	0.010	0.100	0.10	0.086	0.074	0.100	14.5	0.086	57.9	0.016	0.01	0.023	0.010	7.55	0.01	0.05	0.169
196	0.68	8.68	0.100	0.10	0.300	0.386	1.81	0.500	0.009	0.100	0.10	0.068	0.033	0.163	18.6	0.291	294	0.037	0.01	0.014	0.010	16.2	0.01	0.05	0.094
197	0.87	5.84	0.100	0.10	0.289	1.36	0.10	0.500	0.010	0.073	0.10	0.100	0.010	0.196	22.3	0.251	249	0.010	0.01	0.007	0.010	12.4	0.01	0.05	0.086
198	1.03	8.87	4.81	0.10	0.491	0.694	0.10	0.500	0.010	0.100	0.10	0.168	0.079	0.244	19.5	0.408	473	0.520	0.01	0.019	0.010	49.0	0.01	0.05	0.594
199	1.67	6.69	0.100	0.10	0.065	0.010	46.7	10.3	0.099	0.100	0.10	0.100	0.147	0.067	14.9	0.396	231	0.104	0.01	0.021	0.010	55.9	0.01	0.05	0.086
200	0.66	9.05	0.100	0.10	0.304	1.58	0.16	0.500	0.009	0.100	0.10	0.100	0.057	0.183	33.7	0.236	271	0.010	0.01	0.019	0.010	25.4	0.01	0.05	0.193
201	1.84	13.6	0.100	0.10	0.349	0.192	0.22	0.380	0.006	0.275	3.13	5.59	0.136	0.210	37.3	0.374	180	0.054	0.01	0.023	0.010	28.5	0.01	0.14	0.096

n.m. – not measured

Table A4

Results of aqueous speciation calculations: SI (minerals), pCO₂ and TDIC of the collected Hellenic karst springs.

ID	SI Anhydrite	SI Gypsum	SI Halite	SI Aragonite	SI Calcite	SI Dolomite	pCO ₂ (bar)	SI Fluorite	SI Celestite	SI Strontianite	TDIC (mmol L ⁻¹)
1	-3.03	-2.62	-9.15	-0.18	-0.03	-0.83	0.01	-2.44	-3.72	-2.31	4.53
2	-2.99	-2.59	-9.15	-0.23	-0.08	-0.98	0.01	-2.47	-3.57	-2.24	4.78
3	-3.10	-2.71	-9.20	-0.29	-0.14	-0.86	0.02	-2.25	-3.47	-2.10	5.25
4	-3.08	-2.66	-9.52	0.10	0.25	-0.30	0.01	-2.52	-3.93	-2.19	5.06
5	-3.01	-2.60	-9.48	-0.18	-0.03	-0.79	0.02	-2.52	-3.89	-2.50	5.49
6	-3.22	-2.78	-9.50	-0.37	-0.22	-1.06	0.01	-2.75	-3.79	-2.38	3.82
7	-2.98	-2.59	-8.98	0.05	0.20	-0.02	0.01	-2.07	-3.34	-1.76	4.97
8	-3.17	-2.78	-9.08	-0.14	0.01	-0.46	0.01	-2.40	-3.59	-2.01	4.31
9	-2.71	-2.33	-9.01	-0.13	0.02	-0.61	0.01	-2.63	-3.18	-2.03	4.58
10	-2.53	-2.22	-8.40	-0.25	-0.11	-0.78	0.03	-1.87	-2.84	-2.01	6.84
11	-2.89	-2.48	-9.34	-0.19	-0.04	-0.78	0.20	-2.02	-3.61	-2.35	21.4
12	-2.92	-2.52	-9.17	0.00	0.15	-0.43	0.01	-2.75	-3.64	-2.16	4.45
13	-3.10	-2.68	-8.59	-0.09	0.06	-0.50	0.01	-1.87	-3.43	-1.86	5.01
14	-3.07	-2.65	-8.67	-0.12	0.03	-0.58	0.01	-2.26	-3.45	-1.94	4.85
15	-3.33	-2.90	-9.20	-0.09	0.06	-0.25	0.01	-3.30	-4.01	-2.20	5.25
16	-2.85	-2.44	-8.75	0.00	0.15	-0.15	0.01	-2.62	-3.36	-1.95	4.08
17	-2.89	-2.49	-8.91	-0.05	0.10	-0.33	0.01	-2.73	-3.41	-2.01	4.34
18	-2.89	-2.50	-8.87	-0.13	0.02	-0.23	0.01	-2.00	-3.26	-1.95	4.97
19	-2.74	-2.33	-8.68	-0.03	0.12	-0.04	0.05	-2.05	-3.20	-1.93	10.8
20	-3.66	-3.18	-10.44	-0.12	0.04	-0.20	0.00	-3.38	-4.15	-2.04	4.01
21	-2.80	-2.36	-9.03	0.04	0.19	0.07	0.02	-2.89	-3.24	-1.84	7.16
22	-3.03	-2.63	-9.87	0.22	0.37	-0.10	0.00	-3.64	-3.52	-1.70	4.12
23	-2.61	-2.19	-8.51	0.15	0.30	0.43	0.01	-2.77	-3.00	-1.67	7.08
24	-2.95	-2.50	-9.36	-0.03	0.12	-0.14	0.01	-3.02	-3.48	-2.00	5.24
25	-3.25	-2.78	-9.76	-0.05	0.10	-0.17	0.01	-3.16	-3.77	-2.00	4.91
26	-2.76	-2.32	-9.37	-0.02	0.13	-0.13	0.01	-3.01	-3.32	-2.02	5.68
27	-3.04	-2.60	-9.24	-0.20	-0.04	-1.21	0.01	-3.20	-4.02	-2.61	4.33
28	-3.28	-2.84	-9.81	-0.05	0.11	-0.30	0.01	-2.18	-3.97	-2.17	4.90
29	-3.28	-2.84	-9.82	-0.11	0.05	-0.43	0.01	-2.47	-3.96	-2.22	4.96

Appendix A2 – Table A4

ID	SI Anhydrite	SI Gypsum	SI Halite	SI Aragonite	SI Calcite	SI Dolomite	pCO ₂ (bar)	SI Fluorite	SI Celestite	SI Strontianite	TDIC (mmol L ⁻¹)
30	-3.26	-2.82	-9.79	-0.07	0.08	-0.34	0.01	-2.22	-3.93	-2.17	4.98
31	-3.29	-2.84	-9.83	-0.01	0.15	-0.25	0.01	-2.40	-4.00	-2.15	4.91
32	-3.14	-2.74	-9.10	-0.06	0.09	-0.56	0.02	-2.88	-3.73	-2.09	6.50
33	-2.98	-2.56	-9.22	-0.07	0.09	-0.43	0.01	-3.32	-3.57	-2.09	4.60
34	-2.97	-2.52	-9.25	0.09	0.24	-0.33	0.01	-3.23	-3.76	-2.14	4.84
35	-3.36	-2.93	-9.59	0.09	0.24	-0.09	0.01	-3.06	-4.10	-2.09	4.60
36	-3.49	-3.05	-9.08	-0.10	0.05	-0.44	0.01	-2.97	-4.20	-2.24	4.51
37	-3.62	-3.15	-9.24	-0.42	-0.27	-1.27	0.01	-3.24	-4.38	-2.61	3.30
38	-3.29	-2.83	-9.79	-0.24	-0.09	-1.33	0.03	-3.32	-4.12	-2.50	7.95
39	-3.12	-2.70	-8.90	0.08	0.23	-0.07	0.03	-2.17	-3.66	-1.89	9.33
40	-2.60	-2.21	-8.73	-0.01	0.14	-0.30	0.01	-2.84	-3.31	-2.16	6.08
41	-3.03	-2.63	-8.63	-0.17	-0.02	-0.41	0.01	-3.54	-3.50	-2.09	5.62
42	-3.41	-2.95	-9.89	-0.13	0.03	-1.17	0.00	-3.85	-4.45	-2.60	3.56
43	-3.57	-3.11	-10.00	-0.09	0.07	-1.21	0.00	-3.89	-4.47	-2.41	3.69
44	-3.55	-3.09	-9.94	-0.43	-0.27	-1.96	0.01	-3.89	-4.49	-2.79	3.45
45	-3.55	-3.09	-8.85	0.15	0.30	-0.25	0.00	-3.09	-4.04	-1.76	2.44
46	-1.30	-0.93	-3.25	-0.11	0.04	0.47	0.03	-1.89	-1.20	-1.45	7.78
47	-3.65	-3.19	-9.71	0.22	0.37	-0.35	0.00	-3.31	-4.27	-1.83	3.27
48	-3.91	-3.43	-10.01	-0.02	0.14	-0.93	0.00	-2.62	-4.51	-2.05	2.62
49	-3.54	-3.05	-9.66	-0.15	0.00	-1.35	0.00	-3.80	-4.44	-2.47	2.80
50	-3.50	-3.02	-9.49	-0.28	-0.13	-1.85	0.01	-4.08	-4.54	-2.74	5.34
51	-1.25	-0.90	-3.16	-0.14	0.01	0.47	0.01	-1.54	-1.13	-1.46	5.49
52	-3.20	-2.80	-8.62	-0.06	0.09	-0.85	0.01	-3.39	-4.06	-2.36	5.37
53	-2.98	-2.58	-8.03	0.11	0.26	-0.07	0.01	-2.93	-3.50	-1.85	5.57
54	-3.61	-3.14	-9.74	-0.04	0.12	-0.95	0.01	-3.81	-4.60	-2.45	4.69
55	-3.29	-2.83	-9.51	0.03	0.18	-0.95	0.01	-3.56	-4.10	-2.21	4.49
56	-3.35	-2.90	-9.26	0.02	0.18	-0.52	0.01	-3.82	-4.32	-2.37	5.08
57	-3.12	-2.66	-8.93	-0.36	-0.21	-1.39	0.00	-3.03	-3.10	-1.77	2.90
58	-2.76	-2.37	-7.87	-0.18	-0.03	-0.94	0.03	-2.79	-2.90	-1.77	6.73
59	-2.60	-2.16	-8.60	-0.56	-0.40	-1.51	0.02	-2.76	-2.63	-2.02	4.14
60	-3.40	-2.97	-9.01	-0.27	-0.12	-1.33	0.01	-3.36	-3.62	-1.93	3.34
61	-1.72	-1.33	-4.20	-0.13	0.02	0.40	0.01	-2.69	-1.39	-1.24	4.15

Appendix A2 – Table A4

ID	SI Anhydrite	SI Gypsum	SI Halite	SI Aragonite	SI Calcite	SI Dolomite	pCO ₂ (bar)	SI Fluorite	SI Celestite	SI Strontianite	TDIC (mmol L ⁻¹)
62	-1.30	-0.91	-3.30	-0.05	0.10	0.62	0.01	-2.05	-1.05	-1.24	4.95
63	-1.25	-0.86	-3.04	-0.06	0.10	0.75	0.00	-3.59	-0.93	-1.18	3.48
64	-1.75	-1.36	-4.22	-0.04	0.11	0.58	0.02	-3.63	-1.83	-1.57	8.30
65	-3.14	-2.76	-7.23	-0.14	0.01	-0.03	0.02	-3.55	-3.62	-2.05	7.17
66	-2.43	-2.04	-6.36	-0.02	0.13	0.12	0.01	-3.06	-2.78	-1.80	5.16
67	-3.05	-2.71	-9.18	0.16	0.30	0.10	0.01	-4.02	-3.96	-2.20	6.08
68	-3.16	-2.78	-9.20	0.21	0.36	0.41	0.01	-3.41	-4.00	-2.07	5.23
69	-2.85	-2.42	-8.86	-0.03	0.12	-0.27	0.01	-2.94	-3.28	-1.91	5.13
70	-3.00	-2.70	-9.03	-0.08	0.07	-0.35	0.02	-2.06	-3.64	-2.16	5.87
71	-2.53	-2.13	-7.92	-0.11	0.04	-0.82	0.03	-2.60	-2.95	-1.97	7.30
72	-2.28	-1.87	-7.56	-0.11	0.04	-0.11	0.01	-3.03	-1.83	-1.11	4.05
73	-2.10	-1.70	-7.60	-0.10	0.05	-0.02	0.01	-2.85	-1.64	-1.08	4.50
74	-2.62	-2.21	-8.70	-0.03	0.12	-0.70	0.03	-2.94	-3.07	-1.92	7.68
75	-2.30	-1.87	-9.02	-0.15	0.01	-0.36	0.01	-2.59	-2.46	-1.74	4.60
76	-3.59	-3.12	-9.47	-0.18	-0.02	-1.66	0.00	-3.72	-4.12	-2.13	3.43
77	-3.11	-2.64	-9.20	0.00	0.15	-1.08	0.01	-3.59	-3.60	-1.92	5.19
78	-3.21	-2.76	-9.52	-0.34	-0.19	-1.68	0.01	-3.09	-3.45	-2.01	3.86
79	-2.96	-2.53	-9.28	0.02	0.17	-0.62	0.01	-2.96	-3.19	-1.65	4.81
80	-2.73	-2.30	-9.25	-0.06	0.09	-0.37	0.01	-2.87	-2.93	-1.70	4.66
81	-3.23	-2.77	-9.52	-0.20	-0.05	-0.64	0.01	-3.25	-3.66	-2.06	4.35
82	-3.16	-2.72	-9.38	-0.19	-0.03	-0.72	0.01	-3.17	-3.62	-2.08	5.12
83	-3.18	-2.70	-9.72	-0.27	-0.12	-0.76	0.00	-3.64	-3.26	-1.78	3.23
84	-1.43	-1.05	-3.70	-0.23	-0.08	0.23	0.02	-2.74	-1.21	-1.45	6.23
85	-2.53	-2.14	-7.28	-0.15	0.00	-0.64	0.02	-2.93	-2.59	-1.64	6.16
86	-2.71	-2.31	-8.98	-0.15	0.00	-0.75	0.02	-2.75	-2.84	-1.71	6.24
87	-1.52	-1.15	-4.01	-0.11	0.04	0.48	0.03	-2.49	-1.55	-1.59	8.54
88	-1.36	-0.96	-3.38	-0.15	0.00	0.49	0.01	-4.80	-1.10	-1.33	6.32
89	-1.10	-0.71	-2.74	-0.15	0.01	0.69	0.01	-4.94	-0.73	-1.21	5.12
90	-1.10	-0.72	-2.84	-0.13	0.02	0.75	0.02	-4.96	-0.73	-1.20	7.32
91	-1.21	-0.85	-3.35	-0.15	0.00	0.51	0.07	-1.54	-1.01	-1.39	12.9
92	-3.07	-2.67	-8.59	-0.11	0.04	-0.47	0.02	-3.63	-3.94	-2.42	6.33
93	-2.46	-2.12	-7.22	-0.04	0.11	0.21	0.03	-2.28	-2.90	-1.92	8.03

Appendix A2 – Table A4

ID	SI Anhydrite	SI Gypsum	SI Halite	SI Aragonite	SI Calcite	SI Dolomite	pCO ₂ (bar)	SI Fluorite	SI Celestite	SI Strontianite	TDIC (mmol L ⁻¹)
94	-2.79	-2.38	-8.79	-0.06	0.09	-0.35	0.01	-3.49	-3.45	-2.16	4.74
95	-2.72	-2.31	-8.82	-0.04	0.11	-0.70	0.01	-3.78	-3.30	-2.06	4.37
96	-1.91	-1.48	-8.07	0.05	0.20	-0.38	0.01	-2.86	-2.07	-1.54	3.93
97	-1.38	-0.95	-8.34	0.05	0.20	-0.32	0.00	-2.72	-1.43	-1.43	3.37
98	-2.66	-2.21	-8.65	0.01	0.17	-0.63	0.00	-4.11	-3.10	-1.86	3.29
99	-3.00	-2.54	-9.56	0.33	0.49	-0.06	0.00	-3.66	-3.84	-1.94	3.84
100	-2.65	-2.20	-7.64	0.04	0.19	-0.84	0.00	-3.84	-3.09	-1.83	3.18
101	-2.40	-1.94	-6.07	-0.14	0.01	-0.97	0.00	-2.45	-2.46	-1.63	2.38
102	-0.82	-0.37	-9.26	-0.04	0.12	-0.55	0.01	-1.18	-0.68	-1.33	3.81
103	-1.37	-0.91	-8.83	-0.15	0.01	-0.56	0.01	-2.08	-1.13	-1.34	3.65
104	-0.70	-0.25	-8.08	0.10	0.26	-0.17	0.00	-0.43	-0.40	-1.03	2.98
105	-0.66	-0.21	-9.48	0.07	0.22	-0.71	0.01	-1.38	-0.54	-1.25	3.63
106	-3.13	-2.68	-9.23	-0.08	0.07	-1.45	0.01	-4.01	-3.79	-2.17	4.28
107	-1.47	-1.06	-3.79	-0.22	-0.07	0.22	0.02	-4.73	-1.44	-1.63	7.60
108	-1.14	-0.71	-3.02	0.07	0.22	0.90	0.01	-4.72	-0.96	-1.19	6.28
109	-1.16	-0.79	-3.16	-0.10	0.05	0.59	0.02	-4.78	-0.94	-1.33	7.26
110	-2.89	-2.48	-8.77	-0.02	0.14	-0.29	0.05	-2.79	-3.59	-2.15	10.6
111	-2.93	-2.51	-8.89	0.04	0.19	-0.13	0.03	-2.73	-3.54	-2.01	9.04
112	-2.93	-2.49	-9.15	-0.03	0.12	-0.05	0.01	-4.45	-3.72	-2.25	6.43
113	-3.17	-2.74	-9.11	0.08	0.23	-0.48	0.00	-3.88	-3.87	-2.06	2.95
114	-1.93	-1.55	-4.54	-0.18	-0.03	0.03	0.01	-1.76	-1.78	-1.47	5.34
115	-2.19	-1.80	-5.45	-0.18	-0.03	-0.16	0.01	-2.96	-2.22	-1.65	3.89
116	-2.04	-1.62	-5.08	-0.11	0.04	0.02	0.01	-4.56	-2.28	-1.79	5.14
117	-1.99	-1.72	-5.20	0.75	0.89	2.14	0.01	-2.17	-2.30	-1.00	8.64
118	-1.02	-0.82	-3.21	0.95	1.09	2.78	0.01	-4.99	-1.01	-0.48	7.53
119	-1.37	-1.02	-3.72	-0.05	0.10	0.59	0.02	-4.74	-1.38	-1.50	7.46
120	-1.45	-1.07	-3.90	-0.17	-0.03	0.23	0.02	-4.67	-1.43	-1.60	7.11
121	-2.91	-2.52	-8.02	0.43	0.58	0.44	0.00	-2.76	-3.03	-1.13	2.60
122	-3.43	-3.01	-9.49	0.58	0.73	0.04	0.00	-3.37	-3.88	-1.31	3.53
123	-3.45	-3.00	-9.07	-0.07	0.08	-1.26	0.01	-3.55	-3.89	-1.95	4.85
124	-3.20	-2.77	-9.27	-0.18	-0.03	-1.27	0.01	-2.94	-3.49	-1.91	3.94
125	-3.14	-2.69	-9.01	-0.14	0.01	-1.03	0.00	-2.89	-3.40	-1.83	3.59

Appendix A2 – Table A4

ID	SI Anhydrite	SI Gypsum	SI Halite	SI Aragonite	SI Calcite	SI Dolomite	pCO ₂ (bar)	SI Fluorite	SI Celestite	SI Strontianite	TDIC (mmol L ⁻¹)
I26	-3.09	-2.65	-9.22	-0.06	0.10	-1.05	0.01	-2.57	-3.36	-1.76	4.07
I27	-3.26	-2.83	-9.32	-0.01	0.14	-1.17	0.01	-2.63	-3.77	-1.96	5.14
I28	-3.09	-2.70	-8.99	0.88	1.03	0.93	0.00	-2.61	-3.45	-0.93	3.42
I29	-0.42	-0.01	-9.09	0.40	0.55	0.26	0.01	-0.80	-0.20	-0.82	4.25
I30	-1.11	-0.85	-5.42	-0.18	-0.04	-0.21	0.01	-1.58	-1.02	-1.54	1.99
I31	-1.80	-1.41	-4.53	-0.08	0.07	0.06	0.01	-1.86	-1.90	-1.62	5.19
I32	-1.94	-1.50	-9.07	-0.06	0.09	-0.46	0.01	-2.22	-1.94	-1.50	3.60
I33	-2.77	-2.33	-9.24	-0.02	0.14	-0.97	0.00	-3.33	-3.12	-1.81	3.12
I34	-3.27	-2.85	-8.33	-0.14	0.01	-0.61	0.00	-3.29	-3.61	-1.92	3.03
I35	-3.79	-3.32	-10.25	-0.14	0.01	-1.32	0.00	-3.88	-4.64	-2.42	2.46
I36	-2.96	-2.55	-8.89	0.08	0.23	-0.08	0.04	-2.17	-3.59	-1.99	10.1
I37	-2.92	-2.51	-8.85	0.14	0.29	-0.06	0.05	-2.31	-3.66	-2.03	11.5
I38	-3.03	-2.66	-9.34	0.15	0.30	0.43	0.01	-2.60	-3.66	-1.93	6.56
I39	-3.89	-3.36	-11.48	-0.28	-0.12	-1.82	0.00	-3.54	-4.19	-1.99	2.01
I40	-3.47	-3.04	-10.47	0.49	0.65	0.91	0.00	-4.16	-4.26	-1.73	2.76
I41	-3.83	-3.32	-10.53	0.15	0.31	-0.59	0.00	-3.71	-4.59	-2.03	2.41
I42	-3.65	-3.20	-10.10	-0.16	-0.01	-1.49	0.01	-3.68	-4.26	-2.21	3.81
I43	-3.68	-3.23	-10.09	-0.06	0.10	-1.32	0.00	-3.33	-4.12	-1.93	3.46
I44	-1.54	-1.12	-3.93	-0.31	-0.15	0.01	0.01	-2.36	-1.40	-1.60	3.08
I45	-3.19	-2.81	-7.83	-0.17	-0.03	-0.15	0.01	-4.11	-3.12	-1.55	3.88
I46	-3.08	-2.68	-7.62	-0.17	-0.02	-0.31	0.00	-4.36	-3.48	-2.02	2.73
I47	-2.97	-2.57	-7.72	-0.09	0.06	-0.13	0.00	-3.64	-3.45	-2.01	2.78
I48	-1.86	-1.56	-4.77	0.41	0.55	1.43	0.00	-3.97	-2.00	-1.18	4.02
I49	-3.01	-2.62	-7.64	-0.07	0.08	0.11	0.00	-3.57	-3.65	-2.15	3.75
I50	-1.99	-1.63	-6.99	0.06	0.20	0.38	0.01	-3.06	-2.11	-1.51	5.45
I51	-3.23	-2.80	-7.94	0.22	0.38	0.71	0.00	-3.72	-3.75	-1.74	3.28
I52	-3.54	-3.08	-8.72	-0.27	-0.12	-0.89	0.00	-4.14	-3.67	-1.83	2.37
I53	-2.07	-1.61	-8.40	-0.10	0.06	-0.47	0.00	-4.00	-1.89	-1.35	2.31
I54	-3.33	-2.92	-8.44	-0.55	-0.40	-0.98	0.01	-3.95	-3.95	-2.61	2.94
I55	-2.27	-1.86	-8.10	0.04	0.19	-0.03	0.00	-2.46	-2.10	-1.23	3.79
I56	-2.63	-2.25	-7.60	-0.07	0.08	-0.18	0.00	-2.65	-2.53	-1.41	2.28
I57	-1.67	-1.28	-7.77	-0.53	-0.38	-1.04	0.01	-1.96	-1.07	-1.36	3.74

Appendix A2 – Table A4

ID	SI Anhydrite	SI Gypsum	SI Halite	SI Aragonite	SI Calcite	SI Dolomite	pCO ₂ (bar)	SI Fluorite	SI Celestite	SI Strontianite	TDIC (mmol L ⁻¹)
158	-2.97	-2.56	-8.17	-0.70	-0.54	-1.29	0.01	-3.31	-3.21	-2.37	3.62
159	-1.54	-1.24	-6.52	-0.40	-0.25	-0.65	0.01	-2.46	-1.28	-1.58	2.56
160	-1.88	-1.46	-4.81	-0.68	-0.52	-0.96	0.01	-2.62	-1.63	-1.87	3.09
161	-3.29	-2.85	-8.79	-0.57	-0.41	-1.44	0.01	-3.36	-3.65	-2.35	3.58
162	-3.91	-3.44	-9.21	-0.87	-0.72	-2.19	0.00	-3.93	-4.38	-2.77	2.12
163	-3.91	-3.44	-9.20	-0.95	-0.79	-2.37	0.01	-3.88	-4.38	-2.85	2.17
164	-2.55	-2.15	-6.18	-0.56	-0.41	-0.93	0.01	-2.28	-2.54	-1.99	3.32
165	-3.55	-3.11	-8.65	-0.86	-0.70	-1.96	0.01	-3.28	-3.86	-2.59	2.85
166	-3.10	-2.68	-8.40	-0.77	-0.61	-1.56	0.01	-2.59	-3.22	-2.32	2.97
167	-1.91	-1.51	-7.28	-0.31	-0.16	-0.71	0.02	-2.67	-1.78	-1.62	4.64
168	-3.37	-2.92	-8.96	-0.44	-0.29	-1.59	0.00	-3.73	-3.94	-2.44	2.38
169	-2.55	-2.17	-7.15	-0.36	-0.21	-1.12	0.05	-2.40	-2.81	-2.06	8.08
170	-1.65	-1.25	-4.64	-0.30	-0.15	-0.28	0.02	-2.71	-1.53	-1.62	5.68
171	-2.27	-1.90	-6.43	-0.23	-0.08	-0.27	0.02	-3.34	-2.62	-2.02	6.45
172	-1.63	-1.22	-4.11	-0.10	0.05	0.44	0.00	-2.98	-1.27	-1.19	2.99
173	-1.74	-1.34	-4.35	-0.24	-0.09	0.00	0.01	-0.93	-1.69	-1.63	4.38
174	-2.53	-2.13	-9.08	-0.05	0.10	-0.88	0.01	-2.82	-2.91	-1.87	3.99
175	-2.66	-2.25	-9.28	0.04	0.19	-0.62	0.26	-1.33	-3.68	-2.42	28.0
176	-3.84	-3.33	-10.69	-0.17	-0.01	-1.79	0.00	-3.14	-4.39	-2.14	2.01
177	-2.56	-2.11	-6.40	0.01	0.16	-0.64	0.00	-2.01	-2.62	-1.49	2.34
178	-3.63	-3.18	-9.76	-0.07	0.08	-1.42	0.01	-3.02	-4.26	-2.14	3.68
179	-3.59	-3.14	-9.73	0.35	0.50	-0.52	0.00	-2.95	-4.24	-1.74	4.12
180	-0.80	-0.44	-9.06	0.94	1.09	1.40	0.00	-1.37	-0.60	-0.31	1.79
181	-0.81	-0.37	-8.91	0.00	0.15	-0.69	0.02	-0.78	-0.72	-1.34	5.18
182	-2.06	-1.60	-9.12	-0.09	0.06	-0.75	0.00	-2.21	-2.07	-1.53	2.99
183	-3.21	-2.74	-10.10	0.01	0.17	-0.26	0.00	-2.51	-3.43	-1.63	2.25
184	-3.06	-2.61	-9.53	-0.16	-0.01	-1.33	0.00	-2.80	-3.48	-2.01	2.76
185	-2.39	-1.94	-9.60	-0.16	0.00	-1.32	0.01	-3.29	-2.82	-2.03	3.65
186	-2.17	-1.77	-8.47	-0.12	0.04	-1.04	0.01	-2.85	-2.66	-2.05	4.28
187	-1.09	-0.66	-8.75	0.03	0.19	-0.33	0.01	-1.18	-0.95	-1.26	3.35
188	-2.15	-1.75	-8.07	-0.10	0.05	-0.61	0.01	-2.90	-2.42	-1.81	4.88
189	-3.70	-3.19	-10.23	-0.20	-0.04	-1.20	0.00	-3.06	-4.28	-2.18	2.06

Appendix A2 – Table A4

ID	SI Anhydrite	SI Gypsum	SI Halite	SI Aragonite	SI Calcite	SI Dolomite	pCO ₂ (bar)	SI Fluorite	SI Celestite	SI Strontianite	TDIC (mmol L ⁻¹)
190	-1.96	-1.59	-5.29	0.04	0.18	0.13	0.01	-4.53	-2.22	-1.67	5.68
191	-3.37	-2.92	-9.41	-0.19	-0.04	-1.81	0.01	-3.74	-3.85	-2.11	3.37
192	-3.28	-2.88	-8.52	-0.12	0.03	-1.39	0.04	-3.92	-3.83	-2.11	7.78
193	-1.95	-1.49	-9.21	-0.32	-0.17	-1.17	0.01	-2.43	-2.07	-1.88	3.77
194	-3.26	-2.82	-9.27	-0.11	0.04	-0.05	0.01	-2.76	-4.26	-2.55	4.94
195	-3.54	-3.09	-9.44	-0.10	0.05	-0.33	0.00	-3.84	-4.27	-2.26	2.65
196	-3.23	-2.81	-9.27	-0.10	0.05	-1.71	0.02	-2.63	-3.64	-1.95	5.40
197	-3.21	-2.78	-9.18	-0.11	0.04	-1.37	0.02	-2.71	-3.74	-2.09	6.07
198	-2.56	-2.14	-9.23	-0.10	0.05	-0.83	0.02	-2.74	-2.80	-1.77	5.85
199	-3.33	-2.86	-9.54	-0.20	-0.05	-1.45	0.01	-2.74	-3.73	-2.03	4.48
200	-2.87	-2.43	-8.79	-0.15	0.01	-1.27	0.02	-2.80	-3.38	-2.09	6.62
201	-3.07	-2.64	-8.67	-0.03	0.12	-1.00	0.01	-2.67	-3.69	-2.09	5.27

Table A5

Chemical composition of dissolved gases of the collected Hellenic karst springs.

ID	He μmol mol ⁻¹	H ₂ μmol mol ⁻¹	O ₂ μmol mol ⁻¹	N ₂ μmol mol ⁻¹	CH ₄ μmol mol ⁻¹	CO ₂ μmol mol ⁻¹
12	b.d.l.	b.d.l.	170,060	822,800	110	7,010
13	272	b.d.l.	143,956	846,808	19.9	8,944
14	132	7.68	143,089	845,296	6.11	11,468
15	b.d.l.	b.d.l.	145,723	846,800	2.53	7,473
16	b.d.l.	b.d.l.	154,627	839,791	2.86	5,577
17	b.d.l.	b.d.l.	161,474	834,083	2.14	4,438
18	b.d.l.	b.d.l.	136,500	854,502	1.96	8,994
19	91.8	b.d.l.	85,703	857,014	1.36	57,190
20	b.d.l.	b.d.l.	119,669	873,111	1.53	7,218
21	b.d.l.	b.d.l.	87,399	890,214	1.09	22,386
22	b.d.l.	b.d.l.	206,399	787,522	1.67	6,078
23	b.d.l.	b.d.l.	120,294	859,293	4.63	20,408
24	b.d.l.	b.d.l.	188,613	801,314	1.17	10,072
25	b.d.l.	10.8	174,274	817,137	1.63	8,573
26	b.d.l.	6.95	178,747	806,718	1.03	14,527
27	b.d.l.	10.0	184,527	805,272	2.12	10,186
28	b.d.l.	b.d.l.	161,965	829,491	b.d.l.	8,544
29	b.d.l.	10.6	168,830	823,898	b.d.l.	7,262
30	b.d.l.	b.d.l.	161,106	831,726	b.d.l.	7,168
31	b.d.l.	b.d.l.	176,500	816,552	b.d.l.	6,948
32	41.8	b.d.l.	130,351	851,299	1.61	18,302
33	b.d.l.	8.83	163,446	829,855	b.d.l.	6,684
34	b.d.l.	56.5	2,101	985,252	400	12,187
35	b.d.l.	b.d.l.	115,375	876,017	0.808	8,602
36	b.d.l.	b.d.l.	140,988	853,648	b.d.l.	5,359
37	21.8	18.2	155,788	841,635	1.23	2,531
38	b.d.l.	148	125,723	851,124	0.936	22,999
39	130	987	130,934	840,333	b.d.l.	27,609
40	b.d.l.	b.d.l.	98,658	887,444	1.17	13,890
41	26.3	42.6	27,301	957,662	1.16	14,963
42	b.d.l.	15.8	148,401	845,101	b.d.l.	6,475
43	b.d.l.	53.4	201,053	795,083	b.d.l.	3,796
44	b.d.l.	147	181,224	813,135	b.d.l.	5,488
45	b.d.l.	9.00	195,229	803,810	2.48	941
46	b.d.l.	71.2	143,517	815,648	2.79	40,758
47	b.d.l.	16.1	208,669	785,480	5.64	5,824
48	b.d.l.	10.5	192,288	805,938	1.11	1,756
49	b.d.l.	b.d.l.	196,799	796,799	b.d.l.	6,396
50	b.d.l.	b.d.l.	184,386	799,759	b.d.l.	15,849
51	b.d.l.	b.d.l.	129,987	855,041	1.54	14,966
52	b.d.l.	b.d.l.	187,596	790,986	2.01	21,409
53	b.d.l.	14.6	189,826	791,867	b.d.l.	18,283
54	b.d.l.	b.d.l.	192,632	799,886	0.871	7,477
55	b.d.l.	b.d.l.	167,645	825,232	0.830	7,119
56	b.d.l.	68.4	168,024	822,442	0.886	9,461

ID	He	H₂	O₂	N₂	CH₄	CO₂
57	<i>b.d.l.</i>	41.4	153,444	843,734	0.803	2,769
58	26.1	18.6	137,966	841,716	6.39	20,262
59	<i>b.d.l.</i>	9.82	111,911	876,335	0.789	11,740
60	<i>b.d.l.</i>	<i>b.d.l.</i>	199,834	794,590	2.28	5,569
61	40.4	79.3	171,880	821,765	0.809	6,231
62	40.0	17.4	161,065	830,416	0.872	8,457
63	39.3	106	166,542	828,417	0.996	4,890
64	<i>b.d.l.</i>	16.7	111,984	868,958	4.60	19,032
65	<i>b.d.l.</i>	<i>b.d.l.</i>	134,605	843,786	2.73	21,599
66	<i>b.d.l.</i>	19.6	144,265	845,876	5.18	9,828
67	<i>b.d.l.</i>	21.3	167,275	812,712	<i>b.d.l.</i>	19,988
68	<i>b.d.l.</i>	<i>b.d.l.</i>	165,277	825,213	15.8	9,490
69	<i>b.d.l.</i>	37.4	171,465	818,775	1.01	9,717
70	<i>b.d.l.</i>	9.83	151,656	829,850	<i>b.d.l.</i>	18,482
71	<i>b.d.l.</i>	<i>b.d.l.</i>	79,750	886,430	1.48	33,818
72	<i>b.d.l.</i>	18.1	170,646	823,051	1.09	6,283
73	<i>b.d.l.</i>	<i>b.d.l.</i>	148,629	842,745	1.31	8,623
74	<i>b.d.l.</i>	11.4	148,895	824,864	0.860	26,229
75	<i>b.d.l.</i>	<i>b.d.l.</i>	191,330	799,590	<i>b.d.l.</i>	9,080
76	<i>b.d.l.</i>	10.9	185,104	811,376	<i>b.d.l.</i>	3,509
77	<i>b.d.l.</i>	<i>b.d.l.</i>	174,292	812,665	9.80	13,034
78	<i>b.d.l.</i>	17.6	184,042	807,841	<i>b.d.l.</i>	8,100
79	<i>b.d.l.</i>	10.5	190,345	803,904	1.15	5,740
80	<i>b.d.l.</i>	<i>b.d.l.</i>	148,179	844,050	16.4	7,754
81	<i>b.d.l.</i>	<i>b.d.l.</i>	176,627	818,377	<i>b.d.l.</i>	4,996
82	<i>b.d.l.</i>	<i>b.d.l.</i>	176,178	814,136	<i>b.d.l.</i>	9,686
83	<i>b.d.l.</i>	<i>b.d.l.</i>	192,722	804,452	<i>b.d.l.</i>	2,825
84	<i>b.d.l.</i>	61.5	159,951	826,307	<i>b.d.l.</i>	13,679
85	<i>b.d.l.</i>	12.7	163,477	821,099	1.28	15,410
86	<i>b.d.l.</i>	<i>b.d.l.</i>	168,764	811,845	5.57	19,385
87	<i>b.d.l.</i>	63.7	146,129	817,508	43.5	36,256
88	<i>b.d.l.</i>	201	172,061	814,731	0.762	13,006
89	<i>b.d.l.</i>	128	121,231	867,461	3.02	11,176
90	133	9.68	114,849	864,412	9.16	20,586
91	180	12.3	90,573	845,519	<i>b.d.l.</i>	63,715
92	<i>b.d.l.</i>	20.8	168,558	814,340	<i>b.d.l.</i>	17,081
93	<i>b.d.l.</i>	15.8	151,799	812,239	<i>b.d.l.</i>	35,946
94	<i>b.d.l.</i>	44.3	185,502	805,219	<i>b.d.l.</i>	9,233
95	<i>b.d.l.</i>	<i>b.d.l.</i>	171,915	819,006	<i>b.d.l.</i>	9,077
96	<i>b.d.l.</i>	184	149,950	846,406	<i>b.d.l.</i>	3,458
97	<i>b.d.l.</i>	247	138,116	857,617	<i>b.d.l.</i>	4,019
98	<i>b.d.l.</i>	32.7	174,312	821,931	<i>b.d.l.</i>	3,723
99	<i>b.d.l.</i>	<i>b.d.l.</i>	226,568	769,943	72.2	3,415
100	<i>b.d.l.</i>	17.2	169,073	826,746	2.78	4,158
101	29.0	92.8	149,287	848,952	<i>b.d.l.</i>	1,638
102	<i>b.d.l.</i>	86.0	71,006	921,530	2.96	7,375
103	<i>b.d.l.</i>	10.3	117,284	874,766	0.424	7,937
104	82.9	19.7	286,394	705,248	13.2	8,240

ID	He	H₂	O₂	N₂	CH₄	CO₂
105	37.3	36.4	91,372	901,398	13.7	7,142
106	40.9	123	166,803	831,012	2.19	2,017
107	35.0	10.5	77,871	902,966	0.871	19,116
108	48.5	6.66	62,039	926,995	8.34	10,901
109	30.4	10.2	184,014	797,123	1.52	18,820
110	88.9	52.3	134,360	829,323	<i>b.d.l.</i>	36,176
111	83.6	16.5	131,619	841,030	0.496	27,249
112	30.1	<i>b.d.l.</i>	182,889	804,537	0.670	12,541
113	29.8	22.2	190,806	806,399	1.33	2,741
114	13.9	<i>b.d.l.</i>	67,331	920,642	5.33	12,007
115	50.8	<i>b.d.l.</i>	110,289	883,584	19.8	6,054
116	22.8	2091	136,464	853,425	3.49	7,993
119	<i>b.d.l.</i>	63.1	162,283	815,399	6.74	22,247
120	<i>b.d.l.</i>	6.69	124,477	852,844	2.74	22,669
121	<i>b.d.l.</i>	<i>b.d.l.</i>	198,588	799,970	34.2	1,406
123	<i>b.d.l.</i>	<i>b.d.l.</i>	172,281	821,138	1.68	6,578
124	<i>b.d.l.</i>	9.91	143,120	850,116	5.49	6,748
125	<i>b.d.l.</i>	<i>b.d.l.</i>	154,542	840,621	<i>b.d.l.</i>	4,837
126	<i>b.d.l.</i>	29.5	138,629	852,588	1.54	8,752
127	12.6	292	160,365	824,476	2.27	14,850
129	<i>b.d.l.</i>	197	199,971	786,922	1.87	12,907
130	<i>b.d.l.</i>	29.3	275,502	722,203	49.6	2,214
131	<i>b.d.l.</i>	40.1	155,881	829,718	2.48	14,352
132	<i>b.d.l.</i>	<i>b.d.l.</i>	160,138	833,999	1.20	5,861
133	<i>b.d.l.</i>	<i>b.d.l.</i>	190,391	805,706	1.71	3,899
134	<i>b.d.l.</i>	9.17	152,422	844,067	23.2	3,476
135	<i>b.d.l.</i>	205	203,032	794,824	1.42	1,936
137	61.2	<i>b.d.l.</i>	145,028	795,321	29.3	59,559
138	<i>b.d.l.</i>	433	219,310	766,038	58.5	14,159
139	<i>b.d.l.</i>	118	206,966	791,336	1.14	1,578
141	<i>b.d.l.</i>	304	205,061	792,480	1.64	2,151
142	<i>b.d.l.</i>	<i>b.d.l.</i>	187,902	803,489	1.11	8,606
143	<i>b.d.l.</i>	<i>b.d.l.</i>	153,780	841,138	1.61	5,079
144	<i>b.d.l.</i>	21.0	164,956	831,341	2.49	3,679
145	<i>b.d.l.</i>	11.6	188,211	806,100	1.04	5,670
146	<i>b.d.l.</i>	10.1	198,651	798,632	1.40	2,705
147	<i>b.d.l.</i>	10.5	199,560	797,786	1.24	2,641
148	<i>b.d.l.</i>	<i>b.d.l.</i>	146,852	846,270	80.63	6,796
149	<i>b.d.l.</i>	<i>b.d.l.</i>	205,394	790,683	0.835	3,921
150	<i>b.d.l.</i>	<i>b.d.l.</i>	103,347	883,537	35.9	13,080
151	<i>b.d.l.</i>	<i>b.d.l.</i>	203,614	794,448	29.2	1,907
152	<i>b.d.l.</i>	79.8	193,139	804,497	3.75	2,278
153	<i>b.d.l.</i>	175	191,587	806,518	3.22	1,715
154	<i>b.d.l.</i>	<i>b.d.l.</i>	72,261	920,163	5.16	7,570
155	<i>b.d.l.</i>	<i>b.d.l.</i>	181,231	812,351	1.72	6,415
156	<i>b.d.l.</i>	10.0	200,654	797,717	1.29	1,617
157	<i>b.d.l.</i>	<i>b.d.l.</i>	151,574	840,954	<i>b.d.l.</i>	7,472
158	<i>b.d.l.</i>	<i>b.d.l.</i>	160,821	835,591	1.55	3,585

ID	He	H₂	O₂	N₂	CH₄	CO₂
159	<i>b.d.l.</i>	<i>b.d.l.</i>	148,205	849,071	75.2	2,646
160	<i>b.d.l.</i>	8.75	173,606	823,074	2.04	3,306
161	<i>b.d.l.</i>	<i>b.d.l.</i>	171,417	821,108	5.12	7,466
162	<i>b.d.l.</i>	21.4	187,006	811,909	2.07	1,059
163	<i>b.d.l.</i>	<i>b.d.l.</i>	196,150	802,854	1.02	992
164	<i>b.d.l.</i>	<i>b.d.l.</i>	179,276	816,773	1.68	3,947
165	<i>b.d.l.</i>	8,660	187,016	802,845	3.71	1,473
166	<i>b.d.l.</i>	<i>b.d.l.</i>	181,431	816,630	1.52	1,935
167	<i>b.d.l.</i>	<i>b.d.l.</i>	130,941	858,287	1.72	10,767
168	<i>b.d.l.</i>	43.0	198,700	798,978	1.14	2,271
169	<i>b.d.l.</i>	<i>b.d.l.</i>	154,303	811,681	5.51	34,008
170	<i>b.d.l.</i>	<i>b.d.l.</i>	89,236	892,150	1.59	18,611
171	111	7.60	153,864	823,906	0.836	22,110
172	<i>b.d.l.</i>	18.7	163,584	833,642	1.50	2,753
173	<i>b.d.l.</i>	14.9	140,094	852,988	<i>b.d.l.</i>	6,903
174	<i>b.d.l.</i>	16.9	190,934	800,561	1.69	8,486
175	<i>b.d.l.</i>	90.1	147,938	559,917	1.52	291,988
176	<i>b.d.l.</i>	34.9	209,099	787,861	1.48	3,002
178	<i>b.d.l.</i>	8.76	175,192	819,277	1.22	5,519
179	<i>b.d.l.</i>	12.4	154,713	839,864	5.57	5,405
180	<i>b.d.l.</i>	<i>b.d.l.</i>	179,076	817,975	169	2,779
181	<i>b.d.l.</i>	8.26	160,527	819,982	1.16	19,480
182	<i>b.d.l.</i>	<i>b.d.l.</i>	122,546	873,220	0.96	4,232
183	<i>b.d.l.</i>	<i>b.d.l.</i>	127,520	871,114	<i>b.d.l.</i>	1,365
184	<i>b.d.l.</i>	<i>b.d.l.</i>	155,044	842,491	1.08	2,464
185	<i>b.d.l.</i>	114	156,425	834,047	8.10	9,404
186	<i>b.d.l.</i>	8.66	184,125	805,385	1.73	10,477
187	<i>b.d.l.</i>	15.8	152,347	841,955	0.91	5,680
188	<i>b.d.l.</i>	<i>b.d.l.</i>	174,019	813,413	63.1	12,504
189	<i>b.d.l.</i>	9.31	175,894	823,059	0.90	1,034
191	<i>b.d.l.</i>	22.0	199,147	795,355	3.43	5,471
192	<i>b.d.l.</i>	15.2	169,073	789,451	1.59	41,458
193	<i>b.d.l.</i>	14.4	189,592	803,545	0.38	6,846
194	<i>b.d.l.</i>	10.6	195,238	796,955	1.31	7,794
195	<i>b.d.l.</i>	<i>b.d.l.</i>	197,805	797,137	1.94	5,054
196	<i>b.d.l.</i>	34.6	165,703	811,917	7.44	22,337
197	<i>b.d.l.</i>	5.86	154,600	829,855	1.03	15,532
198	<i>b.d.l.</i>	5.83	133,442	848,310	1.03	18,240
199	<i>b.d.l.</i>	<i>b.d.l.</i>	3,862	954,566	29,537	12,036
200	<i>b.d.l.</i>	<i>b.d.l.</i>	188,864	781,898	9.58	29,228
201	<i>b.d.l.</i>	10.5	178,548	809,450	2.15	11,988

b.d.l. – below detection limit

Table A6

Chemical composition of free gases of the collected Hellenic karst springs.

ID	He μmol mol ⁻¹	H₂ μmol mol ⁻¹	O₂ μmol mol ⁻¹	N₂ μmol mol ⁻¹	CH₄ μmol mol ⁻¹	CO₂ μmol mol ⁻¹
1	14.0	<i>b.d.l.</i>	157,200	813,000	<i>b.d.l.</i>	8,300
2	11.0	<i>b.d.l.</i>	195,500	809,300	<i>b.d.l.</i>	10,500
4	15.0	<i>b.d.l.</i>	166,300	813,100	<i>b.d.l.</i>	11,500
5	10.0	<i>b.d.l.</i>	174,400	802,600	2.40	13,200
7	15.0	<i>b.d.l.</i>	147,100	829,300	13.0	11,000
8	13.0	<i>b.d.l.</i>	153,000	822,000	18.0	8,300
11	73.0	<i>b.d.l.</i>	130,900	634,800	<i>b.d.l.</i>	233,400
13	394	648	145,500	830,700	236	9,700
15	<i>b.d.l.</i>	<i>b.d.l.</i>	154,100	821,200	<i>b.d.l.</i>	16,900
16	<i>b.d.l.</i>	<i>b.d.l.</i>	156,300	826,900	2.00	7,200
32	34.0	<i>b.d.l.</i>	146,700	818,000	1.22	13,000
35	16.5	<i>b.d.l.</i>	154,900	811,200	<i>b.d.l.</i>	8,400
36	93.3	<i>b.d.l.</i>	142,400	817,600	2.62	9,400
37	15.2	<i>b.d.l.</i>	178,700	792,300	<i>b.d.l.</i>	5,100
38	32.7	<i>b.d.l.</i>	149,500	799,800	<i>b.d.l.</i>	24,600
39	150	<i>b.d.l.</i>	138,200	796,600	<i>b.d.l.</i>	32,400
40	23.9	<i>b.d.l.</i>	95,500	863,900	<i>b.d.l.</i>	15,200
45	14.2	<i>b.d.l.</i>	189,050	780,400	1.74	534
59	18.6	<i>b.d.l.</i>	115,800	843,200	43.0	12,000
61	116	<i>b.d.l.</i>	149,700	817,700	<i>b.d.l.</i>	7,050
65	20.8	<i>b.d.l.</i>	122,700	830,100	3.71	18,600
69	20.0	<i>b.d.l.</i>	153,300	806,800	1.72	14,200
70	25.3	<i>b.d.l.</i>	142,000	804,300	<i>b.d.l.</i>	26,100
73	<i>b.d.l.</i>	<i>b.d.l.</i>	163,000	816,000	<i>b.d.l.</i>	8,800
74	3.00	<i>b.d.l.</i>	146,000	794,000	<i>b.d.l.</i>	36,200
83	<i>b.d.l.</i>	<i>b.d.l.</i>	193,000	782,000	<i>b.d.l.</i>	3,500
85	<i>b.d.l.</i>	<i>b.d.l.</i>	170,000	783,000	1.00	22,200
86	<i>b.d.l.</i>	<i>b.d.l.</i>	175,000	778,000	12.0	23,400
90	222	<i>b.d.l.</i>	93,400	872,000	<i>b.d.l.</i>	22,500
98	6.00	<i>b.d.l.</i>	175,200	789,600	<i>b.d.l.</i>	5,900
110	138	<i>b.d.l.</i>	143,300	799,400	<i>b.d.l.</i>	47,300
124	<i>b.d.l.</i>	<i>b.d.l.</i>	152,300	817,700	<i>b.d.l.</i>	11,300
136	161	<i>b.d.l.</i>	143,400	784,300	<i>b.d.l.</i>	49,000
162	6.00	<i>b.d.l.</i>	203,200	787,300	<i>b.d.l.</i>	1,400
182	8.00	<i>b.d.l.</i>	138,700	847,300	2.00	8,100
183	6.00	<i>b.d.l.</i>	150,700	840,900	4.10	9,400
187	<i>b.d.l.</i>	<i>b.d.l.</i>	149,900	854,300	<i>b.d.l.</i>	8,800

b.d.l. – below detection limit

Table A7

Isotopic composition of gases of the collected Hellenic karst springs.

ID	$\delta^{13}\text{C}_{\text{TDIC}}$ ‰ vs. PDB	$\delta^{13}\text{C}_{\text{CO}_2}$ ‰ vs. PDB	R/R _A	He/Ne	Rc/R _A	ERROR
1	-10.4	-17.6	n.a.	n.a.	n.a.	n.a.
2	-11.1	-18.5	n.a.	n.a.	n.a.	n.a.
3	-9.89	n.a.	n.a.	n.a.	n.a.	n.a.
4	-11.7	-19.0	n.a.	n.a.	n.a.	n.a.
5	-12.9	-16.7	n.a.	n.a.	n.a.	n.a.
6	-13.5	n.a.	n.a.	n.a.	n.a.	n.a.
7	-10.2	-17.7	n.a.	n.a.	n.a.	n.a.
8	-9.08	-16.7	n.a.	n.a.	n.a.	n.a.
9	-9.66	n.a.	n.a.	n.a.	n.a.	n.a.
10	-4.94	n.a.	n.a.	n.a.	n.a.	n.a.
11	-2.31	-7.4	0.20	6.7	0.16	0.004
12	-11.4	n.a.	n.a.	n.a.	n.a.	n.a.
13	-9.33	-17.6	n.a.	n.a.	n.a.	n.a.
14	-9.23	n.a.	n.a.	n.a.	n.a.	n.a.
15	-8.99	-17.4	n.a.	n.a.	n.a.	n.a.
16	-7.92	-16.2	n.a.	n.a.	n.a.	n.a.
17	-7.95	n.a.	n.a.	n.a.	n.a.	n.a.
18	-8.55	n.a.	n.a.	n.a.	n.a.	n.a.
19	-7.70	n.a.	n.a.	n.a.	n.a.	n.a.
20	-9.90	n.a.	n.a.	n.a.	n.a.	n.a.
21	-7.93	n.a.	n.a.	n.a.	n.a.	n.a.
22	-8.67	n.a.	n.a.	n.a.	n.a.	n.a.
23	-7.65	n.a.	n.a.	n.a.	n.a.	n.a.
24	-9.67	n.a.	n.a.	n.a.	n.a.	n.a.
25	-9.81	n.a.	n.a.	n.a.	n.a.	n.a.
26	-9.34	n.a.	n.a.	n.a.	n.a.	n.a.
27	-9.69	n.a.	n.a.	n.a.	n.a.	n.a.
28	-10.0	n.a.	n.a.	n.a.	n.a.	n.a.
29	-9.91	n.a.	n.a.	n.a.	n.a.	n.a.
30	-10.0	n.a.	n.a.	n.a.	n.a.	n.a.
31	-10.0	n.a.	n.a.	n.a.	n.a.	n.a.
32	-7.58	-7.90	n.a.	n.a.	n.a.	n.a.
33	-10.5	n.a.	n.a.	n.a.	n.a.	n.a.
34	-13.1	n.a.	n.a.	n.a.	n.a.	n.a.
35	-10.6	-18.1	n.a.	n.a.	n.a.	n.a.
36	-9.28	-17.5	n.a.	n.a.	n.a.	n.a.
37	-11.0	-20.4	n.a.	n.a.	n.a.	n.a.
38	-10.4	-20.6	n.a.	n.a.	n.a.	n.a.
39	-3.05	-9.00	n.a.	n.a.	n.a.	n.a.
40	-14.8	-17.0	n.a.	n.a.	n.a.	n.a.
41	-14.5	n.a.	n.a.	n.a.	n.a.	n.a.
42	-5.44	n.a.	n.a.	n.a.	n.a.	n.a.
43	-6.55	n.a.	n.a.	n.a.	n.a.	n.a.
44	-12.0	n.a.	n.a.	n.a.	n.a.	n.a.
45	-12.4	-20.8	n.a.	n.a.	n.a.	n.a.
47	-6.12	n.a.	n.a.	n.a.	n.a.	n.a.
48	-14.5	n.a.	n.a.	n.a.	n.a.	n.a.
49	-11.9	n.a.	n.a.	n.a.	n.a.	n.a.
50	-11.9	n.a.	n.a.	n.a.	n.a.	n.a.
51	-9.71	n.a.	n.a.	n.a.	n.a.	n.a.

ID	$\delta^{13}\text{C}_{\text{TDIC}}$	$\delta^{13}\text{C}_{\text{CO}_2}$	R/R _A	He/Ne	Rc/R _A	ERROR
52	-13.6	n.a.	n.a.	n.a.	n.a.	n.a.
53	-13.8	n.a.	n.a.	n.a.	n.a.	n.a.
54	-14.4	n.a.	n.a.	n.a.	n.a.	n.a.
55	-14.7	n.a.	n.a.	n.a.	n.a.	n.a.
56	-13.5	n.a.	n.a.	n.a.	n.a.	n.a.
57	-10.1	n.a.	n.a.	n.a.	n.a.	n.a.
58	-9.88	n.a.	n.a.	n.a.	n.a.	n.a.
59	-12.8	n.a.	n.a.	n.a.	n.a.	n.a.
60	-11.3	n.a.	n.a.	n.a.	n.a.	n.a.
61	-10.6	-18.7	n.a.	n.a.	n.a.	n.a.
62	-16.6	n.a.	n.a.	n.a.	n.a.	n.a.
63	-6.54	n.a.	n.a.	n.a.	n.a.	n.a.
64	-13.3	n.a.	n.a.	n.a.	n.a.	n.a.
65	-11.1	-16.6	n.a.	n.a.	n.a.	n.a.
66	-12.0	n.a.	n.a.	n.a.	n.a.	n.a.
67	-12.6	n.a.	n.a.	n.a.	n.a.	n.a.
68	-10.3	n.a.	n.a.	n.a.	n.a.	n.a.
69	-14.4	-20.8	n.a.	n.a.	n.a.	n.a.
70	-8.01	-15.3	n.a.	n.a.	n.a.	n.a.
71	-14.8	n.a.	n.a.	n.a.	n.a.	n.a.
72	-10.4	n.a.	n.a.	n.a.	n.a.	n.a.
73	-11.2	-17.2	n.a.	n.a.	n.a.	n.a.
74	-15.0	-19.5	n.a.	n.a.	n.a.	n.a.
75	-12.5	n.a.	n.a.	n.a.	n.a.	n.a.
76	-12.5	n.a.	n.a.	n.a.	n.a.	n.a.
77	-13.1	n.a.	n.a.	n.a.	n.a.	n.a.
78	-12.5	n.a.	n.a.	n.a.	n.a.	n.a.
79	-13.1	n.a.	n.a.	n.a.	n.a.	n.a.
80	-12.2	n.a.	n.a.	n.a.	n.a.	n.a.
81	-11.4	n.a.	n.a.	n.a.	n.a.	n.a.
82	-11.9	n.a.	n.a.	n.a.	n.a.	n.a.
83	-9.59	-19.6	n.a.	n.a.	n.a.	n.a.
84	-10.9	n.a.	n.a.	n.a.	n.a.	n.a.
85	-12.4	-19.3	n.a.	n.a.	n.a.	n.a.
86	-13.8	-20.1	n.a.	n.a.	n.a.	n.a.
87	-13.8	n.a.	n.a.	n.a.	n.a.	n.a.
88	-11.3	n.a.	n.a.	n.a.	n.a.	n.a.
89	-7.24	n.a.	n.a.	n.a.	n.a.	n.a.
90	-3.95	-11.5	0.299	13.5	0.282	0.006
91	-5.72	n.a.	n.a.	n.a.	n.a.	n.a.
92	-12.1	n.a.	n.a.	n.a.	n.a.	n.a.
93	-13.3	n.a.	n.a.	n.a.	n.a.	n.a.
94	-10.5	n.a.	n.a.	n.a.	n.a.	n.a.
95	-10.9	n.a.	n.a.	n.a.	n.a.	n.a.
96	-10.3	n.a.	n.a.	n.a.	n.a.	n.a.
97	-8.63	n.a.	n.a.	n.a.	n.a.	n.a.
98	-9.85	-17.8	1.19	0.337	n.a.	0.029
99	-11.5	n.a.	n.a.	n.a.	n.a.	n.a.
100	-11.5	n.a.	n.a.	n.a.	n.a.	n.a.
101	-9.18	n.a.	n.a.	n.a.	n.a.	n.a.
102	-9.10	n.a.	n.a.	n.a.	n.a.	n.a.
103	-9.00	n.a.	n.a.	n.a.	n.a.	n.a.
104	-9.20	n.a.	n.a.	n.a.	n.a.	n.a.
105	-10.9	n.a.	n.a.	n.a.	n.a.	n.a.

ID	$\delta^{13}\text{C}_{\text{TDIC}}$	$\delta^{13}\text{C}_{\text{CO}_2}$	R/R _A	He/Ne	Rc/R _A	ERROR
106	-12.4	n.a.	n.a.	n.a.	n.a.	n.a.
107	-12.7	n.a.	n.a.	n.a.	n.a.	n.a.
108	-10.6	n.a.	n.a.	n.a.	n.a.	n.a.
109	-11.0	n.a.	n.a.	n.a.	n.a.	n.a.
110	-1.07	-9.10	n.a.	n.a.	n.a.	n.a.
111	-0.91	n.a.	n.a.	n.a.	n.a.	n.a.
112	-12.5	n.a.	n.a.	n.a.	n.a.	n.a.
113	-10.9	n.a.	n.a.	n.a.	n.a.	n.a.
114	-11.5	n.a.	n.a.	n.a.	n.a.	n.a.
115	-9.80	n.a.	n.a.	n.a.	n.a.	n.a.
116	-12.4	n.a.	n.a.	n.a.	n.a.	n.a.
119	-14.2	n.a.	n.a.	n.a.	n.a.	n.a.
120	-13.8	n.a.	n.a.	n.a.	n.a.	n.a.
121	-9.20	n.a.	n.a.	n.a.	n.a.	n.a.
123	-12.5	n.a.	n.a.	n.a.	n.a.	n.a.
124	-12.0	-20.0	n.a.	n.a.	n.a.	n.a.
125	-10.9	n.a.	n.a.	n.a.	n.a.	n.a.
126	-11.9	n.a.	n.a.	n.a.	n.a.	n.a.
127	-10.2	n.a.	n.a.	n.a.	n.a.	n.a.
129	-12.4	n.a.	n.a.	n.a.	n.a.	n.a.
130	-10.4	n.a.	n.a.	n.a.	n.a.	n.a.
131	-12.1	n.a.	n.a.	n.a.	n.a.	n.a.
132	-8.50	n.a.	n.a.	n.a.	n.a.	n.a.
133	-10.0	n.a.	n.a.	n.a.	n.a.	n.a.
134	-9.80	n.a.	n.a.	n.a.	n.a.	n.a.
135	-9.60	n.a.	n.a.	n.a.	n.a.	n.a.
136	n.a.	-9.20	0.24	3.85	0.17	0.007
137	-10.9	n.a.	n.a.	n.a.	n.a.	n.a.
138	-8.00	n.a.	n.a.	n.a.	n.a.	n.a.
139	-9.66	n.a.	n.a.	n.a.	n.a.	n.a.
141	-6.11	n.a.	n.a.	n.a.	n.a.	n.a.
142	-11.1	n.a.	n.a.	n.a.	n.a.	n.a.
143	-10.8	n.a.	n.a.	n.a.	n.a.	n.a.
144	-9.47	n.a.	n.a.	n.a.	n.a.	n.a.
145	-13.2	n.a.	n.a.	n.a.	n.a.	n.a.
146	-13.4	n.a.	n.a.	n.a.	n.a.	n.a.
147	-12.2	n.a.	n.a.	n.a.	n.a.	n.a.
148	-13.7	n.a.	n.a.	n.a.	n.a.	n.a.
149	-14.7	n.a.	n.a.	n.a.	n.a.	n.a.
150	-14.5	n.a.	n.a.	n.a.	n.a.	n.a.
151	-11.9	n.a.	n.a.	n.a.	n.a.	n.a.
152	-9.45	n.a.	n.a.	n.a.	n.a.	n.a.
153	-8.56	n.a.	n.a.	n.a.	n.a.	n.a.
154	-11.3	n.a.	n.a.	n.a.	n.a.	n.a.
155	-13.4	n.a.	n.a.	n.a.	n.a.	n.a.
156	-8.14	n.a.	n.a.	n.a.	n.a.	n.a.
157	-11.6	n.a.	n.a.	n.a.	n.a.	n.a.
158	-13.0	n.a.	n.a.	n.a.	n.a.	n.a.
159	-7.70	n.a.	n.a.	n.a.	n.a.	n.a.
160	-9.79	n.a.	n.a.	n.a.	n.a.	n.a.
161	-11.6	n.a.	n.a.	n.a.	n.a.	n.a.
162	-8.21	n.a.	n.a.	n.a.	n.a.	n.a.
163	-8.76	n.a.	n.a.	n.a.	n.a.	n.a.
164	-11.7	n.a.	n.a.	n.a.	n.a.	n.a.

ID	$\delta^{13}\text{C}_{\text{TDIC}}$	$\delta^{13}\text{C}_{\text{CO}_2}$	R/R _A	He/Ne	Rc/R _A	ERROR
165	-11.2	n.a.	n.a.	n.a.	n.a.	n.a.
166	-10.7	n.a.	n.a.	n.a.	n.a.	n.a.
167	-13.8	n.a.	n.a.	n.a.	n.a.	n.a.
168	-10.4	n.a.	n.a.	n.a.	n.a.	n.a.
169	-14.3	n.a.	n.a.	n.a.	n.a.	n.a.
170	-13.5	n.a.	n.a.	n.a.	n.a.	n.a.
171	-14.5	n.a.	n.a.	n.a.	n.a.	n.a.
172	-10.3	n.a.	n.a.	n.a.	n.a.	n.a.
173	-10.5	n.a.	n.a.	n.a.	n.a.	n.a.
174	-10.4	n.a.	n.a.	n.a.	n.a.	n.a.
175	-0.10	n.a.	n.a.	n.a.	n.a.	n.a.
176	-9.20	n.a.	n.a.	n.a.	n.a.	n.a.
178	-9.90	n.a.	n.a.	n.a.	n.a.	n.a.
179	-10.4	n.a.	n.a.	n.a.	n.a.	n.a.
180	-6.10	n.a.	n.a.	n.a.	n.a.	n.a.
181	-10.00	n.a.	n.a.	n.a.	n.a.	n.a.
182	-8.00	-29.9	n.a.	n.a.	n.a.	n.a.
183	-6.30	-18.7	n.a.	n.a.	n.a.	n.a.
184	-8.40	n.a.	n.a.	n.a.	n.a.	n.a.
185	-10.2	n.a.	n.a.	n.a.	n.a.	n.a.
186	-10.9	n.a.	n.a.	n.a.	n.a.	n.a.
187	-7.10	-16.2	n.a.	n.a.	n.a.	n.a.
188	-10.2	n.a.	n.a.	n.a.	n.a.	n.a.
189	-7.50	n.a.	n.a.	n.a.	n.a.	n.a.
191	-12.6	n.a.	n.a.	n.a.	n.a.	n.a.
192	-14.8	n.a.	n.a.	n.a.	n.a.	n.a.
193	-11.6	n.a.	n.a.	n.a.	n.a.	n.a.
194	-12.3	n.a.	n.a.	n.a.	n.a.	n.a.
195	-10.5	n.a.	n.a.	n.a.	n.a.	n.a.
196	-12.4	n.a.	n.a.	n.a.	n.a.	n.a.
197	-12.8	n.a.	n.a.	n.a.	n.a.	n.a.
198	-13.0	n.a.	n.a.	n.a.	n.a.	n.a.
199	-13.5	n.a.	n.a.	n.a.	n.a.	n.a.
200	-13.2	n.a.	n.a.	n.a.	n.a.	n.a.
201	-13.2	n.a.	n.a.	n.a.	n.a.	n.a.

n.a. – not analysed.

Table A8

Identification number, geographical coordinates, types of emission of the collected gas manifestation of North Macedonia.

ID	Name	Date	Latitude	Longitude	Type I	Type II	Type III
1	Smrdliva Voda	18.08.2019	41.19243	22.28152	free gas	cold	CO ₂ -dominated
2	Smrdliva Voda	18.08.2019	41.19243	22.28152	free gas	cold	CO ₂ -dominated
3	Gornicet	18.08.2019	41.16083	22.41983	free gas	cold	CO ₂ -dominated
4	Gornicet1	18.08.2019	41.16083	22.41983	free gas	cold	CO ₂ -dominated
5	Makedonska Cheshma	18.08.2019	41.18647	22.30188	dissolved gas	cold	CO ₂ -dominated
6	Smokvica	19.08.2019	41.24058	22.49524	free gas	thermal	N ₂ -dominated
7	Smokvica	19.08.2019	41.24058	22.49524	free gas	thermal	N ₂ -dominated
8	Negorci	19.08.2019	41.17315	22.48877	free gas	thermal	N ₂ -dominated
9	Negorci	19.08.2019	41.17315	22.48877	dissolved gas	thermal	N ₂ -dominated
10	Istibanja 3	20.08.2019	41.92204	22.49472	free gas	thermal	CO ₂ -dominated
11	Kezhovica	20.08.2019	41.73288	22.17707	dissolved gas	thermal	N ₂ -dominated
12	Katlanovo borehole	21.08.2019	41.90177	21.68783	free gas	cold	CO ₂ -dominated
13	Katlano fountain	21.08.2019	41.90056	21.68471	free gas	cold	CO ₂ -dominated
14	Strnovac Banja	21.08.2019	42.19602	21.85743	free gas	cold	CO ₂ -dominated
15	Kumanovska Banja	21.08.2019	42.12213	21.74534	free gas	thermal	CO ₂ -dominated
16	Kosel	22.08.2019	41.16932	20.83721	soil gas	cold	H ₂ S-rich
17	Leshok	22.08.2019	42.07404	21.04007	free gas	cold	CO ₂ -dominated
18	Banjiche pool	22.08.2019	42.02493	20.94441	free gas	cold	CO ₂ -dominated
19	Banjishte (Debarska Banja)	23.08.2019	41.55872	20.53068	free gas	thermal	H ₂ S-rich
20	Kosovrasti	23.08.2019	41.53315	20.57759	free gas	thermal	H ₂ S-rich
21	Kosovrasti 1	23.08.2019	41.53290	20.58055	dissolved gas	thermal	H ₂ S-rich
22	Bitola	24.08.2019	40.92422	21.44796	free gas	cold	CO ₂ -dominated
23	Bitola 2	26.08.2019	40.92452	21.43828	dissolved gas	cold	CO ₂ -dominated
24	Gornicet river	01.03.2020	41.16083	22.41983	free gas	cold	CO ₂ -dominated
25	Banjiche_pool	01.03.2020	42.02493	20.94441	free gas	cold	CO ₂ -dominated
26	Kosel	02.03.2020	41.16932	20.83721	soil gas	cold	H ₂ S-rich
27	Kosel A	02.03.2020	41.16932	20.83721	soil gas	cold	H ₂ S-rich
28	Kosel B	02.03.2020	41.16932	20.83721	soil gas	cold	H ₂ S-rich
29	Botun 2	03.03.2020	41.29789	20.77285	free gas	cold	H ₂ S-rich
30	Botun 3	03.03.2020	41.29789	20.77285	free gas	cold	H ₂ S-rich
31	Botun Creek	03.03.2020	41.29789	20.77285	free gas	cold	H ₂ S-rich
32	Botun 1	03.03.2020	41.29789	20.77285	dissolved gas	cold	H ₂ S-rich
33	Geogas	04.03.2020	41.07620	21.41292	free gas	cold	CO ₂ -dominated
34	Pela Rosa	04.03.2020	40.92398	21.46732	free gas	cold	CO ₂ -dominated
35	Pela Rosa deep	04.03.2020	40.92263	21.46620	free gas	cold	CO ₂ -dominated
36	Pelagonka	04.03.2020	40.92404	21.46045	dissolved gas	cold	CO ₂ -dominated
37	Kisela Voda	04.03.2020	40.98811	21.35126	dissolved gas	cold	CO ₂ -dominated
38	Busemak	05.03.2020	40.94094	21.53208	free gas	cold	CO ₂ -dominated
39	Germijan	05.03.2020	40.91100	21.52124	dissolved gas	cold	CO ₂ -dominated
40	Topli Dol 1	06.03.2020	41.18428	21.99180	dissolved gas	cold	CO ₂ -dominated
41	Negorci	07.03.2020	41.17315	22.48877	dissolved gas	thermal	N ₂ -dominated
42	Gornicet	02.10.2022	41.16083	22.41983	free gas	cold	CO ₂ -dominated
43	Smirdliva Voda	02.10.2022	41.19243	22.28152	free gas	cold	CO ₂ -dominated
44	Smokvica	02.10.2022	41.24058	22.49524	free gas	thermal	N ₂ -dominated
45	Bansko	03.10.2022	41.38244	22.75454	free gas	thermal	N ₂ -dominated

ID	Name	Date	Latitude	Longitude	Type I	Type II	Type III
46	Bansko	03.10.2022	41.38244	22.75454	dissolved gas	thermal	N ₂ -dominated
47	Bansko spring	03.10.2022	41.38244	22.75454	dissolved gas	thermal	N ₂ -dominated
48	Raklish	03.10.2022	41.63024	22.48857	dissolved gas	cold	N ₂ -dominated
49	Dobra	03.10.2022	41.89634	22.38409	dissolved gas	thermal	N ₂ -dominated
50	Sabotna Voda	03.10.2022	41.72169	21.80819	dissolved gas	cold	H ₂ S-rich
51	Krusheani	04.10.2022	41.31091	21.34925	free gas	cold	CO ₂ -dominated
52	Gneotino 1	04.10.2022	40.96344	21.50994	free gas	cold	CO ₂ -dominated
53	Gneotino 2	04.10.2022	40.96610	21.51349	free gas	cold	CO ₂ -dominated
54	Logovardi	04.10.2022	41.02987	21.40195	free gas	cold	CO ₂ -dominated
55	Medzitlija	04.10.2022	40.92730	21.42984	dissolved gas	cold	CO ₂ -dominated
56	Kozica 1	05.10.2022	41.42039	20.91659	free gas	cold	CO ₂ -dominated
57	Petkoniva	05.10.2022	41.31439	20.76805	soil gas	cold	H ₂ S-rich
58	Svinjishte	05.10.2022	41.43473	20.91208	dissolved gas	cold	CO ₂ -dominated
59	Kiselo Klajnche	05.10.2022	41.30847	20.77937	dissolved gas	cold	H ₂ S-rich
60	Botun	06.10.2022	41.29789	20.77285	free gas	cold	H ₂ S-rich
61	Kosel	06.10.2022	41.16932	20.83721	soil gas	cold	H ₂ S-rich
62	Kosovrasti	07.10.2022	41.53315	20.57759	free gas	thermal	H ₂ S-rich
63	Banjishte	07.10.2022	41.55872	20.53068	free gas	thermal	H ₂ S-rich
64	Banjiche	08.10.2022	42.02493	20.94441	free gas	cold	CO ₂ -dominated
65	Banjiche fountain	08.10.2022	42.02493	20.94441	free gas	cold	CO ₂ -dominated

Table A9

Chemical and isotope composition of the collected gas manifestation of North Macedonia.

ID	He μmol mol ⁻¹	H ₂ μmol mol ⁻¹	O ₂ μmol mol ⁻¹	N ₂ μmol mol ⁻¹	CO μmol mol ⁻¹	CH ₄ μmol mol ⁻¹	CO ₂ μmol mol ⁻¹	H ₂ S μmol mol ⁻¹	Ar μmol mol ⁻¹	δ ¹³ C _{CO2} ‰ vs. PDB	δ ¹³ C _{CH4} ‰ vs. PDB	δ ² H _{CH4} ‰ vs. SMOW	R/R _A	He/Ne	Rc/R _A	ERROR	⁴⁰ Ar/ ³⁶ Ar	³⁸ Ar/ ³⁶ Ar
1	19.0	b.d.l.	4,600	2,7100	4.60	5,041	967,600	b.d.l.	491	0.90	-20.8	-146	n.a	n.a	n.a	n.a	n.a	n.a
2	11.0	b.d.l.	3,800	15,300	3.70	3,085	966,400	b.d.l.	172	1.0	-20.6	-99	1.64	60.1	1.64	0.02	307	0.192
3	2.11	b.d.l.	2,700	8,500	1.90	9.00	973,700	b.d.l.	279	-2.5	n.a	n.a	0.88	1.13	0.84	0.01	300	0.187
4	12.0	b.d.l.	46,300	94,500	3.70	42.0	843,400	b.d.l.	1,130	-0.3	n.a	n.a	n.a	n.a	n.a	n.a	n.a	n.a
5	b.d.l.	b.d.l.	54,300	273,300	b.d.l.	61.4	672,400	b.d.l.	n.a	n.a	n.a	n.a	n.a	n.a	n.a	n.a	n.a	n.a
6	2,556	60.0	1,100	963,100	5.00	19,800	1,400	b.d.l.	10,000	-15.7	-7.2	-80	0.87	203	0.87	0.01	301	0.189
7	2,363	b.d.l.	12,100	949,800	15.0	20,200	400	b.d.l.	n.a	n.a	n.a	n.a	n.a	n.a	n.a	n.a	n.a	n.a
8	711	b.d.l.	55,200	933,700	10.0	1,223	19,300	b.d.l.	11,100	n.a	n.a	n.a	n.a	n.a	n.a	n.a	n.a	n.a
9	308	18.7	74,400	921,600	b.d.l.	1,220	2,500	b.d.l.	n.a	-22.6	n.a	n.a	1.09	12.8	1.09	0.011	n.a	n.a
10	578	4.20	682	175,800	3.60	2,853	814,400	b.d.l.	2,930	-4.60	-21.1	-110	0.42	321	0.42	0.01	301	0.189
11	3,552	60.3	84,800	900,000	b.d.l.	7,081	4,500	b.d.l.	n.a	n.a	n.a	n.a	0.65	50.3	0.65	0.01	n.a	n.a
12	14.0	b.d.l.	488	9,200	3.40	386	975,300	b.d.l.	216	-2.60	n.a	n.a	0.76	38.4	0.76	0.01	303	0.191
13	0.840	b.d.l.	2,300	8,100	4.60	30.0	971,500	b.d.l.	94.0	-2.60	n.a	n.a	0.61	5.43	0.58	0.01	296	0.198
14	89.0	b.d.l.	136	28,900	3.30	20.0	952,900	b.d.l.	375	-2.90	n.a	n.a	0.22	473	0.22	0.00	302	0.189
15	7.40	b.d.l.	340	24,600	2.00	1.60	963,000	b.d.l.	379	-4.10	n.a	n.a	0.37	36.5	0.36	0.00	299	0.188
16	70.0	38.0	128	17,900	1.90	3,251	966,100	5500	79.0	-0.20	-34.4	-166	0.10	472	0.10	0.00	330	0.190
17	0.270	b.d.l.	109	1,300	1.50	120	980,600	b.d.l.	96.0	-1.50	n.a	n.a	1.02	1.12	1.03	0.02	295	0.190
18	2.31	b.d.l.	50.0	6,600	2.50	466	976,500	b.d.l.	114	-1.20	-19.7	n.a	1.19	22.2	1.19	0.01	304	0.190
19	827	b.d.l.	b.d.l.	218900	4.50	5,212	767,300	3,600	2,890	-1.40	-31.6	-163	0.16	333	0.16	0.00	304	0.189
20	15.0	7.00	b.d.l.	14,600	4.20	334	977,900	11,600	255	-1.60	-30.2	n.a	0.15	48.4	0.15	0.00	301	0.188
21	b.d.l.	b.d.l.	1,800	717,100	b.d.l.	550	280,600	b.d.l.	n.a	n.a	n.a	n.a	n.a	n.a	n.a	n.a	n.a	
22	2.68	b.d.l.	184	4,600	2.80	92.0	998,000	b.d.l.	249	-1.80	-17.5	-84	0.55	5.93	0.52	0.01	306	0.189
23	1.00	b.d.l.	3,900	78,500	b.d.l.	4.19	917,600	b.d.l.	n.a	n.a	n.a	n.a	0.66	0.64	0.38	0.014	n.a	n.a
24	4.40	b.d.l.	9,100	24,900	1.70	13.0	964,500	b.d.l.	432	-3.30	-19.5	n.a.	0.75	10.5	0.74	0.01	293	0.188
25	1.09	b.d.l.	879	5,900	b.d.l.	272	990,700	b.d.l.	92.6	-1.70	-20.0	-103	1.14	21.81	1.14	0.01	300	0.190
26	62.0	b.d.l.	19,300	89,800	2.10	2,875	882,600	5,200	n.a	-0.80	-34.5	-180	0.10	2066	0.10	0.00	372	0.188
27	56.0	b.d.l.	26,600	117,900	1.80	2,744	850,800	3,800	n.a	-0.80	-35.0	-175	n.a	n.a	n.a	n.a	n.a	
28	51.0	b.d.l.	19,000	88,800	1.30	3,190	888,400	4,300	n.a	-0.80	-36.5	-169	n.a	n.a	n.a	n.a	n.a	
29	192	b.d.l.	803	27,200	b.d.l.	2,687	974,900	1,454	n.a	0.10	-51.5	-278	n.a	n.a	n.a	n.a	n.a	
30	188	b.d.l.	691	25,500	b.d.l.	2,409	972,800	2,800	n.a	0.20	-48.2	-249	n.a	n.a	n.a	n.a	n.a	
31	218	b.d.l.	1,600	30,900	b.d.l.	2,844	963,800	785	361	0.40	-49.9	-250	0.08	391	0.08	0.00	297	0.190
32	432	6.16	3,850	681,800	2.71	352	313,500	b.d.l.	n.a	3.98	n.a	n.a	0.08	11.2	0.06	0.006	n.a	n.a

Appendix A2 – Table A9

ID	He	H ₂	O ₂	N ₂	CO	CH ₄	CO ₂	H ₂ S	Ar	$\delta^{13}\text{C}_{\text{CO}_2}$	$\delta^{13}\text{C}_{\text{CH}_4}$	$\delta^2\text{H}_{\text{CH}_4}$	R/R _A	He/Ne	Rc/R _A	ERROR	$^{40}\text{Ar}/^{36}\text{Ar}$	$^{38}\text{Ar}/^{36}\text{Ar}$
33	9.00	b.d.l.	31,700	127,300	0.800	414	839,000	b.d.l.	87.8	-6.50	-57.8	n.a.	0.33	3.72	0.27	0.03	297	0.190
34	0.530	b.d.l.	26,800	108,600	b.d.l.	12.0	877,400	b.d.l.	507	-2.00	n.a	n.a	0.86	0.50	0.61	0.01	294	0.188
35	b.d.l.	b.d.l.	1,000	3,600	0.600	24.0	989,600	b.d.l.	52.6	-2.00	n.a	n.a	0.76	1.16	0.66	0.02	294	0.188
36	1.00	237	3,800	75,400	3.61	14.2	920,600	b.d.l.	n.a	3.27	n.a	n.a	0.62	0.99	0.47	0.012	n.a	n.a
37	1.00	111	2,910	40,500	23.0	908	955,600	b.d.l.	n.a	2.33	n.a	n.a	0.55	2.17	0.49	0.008	n.a	n.a
38	0.860	b.d.l.	35,200	133,500	1.70	20.0	828,500	b.d.l.	24.8	-4.20	n.a	n.a	0.45	12.3	0.44	0.01	285	0.197
39	1.00	255	6,700	59,200	47.5	38.9	933,800	b.d.l.	n.a	4.92	n.a	n.a	0.64	1.06	0.51	0.011	n.a	n.a
40	150	59.7	31,600	493,000	61.3	899	474,200	b.d.l.	n.a	-0.32	n.a	n.a	1.81	9.54	1.83	0.017	n.a	n.a
41	1,133	282	6,600	989,200	4.41	1,644	112	b.d.l.	n.a	n.a	n.a	n.a	n.a	n.a	n.a	n.a	n.a	n.a
42	b.d.l.	b.d.l.	3,100	6,600	1.40	0.800	991,000	b.d.l.	237	-2.00	n.a	n.a	0.94	18.7	0.93	0.01	297	0.190
43	10.0	b.d.l.	1,200	7,000	0.800	2,260	993,000	b.d.l.	n.a	0.80	n.a	n.a	n.a	n.a	n.a	n.a	n.a	n.a
44	2,948	44	461	968,000	1.80	22,500	10,400	b.d.l.	n.a	-3.20	-8.3	-116	n.a	n.a	n.a	n.a	n.a	n.a
45	255	3.40	143,400	822,800	b.d.l.	1,823	30,200	b.d.l.	n.a	-10.6	-59.6	n.a	n.a	n.a	n.a	n.a	n.a	n.a
46	117	b.d.l.	131,300	860,800	2.65	1,109	6,770	b.d.l.	n.a	n.a	n.a	n.a	0.147	11.8	0.13	0.00	n.a	n.a
47	20.8	25.1	157,800	837,600	16.3	251	4,310	b.d.l.	n.a	n.a	n.a	n.a	n.a	n.a	n.a	n.a	n.a	n.a
48	16.5	8.31	138,300	835,600	b.d.l.	32.3	26,100	b.d.l.	n.a	n.a	n.a	n.a	0.601	1.25	0.48	0.01	n.a	n.a
49	522	13.9	37,100	897,600	0.51	457	64,400	b.d.l.	n.a	n.a	n.a	n.a	0.589	40.4	0.59	0.01	n.a	n.a
50	2,063	42.2	3,630	972,700	b.d.l.	2,228	19,300	200	n.a	n.a	n.a	n.a	0.364	209	0.36	0.00	n.a	n.a
51	35	b.d.l.	204	20,200	b.d.l.	6.00	981,000	b.d.l.	227	-7.72	n.a	n.a	0.46	185	0.46	0.00	298	0.186
52	b.d.l.	b.d.l.	17,600	71,000	b.d.l.	4.60	902,000	b.d.l.	n.a	-2.86	n.a	n.a	n.a	n.a	n.a	n.a	n.a	n.a
53	2.20	b.d.l.	b.d.l.	3,200	b.d.l.	264	992,000	b.d.l.	120	-2.80	-41.4	n.a	0.60	46.3	0.60	0.00	296	0.190
54	3.40	b.d.l.	515	5,000	b.d.l.	5.00	999,000	b.d.l.	72.3	-1.95	n.a	n.a	0.76	31.5	0.76	0.01	296	0.187
55	b.d.l.	b.d.l.	3,450	122,000	21.5	11.2	874,500	b.d.l.	n.a	n.a	n.a	n.a	0.841	1.04	0.78	0.01	n.a	n.a
56	20.0	b.d.l.	2,000	106,000	b.d.l.	7.00	898,000	14.0	789	-7.34	n.a	n.a	0.12	20.7	0.11	0.00	298	0.188
57	173	2.00	244	15,800	0.600	1,318	959,000	4,500	908	0.60	-43.6	n.a	0.10	114	0.10	0.00	299	0.186
58	38.6	1549	26,600	389,400	3.39	12.6	582,400	b.d.l.	n.a	n.a	n.a	n.a	0.263	4.35	0.21	0.00	n.a	n.a
59	142	8.4	92,500	697,200	b.d.l.	b.d.l.	210,200	b.d.l.	n.a	n.a	n.a	n.a	n.a	n.a	n.a	n.a	n.a	n.a
60	206	b.d.l.	b.d.l.	21,800	1.10	2,875	974,000	b.d.l.	285	0.70	-52.8	-303	0.10	565	0.10	0.00	330	0.187
61	66.0	5.00	5,100	35,900	b.d.l.	3,121	938,000	7,300	307	n.a	-36.3	-180	0.12	147	0.12	0.00	299	0.186
62	6.00	2.20	3,300	18,400	2.40	154	980,000	12,800	n.a	-1.70	-33.0	-167	n.a	n.a	n.a	n.a	n.a	n.a
63	554	b.d.l.	b.d.l.	208,000	b.d.l.	3,100	787,000	623	n.a	n.a	-41.8	-192	n.a	n.a	n.a	n.a	n.a	n.a
64	b.d.l.	1.7	698	4,200	1.70	270	994,000	b.d.l.	283	-1.10	-20.6	-122	1.25	1.95	1.30	0.01	299	0.192
65	b.d.l.	9.0	14.0	2,600	0.500	74.0	999,000	b.d.l.	n.a.	-1.30	n.a	n.a	n.a	n.a	n.a	n.a	n.a	n.a

b.d.l. – below detection limit; n.a. – not analysed.